Hierachical control of a meshed DC microgrid through constrained optimization

Igyso Zafeiratou

THÈSE

Pour obtenir le grade de

DOCTEUR DE L'UNIVERSITÉ GRENOBLE ALPES

Spécialité : **AUTOMATIQUE - PRODUCTIQUE**

Arrêté ministériel : 25 mai 2016

Présentée par

Igyso ZAFEIRATOU

Thèse dirigée par **Laurent LEFÈVRE,**
co-encadrée par **Ionela PRODAN et Laurent PIÉTRAC**

préparée au sein du **Laboratoire de Conception et d'Intégration des Systèmes**
dans **l' École Doctorale Électronique, Électrotechnique, Automatique, Traitement du Signal EEATS (EEATS)**

Commande hiérarchique d'un micro-réseau maillé en courant continu par optimisation contrainte

Hierarchical control of a meshed DC microgrid through constrained optimization

Thèse soutenue publiquement le **06 Février 2020**,
devant le jury composé de :

M. Laurent LEFÈVRE
Professeur, Institut Polytechnique de Grenoble, Directeur de thèse
Mme. Ionela PRODAN
Maître de Conf., Institut Polytechnique de Grenoble, Co-Encadrante de thèse
M. Laurent PIÉTRAC
Maître de Conf., Université de Lyon, Co-Encadrant de thèse
M. Sorin OLARU
Professeur, CentraleSupélec, Rapporteur
M. Serge PIERFEDERICI
Professeur, Université de Lorraine, Rapporteur
M. Bernhard MASCHKE
Professeur, Claude Bernard Université de Lyon 1, Président
M. Robin ROCHE
Maître de Conf., Université de Belfort Montbéliard, Examinateur

Hierarchical control of a meshed DC microgrid through constrained optimization

Igyso ZAFEIRATOU

PhD Thesis 2020

Laboratoire de Conception et d'Intégration des Systèmes (LCIS)
Université Grenoble Alpes, LCIS, F-26902, France

Dedicated to my beloved husband, Thanos.
For his endless support.

Acknowledgments

This thesis is the result of a three-year work within the laboratory LCIS of Grenoble INP based in Valence, France. It was funded by the French National Research Agency within the framework of the project ANR-15-CE05-004-02 $C^3\mu$ (Components, Control and Communication). During this important period of my life, I have succeeded my objectives due to the help and support of many people and I take this opportunity to express my gratitude to all of them.

Firstly, I would like to express my sincere gratitude to my supervisors Professor Laurent LEFEVRE and Associate Professor Ionela PRODAN who helped and encouraged me at all stages of my thesis with great patience and immense care. Their guidance helped me in all the time of research and writing of this thesis. Their motivation and immense knowledge gave me the passion to develop and continue improving my work. I truly appreciate their high availability, their contributions, ideas and insights that made my PhD productive, fruitful and stimulating. Additionally, after numerous friendly dinners and outdoor activities, I consider them as friends to whom I could always feel free to share and express my opinion and emotion. I could not have imagined better supervisors for my PhD studies.

Next, I would like to thank the jury members, Professor Bernard MASCHKE and Associate Professor Robin ROCHE, and, especially the reviewers, Professor Sorin OLARU and Professor Serge PIERFEDERICI, for their time and effort to evaluate my thesis and their valuable comments, remarks and questions that helped me to improve the quality of the manuscript and will help me to further ameliorate and enhance my work.

I would like also to thank Associate Professor Laurent PIETRAC, the second co-supervisor of my thesis, who was present whenever was needed. Moreover, I thank him for the time he spent evaluating my manuscript and my work through this period of time.

During the last year of my PhD, I had also the chance to visit the University of London and collaborate with Associate Professor Francesca BOEM. I would like to thank her for the warm welcome, for her interesting ideas and the fruitful discussions on combining my work with fault detection mechanisms. Furthermore, I would like to thank Mr. Than Hung PHAM, former PhD student of LCIS, for his kind discussions on various problems concerning the modeling part of the thesis. I thank also M. Ngoc Thinh NGYUEN, former PhD student of LCIS, for helping me to further understand different methods of automation control.

I also take this opportunity to thank Associate Professor David HELY and his family for their immense support and help to me and my husband during our stay in France. Furthermore, I thank Mr. Cedric CARLOTTI in the computing service for his invaluable support and availability whenever we needed it.

I am grateful also to the LCIS administration team, Ms. Carole SEYVET and Ms. Caroline PALISSE, current administration team of the laboratory, and Ms. Jennyfer DUBERVILLE, former member of the administration team, who helped me to easily integrate in the laboratory daily life. They were always available for any administrative issues, giving me this way the time to focus on my work.

I am thankful also to Associate Professor André LAGREZE, Associate Professor at LCIS, for organizing many outdoor activities giving me the opportunity to discover nice and interesting places.

A huge thanks to the numerous friends that I made in the laboratory, that became also part of my life. My time at LCIS was enjoyable. It will remain an unforgettable experience that I will always value.

I would like to dedicate my biggest thank to my family, my mother, my father, and my brother, Maria, Christos and Vangelis, to whom I owe everything I am today. Their endless love and support accompany me all these years giving me always the strength, the courage and the willingness in everything I do.

At the end, I would like to express my endless appreciation to my beloved husband, Thanos, who always supports me and stands by my side. I truly thank him for always believing in me and encouraging my decisions. His infinite support, patience and persistence give me always the strength to accomplish and achieve my goals. This is why this work is dedicated to him, for the faith he has in me.

Igyso ZAFEIRATOU

Abstract

The thesis aims at solving the energy management problem for a meshed DC microgrid. The microgrid under study is composed by a renewable energy source (solar panels (PV)), an energy storage (ES) system composed by lead-acid batteries, a number of DC/DC converters and a number of loads (office and housing devices, electrical vehicles and the like). The microgrid is connected to the external grid, which together with the solar panels constitute the main power sources of the system. The DC microgrid can be disconnected from the utility grid and work in islanded mode avoiding occasional power outages or other unexpected events. The central transmission network, otherwise called the common DC-bus, is a high voltage network for which the power losses are considered. Power balancing, cost minimization, power dissipation, battery scheduling, converters' switching activity are taken into account to solve the optimal energy management problem.

Microgrids are convoluted physical systems and many problems arise and remain open for investigation. Such problems are the power distribution, the power quality, the topology, the sizing of renewable sources and storing devices. Furthermore, the complexity in the dynamics leads to multiple timescales, nonlinearities, constraints, stability issues and uncertainties. Hence, the implementation of an optimization control strategy becomes challenging and specific modeling and control approaches need to be considered according to the defined objectives.

For an effective and reliable operation of the microgrid, it is important to include in the control model the physical properties of the system, specifically the power conservation among the system's interconnections. Port-Hamiltonian (PH) modeling is, therefore, an appropriate method which describes the power-preserving interconnections among the elements of the network. The PH state-space representation may be generated from its associated Bond graph, which provides a graphical representation of multi-physical systems. A PH model is proposed for the considered DC microgrid, including the Bond graphs and the PH representations for each component separately. The PH model is inverted using differential flatness which leads to the flat representation of each component of the micorgrid (PV, ES, loads, connected to the DC/DC converters). With the inverse dynamics, the states and the control inputs are derived in function of the flat outputs and are used, subsequently, in the formulation of the optimization problem. The multi-scale dynamics is controlled through a hierarchical architecture divided in three levels. Firstly, at the high level, optimal profiles are generated under a flatness-based optimization control approach for power balancing, cost minimization and decrease of the power dissipation. B-spline parametrization handles continuous-time constraint validation. At the middle level, a model predictive controller is developed to track the optimal profiles obtained at the high level in the presence of bounded disturbances. Finally, at the low level, the tracking profiles are considered as references for the control of the DC/DC converters through switch regulation. The proposed approach is validated via extensive simulations over a meshed DC microgrid using real profile data for the loads, the external temperature and the solar irradiation.

Résumé

L'objectif principal de la thèse est la résolution du problème de gestion d'énergie dans un microréseau maillé en courant continu (CC). Le microréseau à l'étude est composé d'une source d'énergie renouvelable (panneaux solaires), d'un système de stockage d'énergie, lui-même composé de batteries au plomb-acide, de convertisseurs CC et de charges (appareils domestiques ou professionnels, véhicules électriques, etc.). Le microréseau est connecté au réseau externe qui, avec les panneaux solaires, constituent les sources principales du système. Le microréseau en CC peut être déconnecté du réseau externe et fonctionner ainsi indépendamment en évitant les coupures de courant occasionnelles. Le réseau de transmission central, appelé bus CC commun, est un réseau de haute tension. Les pertes de puissance dans les lignes de transmission sont prises en compte. L'équilibrage de la puissance, la minimisation des coûts, la dissipation de la puissance, la planification de la batterie, le contrôle des interrupteurs dans les convertisseurs seront pris en compte.

Les microréseaux sont des systèmes physiques compliqués et de nombreux problèmes se posent et restent ouverts. Ces problèmes concernent notamment la distribution d'énergie, la qualité d'énergie, la topologie, le dimensionnement des sources d'énergie renouvelables et des éléments de stockage, le type des composants et la structure. La dynamique est complexe avec des échelles temporelles multiples, des non linéarités, des contraintes, des problèmes de stabilité et des incertitudes. Par conséquent, la mise en œuvre d'une stratégie de commande optimale est difficile et des approches de modélisation et de commande spécifiques doivent être considérées.

L'approche hamiltonienne à port est une méthode de modélisation qui décrit la conservation de la puissance et de l'énergie entre les éléments physiques du réseau. La représentation d'état sous forme hamiltonienne peut être générée à partir du Bond graph associé, qui est une représentation graphique intuitive de type circuit du système consideré. Un modèle hamiltonien à port est proposé pour le micro-réseau en CC considéré, comprenant les représentations hamiltoniennes à port pour chaque composant du système séparément. Le modèle hamiltonien à port est inversé en utilisant une méthode de platitude différentielle qui conduit à la représentation plate de chaque partie du micro-réseau (PV, ES, charges, tous connectés aux convertisseurs CC). Avec la dynamique inverse, les états et les entrées de commande sont dérivés en fonction des sorties plates choisies et sont utilisés par la suite dans la formulation du problème d'optimisation. La dynamique multi-échelle est traitée par une approche de commande hiérarchique divisée en trois niveaux. Tout d'abord, au premier niveau, des profils optimaux sont générés pour une approche d'optimisation qui vise à l'équilibrage de la puissance, la réduction de coût et la diminution de la dissipation. La paramétrisation B-spline est considérée pour la validation des contraintes à temps continu dans ce problème d'optimization et pour la génération de trajectoires plates. Au niveau secondaire, un contrôleur de type Model Predictive Control est développé pour suivre les profils optimaux obtenus dans le niveau supérieur. Des perturbations sont prises en compte et les erreurs du système sont analysées. Enfin, au niveau bas, les profils de suivi sont considérés comme consignes pour la régulation des convertisseurs CC. L'approche proposée est validée à travers des simulations approfondies sur un microréseau maillé en CC utilisant des profils réels pour les charges, la température extérieure et le rayonnement solaire.

Notations

A description of some notions is provided in order to facilitate the coherence and the understanding of the techniques discussed in the text.

- **Bond graph** (Karnopp et al., 2012): It is a graph-oriented tool which describes the dynamics of complex physical systems. It allows the conversion from a graphical to a state-space representation maintaining the power conservation among the elements.
- **Depth of discharge of a battery**: It indicates the percentage of the capacity removed with respect to the overall capacity of the battery (Spiers, 2012).
- **State of charge of a battery**: It indicates the percentage of the capacity which remains in the battery with respect to the overall capacity (Spiers, 2012).
- **Duty cycle**: It describes the time of an active signal over one period.
- **Fill factor**: It is defined by the difference between the maximum power and the theoretical expected power generated by a solar cell.
- **Down-conversion in a DC/DC converter**: It is the process during which the converter produces an output voltage lower than the input voltage.
- **Up-conversion in a DC/DC converter**: It is the process during which the converter produces an output voltage higher than the input voltage.
- **Jumper**: It is a small electronic device which operates as a conductor and allows the electricity to flow trough specific paths of the electrical circuits. It functions, also, as a switch which can close or open the path.
- **Manifold**: It is a topological space which is locally similar to an Euclidean space. A n-manifold M is a topological space locally homeomorphic with the Euclidean space at the n point (Cannon et al., 1978).
- **Tangent space**: Consider a n-manifold M and x a point of M. The $\mathcal{R}^n$ tangents attach to the x point form the tangent space of M, which is written as T_xM. If γ is a smooth curve which passes from x, then its derivative is a vector in T_xM (Weisstein, 2019).
- **Tangent bundle**: It is the manifold TM, which gathers all the tangent vectors in T_xM for every point x of the n-manifold M (Berger and Gostiaux, 2012).
- **One-form**: An one-form, ω, is a mapping of the tangent bundle TM of the manifold M, $\omega : TM \longrightarrow \mathbb{R}$. Locally, it is a linear map of the tangent space T_xM, $\omega_x : T_xM \longrightarrow \mathbb{R}$, described by a linear combination of differentials of the points x: $\omega_x = \sum_{i=1}^{n} F_i(x)dx_i$ (Misner et al., 1973).
- **Rank in linear algebra**: Rank of a matrix is the dimension of the vector space generated by its columns or rows. It represents the maximal number of linearly independent columns or rows. For a full column rank or a full row rank matrix, each of its columns or rows, respectively, must be linearly independent. (Bourbaki, 2003; Mackiw, 1995).
- **Open subset**: An open subset of $\mathcal{R}$ is a subset E such that for every x in E there exists $\epsilon > 0$ for which $S_\epsilon(x) \in E$. Note that $S_\epsilon(x) = \{y \in \mathcal{R} : dist(x, y) < \epsilon\}$ (Mike Boyle, 2012).
- **Minkowski sum**: It is the sum of two position vectors X_1 and X_2 which is the result of the addition of each vector in X_1 to each vector in X_2.

- **Pontryagin difference**: It is the difference between two position vectors X_1 and X_2. More precisely, it describes the difference between each vector in X_1 and each vector in X_2 resulting in another vector $X_3 : X_3 + X_2 \subseteq X_1$.
- **Convex set**: A set $\mathcal{S}$ is convex if the line segment of x and y belongs to $\mathcal{S}$ for all $x \in \mathcal{S}$ and $y \in \mathcal{S}$ (Lauritzen, 2009).
- **Convex hull**: The convex hull, $conv(\mathcal{S})$, of a set of points $\mathcal{S}$ is the intersection of all convex sets that contain the $\mathcal{S}$ (Weisstein, 2006).

Nomenclature

Bond graph (causal and bicausal) and port-Hamiltonian systems

Notation	Description
JS	Junction structure
S_e	voltage sources
S_f	current sources
F	flow matrix
E	effort matrix
f	flow
e	effort
SS	source-sensor elements
D_e	effort detector
D_f	flow detector
p	magnetic flux
q	charge
H	the Hamiltonian, the energy stored in a physical system
DS	Dirac structure
PH	port-Hamiltonian
x	state vector of the system $\in R^n$
u	input vector of the system $\in R^m$
y	output vector of the system $\in R^m$
J	skew-symmetric matrix $\in R^{n\times n}$ in function of time for linear case
Q	diagonal matrix of circuit's parameters $\in R^{n\times n}$
R	dissipation matrix of the system $\in R^{n\times n}$
G	control matrix of the system $\in R^{n\times m}$
D	throughput matrix of the system $\in R^{m\times m}$

Differential flatness and B-splines parametrization

Notation	Description
z	flat output
n	number of states
m	number of control inputs
l	number of outputs
N	number of control points p
n_α	number of control points p for the α factor
$\boldsymbol{d}$	order of the B-spline
$\boldsymbol{d}_a$	order of the B-spline for the α factor
r	derivative of the B-spline
$\boldsymbol{p}_i$	i_{th} control point
$\boldsymbol{b}_{i,\boldsymbol{d}}(t)$	i_{th} B-spline of order d
$\mathcal{B}(t)$	vector of the B-splines $\in R^{d\times N}$
$\mathcal{P}$	vector of control points $\in R^{3\times N}$

$\mathcal{S}_{\kappa,\boldsymbol{d}-r,\boldsymbol{d}}$	translation matrix from higher to lower degree basis functions
$\mathcal{M}_{\boldsymbol{d},\boldsymbol{d}-r}$	matrix performing the linear combinations of the lower-degree basis functions
T	knot vector $\in R^{N+\boldsymbol{d}}$
τ_κ	κ^{th} knot
κ	number of knots
t	time in seconds

Electrical network

Notation	Description
AC	alternative current
DC	direct current
PCC	point of common coupling
PV, pv	solar panel system
ES, es	energy storage system
DOD	depth of discharge
UG, ug	utility grid
EV	electrical vehicle system
DER	distributed energy resources
DC/DC	direct to direct current
SN, sn	smart node
$KiBaM$	Kinetic Battery Model
P	electrical power
d	duty cycle of the switches in the converters
d_{1sc}	duty cycle which for Sw_4 is $1 - d_{1sc}$ and Sw_3 is d_{1sc}
d_{2sc}	duty cycle which for Sw_1 is $1 - d_{2sc}$ and Sw_2 is d_{2sc}
Sw	switches of the Split-Pi converter
e	effort representing the voltage in an electrical circuit
f	flow representing the current in an electrical circuit
q_{1b}	available charge state of the KiBaM battery
q_{2b}	bound charge state of the KiBaM battery
b	KiBaM battery
sc	Split-Pi Converter
cc	Ćuk Converter
c	cyclic network
s	power source
C	capacitor
I	inductor
$R_{1pv},\ R_{2pv}$	resistances of the PV cell
Di	diode
R_{1b}	resistance between the KiBaM battery and the Split-Pi converter
R_{2b}	resistance of the KiBaM battery
$R_1,\ R_2,\ R_3,\ R_4$	resistances of the transmission network
R_{1sc}	resistance among the DC network and the Split-Pi converters
i	current
v	voltage
i_{sc_out}	output current of the Split-Pi converter
v_{sc_out}	output voltage of the Split-Pi converter
i_{sc_in}	input current of the Split-Pi converter
v_{sc_in}	input voltage of the Split-Pi converter
i_{DC}	current coming from the common DC-bus
nc	number of the connecting nodes in the electrical transmission network
nl	number of the transmission lines
C_n	number of the capacitors
I_n	number of the inductors

Hierarchical control

Notation	Description
MPC	Model Predictive Control
$NMPC$	Nonlinear Model Predictive Control
RHC	Receding Horizon Control
OPF	Optimal Power Flow
t_f	final time in seconds
k	discrete-time step
ep	electricity price
min	minimum
max	maximum
$\mathbf{h}$	high level of the hierarchical control
$\mathbf{m}$	middle level of the hierarchical control
i_{ref}	reference profile of current
v_{ref}	reference profile of voltage
ref	reference profile
T_s	discretization sampling time
w	perturbation added in the middle level
$Q_{\tilde{x}}$, $Q_{\tilde{y}}$, $R_{\tilde{u}}$	weight matrices
N_p	prediction horizon
RPI	Robust Positively Invariant set
$SIMO$	Single Input Multiple Output system
CU	Commercial usage profile
DU	Domestic usage profile
$\oplus$	Minkowski sum
$\ominus$	Pontryagin difference

Contents

List of Figures

List of Tables

Chapter 1

Introduction

The demand for independent power systems connected to the main grid has been continuously increasing over the past few years. Their existence plays a vital role since it leads to a more efficient operation for the main grid. They minimize the power losses, store the energy excess and manage load sharing. These systems include distributed generators (DG), renewable resources (e.g. solar panels (PV) or wind turbines) and storage systems (batteries, ultra-capacitors), linked to a variety of loads (industrial or residential) (Planas et al., 2015). In this regard, microgrids (Fig.1.0.1) have gained important attention and they are considered as suitable systems able to contain DGs within the existing electrical grid system. Their appearance ensures a reliable power distribution and, hence, their existence into the grid operation support have become necessary (Lotfi and Khodaei, 2017b).

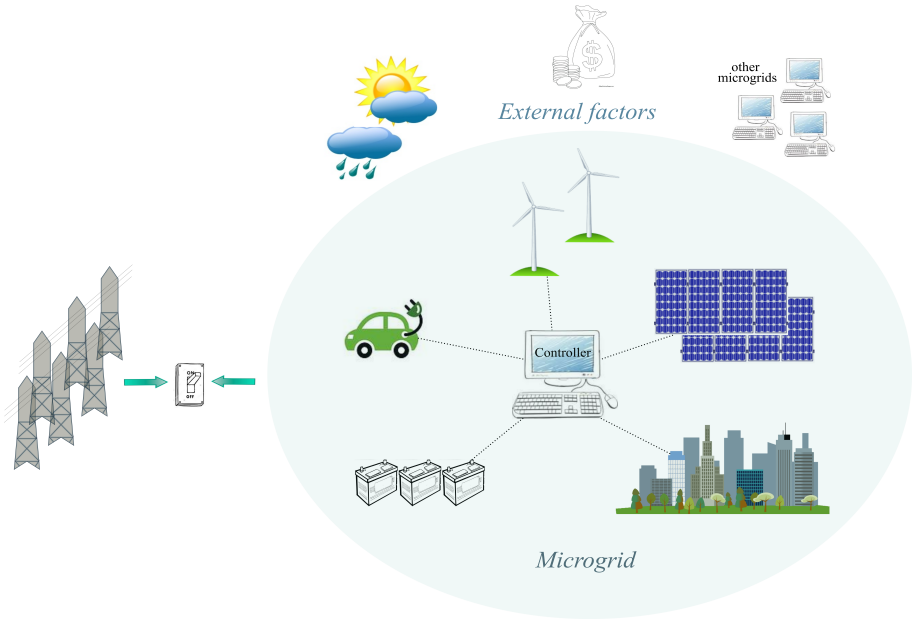

Figure 1.0.1: General architecture of the microgrid.

Although the concept of microgrids seems to have become increasingly popular in the latest years, their applications appeared long ago. In 1882, Tomas Edison opened the first commercial central power plant in Manhattan, USA, a self-maintained electrical system powered by coal with an energy storage (ES) unit and a limited distribution DC network (Escobar et al., 2015; Hughes, 1993). Afterwards, in the 90's, several projects in USA and in Europe held by the CERTS (Consortium for Electric Reliability Technology Solutions) (Lasseter et al., 2002) and the CIGRE (International Council of Large Electric Systems) (Hatziargyriou et al., 2006) implemented some of the first modern grid-connected microgrids. This concept can incorporate multiple distributed energy resources and, in this way, create autonomous systems working in islanded mode under different control strategies (Hirsch et al., 2018). Since then, several examples of microgrids can be found all

around the world, like the Kythnos Island in Greece, the MVV[1] Residential demonstration in Germany and the Continuon MV/LV[2] microgrid in Netherlands (Katiraei et al., 2008; Moehrke and Myrzik, 2014). Since the microgrids are complex power systems composed by a large number of sources, a huge amount of power electronic converters, a set of numerous loads and a multi-line transmission network, many issues arise for further study.

An important aspect is the type of the transmission network: AC or DC (Fig.1.0.2). Despite the domination of AC transmission networks, the interest on DC microgrids grew lately as a result of the constant development and production of the DC equipment for renewable sources (e.g. PVs), storage systems (e.g. lead-acid or lithium-ion batteries) and loads (e.g. electrical vehicles, elevator and escalator systems and various smaller DC loads such as computers, LED lights and the like). Several works have shown that DC microgrids may have numerous advantages over an AC distribution. For instance in Whaite et al. (2015) they mention that a properly structured DC microgrid provides better power quality with ES devices and DC loads integration without frequency or phase control. Furthermore, easier integration of DC power sources and compact power electronics equipment are some of the other advantages according to Jin et al. (2016). Besides, the power losses minimization obtained by reducing the number of converters, avoidance of the multiple DC buses synchronization and an effective power delivery towards DC loads, such as electrical vehicles (EVs), are other beneficial aspects as reported by Lotfi and Khodaei (2017a) and Zubieta (2016). In general, the main goal is always to handle the load balancing problem (Kanchev et al., 2011) minimizing the cost, reducing the power losses and preventing the fault occurrences (e.g. power outages and lines under faults).

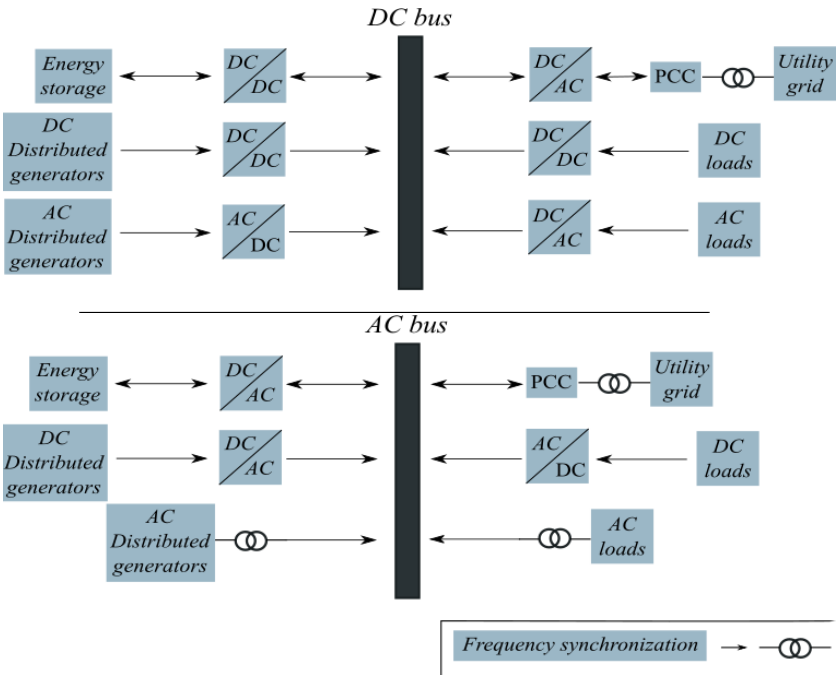

Figure 1.0.2: General structure of AC and DC microgrids.

However, the reliability, the stability and the quality of the power distribution in microgrids continue to be critical issues for the researcher community. Microgrids, as a group of distributed energy resources (DERs), interconnected loads and a large amount of transmission lines, are complex dynamical systems and up to date numerous problems have arisen and remain open for investigation:

- Firstly, an important factor is the topology of the system. There are two main types of topologies: the radial and the meshed topology. In the radial topology, also called point-to-point component interconnection, the electricity is distributed from an energy source to a number of loads. The disadvantage of this topology is that as the electricity passes through the power lines, its strength ends up reduced at the side of the load (Flick and Morehouse, 2011). Additionally, in the case of power outages, the whole system gets influenced and suffers from constant power interruptions. Contrariwise, a meshed topology offers greater reliability since the electricity can be transmitted through a variety of sources and

[1]MVV acronyms stands for Mannheimer Versorgungs und Verkehrsgesellschaft, which is a German energy company.
[2]MV/LV acronyms are for Medium Voltage and Low Voltage respectively.

transmission lines. Thus, the efficiency and the continuity of the power transmission can be guaranteed and the safe operation of the system can be ensured (Flick and Morehouse, 2011; Guerrero et al., 2013; Haileselassie and Uhlen, 2013).

- Another important aspect is the sizing of the renewable sources and the energy storing elements. Sizing algorithms have been developed which consider optimal power sizing of the PVs or the wind turbines depending on the economical cost, on the fuel emission minimization, the ES system or the type of the DC loads, like EVs (Atia and Yamada, 2016; Iovine et al., 2017; Kumar and Bhimasingu, 2015). Besides, the ES system plays an important role in microgrids and ensures the efficient operation of the system (Fossati et al., 2015; Khorramdel et al., 2015). Its proper sizing can provide a backup energy source in case of power transfer interruption from the utility grid (UG) with concurrent inability of the renewable sources system to support the consumers' demand.

- Another critical issue is the configuration of the energy management system (EMS), which manages the power balancing problem, minimizes the power dissipation and ameliorates the power quality. The EMS deals with the appropriate use of the energy sources and decides the proper power flow distribution to satisfy the consumers' demand (Shayeghi et al., 2019). An EMS can operate under a centralized or a decentralized strategy framework (Meng et al., 2016). Under a centralized supervision, the system takes global optimal decisions collecting information from the components of the microgrid. Contrariwise, in the decentralized management, local supervision is possible which allows flexibility during operation and isolation of the events under fault. Furthermore, off-line and on-line EMS approaches have been developed which either predict the functional behavior of the system or study the real-time operation of the microgrid respectively (Shi et al., 2015).

To deal with the above enumerated problems, a modeling and a supervision approach are necessary depending on the architecture of the system and the control objectives. In the following, an overview for the hierarchical control approach will be presented focusing mostly on the energy management of the meshed DC microgrids.

1.1 Hierarchical control

In microgrids, many matters emerge concerning multiple dynamics, nonlinearities, constraints, reliability, stability and so on. To cope with all these challenges, hierarchical control strategies have been developed which handle the aforementioned problems by decomposing them into smaller subproblems.

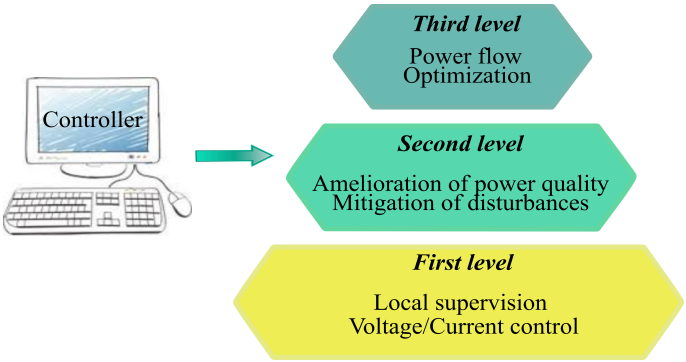

Figure 1.1.1: Hierarchical control general structure.

A typical hierarchical control architecture is categorized into three control levels as follows (Papadimitriou et al., 2015):

- the third level (tertiary control), which handles the energy distribution problems optimizing the power sharing among the energy sources and the consumers;

- the second level (secondary level), which is responsible for the voltage regulation alleviating the disturbances. Besides, in the case of multiple DC buses, this controller synchronizes also the connection among them;

- the first level (primary control), which deals with the local supervision of the power converters linked to the sources and the loads. This controller handles also the voltage and current sharing among them.

Since this approach can manage different control objectives at the same time, it appears to be a suitable and advantageous tool for DC microgrid control. Some of the benefits are enlisted below:

- handling of both fast and slow dynamics of the system. The slow dynamics accounts for the sources and the power flow. On the other hand, the fast dynamics describes the switching activity in the DC/DC converters;

- integration of different control methods at every level to deal with the nonlinear dynamics under constraints. For instance, at one level, the optimal power profiles can be generated and, at another level, the error dynamics can be studied for discrepancies' mitigation (Pham et al., 2017; Zafeiratou et al., 2018a);

- considering energy management strategies to satisfy economical and technological criteria, such as minimization of the power losses, amelioration of the microgrid's architecture and the like;

- study of each component separately which gives the possibility of local supervision without influencing the rest of the system (Cairoli and Dougal, 2017);

- taking into account stability and robustness of the system, which guarantee the continuous and secure operation (Guo et al., 2016; Herrera et al., 2015);

- reconfiguration of the system under unexpected faulted events, when, for example, a line stops transmitting power or a source is not capable of delivering the requested amount of energy.

Certainly, the advantages of the DC microgrids facilitate the implementation of the hierarchical control, since synchronization or reactive power issues no longer exist. Hereinafter, some significant factors will be described which are considered in order to choose the appropriate modeling and control approaches to use in the hierarchical control problem.

1.1.1 Components of the DC microgrids

Hereinafter we concentrate on describing the relevant DC microgrid components, namely, their dynamics and the subsequent modeling choices which are made.

Distributed energy sources: Two types of renewable sources are most commonly considered in DC microgrids:

1. *Solar panels*: Photovoltaics are one of the most commonly used renewable sources in DC microgrids. PVs generate electricity using solar energy, which is abundant and costless (Iovine et al., 2017). Their performance depends on the external temperature, the solar irradiation and their location. An important advantage is that they can be connected directly to the DC transmission network through a DC/DC converter;

2. *Wind turbines*: Wind farms convert the wind energy to electricity through the rotation of the blades (Mariam et al., 2016). Wind turbines produce voltage with a variable frequency and AC/DC converters are indispensable to connect with the DC network.

Energy storage devices: As aforementioned, the ES in DC microgrids is very important and necessary for the efficient and continuous operation of the system. The ES system contributes to the cost minimization and the autonomous operation of the microgrid (islanded mode) by storing energy to use when the electricity price is high or when the UG is unable to generate power. Different types of storing devices have been proposed through the years and their development is still in progress. Some of them are mentioned below:

1. *Lead acid batteries*: This is the most popular type of batteries because they store large amounts of energy and they use a well-established technology which is less costly and more reliable (Mutarraf et al., 2018). Lead acid batteries are widely available in several sizes and shapes, they are able to handle overcharging situations and they can withstand low and high temperatures. However, some drawbacks exist which influence their capacitance and lifetime such as the number of discharging cycles or the depth of discharges (Pavlov, 2011);

2. *Lithium-ion batteries*: Recently, the technology of lithium-ion batteries has been ameliorated and they are lately used in DC networks due to their high energy density rate (Ma et al., 2016). Nevertheless, their technology is still under development and changes continuously, a fact which affects their robustness and reliability. Additionally, their intolerance in overcharging or fast discharging and their high cost are significant disadvantages;

3. *Ultra-capacitors*: Apart from the batteries, ultra-capacitors can be also used since they can deliver current rapidly. Their charging and discharging is fast and they are tolerant of multiple charging and discharging cycles (Kanchev et al., 2011). Consequently, they can be used for local real-time control to restore the operation of the system in case of emergencies (e.g., blackouts). One major disadvantage is their high self-discharge rate which affects a possible long-term energy storage. Therefore, they are often combined with other types of batteries (Morstyn et al., 2015);

4. *Flywheels*: This storing device is composed by a motor and uses rotational speed to store kinetic energy. Although their energy density is high and their lifetime doesn't get affected by the discharging cycles, they suffer from important friction losses (Yoldaş et al., 2017).

5. *Vanadium redox batteries*: Longevity, fast charging and discharging response, high capacitance, high energy density are some of the advantages of this type of batteries. However, this technology is very recent and the costs of maintenance and installation remain still very high (Yoldaş et al., 2017; Zubieta, 2016).

All the aforementioned energy storing devices generate DC current and are connected to the DC microgrid through DC/DC converters for voltage regulation.

DC/DC converters: They are electronic regulators which convert the input voltage value to the requested output value. In the industry, two types of regulators exist, linear and switching-based. The linear regulator topology uses linear components (e.g. resistors) to convert the input voltage. Although it is a simpler, less noise-affected electrical circuit, it lacks in efficiency and only the down-conversion operation is possible (higher to lower voltage conversion). On the contrary, the switching regulators use switches to regulate the voltage through a collection of electronic elements like capacitors, inductors and others. Despite their complicated architecture, they are more efficient with lower power losses and have multiple operating modes (Rohm Semiconductors Company, 1997). The main types of switching DC/DC converters are referred below:

1. the buck converter which adjusts a higher voltage to a lower voltage;

2. the boost converter which steps up the input voltage value;

3. the buck-boost converter which implements both of the previously mentioned actions generating a higher or a lower voltage at the output in comparison with the input value.

The majority of the DC/DC converters are unidirectionally supplying voltage from the input to the output. For instance, the Ćuk converter (Smedley and Cuk, 1995) is a unidirectional buck-boost DC/DC converter which can be connected either to the renewable sources or the loads for voltage adjustment. However, the switching topology allows the possibility of bidirectional functionalities. Such an example is the Split-Pi converter which is a buck-boost bidirectional DC/DC converter and, for instance, can be connected to the ES system for voltage regulation in both directions during charging and discharging (Crocker, 2005; Zafeiratou et al., 2018b).

DC loads: There are two types of loads, the loads which require alternative current (AC loads) and the loads supplied by direct current (DC loads). DC loads have been immensely developed lately due to the rapid evolution of power electronics. Mobile phones, computers, laptops, printers are some of the DC loads used in residential or commercial environments. Besides, LED lighting is another recent technology which operates in DC networks. Finally, the EVs represent a very important chapter of DC loads often considered in DC microgrids (Locment and Sechilariu, 2015).

1.1.2 Modeling methodologies

Different modeling methodologies have been already proposed in the literature to describe such complex dynamical systems. The selection of the proper modeling approach depends on the components and the research objectives, i.e. energy management, voltage/current regulation, power balancing, ES sizing and the like. Some modeling methodologies employed through the years are cited below:

- the ***Takagi–Sugeno fuzzy modeling*** approach (Takagi and Sugeno, 1985) which describes linear models based on input/output datasets covering multiple operation conditions of the system. For instance, in Sáez et al. (2014), the authors use fuzzy modeling to predict the power generation of the renewable source and the loads' demand;

- the ***multi-agent based modeling*** (Karavas et al., 2015; Khan et al., 2016) which concerns agents operating as active entities, individual or collective, and representing a computer model. Using the multi-agent paradigm in a microgrid system, different types of agents can be employed: control agents for controlling the physical units of the system; management agents for managing the microgrid and take decisions; ancillary agents for performing tasks like communication and storage of data (Mahmoud et al., 2014). The global dynamics of the system emerges from the interaction among them;

- the ***differential equations modeling*** (Parisio et al., 2016), which gives an explicit representation of the system dynamics through constitutive equations. However, through this model description, the power conservation property and the components interconnections are not explicitly deduced;

- the ***port-Hamiltonian modeling*** (Duindam et al., 2009; Pham et al., 2015; Schiffer et al., 2016; Zafeiratou et al., 2018b) which generates dynamical models of physical systems taking into account the power-conserving interconnections among the components. The advantage of this method is that the power exchange among the elements is given explicitly and can be used directly for analysis, simulation and control. Besides, PH systems representations can be derived in a straightforward way from their Bond graph models. PH modeling will be employed in this work in combination with Bond graphs and its advantages will be further analyzed in Chapter 2.

Furthermore, the reduction of the model is usually taken into account as a forward step after all the aforementioned methods because of the system's complexity. Sometimes the structure of a system has to be simplified (Parisio et al., 2015; Wang et al., 2012) and replaced by simpler dynamical system in order to proceed to its study and supervision. As a next step after the application of the modeling method, the optimal functioning levels of the system must be defined.

1.1.3 Reference profile generation at the upper level control

The reference profile generation aims at determining the optimal operating points in order to respond to the requirements of the system. The optimal profiles are produced providing the optimal power flow over a set of objectives, i.e., cost minimization, power losses reduction, operation of energy storing devices, power balancing. Several methods have been developed for optimal profile generation to deal with the complex dynamics, the nonlinearities, the uncertainties and the constraints. Some of these methods are presented below:

- **Rule-based controllers** take into account a set of statements and limitations which concern the energy management problem of the system. For instance, in Fossati et al. (2015) the authors study the capacity of the energy storage system for cost minimization and load forecasting. Furthermore, an energy management algorithm is developed in Moghimi et al. (2016) to generate forecasting profiles for a DC microgrid optimizing the operation of the energy storage system and extracting the maximum power possible from the PV source. The advantage of this method is the easy interpretation which is based on a collection of generic rules under which the system must operate. However, to gather all the possible rules is challenging especially for complex dynamics. Furthermore, the detailed dynamics of the system is not considered and, hence, there are scenarios which cannot be studied.

- **Mixed integer programming** (MIP) is an optimization algorithm which uses the systems' variables as integers. The objective functions and the constraints are presented with linear formulations. In Sechilariu et al. (2014), a MIP algorithm is applied to solve the power balancing problem over the simple dynamics of a DC microgrid composed from PV arrays, ES, microturbines and DC loads. The simplicity of the model gives a fast and feasible solution. Noteworthy, the detailed description of the system and the nonlinear constraints are not considered which can lead to inaccurate or unsatisfactory results (Braunschweig and Gani, 2002).

- **Economic Model Predictive Control** (MPC) is a closed-loop controller which predicts the behavior of the system under a set of constraints for discrete-time models (Rawlings and Mayne, 2009). Considering a finite horizon, the controller generates at each time slot an optimal open-loop trajectory profile.

Then, only the first step is applied as input to the system to recalculate the states and regenerate the next optimal profile. In Parisio et al. (2016); Prodan and Zio (2014), the authors implement economic MPC for on-line optimal profiles generation to solve the energy management problem.

- **Differential flatness** is an advantageous method used for the analysis of the nonlinear dynamics of the system. To proceed to the optimal profiles generation, it is necessary to isolate concrete physical quantities of the system such as the voltage, the current, the power and others. Therefore, differential flatness can be considered as a suitable tool to inverse the system dynamics, generating in this way all the states and inputs in function of the flat outputs and reducing the number of differential equations. Furthermore, the controllability of the system can be ensured since, according to Fliess et al. (1995), a nonlinear system is flat if and only if it is controllable. Recently, differential flatness has been applied in DC microgrids (Soheil-Hamedani et al., 2016). For instance, in Pham et al. (2015) the flat representation is applied to generate the optimal profiles for the velocity of an elevator system, while minimizing the energy dissipation. A main advantage of differential flatness is that the resulting profiles implicitly (by their construction from the flat output) respect the system's dynamics. In addition to this, in combination with B-splines approximations, continuous-time constraint validation can be ensured. This method will be further explained and implemented in Chapter 3.

1.1.4 Control approaches

The previous subsection introduced some methods employed in the third level of hierarchical control for optimal power profile generation forecasting the behavior of the system. In general, a control strategy for DC microgrids must be implemented to achieve (Unamuno and Barrena, 2015):

- Optimization, as previously mentioned, for optimal power flow and cost minimization;
- Power quality obtained by a proper power transmission among the sources and the consumers;
- Power balancing meaning appropriate load sharing among the components;
- Reliability by protecting the microgrid from faulted events or blackouts;
- Stability by bounding the error dynamics and ensuring voltage regulation.

Therefore, in here, control approaches mostly used at the second or the first level for voltage regulation, power transmission or error mitigation will be presented.

Droop control in DC microgrids is a primary control method which decreases linearly the voltage while the current at the output increases, without ensuring accurate current sharing. For example in Lu et al. (2013), the voltage restoration in the DC bus is achieved over a droop controller implementation. However, the droop control method is not suitable for nonlinear models and its performance in voltage adjustment with accurate load sharing is weak (Guerrero et al., 2012).

Plug and play methods (PnP) include information about the subsystems of the microgrid. In this way, the subsystems are able to work independently, meaning that for each component that is added or removed, the stability of the system and the constraints validation are reverified. Furthermore, the controllers of the affected subsystems are readjusted (Stoustrup, 2009). For instance, in Tucci et al. (2017), they aim to prove stability of the linear system using PnP control for voltage regulation. Furthermore, in Riverso et al. (2016), the authors use the PnP method in combination with MPC to handle nonlinear networks under constraints and detect faulty behaviors.

Tracking MPC is used for reference tracking. The goal is to alleviate the fluctuations between the reference and the actual profiles satisfying a set of constraints. Tracking MPC is usually combined with economic MPC. Economic MPC generates the optimal reference profiles which, subsequently, are sent to the tracking MPC as inputs to follow them under perturbations (Legry et al., 2018; Zafeiratou et al., 2018a). Tracking MPC will be implemented in this work at the second level of the hierarchical control. Additionally, there is the **robust MPC** variant which builds upon an optimization problem influenced by uncertainties and tends to increase the robustness of the system (Dragičević, 2017).

Agent-based controllers exchange information among local entities with limited knowledge. The agents can interact to each other to solve an optimization problem for load balancing, voltage regulation or battery charging. This method provides autonomy and many controllers can be implemented in an agent-based framework. For instance, the authors of Li et al. (2015) propose a two-layer decentralized control, where the lower layer controls the power distribution while at the upper layer the communication among the agents is applied.

In general, the control methods are divided into two categories, centralized and decentralized. In a centralized supervision, a central controller performs the requested actions to achieve proper power distribution and secure operation of the microgrid. Although, it is an advantageous method because it facilitates the controllability and the observability of the system, the controller can collapse under a single failure. Furthermore, the complexity in computation does not allow its implementation in large-sized microgrids. On the other hand, the decentralized control does not demand global information of the system, since this method is based on the local supervision of a subsystem or a unit. The decentralized controllers do not require real-time communication, but the observability on the global behavior of the system is limited (Meng et al., 2017).

1.2 Thesis orientation

The aforementioned literature demonstrates a wide variety of modeling and control approaches performed in DC microgrids. This thesis will concentrate on the analysis of a meshed DC microrgid proposed in the ANR $C^3\mu$ project (Components, Control, Communication) (Agence Nationale de la Recherche, 2016). The project aims at optimizing the power distribution in commercial or residential buildings employing a central management system. The goal is, firstly, to satisfy the consumers' needs associated with an effective power generation from the renewable energy sources and the ES system. The originality of the project resides upon the definition of a smart node (SN), which is composed by two Split-Pi DC/DC converters explicitly described in Chapter 2. The SN will manage the central transmission network and the power exchange among the components as well as the reconfiguration of the system. The main tasks of the project are summarized below:

- Design and implementation of the DC/DC converters and the components;
- Modeling of the EMS and study of the reliability of the DC microgrid;
- Verification under simulations to estimate the proposed method's viability for the power balancing problem;
- Design of the communication network among the SNs.

The end goal is to remove the central EMS and to integrate all the implemented actions in the SNs, which will supervise directly the DC microgrid's operation.

In this manuscript, the energy management problem is considered. The main objective is to formulate a hierarchical control problem which will optimize the power distribution within the DC microgrid. It will also provide a solution for the voltage regulation and the discrepancies' mitigation among the optimal and the real profiles. The power flow will be optimized regarding the electricity cost, the consumers' demand, the power dissipation and the ES system. To handle all these aspects, the following must be considered:

- the switching control of the converters is necessary. To achieve this, the detailed knowledge of their physical characteristics (capacitors, inductors, resistors and so on) is indispensable;
- the number of converters must be limited to prevent an increase in power losses. Note that the converters will handle both the power flow and the voltage/current regulation of the system;
- the best possible exploitation of the renewable energy sources is important. The unused energy must be either stored or sold to the main grid;
- a collection of batteries must be considered which will ensure the safe and reliable operation of the system in case of faults or uncertainties;
- a specific amount of transmission lines must be placed in a way that the power will be distributed under the less potential power losses. The lines under fault could be also isolated.

Therefore, it is clear that the overall problem has many aspects and many problems remain open. The main target is to have a unique dynamical model where every physical component will be explicitly described. Port-Hamiltonian (PH) representations give this flexibility of describing the dynamical model in detail. The DC microgrid system will be, firstly, presented in PH form giving high importance to the ES system. Next, the computation of the flat outputs of each component will be provided, generated by an already-proposed algorithm in Franke and Robenack (2013). In addition, the flat representations of the PH systems will be

further analyzed under the bicausality notion which investigates the inverse dynamics of the system. Afterwards, the constrained optimization-based control approach will be introduced by employing the differential flatness method in combination with a B-splines parametrization.

In the sequel, the hierarchical control approach will be implemented as a three-levels scheme: the high, the middle and the low level. At the high level, optimal profiles will be produced to be followed by the middle and lower levels, respectively. Power balancing requirements at the high level will lead to an optimal profile generation for the battery, to be tracked at the middle level. Then, the middle level will provide voltage and current references for the battery. These profiles will be tracked at the low level by an explicit switching law used in the DC/DC converters. The different timescales, the nonlinearities and the constraints of the system will be also included firstly for the cost minimization. Afterwards, the power losses of the central transmission network will be considered to generate an optimal power flow. The reference profiles generated by differential flatness and the B−splines parametrization will be compared with the optimal profiles obtained by economic MPC. Furthermore, other scenarios will be taken into account as for example for different distances among the power sources or when lines under fault appear.

1.3 Contributions of the thesis

This thesis presents a meshed DC microgrid architecture in PH representation supervised by a hierarchical control strategy to manage load balancing and efficient power distribution. A novel combination of PH modeling with differential flatness and B−splines parametrization is introduced and leads to an off−line constrained optimization problem. This method provides continuous−time optimal profiles not only for the power, but also for the voltage, the current and other physical quantities of the electrical circuits (the charge, the magnetic flux and the like). Hence, it can be an advantageous and reliable solution to study thoroughly and predict the behavior of the system.

More precisely, the main contributions of this work are summarized below:

- the dynamical model representation with PH formalism through its associated Bond graph: PH method generates a well−structured dynamical representation of the system. This method naturally provides power−preserving differential equations. Additionally, its structure allows the isolation of any physical quantity for investigation (voltage, current, charge, magnetic flux) without changing the primary mathematical model. The proposed meshed DC microgrid is presented in PH form. Firstly, the PH state-space representation is given for every part of the microgrid separately. Next, the PH state-space representation of the central transmission network is analytically introduced;

- the algorithm proposed in Franke and Robenack (2013): the algorithm is implemented for the PH system to find its flat representation. Furthermore, the bicausality notion is applied to further analyze the flat representation of the PH models and study a more direct way to calculate the set of flat outputs. Comparisons amongst the different set of flat outputs are realized through simulations. The goal is to find a straightforward way to calculate the flat outputs of the PH systems. A method is proposed for electrical circuits with illustrative examples;

- the use of differential flatness and B−splines parametrization for optimal profile generation: microgrids are complex systems with complicated mathematical models and numerous states. In this work, differential flatness seems to be an appropriate tool which can inverse the dynamics of the system and describe the states in function of the flat outputs. Furthermore, using B-splines to parametrize the flat output allows, due to the properties of B-splines, to characterize the system's functioning in continuous time. Optimal reference profiles for the UG and ES power will be obtained. In addition to the previously referenced publications, which concentrate more in obtaining optimal profiles for the power or the energy generated from each source, in here we go further and produce optimal profiles in continuous−time not only for the power but also for the current and the voltage of the components;

- the proposed hierarchical control approach to solve the power balancing problem: works in the literature concentrated mostly on one control level. In the case where they used more than one level, they simplified either the model or the control method. In this work, a complete hierarchical control framework is presented which investigates many important factors at the same time: cost minimization, power balancing, power losses, constraints, tracking errors (decreasing the voltage and current discrepancies) and regulation of the switches in converters.

We provide, hereinafter, the list of publications accepted/submitted to various conferences and journals, and the presentations given by the candidate at various scientific days or mobility projects:

Conferences and journals:

- **Zafeiratou, I.**, Prodan, I. Boem, F., Lefèvre, L. Handling power losses in a DC microgrid through constrained optimization, *In Proceedings of the 21st IFAC World Congress, Berlin, Germany, 2020 (submitted)*;
- **Zafeiratou, I.**, Prodan, I., Lefèvre, L. On the flat representation for a class of port-Hamiltonian systems, *In Proceedings of the 21st IFAC World Congress, Berlin, Germany, 2020 (submitted)*;
- **Zafeiratou, I.**, Prodan, I., Lefèvre, L., Piétrac, L. (2019). Meshed DC microgrid hierachical control: a differential flatness approach, *Journal of Electric Power Systems Research (accepted, December, 2019)*;
- **Zafeiratou, I.**., Prodan, I., Lefèvre, L., Piétrac, L. (2018). Dynamical modelling of a DC microgrid using a port-Hamiltonian formalism, *In proceedings of the IFAC Conference on Mathematical Modeling, Vienna, Austria, 51(2), 469-474*, DOI: 10.1016/j.ifacol.2018.03.079;
- **Zafeiratou, I.**, Nguyen, D. V. A., Prodan, I., Lefèvre, L., Piétrac, L. (2018). Flatness-based hierarchical control of a meshed DC microgrid, *In proceedings of the IFAC Conference on Nonlinear Model Predictive Control, Madison, Wisconsin (USA), 51(20), 222-227*, DOI: 10.1016/j.ifacol.2018.11.017;
- **Zafeiratou, I.**., Prodan, I., Lefèvre, L., Piétrac, L. (2017). Control and optimization scheduling within a meshed DC microgrid, *In IFAC 20th World Congress, Toulouse, France,* HAL Id: hal-01656982.

Presentations:

- **Zafeiratou, I.**, Prodan, I., Lefèvre, L., Piétrac, L., Hierarchical control of a meshed DC microgrid under constraints, University College London, London, May 2019 (mobility project);
- **Zafeiratou, I.**, Prodan, I., Lefèvre, L., Piétrac, L., Hierarchical control of a meshed DC microgrid under constraints, National Scientific Workshop - GT Micro-réseaux, Compiègne, France, November 2018;
- **Zafeiratou, I.**, Nguyen, D. V. A., Prodan, I., Lefèvre, L., Piétrac, L., Hierarchical control of a meshed DC microgrid, National Scientific Workshop - GDR SEEDS et MACS, Smart Energies 2018, Paris, France, July 2018;
- **Zafeiratou, I.**., Prodan, I., Lefèvre, L., Piétrac, Modeling and load balancing of a DC microgrid using port-Hamiltonian formulation, National Scientific Workshop - Micro and Smart Grid, Paris, France, October 2017.

1.4 Organization of the manuscript

This thesis consists of 5 chapters (see Fig. 1.4.1 on page 11), including the introduction.

- Chapter 2, firstly, presents some notions and definitions for the Bond graphs and the PH systems. Next, the Bond graph of each component of the meshed DC microgrid is developed. The associated PH state-space representations are provided. Furthermore, a simplified version of the central transmission network is presented. The transformation from the complex to the simplified version is described through their PH formulations. Finally, the constraints and the control objectives of the system are introduced;
- Chapter 3 presents the flat representation of each component of the system. The detailed explanation of the algorithm's implementation is provided taking as an example the ES PH representation. Simulations for the verification of the computed flat outputs are also included. Then, the theory of bicausality is introduced. The flat representation through bicausality is presented through illustrative examples of some electrical circuits of the system;
- Chapter 4 describes the hierarchical control problem. Firstly, some basic tools of the hierarchical control problem formulation are provided. Afterwards, the energy management problem is presented together with the control objectives, the reference profiles and the set of constraints. Next, the multi-layer supervision problem is analyzed explicitly with extensive simulation results which are explained in detail. Furthermore, a comparison with MPC as another method of optimal profile generation is implemented. Finally, different scenarios for the DC microgrid are investigated (e.g. lines under fault);

- Chapter 5 draws the conclusions of the thesis and analyzes the short-term and long-term perspectives.

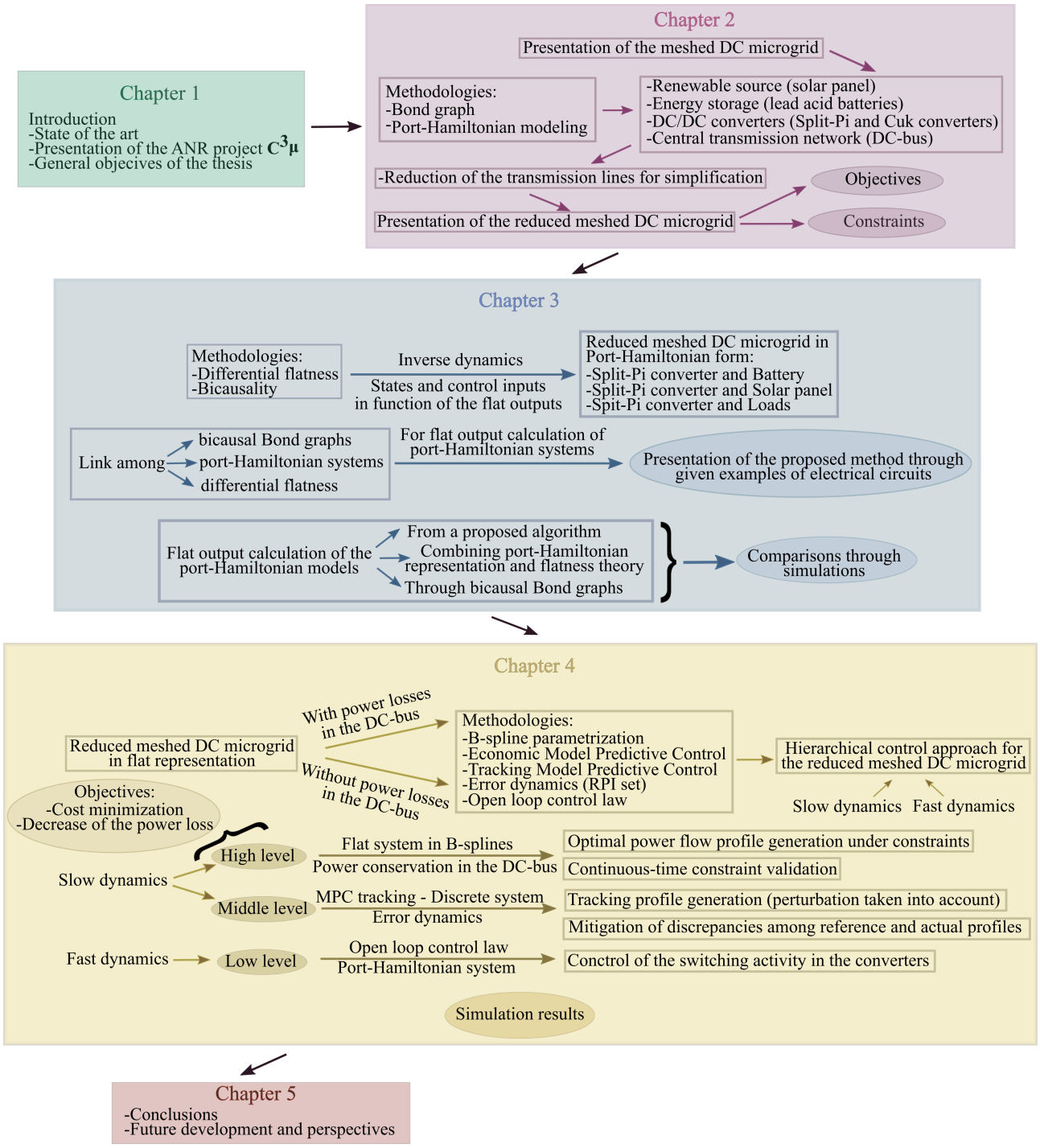

Figure 1.4.1: Organization scheme of the thesis.

Chapter 2

DC microgrid dynamical representation

2.1 Introduction

Through the years, microgrids have become progressively convoluted power systems since they are composed by a large number of small-scale subsystems such as a collection of renewable energy resources, an enormous ensemble of power electronics converters, a set of numerous loads, an assortment of batteries for energy storage (ES) and a multi-line transmission network. Therefore, an appropriate structure plays a crucial role for an effective operation and, towards this direction, there are many aspects to investigate. For this reason, results from the state of the art implement mathematical models to represent and study the dynamics of such systems. The complexity of these networks requires a concrete modeling methodology according to the objectives, some of which are enlisted below:

- which microgrid type to use, AC, DC or a combination of both, depending on the distributed energy resources (DERs) included, the kind of loads, the amount and the category of converters;
- the selection of the transmission lines and the network topology, radial or meshed, the number of transmission lines and the distance among the DERs and the loads. These characteristics rely upon the financial planning of the consumers, the cost of the energy purchase from the main grid, the power dissipation and the like;
- the energy management method, centralized, decentralized or distributed. Each approach needs a different analysis, meaning a different modeling method and control strategy;
- the analysis of the power flow, signifying, primarily, the in-depth study of the variables of the electronic devices included in the system, such as the input/output voltage of the sources, the switches of the power converters, the analysis of the fast and the slow scale dynamics of each part;
- the necessity of the ES, which influences the reliability and the efficiency of the system. The sizing of the batteries, the depth of discharge, the deterioration and the lifetime are some of the factors that influence the cost and the performance in such systems;
- which renewable energy sources to use, depending on their type, AC or DC sources, current or voltage sources. The buying cost must be also considered not only for the sources themselves but also for the converters needed for their synchronization with the central transmission network.

This work, as already mentioned, is part of the ANR-15-CE05-004-02 $C^3\mu$ project (Components, Control and Communication) which proposes a meshed DC microgrid architecture to deliver electrical energy to the interior of a building (commercial or residential) under a decentralized energy management. The project is investigating the energy saving potentials, the benefits, the barriers and the efficiency of employing directly the DC current for local power distribution rather than the AC current which needs to be converted for the supply of the DC loads. The main target is to have a well-structured, explicit dynamical model which respects and follows the constitutive laws of physics and engineering. Port-Hamiltonian (PH) representation offers this flexibility by describing a physical system in detail and by giving information separately for each

physical quantity, such as the charge, the voltage, the dissipation and the like, to use it afterwards for further analysis.

In the literature, PH modeling has been considered for various dynamical systems. For instance, in Adibi et al. (2017), they use PH representation for voltage regulation in a small scale microgrid in islanded mode. Furthermore, Fiaz et al. (2013); Pham et al. (2015); van der Schaft et al. (2014) design and analyze a large scale power network composed by distributed generators (DGs) and loads. The authors use PH modeling to obtain a unified mathematical structure which contains the dynamics of the energy sources, the storing devices and their components and defines the energy preserving interconnections. Moreover, in electronics, they develop PH models for inverters, converters, transformers and other electrical devices for input/output voltage regulation, internal analysis of the components' dynamics and power balancing (Meshram et al. (2017), Bergna-Diaz et al. (2017), Schiffer et al. (2014)). PH modeling has been proposed even for economical modeling in Machado and Mata (2015). Moreover, in Macchelli (2013), the authors take advantage of the energy storing and dissipative elements, the power exchange and power conservation in order to analyze the market's supply and demand.

In general, PH modeling is a structural approach which focuses on providing an exhaustive, explicit and modular description of the power routing in a system through a complex port-based network. The PH state-space representation represents the constitutive equations of its energy storing elements coming from various domains, chemical, mechanical, electrical, thermodynamical and the like. Furthermore, it can be derived in a straightforward way from its associated Bond graph model, a graph-oriented approach which leads to the direct acquisition of the PH state-space representation, as will be explained later in the text (Karnopp et al., 2012).

In this chapter, the meshed DC microgrid system will be presented composed by: an external utility grid (UG), a set of solar panels (PV), a series of electrical vehicles (EV), a collection of lead-acid batteries and a group of loads. DC/DC converters are also included for voltage regulation and for power flow direction. The main idea of this chapter stems from the detailed representation of the DC microgrid describing each component separately, presenting its Bond graph and its associated PH formulation.

In the sections that follow, the main components of the DC microgrid will be presented. Afterwards, we will introduce the basic theory and definitions of the Bond graph representation and the PH formalism. Then, we will apply these methods in the DC microgrid replacing the components (sources, converters, transmission network) with electrical circuits. Next, after introducing the complete version of the DC microgrid, we will develop a reduced version preserving the primary characteristics. In this version, the ES system will play an important role and will be described explicitly. At the end, the contributions of this chapter will be mentioned. Note that, for the sake of convenience, wherever it is straightforward implied by the text, the time dependence will be ignored.

2.2 DC microgrid architecture

The meshed DC microgrid considered in the project (Fig. 2.2.1), as already mentioned, is composed by a renewable energy source (PV), an ES system composed from lead-acid batteries and a number of loads (office and housing devices, electrical vehicles (EV) and the like). The microgrid is connected to a three-phase UG through a bi-directional AC/DC inverter and with the PV, they constitute the main power sources of the system. Between the UG and the DC microgrid, there is a DC breaker with a switch which disconnects the DC microgrid from the AC-grid avoiding occasional blackouts or other fault events. When the DC breaker's switch is open, the DC microgrid is able to operate autonomously in islanded mode. The common DC bus is a high-voltage transmission network of 400 V DC.

In the following, the switching DC/DC converters of the system will be presented. These components are regulating the input/output variables among the sources, the loads and the DC bus. Furthermore, they control the power flow direction within the central transmission network. In this work, two types of converters will be used:

- a bi-directional buck-boost converter, called Split-Pi converter (Crocker, 2005), which produces an output voltage higher or lower than the input voltage. At the same time, this converter can operate in both directions which makes it suitable for sources which generate and accept energy, such as the battery (charging/discharging). To implement these parallel functionalities, four switches exist, which are the main components responsible for its efficient operation. A pair of Split-Pi converters constitutes the smart node (SN) (see also Fig. 2.2.1) of the system which takes decisions related to the power demand, the electricity cost, the load balancing and the state of charge of the ES. In other words, this

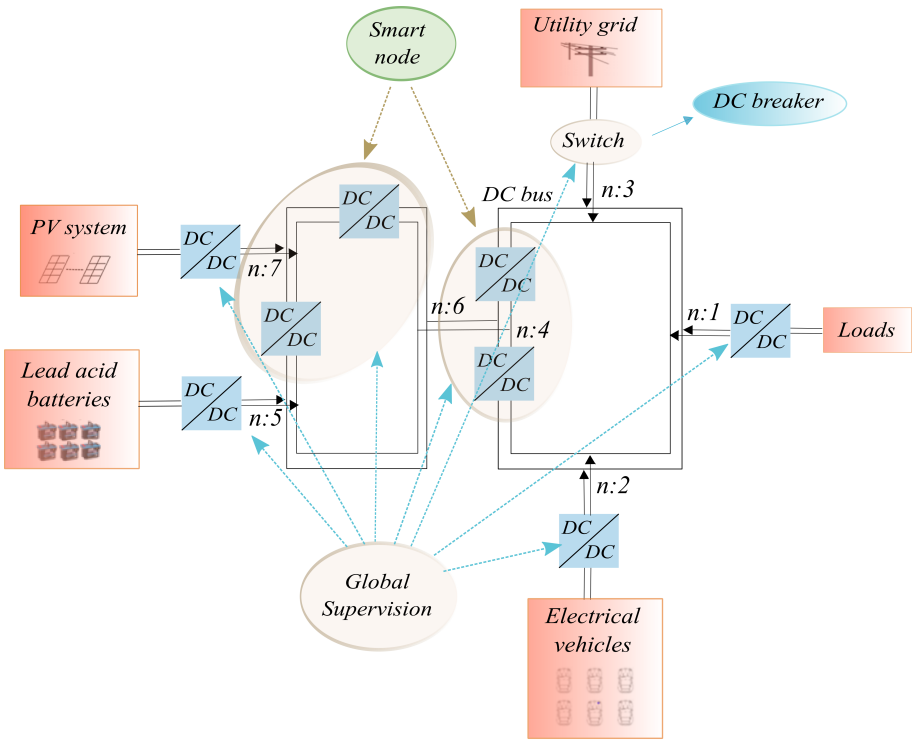

Figure 2.2.1: Structure of the meshed DC microgrid.

element guides and supervises the power flow finding the best routing solution in favor of the consumers' satisfaction;

- an unidirectional buck-boost converter, called Ćuk converter (Pyrkin et al., 2015). This converter regulates the output voltage which can be lesser or greater than the input. It is appropriate for sources or loads which either generate or receive power.

A significant factor of the converters is the duty cycle[1], d, of the switches which characterizes the converters' activity. In the following, the aforementioned components of the microgrid will be described.

2.2.1 Description of the meshed DC microgrid components

2.2.1.1 Solar panel

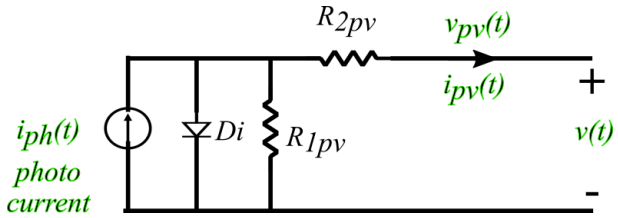

Figure 2.2.2: General circuit of a PV cell.

As mentioned before, the main renewable source of the system is the solar panel. The solar panel is composed by arrays of solar cells in parallel or in series. The solar cell is an electrical device that collects the solar irradiation and generates electricity. A classical solar cell can be illustrated with a current source and a diode in parallel. Since the solar cell is not an ideal element without power losses, two resistances are added in the circuit, a shunt resistance R_{1pv} and a series resistance R_{2pv} (Villalva et al., 2009). The shunt resistance decreases the amount of the current passing through the electrical circuit. On the other hand, the

[1]The duty cycle describes the time for which a signal is active over one period.

series resistance lowers the quality of the solar cell by reducing the fill factor[2]. In Fig. 2.2.2, the equivalent electrical circuit is depicted. The PV panels produces direct current and they are appropriate renewable sources for a DC network.

2.2.1.2 Lead acid battery

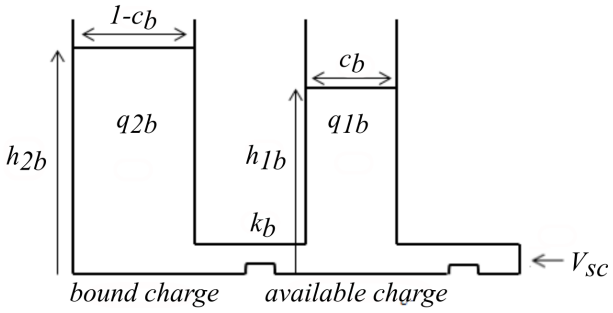

Figure 2.2.3: Two-tank model of the KiBaM

In the literature, several models have been proposed which describe the battery's output voltage and the operations during charging, discharging and recovery. The model selected for this work is based on the chemical kinetics process and is called Kinetic Battery Model (KiBaM)(Manwell and McGowan, 1993). It is considered as a two-tank model, the bound charge and the available charge, separated by a conductance k_b (Fig. 2.2.3). The tank q_{1b} supplies electrons directly to the load and the tank q_{2b} supplies electrons only to the available charge tank (Jongerden and Haverkort, 2017).

The flow between the two tanks depends on their height difference and on the parameter k_b, which is constant. As we can see from fig.2.2.3, the two heights h_{1b} and h_{2b} are given by the following equations (Jongerden and Haverkort, 2017):

$$h_{1b}(t) = \frac{q_{1b}(t)}{c_b}, \tag{2.2.1}$$

$$h_{2b}(t) = \frac{q_{2b}(t)}{1 - c_b} \tag{2.2.2}$$

with the charging variations equal to:

$$\frac{dy_{1b}}{dt} = -i_b(t) + k\big[h_{2b}(t) - h_{1b}(t)\big], \tag{2.2.3}$$

$$\frac{dy_{2b}}{dt} = -k_b\big[h_{2b}(t) - h_{1b}(t)\big], \tag{2.2.4}$$

with initial conditions $y_{1b} = c_b C_b$ and $y_{2b} = (1 - c_b)C_b$, where q_{1b} is the available charge, q_{2b} is the bound charge, c_b is the width of the tank q_{1b}, which refers to the total capacity of the available charge, $1 - c_b$ is the width of the tank q_{2b}, which refers to the total capacity of the bound charge, and C_b is the total capacity of the battery. Moreover, i_b is the current of the battery delivered to the load. When a load is applied to the battery, the available charge decreases. When, the load stops consuming, the bound charge starts to flow in the available charge tank until the heights are equal again.

In the following, the KiBaM model is replaced by an equivalent electrical circuit (Pham et al., 2015). Considering the two tanks as two storage elements, C_{1b} and C_{2b}, connected together with a resistance, R_{2b}, we obtain the electrical circuit depicted in Fig. 2.2.4. Furthermore, a resistor, R_{1b}, is added to represent the transmission line between the source, v_{sc}, and the battery.

2.2.1.3 Split-Pi converter

Next, the Split-Pi converter and its operation are presented. This converter is bi-directional and produces an output voltage which can be higher or lower than the input voltage in both directions. It is a buck-boost

[2]The fill factor is defined by the difference between the maximum generated power and the theoretical expected power of a solar cell.

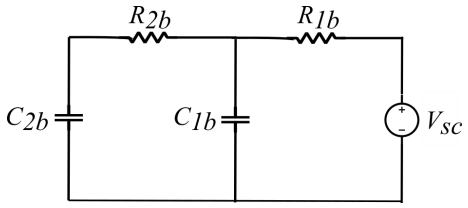

Figure 2.2.4: Electrical circuit model of the KiBaM in state of charge.

converter (DC/DC converter) and it is controlled by four switches. It has four modes of operation: two up-conversions (higher output voltage than the input) and two down-conversions (lower output voltage than the input) (Crocker, 2005; Singhai et al., 2014). We start by presenting in Fig. 2.2.5 the electrical circuit of the Split-Pi converter and in Fig. 2.2.6 its operation modes as presented also in Table 2.2.1. We mention at this point that we consider the switches as ideal, lossless elements, which can conduct current at zero voltage, when Sw is equal to 1 and hold a voltage at zero current, when Sw is equal to 0 (Escobar et al., 2015; van der Schaft and Jeltsema, 2014).

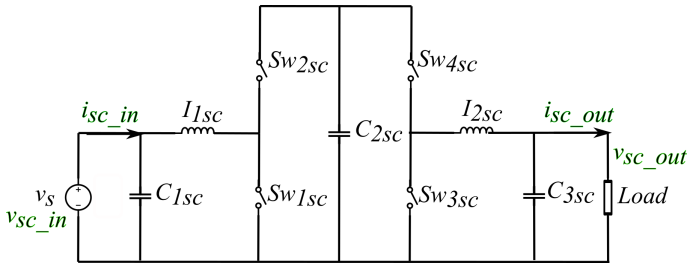

Figure 2.2.5: Split-Pi converter electrical circuit.

Table 2.2.1: Different phases of operation in Split-Pi converter.

Modes of operation	Switching activity
	Positive direction
Down-conversion	Phase 1: Sw_{2sc}=Sw_{4sc}=1 and Sw_{1sc}=Sw_{3sc}=0 Phase 2: Sw_{2sc}=Sw_{3sc}=1 and Sw_{1sc}=Sw_{4sc}=0
Up-conversion	Phase 1: Sw_{2sc}=Sw_{4sc}=1 and Sw_{1sc}=Sw_{3sc}=0 Phase 2: Sw_{1sc}=Sw_{4sc}=1 and Sw_{2sc}=Sw_{3sc}=0
	Negative direction
Down-conversion	Phase 1: Sw_{2sc}=Sw_{4sc}=1 and Sw_{1sc}=Sw_{3sc}=0 Phase 2: Sw_{1sc}=Sw_{4sc}=1 and Sw_{2sc}=Sw_{3sc}=0
Up-conversion	Phase 1: Sw_{2sc}=Sw_{4sc}=1 and Sw_{1sc}=Sw_{3sc}=0 Phase 2: Sw_{2sc}=Sw_{3sc}=1 and Sw_{1sc}=Sw_{4sc}=0

2.2.1.4 Ćuk converter

Hereinafter, we continue with the Ćuk converter which is unidirectional, based on a buck-boost topology and produces voltages which can be higher or lower than the input voltage (Escobar et al., 2015). This kind of converter regulates the input voltage of the loads and the EVs and the output voltage of the PV system. In the following figures, we present the electrical circuit of the Ćuk converter (Fig. 2.2.7) and its modes of operation (Fig. 2.2.8).

In the sequel, the mathematical model of the aforementioned components will be presented. The Bond graph method will be employed in order to develop the PH state-space representations of the system.

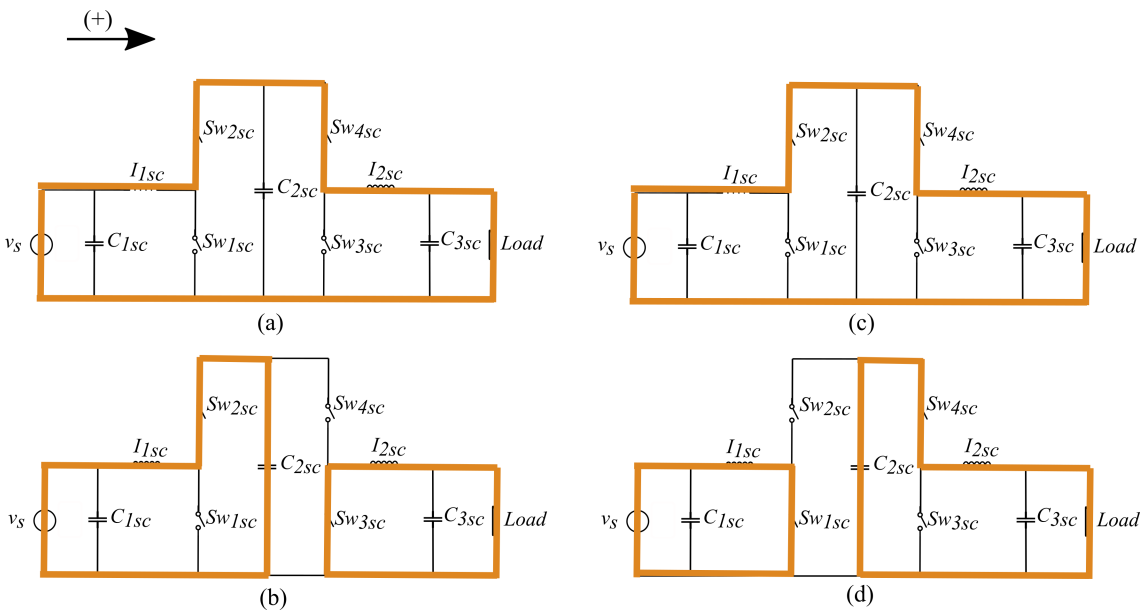

Figure 2.2.6: Two functionalities of the Spit-Pi converter. (a) and (b) represent the down-conversion, while (c) and (d) represent the up-conversion process in positive direction. Similarly, we have the same two functionalities at the opposite direction, where the *load* takes the place of the source and the source, v_s, takes the place of the load.

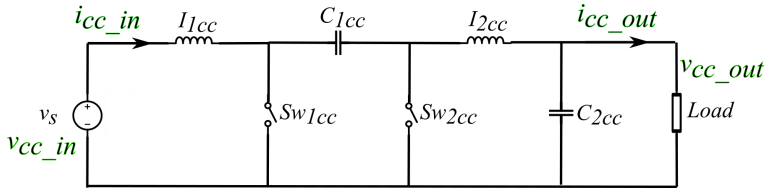

Figure 2.2.7: Electrical circuit of the Ćuk converter.

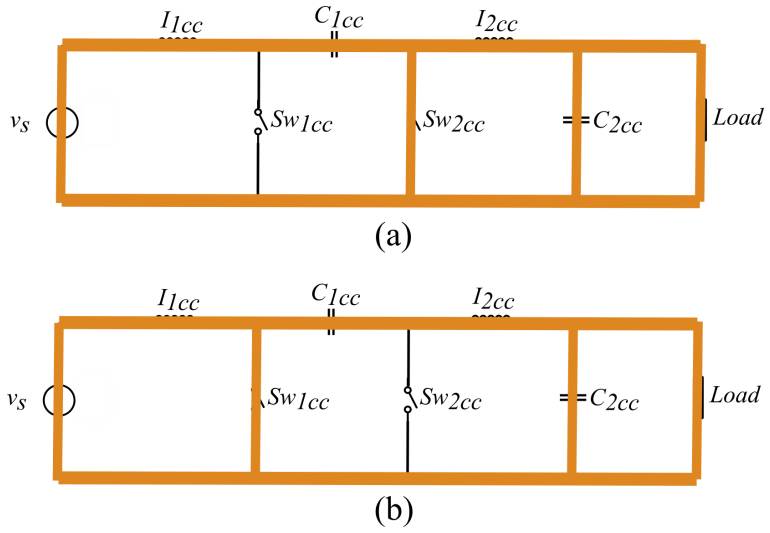

Figure 2.2.8: Operation modes of the Ćuk converter.

2.3 Bond graph and port-Hamiltonian systems

2.3.1 Bond graph

The Bond graph is a graphical representation which describes the energy-preserving structure of a dynamical system. This method, built upon the power interconnections amongst the physical elements, clarifies the system's behavior and contributes to the formulation of the system's equations.

Primarily, the Bond graph is regarded as an interconnection of three types of components, as you can see also in Fig. 2.3.1 (Karnopp et al., 2012; Paynter, 1961):

- energy-storing elements (inductors I, capacitors C),
- energy-dissipating elements (resistors R),
- energy sources (voltage S_e and current S_f sources).

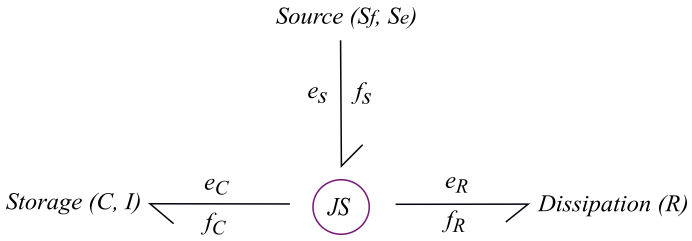

Figure 2.3.1: Bond graph (Junction structure).

Table 2.3.1: Efforts and flows in several physical fields.

Physical system	Effort e	Flow f
Electrical	Voltage	Current
Mechanical	Force Torque	Velocity Angular velocity
Chemical	Chemical potential	Mass flow rate
Thermal	Temperature Pressure	Entropy change rate Volume change rate

With these three components, Bond graphs cover multiple domains and describe various systems, such as mechanical, electrical, thermodynamical and others. Regarding the multi-scale systems, using the notion of Bond graph, they can be decomposed and analyzed as reduced interconnected parts. The strokes in the Bond graph represent the power flow through the elements with a half-arrow pointing the power flow direction. Each arrow is characterized by a pair of effort, e, and flow, f, and their product is the power passing through, $P = e \cdot f$. The components are connected together in the Junction Structure, JS (Fig. 2.3.1). In Table 2.3.1, several interpretations of e and f are depicted for different types of systems. Afterwards, the main characteristics (Borutzky, 2010) of the Bond graph will be explained through an example of an electrical circuit (Fig. 2.3.2):

- according to Fig. 2.3.2, the electrical circuit has two storing elements, one capacitor C and one inductor I, one dissipative element R and two sources, one voltage source S_e and one current source S_f. These elements are considered as one-port elements referring to one single port and one pair of e and f;
- in Fig. 2.3.3 the corresponding Bond graph of the electrical circuit is presented. The arrows demonstrate the power flow, $P = e \cdot f$, within the system and compose the Junction Structure;
- in the Bond graph 0 and 1 junctions also exist. Their major characteristics is the power conservation and the reversibility. 0 junction has equal efforts and the sum of flows is equal to 0 ($e_1 = e_2 = e_3 = ... = e_n$,

$f_1 + f_2 + f_3 + ... + f_n = 0$). On the other hand, 1 junction has equal flows and the addition of flows sums up to 0 ($f_1 = f_2 = f_3 = ... = f_n$, $e_1 + e_2 + e_3 + ... + e_n = 0$). This is equivalent to the rules which the electrical circuits follow in parallel and in series respectively;

- finally, the storing and dissipative elements obey to the following constitutive equations: the R element respects $e_R = f_R \cdot R$ and $P = \frac{e_R^2}{R} = f_R^2 \cdot R$, C follows $e_C = \frac{q_C}{C}$ and I obeys to $f_I = \frac{p_I}{I}$.

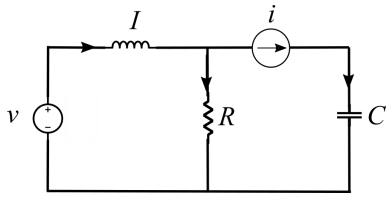

Figure 2.3.2: Electrical circuit.

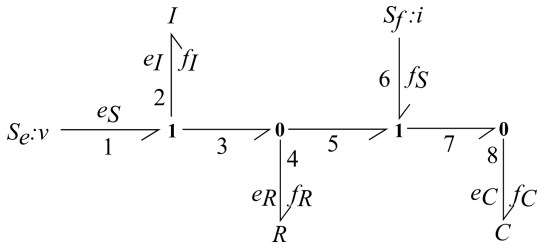

Figure 2.3.3: Bond graph of the electrical circuit of Fig. 2.3.2.

The Bond graph is not yet completely defined because a very important feature must be added, the causality. Causality introduces a cause-effect relation among the variables of each port. When the causality is applied in a Bond graph, the strokes are replaced by causal strokes (Fig. 2.3.4) and determine the inputs and outputs of each junction.

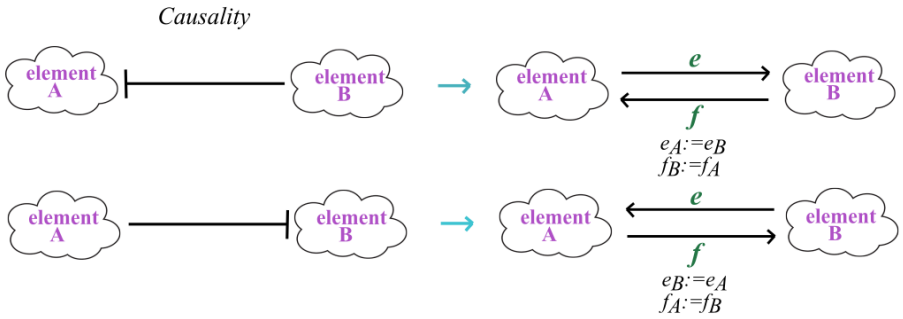

Figure 2.3.4: Causal strokes definition for effort and flow.

An important characteristic of the Bond graphs is the causality property which indicates the direction of the power flow and the dependence among the port-elements characterized by pairs of efforts e and flows f as in Fig. 2.3.5. Every element has different causality structure. In here, we will focus on the storage elements which define the states of the electrical systems referred in this work. There are two types of causalities, the integral and the differential causality:

- *Integral causality*: The input is integrated to generate the output (see also Fig. 2.3.5a). For the capacitors we have $e = \frac{1}{C}\int f dt$ and for the inductors $f = \frac{1}{I}\int e dt$ (where C is the capacitance and I is the inductance). More specifically, the capacitors, C, generate effort and receive flow, while the

inductors, I, generate flow which depends on the upcoming effort (Fig. 2.3.6). Besides, the current source S_f imposes a flow to the system which is independent from the effort (Fig. 2.3.6). On the other hand, the voltage source S_e imposes an effort independent from the flow (Fig. 2.3.6). Concerning the dissipative elements, R, they obey a static constitutive law which provides only algebraic relations between the effort and flow, $e = f \cdot R$ and $f = \frac{e}{R}$. Consequently, the resistors don't have a specific causality assignment (Fig. 2.3.6).

- *Differential causality*: The input's time derivative equals to the ratio of the output (see also Fig. 2.3.5b). For the capacitors will be $\frac{de}{dt} = \frac{f}{C}$ and for the inductors $\frac{df}{dt} = \frac{e}{I}$. Differential causality is used in the inverse Bond graphs, otherwise called bicausal Bond graphs, as in Fig. 3.4.8.

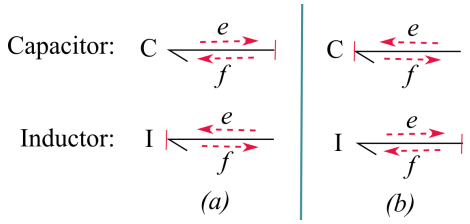

Figure 2.3.5: (a) Integral causality of the storage elements. (b) Differential causality of the storage elements.

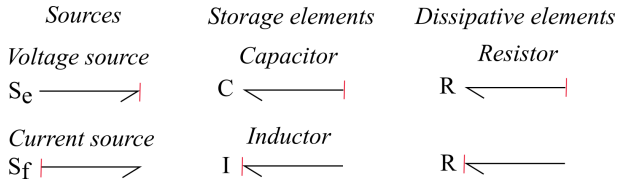

Figure 2.3.6: Energy sources, storage and dissipative elements with their causal strokes structure.

In addition to the previous statements, the 0 and 1 junctions follow also specific causality rules. In 0 junctions the effort is established and there is only one causal stroke with the causality symbol pointing towards the junction as in Fig. 2.3.7(a). Whereas, for 1 junctions, the flow is established, hence there can be only one causal stroke with the causality symbol pointing towards the element as in Fig. 2.3.7(b). For better comprehension, the causal Bond graph of the aforementioned electrical circuit(Fig. 2.3.2) is provided as well as the procedure of the causality assignment.

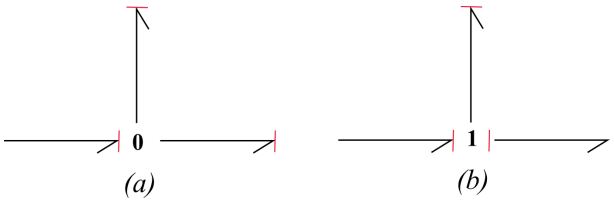

Figure 2.3.7: Causality assignment for junctions 0 and 1 in causal Bond graphs.

Following the example given in Fig. 2.3.2, the causality assignment is defined as follows:

- assignment of sources' causalities (Fig. 2.3.8);
- specification of the integral causality of the storage elements (Fig. 2.3.9);
- assignment of the dissipative elements (Fig. 2.3.10);

- in the case of possible differential causalities on the storage elements, a neutral element is added close to the storing element, such as the resistors R_{1sc} and R_{1b} added in the Split-Pi converter's and in the battery's Bond graphs presented later in Fig. 2.4.7 and Fig. 2.4.6 respectively.

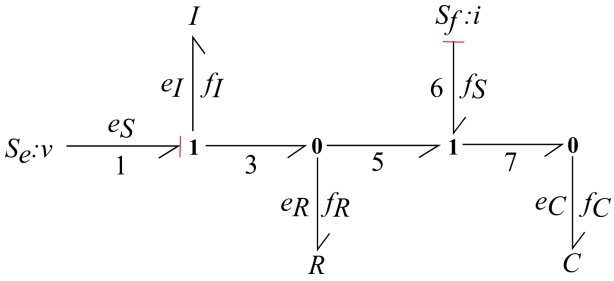

Figure 2.3.8: Causality assignment on the sources.

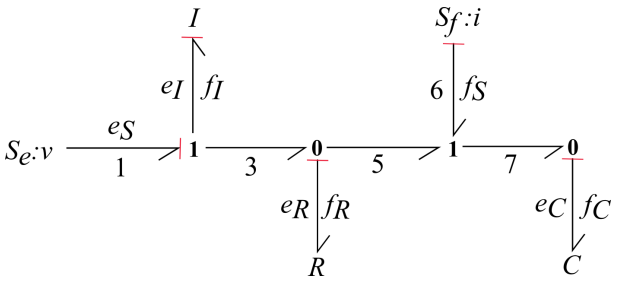

Figure 2.3.9: Causality assignment on the storing elements.

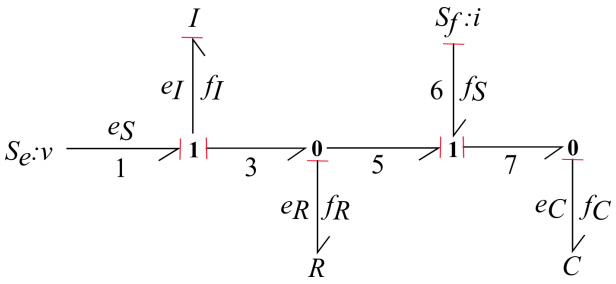

Figure 2.3.10: Causality on the dissipative elements. Numbering of causal strokes.

Finally, we proceed to the relations of the junctions 0 and 1:

- first 1 junction from the left: $e_1 - e_2 - e_3 = 0$ and $f_1 = f_2 = f_3$;
- first 0 junction: $e_3 = e_4 = e_5$ and $f_3 - f_4 - f_5 = 0$;
- second 1 junction: $e_5 - e_6 - e_7 = 0$ and $f_5 = f_6 = f_7$;
- second 0 junction: $e_7 = e_8$ and $f_7 = f_8$.

Furthermore, two more variables must be explained, which are necessary for the formulation of the system's state-space representation. These are the momentum, p, and the displacement, q, variables. The p variable is considered to be the e time integral ($p(t) = \int e(t)dt$) and the q variable is the f time integral ($q(t) = \int f(t)dt$). In the case of electrical circuits, p represents the magnetic flux of the inductors and q the charge of the capacitors. Therefore, according to the integral causality, we further obtain:

$$for\ C: \quad e = \frac{q}{C}, \qquad for\ I: \quad f = \frac{p}{I}.$$

Therefore, from the causal Bond graph of the electrical circuit example (Fig. 2.3.10), e_C and f_I can be replaced by:

$$for\ C: \quad e_C = \frac{q_C}{C}, \qquad for\ I: \quad f_I = \frac{p_I}{I}.$$

In the aforementioned description, only the elements which will be used in this work were presented. Although, in a Bond graph, two-port elements can also be considered (transformers, TF, and gyrators GY). These elements do not create or store energy. They transmit power by changing the $\frac{e}{f}$ ratio (Fig. 2.3.11).

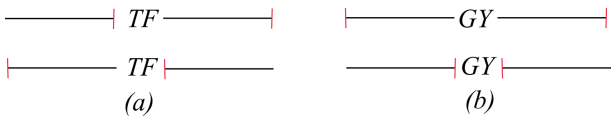

Figure 2.3.11: Routing elements: (a) Transformers. (b) Gyrators.

2.3.2 Port-Hamiltonian systems

In this section, we introduce the port-Hamiltonian (PH) systems together with some basic definitions. Additionally, the conversion from Bond graphs to port-Hamiltonian state-space representations will be presented. These notions will be instrumental for the mathematical model representation of the DC microgrid of Fig. 2.2.1.

Primarily, the Bond graph, as in Fig. 2.3.10, can be mathematically portrayed as a PH state-space representation. The explicit formulation of a PH system is written below (Duindam et al., 2009; van der Schaft et al., 2014):

$$\begin{aligned} \dot{x}(t) &= [J(t) - R]Qx(t) + Gu(t), \\ y(t) &= G^\top Qx(t) + Du(t). \end{aligned} \tag{2.3.1}$$

This is a typical PH representation and each of the components has a clear physical justification:

- $x(t) \in \mathbb{R}^n$ is the state vector of the extensive energy variables $p(t)$ and $q(t)$, referred before as the displacement variables and derived from the energy storing elements;
- $u(t) \in \mathbb{R}^m$ is the input vector, which contains voltage or current variables, generated by the sources or received by the loads;
- $y(t) \in \mathbb{R}^m$ is the output vector, which contains voltage or current variables, generated by the PH system;
- $J(t) \in \mathbb{R}^{n\times n}$ describes the interconnections of the system and defines the power continuity, meaning the structural balance equations which typically contain no numerical parameters. It is a skew-symmetric and positive semi-definite matrix;
- $R \in \mathbb{R}^{n\times n}$ is likewise a skew-symmetric positive semi-definite matrix which outlines the dissipative elements;
- $Q \in \mathbb{R}^{n\times n}$ is a positive definite matrix which, in the linear case, is a diagonal matrix including the system's physical parameters, such as the capacitance C of the capacitors and the inductance I of the inductors. More complex non linear constitutive equations may also be included;
- $D \in \mathbb{R}^{m\times m}$ describes the direct interconnection of the input variables;
- $G \in \mathbb{R}^{n\times m}$ is the control matrix of the PH system.

The output vector $y(t)$ in (2.3.1) is determined according to the inputs selection and the input map G. The inner product among the input and the output vectors minus the dissipative energy gives always the external power supplied to the system (Escobar et al., 2015). Below, we examine the Hamiltonian in linear cases:

1. The Hamiltonian, H, is the total energy stored in the storage elements of the system equal to:

$$H(x) = \frac{1}{2}x(t)^\top Qx(t); \tag{2.3.2}$$

2. From (2.3.1) and (2.3.2), when $D \neq 0$, we obtain the external power supplied to the system:

$$\frac{d}{dt}H = u(t)^\top y(t) - x(t)^\top Q^\top RQx(t) - u(t)^\top Du(t). \tag{2.3.3}$$

In general, PH systems are determined by the power-preserving interconnections of the elements of a physical system through a Dirac structure (DS) (van der Schaft et al., 2014). As in the Bond graphs with the Junction structures, a DS classifies equally power-conserving interconnections into three types of elements: i) energy-routing elements; ii) energy-storing elements ; iii) energy-dissipative elements. Energy-routing elements are the transformers and gyrators. Additionally, energy-dissipative elements are the resistors and energy-storing elements are the capacitors and the inductors. Besides, in a DS, we have external ports which determine the interaction of the system with its external environment.

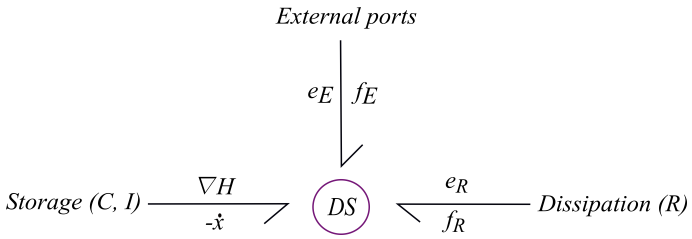

Figure 2.3.12: Dirac structure of a port-Hamiltonian system.

In Fig. 2.3.12, we observe the correspondence between Bond graphs and DS which both account for the continuous power balance equations (e.g., Kirchoff's laws in electrical networks). The DS connects all the port variables together and obeys the power conservation law which means that the total power $e^\top f$ of the central network is equal to 0 (Duindam et al., 2009; van der Schaft et al., 2014). To define a DS, we consider a finite-dimensional linear space of flows $\mathcal{F}$ with f elements, called flow vectors. The efforts' linear space will be denoted as $\mathcal{E} = \mathcal{F}^*$ and contains the e variables. The total space is equivalent to $\mathcal{F} \times \mathcal{E}$ and it is called the space of port variables and the total power is their duality product (van der Schaft et al., 2014):

$$< e|f >= e^\top f, \quad (f, e) \in F \times E, \tag{2.3.4}$$

where $e = \begin{bmatrix} e_1 & e_2 & e_3 & \dots & e_n \end{bmatrix}^\top$ and $f = \begin{bmatrix} f_1 & f_2 & f_3 & \dots & f_n \end{bmatrix}$.

Definition 2.3.1 (Power-conservation property - van der Schaft et al. (2014))**.** *: Consider a finite dimensional linear space $\mathcal{F}$ with $\mathcal{E} = \mathcal{F}^*$. The subspace $\mathcal{D}$, $\mathcal{D} \subset \mathcal{F} \times \mathcal{E}$ is defined as a Dirac structure if and only if:*

$$e^\top f = 0,$$
$$dim\mathcal{D}{=}dim\mathcal{F}.$$

Looking into the geometrical structure of the total space $\mathcal{F} \times \mathcal{E}$, according to the power definition, the canonically bilinear form of a DS can be defined as follows (van der Schaft et al., 2014):

$$<< (f^a, e^a), (f^b, e^b) >>:=< e^a|f^b > + < f^a|e^b >,$$

with $(f^a, e^a), (f^b, e^b) \in \mathcal{F} \times \mathcal{E}$. □

Definition 2.3.2. *(Dirac structure - van der Schaft et al. (2014)): A Dirac structure on $\mathcal{F} \times \mathcal{E}$ is a subspace $\mathcal{D} \subset \mathcal{F} \times \mathcal{E}$ such that $\mathcal{D} = \mathcal{D}^\perp$, where $\perp$ denotes the orthogonal supplement with respect to the bilinear form $\langle\langle , \rangle\rangle$.* □

From the DS port-based graph, we can derive the state-space representation of a dynamical system in PH form. The PH system results from the linkage of the DS with the elements associated to the storage, the dissipation and the external environment.

Definition 2.3.3. *(PH system - van der Schaft et al. (2014)): Consider the total storing energy as the Hamiltonian H defined by a state space $\mathcal{X}$, where $H : \mathcal{X}\ \mathcal{R}$, its tangent space $\mathcal{T}_x\mathcal{X}$ and co-tangent space $\mathcal{T}_x^*\mathcal{X}$. Then, the PH system is a DS defined by:*

$$\mathcal{D} \subset \mathcal{T}_x\mathcal{X} \times \mathcal{T}_x^*\mathcal{X} \times \mathcal{F}_R \times \mathcal{E}_R \times \mathcal{F}_E \times \mathcal{E}_E,$$

with the ES ports regarded as $(f_S, e_S) \in T_xX \times T_x^*X$, for which $f_S = -\dot{x}$ and $e_S = \nabla H(x)$, the dissipative port variables regarded as:

$$\mathcal{R}_R = \{(f_R, e_R) \in \mathcal{F}_R \times \mathcal{E}_R | R(f_R, e_R) = 0, < e_R | f_R > \leq 0\}$$

and the external ports as $(f_E, e_E) \in \mathcal{F}_E \times \mathcal{E}_E$*. In general, a PH system is expressed as noted below:*

$(-\dot{x}, \nabla H(x), f_R, e_R, f_E, e_E) \in \mathcal{D}$. □

In the following, the Bond graph theory in combination with the PH state-space representations will be employed to describe explicitly the dynamical model of each of the DC microgrid component mentioned before in Section 2.2.1.

2.4 DC microgrid dynamical model

In this section, we will present the complete model of the meshed DC microgrid and introduce its global Bond graph representation. Hereinafter, we will provide the mathematical models of the energy sources, the PV panel and the lead-acid batteries, in PH form based on their Bond graphs. Afterwards, we will describe also the central transmission network and its characteristics.

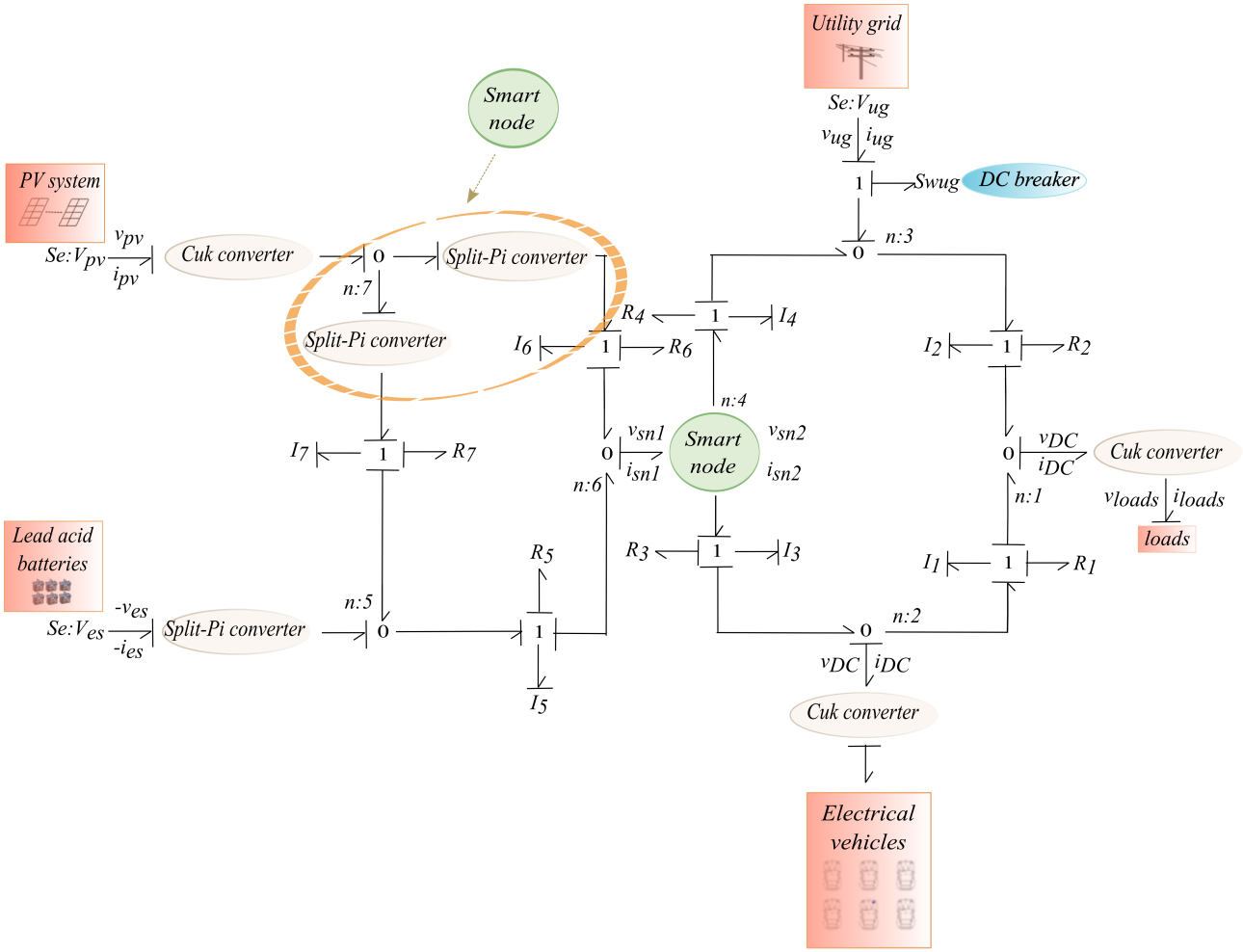

Figure 2.4.1: Bond graph of the meshed DC microgrid.

In Fig. 2.4.1 we present the Bond graph of the overall meshed DC microgrid illustrated in Fig. 2.2.1. In general, it is composed by three meshes, the PV station with its ES system, the EV station and the various loads (printers, computers, LED lighting, mobile phones and the like). Furthermore, the transmission lines have been replaced with an 'inductor plus resistance' block. This is the so-called *RL* circuit in which the two components are placed in series. In DC networks, an inductor behaves as a static resistance and contributes to the reduction of the power losses.

2.4.1 Dynamical model of the sources

Before beginning to elaborate separately each part of the DC microgrid, we mention, at this point, that the DC microgrid will be considered and analyzed as an ensemble of electrical circuits, where the storage elements are the inductors, I, and the capacitors, C, the dissipative elements are the resistors, R, and the energy sources are the voltage sources, as has been described in Section 2.3.1. The energy stored in the electrical circuits (Fig. 2.3.2 for instance), otherwise called the Hamiltonian, is a function of the magnetic flux of the inductors, p, and the charge of the capacitors, q. Therefore, from the general description of the Hamiltonian in linear cases (2.3.1), a particularization for the case at hand is given below:

$$H(x) = \frac{1}{2}x(t)^\top Q x(t),$$

where $x(t) = \begin{bmatrix} p_1 & p_2 & ... & p_{n_I} & q_1 & q_2 & ... & q_{n_C} \end{bmatrix}^\top \in \mathbb{R}^{n\times 1}$ is the state vector ($n = n_C + n_I$, where n_I is the number of inductors and n_C the number of the capacitors). Q is the circuit parameter matrix equal to $Q = diag\left\{\frac{1}{I_1}, \frac{1}{I_2}, ..., \frac{1}{I_{n_I}}, \frac{1}{C_1}, \frac{1}{C_2}, ..., \frac{1}{C_{n_C}}\right\} \in \mathbb{R}^{n\times n}$. Therefore, the Hamiltonian becomes:

$$H(x) = \frac{1}{2}\left(\frac{p_1^2}{I_1} + \frac{p_2^2}{I_2} + ... + \frac{p_{n_I}^2}{I_{n_I}}\right) + \frac{1}{2}\left(\frac{q_1^2}{C_1} + \frac{q_2^2}{C_2} + ... + \frac{q_{n_C}^2}{C_{n_C}}\right). \tag{2.4.1}$$

2.4.1.1 PV source model

The equivalent general circuit of a solar cell has been already depicted in Fig. 2.2.2. Its corresponding Bond graph is obtained below (Fig. 2.4.2). The electrical circuit of the solar cell does not have any storing elements, meaning no states available, and the Bond graph relies upon the power continuity equation written as follows:

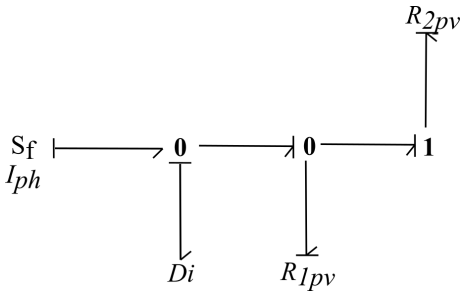

Figure 2.4.2: Bond graph of the solar cell circuit.

$$v_s i_{ph} + v_{Di} i_{Di} + v_{R_{1pv}} i_{R_{1pv}} + v_{R_{2pv}} i_{R_{2pv}} = 0, \tag{2.4.2}$$

where s is the sunlight source, the series resistance R_{2pv} resists to the current flow, R_{1pv} is the shunt resistance of the system, Di is the diode and v declines the output voltage. Additionally, from the 0/1 junctions, the equations below are deduced:

$$\begin{aligned} i_{ph} &= i_{Di} + i_{R_{1pv}} + i_{2pv}, \\ v_{R_{2pv}} &= v_{Di}. \end{aligned} \tag{2.4.3}$$

However, the model of a PV panel is rather complicated and obeys a set of constitutive equations that have been established the past decades from the researchers and can be found in the literature (Enrique et al., 2007; Villalva et al., 2009). Therefore, all the unknown variables of (2.4.2) and (2.4.3) are calculated by the classical PV mathematical model. The parameters of the PV panel depend on the selected model which, in our case, is the DS-100 MPV module (180 W peak PV generation). The final equation of the PV

panel composed by cell arrays is the following:

$$i(t) = N_{pa} i_{ph}(t) - N_{pa} i_0(t) \left[\exp\left(\frac{\frac{v(t)}{N_{se}} + i\frac{R_{2pv}}{N_{pa}}}{n v_{Di}(t)} \right) - 1 \right] - i_{1pv}(t), \quad \text{where} \tag{2.4.4}$$

$$v_{Di}(t) = \frac{k_B Temp}{q_{el}}, \tag{2.4.5}$$

$$i_{1pv}(t) = \frac{v(t)\frac{N_{pa}}{N_{se}} + i(t)R_{2pv}}{R_{1pv}}, \tag{2.4.6}$$

$$P(t) = v(t)i(t), \tag{2.4.7}$$

where i is the output current, N_{pa} is the number of cells in parallel, N_{se} is the number of cells in series, i_0 is the saturation current of the cell, k_B is the Boltzmann's constant, q_{el} is the electron charge and $Temp$ is the working temperature of the solar cell.

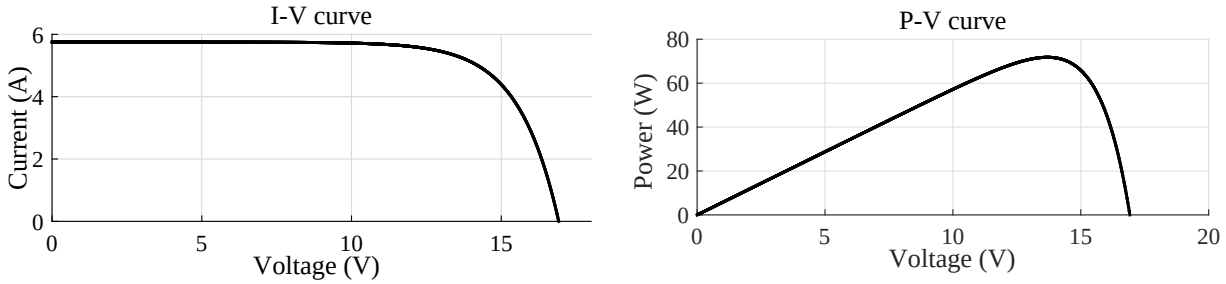

(a) (b)

Figure 2.4.3: (a) $I - V$ curve of the PV model. (b) $P - V$ curve of the PV model.

To proceed to the PV profiles generation, the model was developed in MATLAB/Simulink. For model testing, the aforementioned PV model is studied under a constant input solar irradiation equal to $800 W/m^2$ and a constant external temperature equal to 25 °C to obtain the I-V curve in Fig. 2.4.3a and the P-V curve in Fig. 2.4.3b.

For further validation, we generate also power profiles (Fig. 2.4.5) based on different weather scenarios (Fig. 2.4.4a) for a PV array of 28 panels with 72 solar cells. Besides, we take into account that a solar cell produces about $0,5V$. A typical PV that produces about $12V$ contains 36 cells wired in series. For a PV with 72 cells, we consider two $12V$ PV panels of 36 cells wired in series, usually with a jumper, allowing an output voltage equal to $24V$. Therefore, we proceed to the following simulations and the obtained profiles will be used later in Chapter 4.

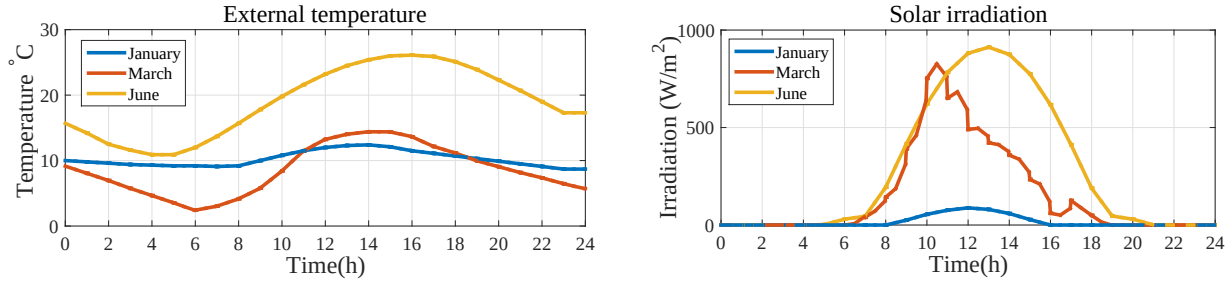

(a) (b)

Figure 2.4.4: (a) Temperature profiles for three days of different months, on January, on March and on June, within a year. (b) Irradiation profiles corresponding to the days chosen for the temperature profiles in Fig. 2.4.4a.

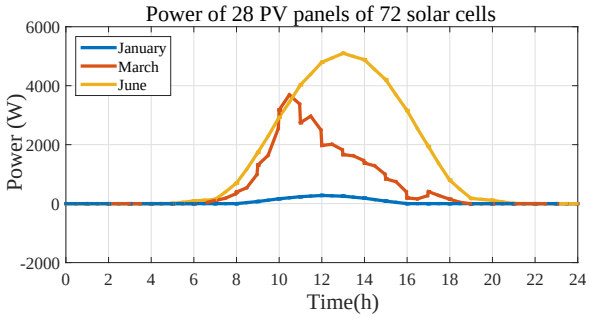

Figure 2.4.5: Profiles of the extracted power of the PV module DS-100M composed by 72 cells.

2.4.1.2 Lead-acid battery model

In the following, the Bond graph of the KiBaM battery is introduced. Fig. 2.4.6 portrays the corresponding Bond graph of the proposed electrical circuit of the KiBaM battery (Fig. 2.2.4). As already mentioned, between the battery and the source, v_s, there is a resistance which models the transmission line. The resistance, R_{1b}, is necessary in order to avoid the differential causality at the C_{1b} capacitor (see also the causality discussion carried out in Section 2.3.1).

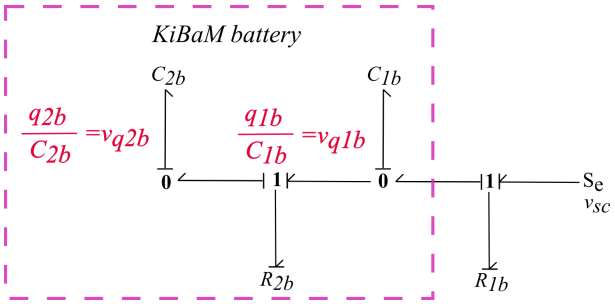

Figure 2.4.6: Bond graph representation of the KiBaM.

Consequently,from the Bond graph, we arrive directly to the following PH state-space representation:

$$\begin{cases} \begin{bmatrix} \dot{q}_{1b} \\ \dot{q}_{2b} \end{bmatrix} &= [J_b - R_b] Q_b x_b + \begin{bmatrix} -\dfrac{1}{R_{1b}} \\ 0 \end{bmatrix} (-v_{sc}), \\ i_{sc} &= \begin{bmatrix} -\dfrac{1}{R_{1b}} & 0 \end{bmatrix} Q_b x_b + \begin{bmatrix} \dfrac{1}{R_{1b}} \end{bmatrix} v_{sc}, \end{cases} \tag{2.4.8}$$

where $x_b = \begin{bmatrix} q_{1b} & q_{2b} \end{bmatrix}^\top \in \mathbb{R}^{2\times 1}$ is the state vector, $v_{sc} \in \mathbb{R}$ is the system's input vector denoting the input voltage coming from the Split-Pi converter, presented afterwards, $i_{sc} \in \mathbb{R}$ is the output vector and where i_{sc} is the battery's current during charging. The dissipation matrix $R_b \in \mathbb{R}^{2\times 2}$ is equal to:

$$R_b = \begin{bmatrix} \dfrac{1}{R_{1b}} + \dfrac{1}{R_{2b}} & -\dfrac{1}{R_{2b}} \\ -\dfrac{1}{R_{2b}} & \dfrac{1}{R_{2b}} \end{bmatrix}. \tag{2.4.9}$$

All the unknown variables and parameters of the battery model can be found similarly in the literature (Manwell and McGowan, 1993) and depend on the type of the lead-acid battery. The charging and discharging processes of the battery will be controlled by the Split-Pi converter, presented in the next section. As it can be deduced by (2.4.8), the matrix J_b of the battery PH representation is equal to 0. The matrix J includes the internal power-preserving interconnections representing the oscillations between the electrical and the magnetic field of the storing elements. Since, there is only capacitors in the electrical circuit and no inductors, no oscillations exist and the J_b matrix becomes 0. Therefore, by connecting the battery circuit to the Split-Pi converter, as it will be shown later, we obtain the J_{es} matrix of the ES system. For the

simulations, an AGM 12-165 battery (165 Ah battery capacity) is considered and is validated later within the ES system (subsection 2.5.1).

2.4.2 Dynamical model of the converters

2.4.2.1 Split Pi converter model

This subsection introduces the corresponding Bond graph (Fig. 2.4.7) of the Split-Pi converter (Fig. 2.2.5). In the Bond graph, we add a resistor element after the source, R_{1sc}, in order to respect the causality property (integral causality) and avoid the differential causality (see also the causality discussion carried out in Section 2.3.1). According to the Bond graph of the converter, its PH state-space representation is provided below:

$$\begin{cases} \begin{bmatrix} \dot{p}_{1sc} \\ \dot{p}_{2sc} \\ \dot{q}_{1sc} \\ \dot{q}_{2sc} \\ \dot{q}_{3sc} \end{bmatrix} = [J_{sc} - R_{sc}]Q_{sc}x_{sc} + \begin{bmatrix} 0 & 0 \\ 0 & 0 \\ \frac{-1}{R_{1_{sc}}} & 0 \\ 0 & 0 \\ 0 & 1 \end{bmatrix} u_{sc}, \\ y_{sc} = \begin{bmatrix} 0 & 0 & \frac{-1}{R_{1_{sc}}} & 0 & 0 \\ 0 & 0 & 0 & 0 & 1 \end{bmatrix} Q_{sc}x_{sc} + \begin{bmatrix} -\frac{1}{R_{1_{sc}}} & 0 \\ 0 & 0 \end{bmatrix} \begin{bmatrix} -v_s \\ -i_{R_{Lsc}} \end{bmatrix}, \end{cases} \tag{2.4.10}$$

where $x_{sc} = \begin{bmatrix} p_{1sc} & p_{2sc} & q_{1sc} & q_{2sc} & q_{3sc} \end{bmatrix}^\top \in \mathbb{R}^{5\times 1}$ is the state vector, $u_{sc} = \begin{bmatrix} -v_s & -i_{R_{Lsc}} \end{bmatrix}^\top \in \mathbb{R}^{2\times 1}$ is the system's input represented by the input voltage v_S generated from the source, the PV or the ES, and the current of the load $i_{R_{Lsc}} = \frac{q_{3sc}}{R_{Lsc}C_{3sc}}$, $y_{sc} = \begin{bmatrix} i_s & v_{R_{Lsc}} \end{bmatrix}^\top \in \mathbb{R}^{2\times 1}$ is the output vector, i_S is the current of the source and $v_{R_{Lsc}}$ is the output voltage of the converter. The matrix $J_{sc} \in \mathbb{R}^{5\times 5}$ and the dissipation

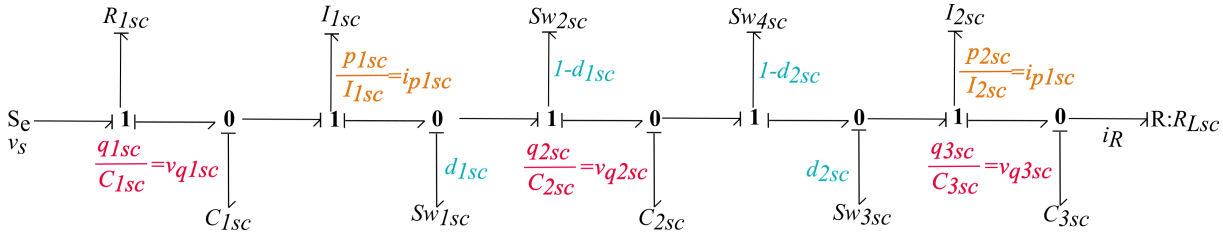

Figure 2.4.7: Bond graph of the Split-Pi converter.

matrix $R_{sc} \in \mathbb{R}^{5\times 5}$ are described below:

$$J_{sc} = \begin{bmatrix} 0 & 0 & 1 & -(1-d_{1sc}(t)) & 0 \\ 0 & 0 & 0 & (1-d_{2sc}(t)) & -1 \\ -1 & 0 & 0 & 0 & 0 \\ 1-d_{1sc}(t) & -(1-d_{2sc}(t)) & 0 & 0 & 0 \\ 0 & 1 & 0 & 0 & 0 \end{bmatrix}, \tag{2.4.11}$$

$$R_{sc} = diag(0,\ 0,\ \frac{1}{R_{1_{sc}}},\ 0,\ 0), \tag{2.4.12}$$

where values $d_{1sc}(t), d_{2sc}(t)$ are the control variables representing the duty cycles of the converter's switches.

As a next step, the relations among the duty cycles needs to be defined. This will help us to develop an open-loop control law for the switches. According to the patent of the United States Patent and Trademark Office No: US 6914420 B2 published on July 2005 (Crocker, 2005), the following statements can be deduced for the down and the up-conversion (see also Table 2.2.1):

- During the down-conversion (phase 1), the C_{2sc} voltage equals the input voltage v_S, while the current rate of the inductor I_{2sc} is equal to $\frac{di_{I_{2sc}}}{dt} = \frac{\triangle v_{I_{2sc}}}{I_{2sc}}$.

- During the down-conversion (phase 2), when the voltage around I_{2sc} is reversed, the current rate of the inductor I_{2sc} is equal to $\frac{di_{I_{2sc}}}{dt} = \frac{-v_{C_{3sc}}}{I_{2sc}}$.

Therefore, the absolute values of the two current ratios over a cycle must be equal and for each ratio we can define a period of time, t_4 for the first ratio and t_3 for the second:

$$t_4 \frac{v_{C_{2sc}} - v_{C_{3sc}}}{I_{2sc}} + t_3 \frac{-v_{C_{3sc}}}{I_{2sc}} = 0 \tag{2.4.13}$$

$$\frac{v_{C_{3sc}}}{v_{C_{2sc}}} = \frac{t_4}{t_3 + t_4} = \alpha, \tag{2.4.14}$$

where α is a factor that will help us to determine the switching action within the converter. Now, if we take into consideration that, by definition, $d_{2sc} = \frac{t_3}{t_3 + t_4}$, then $a = 1 - d_{2sc}$. For the up-conversion, we have similarly:

- During the up-conversion (phase 1), the C_{2sc} voltage equals to the output voltage of the circuit, while the current rate of the inductor I_{1sc} being equal to $\frac{di_{I_{1sc}}}{dt} = \frac{\triangle v_{I_{1sc}}}{I_{1sc}}$.

- During the up-conversion (phase 2), the current rate of the inductor I_{1sc} is equal to $\frac{di_{I_{1sc}}}{dt} = \frac{v_{C_{1sc}}}{I_{1sc}}$.

Consequently, as before, the absolute value of the two current ratios over a cycle must be equivalent and for each ratio we define another two periods of time, t_2 and t_1:

$$t_2 \frac{v_{C_{1sc}} - v_{C_{2sc}}}{I_{1sc}} + t_1 \frac{v_{C_{1sc}}}{I_{1sc}} = 0 \tag{2.4.15}$$

$$\frac{v_{C_{2sc}}}{v_{C_{1sc}}} = \frac{t_1 + t_2}{t_2} = \alpha. \tag{2.4.16}$$

If we account that $d_{1sc} = \frac{t_1}{t_1 + t_2}$, then $a = \frac{1}{1 - d_{1sc}}$. As a result, in the general case, we obtain the relation referred below:

$$a = \frac{1 - d_{2sc}}{1 - d_{1sc}}, \tag{2.4.17}$$

where for the down-conversion $d_{2sc} \in (0, 1)$ and $d_{1sc} = 0$ and for the up-conversion $d_{1sc} \in (0, 1)$ and $d_{2sc} = 0$.

Furthermore, considering that the Split-Pi converter is an electrical circuit with no interior power loss, we may apply a power conservation rule. Hence, the input power will be equal to the output power as referred below (see also Fig. 2.2.5):

$$P_{sc\_in} = P_{sc\_out} \tag{2.4.18}$$

$$v_{sc\_in} i_{sc\_in} = v_{sc\_out} i_{sc\_out} \tag{2.4.19}$$

$$\frac{i_{sc\_in}}{i_{sc\_out}} = \frac{v_{sc\_out}}{v_{sc\_in}} = \alpha, \tag{2.4.20}$$

where v_{sc_in}, by considering the resistance R_{1sc} added in the Bond graph (Fig. 2.4.7), is equal to $v_{sc\_in} = v_s - i_s R_{1sc}$, respecting Ohm's law, and $v_{sc\_out} = \frac{q_{3sc}}{C_{3sc}} = v_{R_{Lsc}}$. The v_s, i_s, q_{3sc} and $v_{R_{Lsc}}$ can be found from the converter's PH model in (2.4.10)-(2.4.11).

For the simulation, we build the Split-Pi PH model in MATLAB/Simulink. We set the parameters according to Table 2.4.1 and we proceed to the simulations. In order to validate the PH model, we consider concrete values for the output voltage of the Split-Pi, u_{sc_out}, and we observe if, through the PH model, these values can be followed. Therefore, we consider, the first $300s$, an output voltage equal to $13V$, then we change the voltage to $15V$ and, finally, at $700s$ we change again to $14V$ in order to observe the response of the converter. Fig. 2.4.8 depicts the simulation results where the expected output voltage is well-followed by the Split-Pi PH representation. In Fig. 2.4.9, the corresponding duty cycle, d_{2sc}, is presented.

Table 2.4.1: Parameters of the Split-Pi converter.

Parameters	Values
I_{1sc}, I_{2sc}	0.25 H
C_{1sc}, C_{2sc}, C_{3sc}	0.0008 F
R_{1sc}	0.1 Ω

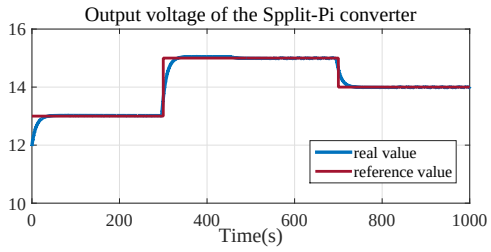

Figure 2.4.8: Expected output voltage during down-conversion in the Split-Pi converter.

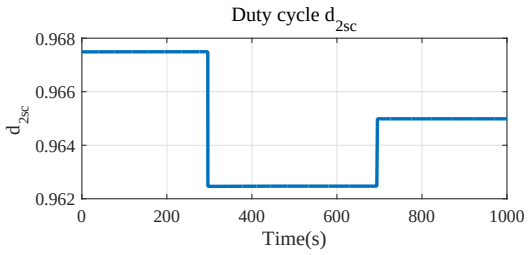

Figure 2.4.9: Corresponding duty cycle.

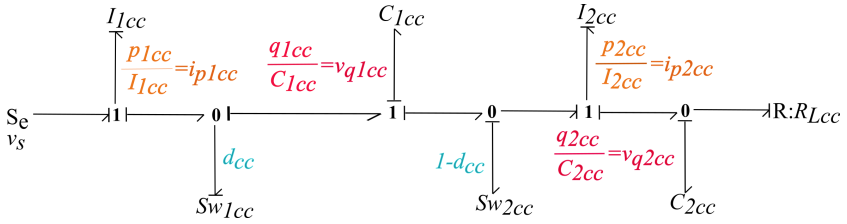

Figure 2.4.10: Ćuk converter Bond graph.

2.4.2.2 Ćuk converter model

In the following, we present the PH representations of the Ćuk converter according to its Bond graph indicated in Fig. 2.4.10 (Escobar et al., 2015). The Bond graph is based on the electrical circuit of Fig. 2.2.7:

$$\begin{cases} \begin{bmatrix} \dot{p}_{1cc} \\ \dot{p}_{2cc} \\ \dot{q}_{1cc} \\ \dot{q}_{2cc} \end{bmatrix} = [J_{cc} - R_{cc}]Q_{cc}x_{cc} + \begin{bmatrix} 1 & 0 \\ 0 & 0 \\ 0 & 0 \\ 0 & 1 \end{bmatrix} \begin{bmatrix} v_S \\ -\frac{q_{2cc}}{R_{Lcc}C_{2cc}} \end{bmatrix}, \\ \begin{bmatrix} i_S \\ v_{R_{Lcc}} \end{bmatrix} = \begin{bmatrix} 1 & 0 & 0 & 0 \\ 0 & 0 & 0 & 1 \end{bmatrix} Q_{cc}x_{cc}, \end{cases} \tag{2.4.21}$$

where $x_{cc} = \begin{bmatrix} p_{1cc} & p_{2cc} & q_{1cc} & q_{2cc} \end{bmatrix}^\top \in \mathbb{R}^{4\times 1}$ is the state vector, $u_{cc} = \begin{bmatrix} v_S & -\frac{q_{2cc}}{R_{Lcc}C_{2cc}} \end{bmatrix} \in \mathbb{R}^{2\times 1}$ is the system's input vector denoting the input voltage v_s from the DC bus and the load's current $i_{R_{Lcc}} = \frac{q_{2cc}}{R_{Lcc}C_{2cc}}$, $y_{cc} = \begin{bmatrix} i_S & v_{R_{Lcc}} \end{bmatrix}^\top \in \mathbb{R}^{2\times 1}$ is the output vector, i_{dc} is the input current and $v_{R_{Lcc}}$ is the output voltage of the converter. The matrix R_{cc} is equal to 0 and $J_{cc} \in \mathbb{R}^{4\times 4}$ is depicted below:

$$J_{cc} = \begin{bmatrix} 0 & 0 & -(1 - d_{cc}(t)) & 0 \\ 0 & 0 & -d_{cc}(t) & -1 \\ 1 - d_{cc}(t) & d_{cc}(t) & 0 & 0 \\ 0 & 1 & 0 & 0 \end{bmatrix}. \tag{2.4.22}$$

The value $d_{cc}(t) \in (0, 1)$ is the control variable of the converter that corresponds to the duty cycle of the two converter's switches.

For the simulation, we construct the Ćuk converter PH model in MATLAB/Simulink. Based on Table 2.4.2, we move forward to the simulations. As for the Split-Pi converter, we consider several values for the

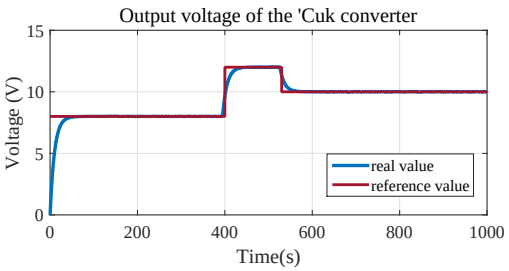

Figure 2.4.11: Expected output voltage.

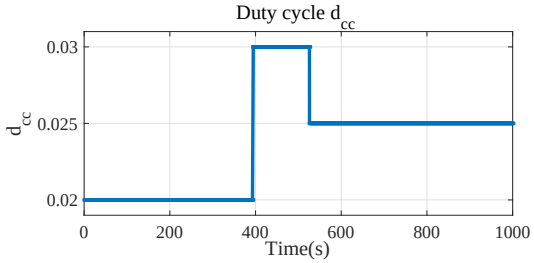

Figure 2.4.12: Corresponding duty cycle.

expected output voltage v_{cc_out} and we observe if, through the PH model, they can be followed. Thus, we set an expected output voltage, firstly, equal to $8V$, then changed to $12V$ and, finally, to $10V$. Fig. 2.4.11 illustrates the output voltage generated by the PH model of the Ćuk converter. The expected output voltage is well-followed. In Fig. 2.4.12 the corresponding duty cycle, d_{cc}, is depicted.

Table 2.4.2: Parameters of the Ćuk converter.

Parameters	Values
I_{1cc}, I_{2cc}	0.25 H
C_{1cc}, C_{2cc}	0.0008 F
R	0.025 Ω

For the simulation, similarly to (2.4.18) for the Split-Pi converter, we applied again the input/output power conservation for the Ćuk converter, as an electrical circuit without power losses, as follows:

$$P_{cc\_in} = P_{cc\_out} \tag{2.4.23}$$

$$v_{cc\_in} i_{cc\_in} = v_{cc\_out} i_{cc\_out} \tag{2.4.24}$$

$$\frac{i_{cc\_in}}{i_{cc\_out}} = \frac{v_{cc\_out}}{v_{cc\_in}} = d_{cc}, \tag{2.4.25}$$

where $v_{cc\_in} = v_s$ and $v_{cc\_out} = v_{R_{Lcc}}$. The v_s and $v_{R_{Lcc}}$ variables can be found through the PH model in (2.4.21)-(2.4.22).

2.4.3 Central transmission network

This section analyzes the global central transmission network as a collection of meshgrids, which will be applied in the load balancing problem. This problem concerns the regulation of the DC-voltage in multi-terminal DC networks and aims to achieve an optimal power flow (OPF) among the transmission lines, that is, finding the optimal working point of the system by using a set of constraints for the power, the current and the voltage (Gavriluta et al., 2015). In order to optimize the power flow of the system, the power losses in the transmission-line network, caused by the Joule effect, must be reduced , i.e., an associated cost function has to be minimized.

Regarding the meshed DC microgrid considered in this work, the central transmission network is a cyclic network, because when the connecting nodes[3] are linked together, they form cycles and, consequently, loops. In general, the transmission network is represented as a circuit with storage and dissipative elements. In here, the transmission lines, as already referred, are replaced by RL circuits as in Fig. 2.4.13. Every connecting node in this network can be connected to another meshgrid (Fig. 2.4.13) which leads to a meshed topology.

In order to analyze the network, we will develop a general PH state-space representation that can be used for each meshgrid separately. Then, the Bond graph of Fig. 2.4.1 will be used as an example to apply the

[3]Connecting node is the point where a source or a load is linked to the central network as in Fig. 2.2.1 for the connecting nodes $1 \ldots 7$.

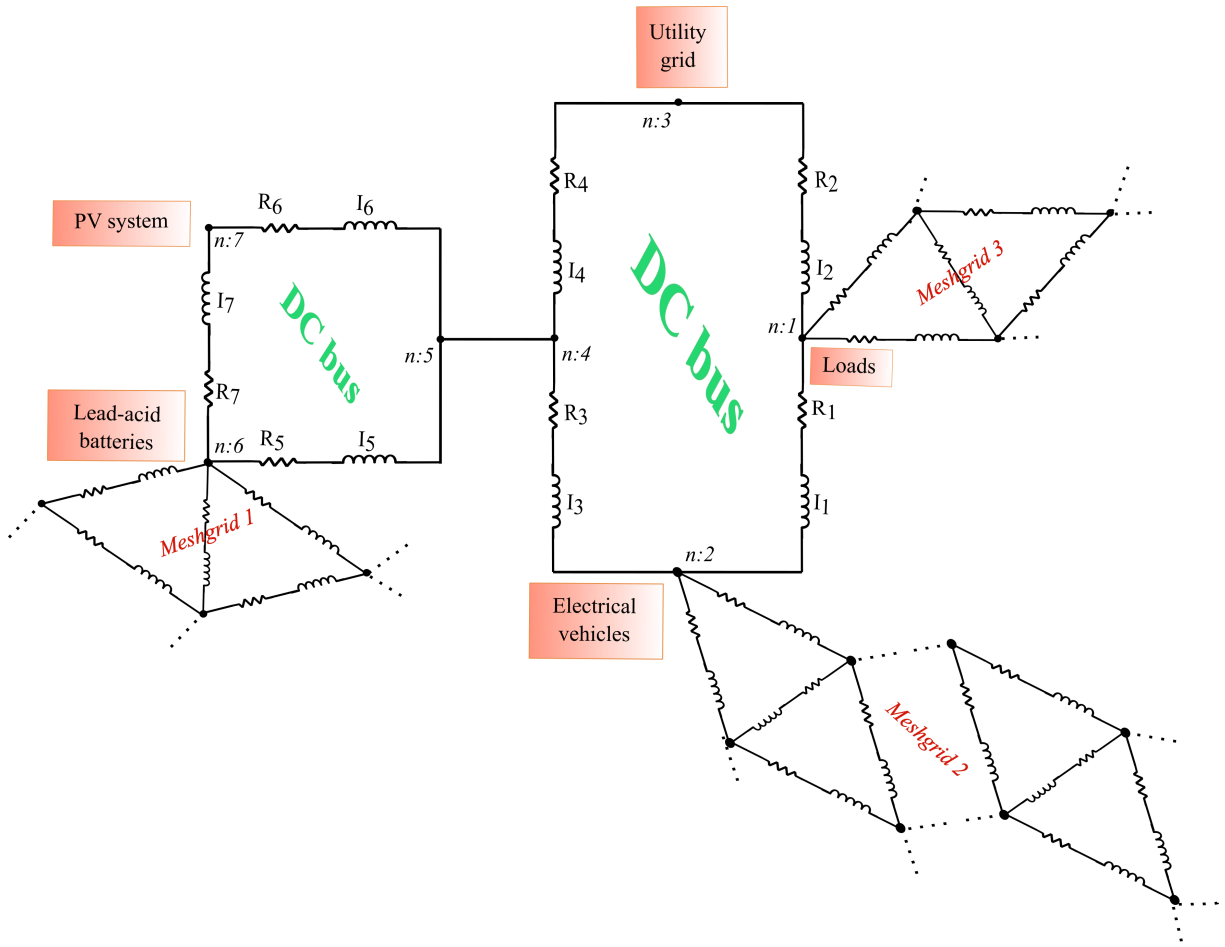

Figure 2.4.13: Cyclic network of loads.

general PH representation presented below:

$$\begin{cases} \begin{bmatrix} \dot{p}_{1c} \\ \dot{p}_{2c} \\ \dot{p}_{3c} \\ \vdots \\ \dot{p}_{nl} \end{bmatrix} = [J_c - R_c]Q_c x_c + G_c \begin{bmatrix} v_1 \\ v_2 \\ v_3 \\ \vdots \\ v_{nc} \end{bmatrix}, \\ \begin{bmatrix} i_1 \\ i_2 \\ i_3 \\ \vdots \\ i_{nc} \end{bmatrix} = G_c^\top Q_c x_c, \end{cases} \tag{2.4.26}$$

where $x_c = \begin{bmatrix} p_{1c} & p_{2c} & p_{3c} & \dots & p_{nl} \end{bmatrix}^\top \in \mathbb{R}^{n\times 1}$ is the state vector, $u_c = \begin{bmatrix} v_1 & v_2 & v_3 & \dots & v_{nc} \end{bmatrix}^\top \in \mathbb{R}^{node\times 1}$ is the input vector and $y_c = \begin{bmatrix} i_1 & i_2 & i_3 & \dots & i_{nc} \end{bmatrix}^\top \in \mathbb{R}^{node\times 1}$ is the output vector of the system. The skew-symmetric matrix J_c is equal to 0 for each meshgrid. As aforementioned, the J matrix (2.3.1) represents the oscillations among the electrical and the magnetic field. However, in this case, we consider only inductors, which lead to $J_c = 0$. As regards the dissipation matrix, $R_c \in \mathbb{R}^{n\times 4}$, it is equal to:

$$R_c = diag(R_{1c}, R_{2c}, R_{3c}, ..., R_{nl}), \tag{2.4.27}$$

where nl is the number of the transmission lines. Additionally to the PH model, we always consider the

conservation property inside the transmission network, as written below:

$$\sum_{i=1}^{I_n} P_{I_n} + \sum_{i=1}^{R_n} P_{R_n} + \sum_{i=1}^{nc} P_{nc} = 0, \tag{2.4.28}$$

where R_n is the number of resistors, I_n is the number of inductors and nc is the number of connecting nodes.

Therefore, according to (2.4.26), (2.4.27), (2.4.28), from the Bond graph in Fig. 2.4.1, we conclude to the following PH state-space representation (where we have 7 connecting nodes and 7 RL circuits for the transmission lines):

$$\begin{cases} \begin{bmatrix} \dot{p}_1 \\ \dot{p}_2 \\ \dot{p}_3 \\ \dot{p}_4 \\ \dot{p}_5 \\ \dot{p}_6 \\ \dot{p}_7 \end{bmatrix} = [J_c - R_c] Q_c x_c + \begin{bmatrix} 0 & 0 & -1 & 1 & 0 & 0 & 0 \\ 0 & -1 & 0 & 1 & 0 & 0 & 0 \\ 1 & 0 & 1 & 0 & 0 & 0 & 0 \\ 1 & 1 & 0 & 0 & 0 & 0 & 0 \\ 0 & 0 & 0 & 0 & 0 & -1 & 1 \\ 0 & 0 & 0 & 0 & 1 & 0 & 1 \\ 0 & 0 & 0 & 0 & 1 & 1 & 0 \end{bmatrix} \begin{bmatrix} v_{sn1} \\ -v_{ug} \\ -v_{ev} \\ -v_{loads} \\ v_{pv} \\ -v_b \\ -v_{sn2} \end{bmatrix}, \\ \begin{bmatrix} i_{sn1} \\ i_{ug} \\ i_{ev} \\ i_{loads} \\ i_{pv} \\ i_b \\ i_{sn2} \end{bmatrix} = \begin{bmatrix} 0 & 0 & 1 & 1 & 0 & 0 & 0 \\ 0 & -1 & 0 & 1 & 0 & 0 & 0 \\ -1 & 0 & 1 & 0 & 0 & 0 & 0 \\ 1 & 1 & 0 & 0 & 0 & 0 & 0 \\ 0 & 0 & 0 & 0 & 0 & 1 & 1 \\ 0 & 0 & 0 & 0 & -1 & 0 & 1 \\ 0 & 0 & 0 & 0 & 1 & 1 & 0 \end{bmatrix} Q_c x_c, \end{cases} \tag{2.4.29}$$

where $x_c = \begin{bmatrix} p_1 & p_2 & p_3 & p_4 & p_5 & p_6 & p_7 \end{bmatrix}^\top \in \mathbb{R}^{7\times 1}$ is the state vector, $u_c = \begin{bmatrix} v_{sn1} & -v_{ug} & -v_{ev} & -v_{loads} & v_{pv} & -v_b & -v_{sn2} \end{bmatrix}^\top \in \mathbb{R}^{7\times 1}$ is the input vector and $y_c = \begin{bmatrix} i_{sn1} & i_{ug} & i_{ev} & i_{loads} & i_{pv} & i_b & i_{sn2} \end{bmatrix}^\top \in \mathbb{R}^{7\times 1}$ is the output vector of the system. In addition, the dissipation matrix $R_c \in \mathbb{R}^{7\times 7}$ is equal to:

$$R_c = diag(R_1, R_2, R_3, R_4, R_5, R_6, R_7). \tag{2.4.30}$$

Hence, the G_c matrix contains all the power-preserving interconnections within the transmission line network and the R_c matrix includes the power losses.

In the upcoming section, more details for the central transmission network will be given through a simplified architecture. The reduction of a model is usually considered as a forward step because of the systems' complexity. Sometimes the structure of a system has to be simplified (Parisio et al., 2015; Wang et al., 2012) and replaced by a simpler dynamics, manageable from the viewpoint of further control design procedures and analysis.

2.5 Reduced model of the DC microgrid

In the sequel, the simplified version of the meshed DC microgrid will be described. To implement this simplification of the system, the number of the transmission lines will be reduced. This new scheme will facilitate the construction of the optimization problem in Chapter 4. The purpose is to consider a macroscopic view of the same meshed DC microgrid (Fig. 2.2.1), on which we will be able later to add the erased components. To proceed with this approach, the following assumptions have been made:

- reduction of the meshgrids down to one central transmission network;
- reduction of the transmission lines, setting $R_5 = R_6 = R_7$ equal to 0 and erasing $I_5 = I_6 = I_7$. Moreover, considering the EVs station as the main energy storage, the batteries' section of the corresponding meshgrid can be removed and only the PV system remains;
- considering the EVs station as a storage system will account both for power storage and charging the EVs;

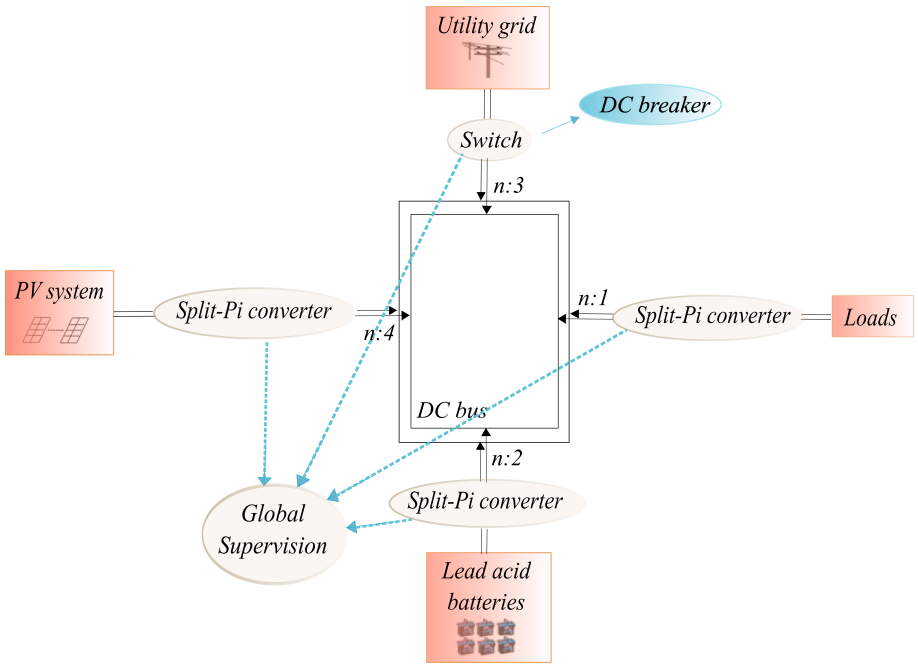

Figure 2.5.1: Reduced architecture of the DC microgrid.

- considering the loads as having an universal power consumption profile;
- setting limitations to the power produced by the UG;
- replacing all the DC/DC converters with a Split-Pi converter. The central network is a high-voltage network which means that the DC/DC converters will always operate in up-conversion mode, considering the direction from the source to the system as positive.

Applying all these simplifications, we arrive to the system presented in Fig. 2.5.1. The meshed DC microgrid, at this point, contains a four-line transmission network with four nodes, on which the three power sources (UG, PV and ES) and the loads are connected. Below, we will deduce explicitly the dynamical models of the ES system (the battery linked together with the Split-Pi converter) and the latter proposed central transmission network.

2.5.1 Energy storage system

This subsection presents the mathematical model of the ES system which is highly relevant for the rest of the analysis and is required in order to provide a backup energy source. Below, the detailed electrical circuit of the KiBaM battery connected to the Split-Pi converter is introduced. In Fig. 2.5.2, we present the complete circuit of the ES system and its related Bond graph (Fig. 2.5.3).

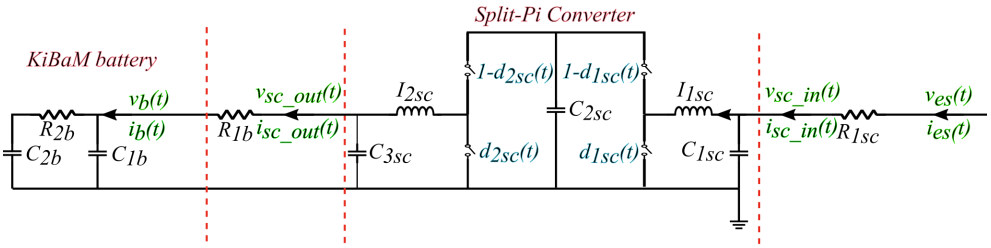

Figure 2.5.2: Detailed electrical network of the KiBaM battery connected to the electrical circuit of the Split-Pi converter during charging mode.

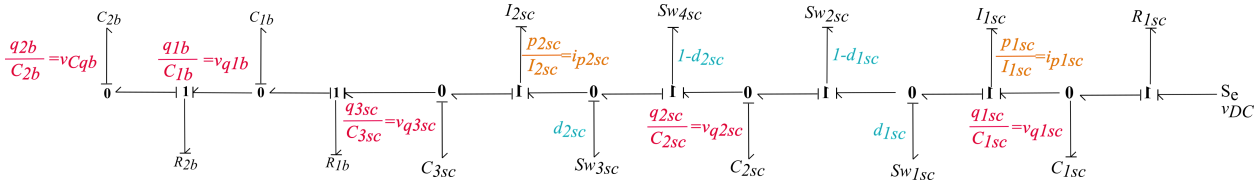

Figure 2.5.3: Corresponding Bond graph of the electrical network of the KiBaM battery connected to the Split-Pi converter.

From the associated Bond graph, the PH formalism of the system is provided below:

$$\begin{cases} \dot{x}_{es}(t) &= [J_{es}(d(t)) - R_{es}]Q_{es}x_{es}(t) + G_{es}u_{es}(t), \\ y_{es}(t) &= G_{es}^{\top}Q_{es}x_{es}(t) + D_{es}u_{es}(t), \end{cases} \tag{2.5.1}$$

where $x_{es}(t) = \begin{bmatrix} p_{1sc}(t) & p_{2sc}(t) & q_{1sc}(t) & q_{2sc}(t) & q_{3sc}(t) & q_{1b}(t) & q_{2b}(t) \end{bmatrix}^{\top} \in \mathbb{R}^{7\times 1}$, $u_{es}(t) = [-v_{DC}(t) \; -i_{R_{1b}}(t)]^{\top} \in \mathbb{R}^{2\times 1}$ denotes the input voltage coming from the central network, otherwise called the DC bus of the DC microgrid, $y_{es}(t) = \begin{bmatrix} i_{DC}(t) & v_{R_{1b}}(t) \end{bmatrix}^{\top} \in \mathbb{R}^{1\times 2}$, where $i_{DC}(t)$ is the current during charging mode, and $d(t)$ is the duty cycle of the converter's switches. Additionally, the diagonal matrix Q_{es} is equal to diag($1/I_{1sc}$, $1/I_{1sc}$, $1/C_{1sc}$, $1/C_{2sc}$, $1/C_{3sc}$, $1/C_{1b}$, $1/C_{2b}$) $\in \mathbb{R}^{7\times 7}$.The skew-symmetric matrix $J_{es}(t) \in \mathbb{R}^{7\times 7}$, the dissipation matrix $R_{es} \in \mathbb{R}^{7\times 7}$, the $G_{es}^{\top} \in \mathbb{R}^{2\times 7}$ and $D_{es} \in \mathbb{R}^{2\times 2}$ are equal to:

$$J_{es}(t) = \begin{bmatrix} 0 & 0 & 1 & -(1-d_{1sc}(t)) & 0 & 0 & 0 \\ 0 & 0 & 0 & (1-d_{2sc}(t)) & -1 & 0 & 0 \\ -1 & 0 & 0 & 0 & 0 & 0 & 0 \\ 1-d_{1sc}(t) & -(1-d_{2sc}(t)) & 0 & 0 & 0 & 0 & 0 \\ 0 & 1 & 0 & 0 & 0 & 0 & 0 \\ 0 & 0 & 0 & 0 & 0 & 0 & 0 \\ 0 & 0 & 0 & 0 & 0 & 0 & 0 \end{bmatrix}, \tag{2.5.2a}$$

$$R_{es} = \begin{bmatrix} 0 & 0 & 0 & 0 & 0 & 0 & 0 \\ 0 & 0 & 0 & 0 & 0 & 0 & 0 \\ 0 & 0 & \frac{1}{R_{1sc}} & 0 & 0 & 0 & 0 \\ 0 & 0 & 0 & 0 & 0 & 0 & 0 \\ 0 & 0 & 0 & 0 & 0 & 0 & 0 \\ 0 & 0 & 0 & 0 & 0 & \frac{1}{R_{1b}} + \frac{1}{R_{2b}} & -\frac{1}{R_{2b}} \\ 0 & 0 & 0 & 0 & 0 & -\frac{1}{R_{2b}} & \frac{1}{R_{2b}} \end{bmatrix}, \tag{2.5.2b}$$

$$G_{es}^{\top} = \begin{bmatrix} 0 & 0 & \frac{-1}{R_{1sc}} & 0 & 0 & 0 & 0 \\ 0 & 0 & 0 & 0 & 1 & -1 & 0 \end{bmatrix}, D_{es} = \begin{bmatrix} \frac{1}{R_{1sc}} & 0 \\ 0 & 0 \end{bmatrix} \tag{2.5.2c}$$

where the duty cycles, $d_{1sc}(t)$, $d_{2sc}(t)$, are the control variables of the system.

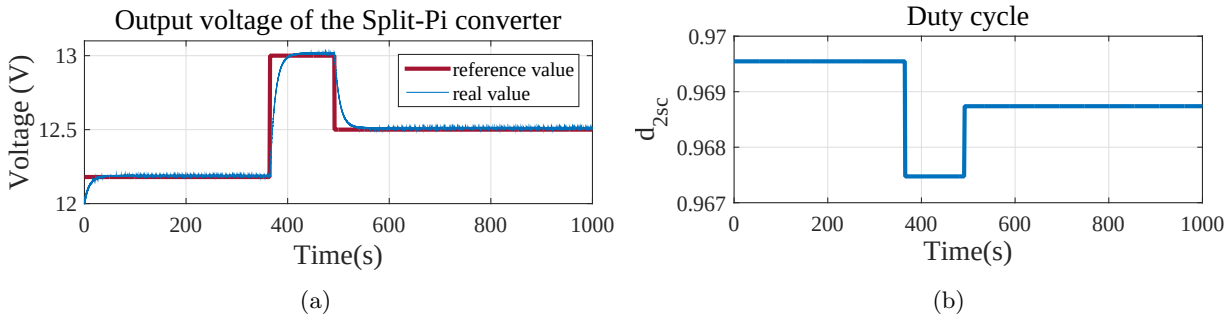

Figure 2.5.4: (a) Output voltage of the Split-pi converter generated by the ES PH model. (b) Corresponding duty cycle d_{2sc}.

The battery's charging and discharging are controlled by the Split-Pi converter's switches. For the validation of the ES model, we consider several simulations. In Fig. 2.5.4 and Fig. 2.5.5 we provide the output

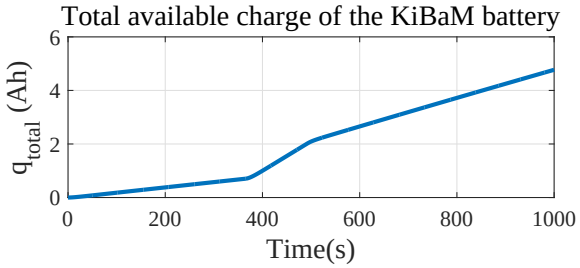

Figure 2.5.5: Total available charge of the KiBaM battery according to Fig. 2.5.4.

voltage of the Split-Pi (reference and real output voltage), considering as input to the system the voltage of the common DC bus, v_{DC}, equal to $400V$. In Fig. 2.5.4, the reference voltage is tracked by the PH model. The corresponding duty cycle, d_{2sc}, is illustrated in Fig. 2.5.4b. The duty cycle d_{1sc} is equal to 0, since the converter works in down-conversion. Fig. 2.5.5 indicates the total available charge of the battery after $1000s$ of charging, which is the summation of the available charge, q_{1b}, and the bound charge, q_{2b}, as in (2.5.1). Note that for the simulation, we used the parameters illustrated in Table 2.4.1 plus the values for C_{1b} and C_{2b} equal to $86400F$ and $21600F$ respectively. The capacitors values have been calculated are based on the AGM 12-165 battery parameters (Victron Energy, 2015).

2.5.2 Reduced transmission line network

2.5.2.1 Transmission lines modeled with RL circuits

Afterwards, we analyze the four-line reduced transmission network depicted in Fig. 2.5.1. To develop its PH model, we start from the PH model of the complete DC microgrid architecture (2.4.29) in order to produce the simplified version under the assumptions we made. Taking into account that there is no power loss in the transmission lines 5, 6, 7, the corresponding RL circuits will be erased. In addition, since only the part of the EV's will be regarded as an ES system, the v_b variable will be equal to 0. The power resulting on the connecting node $n = 5$ and, subsequently, on the connecting node $n = 4$ will be generated by the PV system ($v_{sn1} = v_{sn2} = v_{pv}$). Therefore, considering that $p_{5sc}^{\cdot}$, $p_{6sc}^{\cdot}$, $p_{7sc}^{\cdot}$ and R_5, R_6, R_7 are equal to 0 in (2.4.29), we arrive at the following PH state-space representation:

$$\begin{cases} \begin{bmatrix} \dot{p}_1 \\ \dot{p}_2 \\ \dot{p}_3 \\ \dot{p}_4 \end{bmatrix} = [J_c - R_c]Q_c x_c + \begin{bmatrix} 0 & 0 & -1 & 1 \\ 0 & -1 & 0 & 1 \\ 1 & 0 & 1 & 0 \\ 1 & 1 & 0 & 0 \end{bmatrix} \begin{bmatrix} v_{pv} \\ -v_{ug} \\ -v_{es} \\ -v_{loads} \end{bmatrix}, \\ \begin{bmatrix} i_{pv} \\ i_{ug} \\ i_{es} \\ i_{R_L} \end{bmatrix} = \begin{bmatrix} 0 & 0 & 1 & 1 \\ 0 & -1 & 0 & 1 \\ -1 & 0 & 1 & 0 \\ 1 & 1 & 0 & 0 \end{bmatrix} Q_c x_c, \end{cases} \tag{2.5.3}$$

where $x_c = \begin{bmatrix} p_1 & p_2 & p_3 & p_4 \end{bmatrix}^\top \in \mathbb{R}^{4\times 1}$ is the state vector, $u_c = \begin{bmatrix} v_{pv} & -v_{ug} & -v_{es} & -v_{loads} \end{bmatrix}^\top \in \mathbb{R}^{4\times 1}$ is the input vector and $y_c = \begin{bmatrix} i_{pv} & i_{ug} & i_{es} & i_{loads} \end{bmatrix}^\top \in \mathbb{R}^{4\times 1}$ is the output vector of the system. The skew-symmetric matrix J_c is equal to 0 and the dissipation matrix $R_c \in \mathbb{R}^{4\times 4}$ is equal to:

$$R_c = \text{diag}(R_1, R_2, R_3, R_4). \tag{2.5.4}$$

Fig. 2.5.6 addresses the corresponding Bond graph of Fig. 2.5.1, which provides also the PH model in (2.5.3).

Since, the J_c is equal to 0 (2.5.3) and the knowledge of the interconnections among the elements is indispensable, another method can be employed and is called *kernel representation* (van der Schaft et al., 2014):

Definition 2.5.1. *(Kernel representation - van der Schaft et al. (2014)): Every Dirac structure $\mathcal{D} \subset \mathcal{F} \times \mathcal{E}$, with $\mathcal{E} = \mathcal{F}^*$ can be described in kernel representation as follows:*

$$\mathcal{D} = (f, e) \in \mathcal{F} \times \mathcal{E} \mid \mathcal{E}e + \mathcal{F}f = 0, \tag{2.5.5}$$

where for linear maps F:$\mathcal{F} \to \mathcal{V}$ and E:$\mathcal{E} \to \mathcal{V}$ obeying to:

$$\begin{aligned} EF^* + FE^* &= 0, \\ rank(F+E) &= dimF, \end{aligned} \tag{2.5.6}$$

where $\mathcal{V}$ is a linear space of equal dimension with $\mathcal{F}$, and where F^*:$\mathcal{V}^* \to \mathcal{E}$ and E^*:$\mathcal{V}^* \to (\mathcal{F}^*)^* = \mathcal{F}$ represent the adjoint maps of F and E respectively. The linear maps F and E are described by $n_L \times n_L$ matrices F and E which satisfy:

$$\begin{aligned} EF^\top + FE^\top &= 0, \\ rank(F+E) &= dimF, \end{aligned}$$

which is the matrix kernel representation. □

For the cyclic reduced network (Fig. 2.5.6), the kernel representation is given below:

$$\underbrace{\begin{bmatrix} 0 & 0 & 0 & 0 & 0 & 0 & 0 & 0 & 0 & 0 & 0 & 0 \\ 0 & 0 & 0 & 0 & 0 & 0 & 0 & 0 & 0 & 0 & 0 & 0 \\ 0 & 0 & 0 & 0 & 0 & 0 & 0 & 0 & 0 & 0 & 0 & 0 \\ 0 & 0 & 0 & 0 & 0 & 0 & 0 & 0 & 0 & 0 & 0 & 0 \\ 1 & 0 & 0 & 0 & -1 & 0 & 0 & 0 & 0 & 0 & 0 & 0 \\ 0 & 1 & 0 & 0 & 0 & -1 & 0 & 0 & 0 & 0 & 0 & 0 \\ 0 & 0 & 1 & 0 & 0 & 0 & -1 & 0 & 0 & 0 & 0 & 0 \\ 0 & 0 & 0 & 1 & 0 & 0 & 0 & -1 & 0 & 0 & 0 & 0 \\ 1 & 1 & 0 & 0 & 0 & 0 & 0 & 0 & 0 & 0 & 0 & -1 \\ 0 & -1 & 0 & 1 & 0 & 0 & 0 & 0 & 0 & 1 & 0 & 0 \\ 0 & 0 & -1 & -1 & 0 & 0 & 0 & 0 & 1 & 0 & 0 & 0 \\ -1 & 0 & 1 & 0 & 0 & 0 & 0 & 0 & 0 & 0 & -1 & 0 \end{bmatrix}}_{F} \underbrace{\begin{bmatrix} i_1 \\ i_2 \\ i_3 \\ i_4 \\ i_{R_1} \\ i_{R_2} \\ i_{R_3} \\ i_{R_4} \\ i_{pv} \\ i_{ug} \\ i_{es} \\ i_{loads} \end{bmatrix}}_{f} +$$

$$+ \underbrace{\begin{bmatrix} -1 & 0 & 0 & 0 & -1 & 0 & 0 & 0 & 0 & 0 & 1 & -1 \\ 0 & -1 & 0 & 0 & 0 & -1 & 0 & 0 & 0 & -1 & 0 & -1 \\ 0 & 0 & -1 & 0 & 0 & 0 & -1 & 0 & -1 & 0 & -1 & 0 \\ 0 & 0 & 0 & -1 & 0 & 0 & 0 & -1 & -1 & 1 & 0 & 0 \\ 0 & 0 & 0 & 0 & 0 & 0 & 0 & 0 & 0 & 0 & 0 & 0 \\ 0 & 0 & 0 & 0 & 0 & 0 & 0 & 0 & 0 & 0 & 0 & 0 \\ 0 & 0 & 0 & 0 & 0 & 0 & 0 & 0 & 0 & 0 & 0 & 0 \\ 0 & 0 & 0 & 0 & 0 & 0 & 0 & 0 & 0 & 0 & 0 & 0 \\ 0 & 0 & 0 & 0 & 0 & 0 & 0 & 0 & 0 & 0 & 0 & 0 \\ 0 & 0 & 0 & 0 & 0 & 0 & 0 & 0 & 0 & 0 & 0 & 0 \\ 0 & 0 & 0 & 0 & 0 & 0 & 0 & 0 & 0 & 0 & 0 & 0 \\ 0 & 0 & 0 & 0 & 0 & 0 & 0 & 0 & 0 & 0 & 0 & 0 \end{bmatrix}}_{E} \underbrace{\begin{bmatrix} v_1 \\ v_2 \\ v_3 \\ v_4 \\ v_{R_1} \\ v_{R_2} \\ v_{R_3} \\ v_{R_4} \\ -v_{pv} \\ -v_{ug} \\ v_{es} \\ v_{loads} \end{bmatrix}}_{e} = \begin{bmatrix} 0 \\ 0 \\ 0 \\ 0 \\ 0 \\ 0 \\ 0 \\ 0 \\ 0 \\ 0 \\ 0 \\ 0 \end{bmatrix}. \tag{2.5.7}$$

Proposition 2.5.2. *(Constrained input-output representation - van der Schaft et al. (2014)): Every Dirac structure, $\mathcal{D} \subset \mathcal{F} \times \mathcal{F}^*$ can be represented as*

$$\mathcal{D} = \{(f,e) \in \mathcal{F} \times \mathcal{E} | f = Je + \mathcal{G}\lambda,\ \mathcal{G} = 0,\ \lambda \in \mathcal{V}\}, \tag{2.5.8}$$

with a skew-symmetric mapping $\mathcal{J} : \mathcal{F} \to \mathbb{E}$, a linear mapping $\mathcal{G}$ such that $im\mathcal{G} = \{f \in \mathcal{F} | (f,0) \in \mathcal{D}\}$ and $ker\mathcal{J} = \{e \in \mathcal{E} | (0,e) \in \mathcal{D}\}$. □

Proposition 2.5.3. *(Hybrid input-output representation - van der Schaft et al. (2014)): Consider that a Dirac structure is represented in kernel representation with matrices E and F, as mentioned in Theorem 2.5.1. Assuming that $F = m_L (\leq n_L)$, then m_L independent columns of F can be selected and placed in a matrix F_1. As a next step, $F = [F_1 \mid F_2]$ and, accordingly, $E = [E_1 \mid E_2]$, where $f = \begin{bmatrix} f_1 & f_2 \end{bmatrix}^\top$ and $e = \begin{bmatrix} e_1 & e_2 \end{bmatrix}^\top$. Hence, the matrix $[F_1 \mid E_2]$ is invertible and the Dirac structure can be written as follows:*

$$\mathcal{D} = \left\{ \begin{bmatrix} f_1 \\ f_2 \end{bmatrix} \in \mathcal{F}, \begin{bmatrix} e_1 \\ e_2 \end{bmatrix} \in \mathcal{E} | \begin{bmatrix} f_1 \\ e_2 \end{bmatrix} = J \begin{bmatrix} e_1 \\ f_2 \end{bmatrix} \right\}, \tag{2.5.9}$$

where J:=-$[F_1 \mid E_2]^{-1}[F_2 \mid E_1]$ which is a skew-symmetric matrix. □

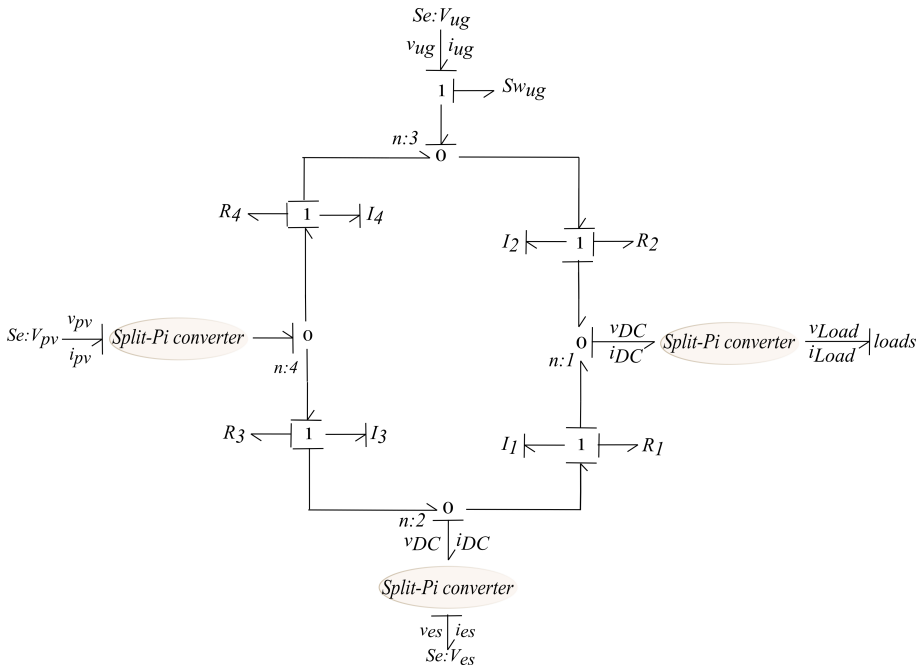

Figure 2.5.6: Bond graph of the DC micogrid's central transmission network.

Therefore, through the kernel representation given in (2.5.7), we obtain the hybrid input-output representation (Proposition 2.5.3) of the reduced transmission network (Fig. 2.5.1, Fig. 2.5.6), where all the possible power-preserving interconnections among the components of the microgrid are presented. The hybrid input-output representation is shown below:

$$\begin{bmatrix} i_{R_1} \\ i_{R_2} \\ i_{R_3} \\ i_{R_4} \\ i_{pv} \\ i_{ug} \\ i_{es} \\ i_{loads} \\ v_1 \\ v_2 \\ v_3 \\ v_4 \end{bmatrix} = \begin{bmatrix} 0 & 0 & 0 & 0 & 0 & 0 & 0 & 0 & 1 & 0 & 0 & 0 \\ 0 & 0 & 0 & 0 & 0 & 0 & 0 & 0 & 0 & 1 & 0 & 0 \\ 0 & 0 & 0 & 0 & 0 & 0 & 0 & 0 & 0 & 0 & 1 & 0 \\ 0 & 0 & 0 & 0 & 0 & 0 & 0 & 0 & 0 & 0 & 0 & 1 \\ 0 & 0 & 0 & 0 & 0 & 0 & 0 & 0 & 0 & 0 & -1 & -1 \\ 0 & 0 & 0 & 0 & 0 & 0 & 0 & 0 & 0 & -1 & 0 & 1 \\ 0 & 0 & 0 & 0 & 0 & 0 & 0 & 0 & 1 & 0 & -1 & 0 \\ 0 & 0 & 0 & 0 & 0 & 0 & 0 & 0 & -1 & -1 & 0 & 0 \\ -1 & 0 & 0 & 0 & 0 & 0 & -1 & 1 & 0 & 0 & 0 & 0 \\ 0 & -1 & 0 & 0 & 0 & 1 & 0 & 1 & 0 & 0 & 0 & 0 \\ 0 & 0 & -1 & 0 & 1 & 0 & 1 & 0 & 0 & 0 & 0 & 0 \\ 0 & 0 & 0 & -1 & 1 & -1 & 0 & 0 & 0 & 0 & 0 & 0 \end{bmatrix} \begin{bmatrix} v_{R_1} \\ v_{R_2} \\ v_{R_3} \\ v_{R_4} \\ -v_{pv} \\ -v_{ug} \\ v_{es} \\ v_{loads} \\ i_1 \\ i_2 \\ i_3 \\ i_4 \end{bmatrix}. \tag{2.5.10}$$

Additionally to the PH model, we always take into consideration the power conservation equation of the transmission network written below:

$$P_{ug} + P_{pv} - P_{es} - P_{loads} - P_{R_1} - P_{I_1} - P_{R_2} - P_{I_2} - P_{R_3} - P_{I_3} - P_{R_4} - P_{I_4} = 0. \tag{2.5.11}$$

The problem in this form becomes complicated and many difficulties can still emerge during the construction of the optimization problem. Therefore, eliminating a number of states in the transmission network would be useful. In the subsequent section, a further reduction of the transmission-line network will be proposed.

2.5.2.2 Replacing transmission lines by resistors

This section presents a further simplification of the central transmission network according to which the inductors, I_1, I_2, I_3 and I_4 will be eliminated. In DC networks, the existence of the inductors is necessary only when the current flow of the system starts increasing. But once the system comes to its steady state, where the current flow is stable, the inductors have no effect in the DC networks. Furthermore, in DC networks the distances among the components are small meaning that the length of the transmission lines is

negligible. Together with the continuous development of the DC equipment, these are two factors which lead towards the decrease of the power loss within DC networks (Elsayed et al., 2015; Lotfi and Khodaei, 2015).

Therefore, in this work, to study the load balancing problem of the central transmission network of the simplified DC microgrid (Fig. 2.5.1), the inductors will be discarded. Thus, we illustrate the correspondingly-modified Bond graph for the central DC bus in Fig. 2.5.7.

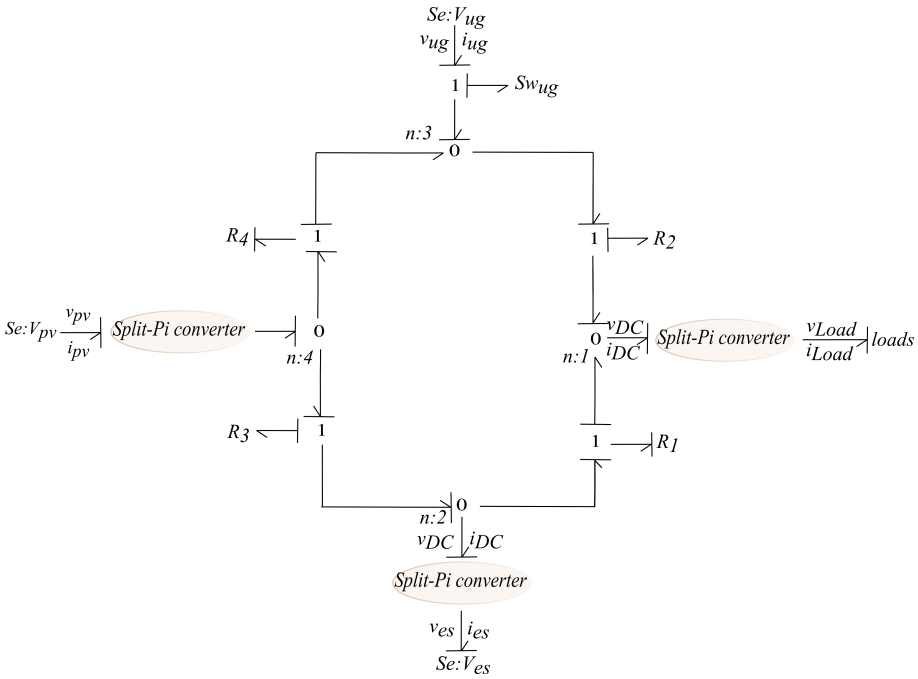

Figure 2.5.7: Bond graph of the DC micogrid's central transmission network with resistors for transmission lines.

Hence, from the kernel representation in (2.5.7), erasing the inductors' variables (current, i_1, i_2, i_3, i_4, and voltage, v_1, v_2, v_3, v_4), we obtain the following for the Bond graph in Fig. 2.5.7:

$$\underbrace{\begin{bmatrix} 0 & 0 & 0 & 0 & 0 & 0 & 0 & 0 \\ 0 & 0 & 0 & 0 & 0 & 0 & 0 & 0 \\ 0 & 0 & 0 & 0 & 0 & 0 & 0 & 0 \\ 0 & 0 & 0 & 0 & 0 & 0 & 0 & 0 \\ 1 & 1 & 0 & 0 & 0 & 0 & 0 & -1 \\ 0 & -1 & 0 & 1 & 0 & 1 & 0 & 0 \\ 0 & 0 & -1 & -1 & 1 & 0 & 0 & 0 \\ -1 & 0 & 1 & 0 & 0 & 0 & -1 & 0 \end{bmatrix}}_{F} \underbrace{\begin{bmatrix} i_{R_1} \\ i_{R_2} \\ i_{R_3} \\ i_{R_4} \\ i_{pv} \\ i_{ug} \\ i_{es} \\ i_{loads} \end{bmatrix}}_{f} + \underbrace{\begin{bmatrix} -1 & 0 & 0 & 0 & 0 & 0 & 1 & -1 \\ 0 & -1 & 0 & 0 & 0 & -1 & 0 & -1 \\ 0 & 0 & -1 & 0 & -1 & 0 & -1 & 0 \\ 0 & 0 & 0 & -1 & -1 & 1 & 0 & 0 \\ 0 & 0 & 0 & 0 & 0 & 0 & 0 & 0 \\ 0 & 0 & 0 & 0 & 0 & 0 & 0 & 0 \\ 0 & 0 & 0 & 0 & 0 & 0 & 0 & 0 \\ 0 & 0 & 0 & 0 & 0 & 0 & 0 & 0 \end{bmatrix}}_{E} \underbrace{\begin{bmatrix} v_{R_1} \\ v_{R_2} \\ v_{R_3} \\ v_{R_4} \\ -v_{pv} \\ -v_{ug} \\ v_{es} \\ v_{loads} \end{bmatrix}}_{e} = \begin{bmatrix} 0 \\ 0 \\ 0 \\ 0 \\ 0 \\ 0 \\ 0 \\ 0 \end{bmatrix}. \tag{2.5.12}$$

Similarly, from (2.5.12), the hybrid input-output representation of the cyclic network in Fig. 2.5.7 is:

$$\begin{bmatrix} i_{pv} \\ i_{ug} \\ i_{es} \\ i_{loads} \\ v_{R_1} \\ v_{R_2} \\ v_{R_3} \\ v_{R_4} \end{bmatrix} = \begin{bmatrix} 0 & 0 & 0 & 0 & 0 & 0 & 1 & 1 \\ 0 & 0 & 0 & 0 & 0 & 1 & 0 & -1 \\ 0 & 0 & 0 & 0 & -1 & 0 & 1 & 0 \\ 0 & 0 & 0 & 0 & 1 & 1 & 0 & 0 \\ 0 & 0 & 1 & -1 & 0 & 0 & 0 & 0 \\ 0 & -1 & 0 & -1 & 0 & 0 & 0 & 0 \\ -1 & 0 & -1 & 0 & 0 & 0 & 0 & 0 \\ -1 & 1 & 0 & 0 & 0 & 0 & 0 & 0 \end{bmatrix} \begin{bmatrix} -v_{pv} \\ -v_{ug} \\ v_{es} \\ v_{loads} \\ i_{R_1} \\ i_{R_2} \\ i_{R_3} \\ i_{R_4} \end{bmatrix}. \tag{2.5.13}$$

Furthermore, the power conservation equation of the transmission network (Fig. 2.5.7) becomes:

$$P_{ug} + P_{pv} - P_{es} - P_{loads} - P_{R_1} - P_{R_2} - P_{R_3} - P_{R_4} = 0. \tag{2.5.14}$$

From the Bond graph in Fig. 2.5.7, the PH representation is presented below, where there are no states and only dissipative elements are included:

$$\begin{bmatrix} i_{pv} \\ i_{ug} \\ i_{es} \\ i_{loads} \end{bmatrix} = \begin{bmatrix} \frac{1}{R_3}+\frac{1}{R_4} & -\frac{1}{R_4} & -\frac{1}{R_3} & 0 \\ \frac{1}{R_4} & -\frac{1}{R_4}-\frac{1}{R_2} & 0 & \frac{1}{R_2} \\ \frac{1}{R_3} & 0 & -\frac{1}{R_3}-\frac{1}{R_1} & \frac{1}{R_1} \\ 0 & \frac{1}{R_2} & \frac{1}{R_1} & -\frac{1}{R_1}-\frac{1}{R_2} \end{bmatrix} \begin{bmatrix} v_{pv} \\ v_{ug} \\ v_{es} \\ v_{loads} \end{bmatrix}. \tag{2.5.15}$$

Therefore, the following equations describe for the current flows:

- from node 1:
$$i_{loads} = i_{R_1} + i_{R_2} = \frac{v_{es} - v_{loads}}{R_1} + \frac{v_{ug} - v_{loads}}{R_2}; \tag{2.5.16}$$
- from node 2:
$$i_{es} = i_{R_3} - i_{R_1} = \frac{v_{pv} - v_{es}}{R_3} - \frac{v_{es} - v_{loads}}{R_1}; \tag{2.5.17}$$
- from node 3:
$$i_{ug} = i_{R_4} - i_{R_2} = \frac{v_{pv} - v_{ug}}{R_4} - \frac{v_{ug} - v_{loads}}{R_2}; \tag{2.5.18}$$
- from node 4:
$$i_{pv} = i_{R_3} - i_{R_4} = \frac{v_{pv}(t) - v_{es}(t)}{R_3} - \frac{v_{ug}(t) - v_{pv}(t)}{R_4}. \tag{2.5.19}$$

Through (2.5.13), (2.5.16), (2.5.17), (2.5.18), (2.5.19), every power variable of the DC network can be expressed below in function of the voltages on the connecting nodes:

$$P_{ug} = v_{ug} i_{ug} = v_{ug}[i_{R_4} - i_{R_2}] = v_{ug}\left[\frac{v_{ug} - v_{pv}}{R_4} - \frac{v_{loads} - v_{ug}}{R_2}\right] \tag{2.5.20a}$$

$$P_{es} = v_{es} i_{es} = v_{es}[i_{R_3} - i_{R_1}] = v_{es}\left[\frac{v_{pv} - v_{es}}{R_3} - \frac{v_{es} - v_{loads}}{R_1}\right] \tag{2.5.20b}$$

$$P_{pv} = v_{pv} i_{pv} = v_{pv}[i_{R_3} - i_{R_4}] = v_{pv}\left[\frac{v_{pv} - v_{es}}{R_3} - \frac{v_{ug} - v_{pv}}{R_4}\right] \tag{2.5.20c}$$

$$P_{loads} = v_{loads} i_{loads} = v_{loads}[i_{R_1} - i_{R_2}] = v_{loads}\left[\frac{v_{es} - v_{loads}}{R_1} - \frac{v_{loads} - v_{ug}}{R_2}\right], \tag{2.5.20d}$$

where P_{ug}, P_{es}, P_{pv}, P_{loads} are the powers of the UG, ES, PV and loads systems respectively. Furthermore, regarding the power losses within the DC bus, P_{R_1}, P_{R_2}, P_{R_3}, P_{R_4}, the following relations are also deduced:

$$P_{R_1} = \frac{[v_{es} - v_{loads}]^2}{R_1}, \tag{2.5.16e}$$

$$P_{R_2} = \frac{[v_{loads} - v_{ug}]^2}{R_2}, \tag{2.5.16g}$$

$$P_{R_3} = \frac{[v_{pv} - v_{es}]^2}{R_3}, \tag{2.5.16f}$$

$$P_{R_4} = \frac{[v_{ug} - v_{pv}]^2}{R_4}. \tag{2.5.16h}$$

The previous relations (2.5.20a-2.5.16h) are important and will be applied in the construction of the objective function for the power loss minimization problem in chapter 4.

2.6 Optimization objectives and constraints

Before starting to elaborate the optimization problem, it is important to present the overall electrical circuit of the simplified version of the DC microgrid (Fig. 2.5.1). Fig. 2.6.1 introduces all the inner interconnections of the circuits of the sources and the Split-Pi converters.

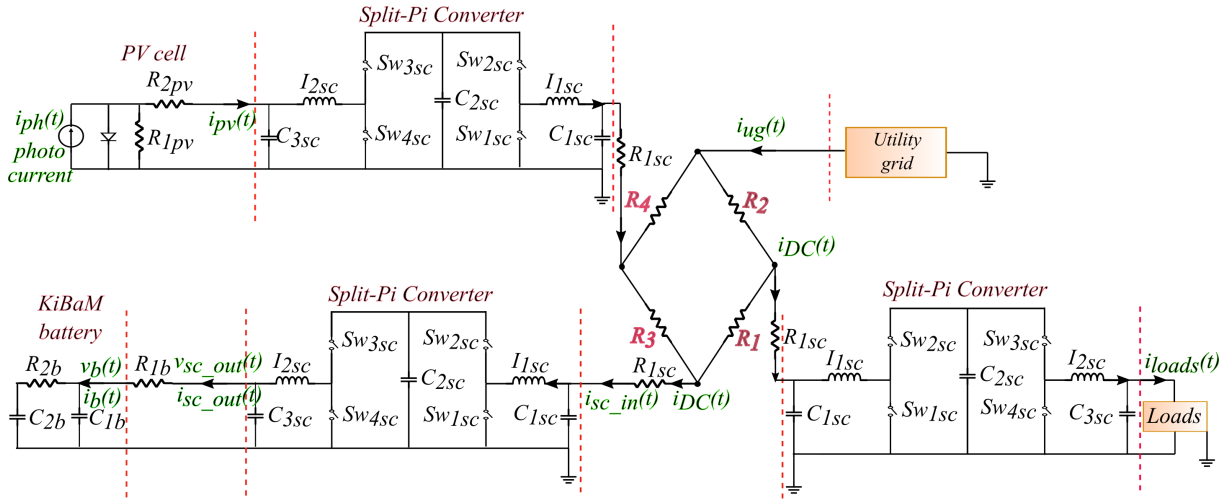

Figure 2.6.1: Electrical circuit of the reduced meshed DC micogrid.

2.6.1 Objectives

The main objective of this work is to solve the load balancing problem. To achieve this, the problem will be divided into two sub-problems:

- the cost minimization, according to which the electricity cost of the UG power purchase will be penalized. The goal is to sell power to the UG, generated by the renewable resources, and to exploit the ES system towards the consumers' benefit. The cost function which penalizes the electricity cost is written below:

$$J^1(d(t)) = \int_{t_0}^{t_f} ep(t)P_{ug} = \int_{t_0}^{t_f} ep(t)(P_{loads} + P_{es} - P_{pv}) = \int_{t_0}^{t_f} ep(t)(P_{loads} + v_{es}i_{es} - P_{pv}), \quad (2.6.1)$$

  where reference profiles will be taken into account for the PV and the loads. The P_{ug} is replaced by the power conservation among the sources and loads ($P_{ug} = P_{loads} + P_{es} - P_{pv}$), without considering the power loss (2.5.14);

- the optimal power flow, minimizing the power dissipation in the DC bus. This problem aims to find the best possible direction for the power to flow in order to have the less possible power losses during transmission. Therefore, the cost function which minimizes the energy dissipation will be the following:

$$J^2(d(t)) = -\int_{t_0}^{t_f} P_R = -\int_{t_0}^{t_f} (P_{R1} + P_{R2} + P_{R3} + P_{R4}), \quad (2.6.2)$$

  where P_{R1}, P_{R2}, P_{R3}, P_{R4} corresponds to the power loss inside the central network (2.5.16e-2.5.16h), for which again the PH model through hybrid input-output representation of the central transmission network will be considered. Relation (2.5.14) is taken into account.

We observe that in both cases the power conservation is taken into account and the control variable is the duty cycle of the switches in the converters, $d(t)$. The ES system and the central transmission network will be analytically included in the optimization problem, utilizing the PH models previously developed in this chapter.

2.6.2 Constraints

This subsection will describe the general constraints which will be taken into account for the energy management problem. As already mentioned, the ES system is a major component of the overall scheme and will be thoroughly analyzed. The batteries have a limited lifetime which demands to respect certain constraints concerning the battery's characteristics. Therefore, the constraints considered in this work for the ES system

are (see also Fig. 2.6.1):

$$
\begin{aligned}
q_{1b}^{min} &\leq q_{1b}(t) \leq q_{1b}^{max}, \\
q_{2b}^{min} &\leq q_{2b}(t) \leq q_{2b}^{max}, \\
Charging\ \ mode: & \\
v_{b,charging}^{min} &\leq v_{b,charging}(t) \leq v_{b,charging}^{max}, \\
i_{b,charging}^{min} &\leq i_{b,charging}(t) \leq i_{b,charging}^{max}, \\
Dischaging\ \ mode: & \\
v_{b,dicharging}^{min} &\leq v_{b,dicharging}(t) \leq v_{b,dicharging}^{max}, \\
i_{b,dicharging}^{min} &\leq i_{b,dicharging}(t) \leq i_{b,dicharging}^{max}.
\end{aligned}
$$

In addition to these constraints, the output voltage on the connecting nodes in the DC-bus must be always close to a certain voltage value, 400 V in this case, because we consider DC networks. Therefore, according to Fig. 2.6.2, the limitations considered for the connecting nodes are given below:

$$v_{DC}^{min,h} \leq v_{ug}(t) \leq v_{DC}^{max,h}, \tag{2.6.3a}$$
$$v_{DC}^{min,h} \leq v_{pv}(t) \leq v_{DC}^{max,h}, \tag{2.6.3b}$$
$$v_{DC}^{min,h} \leq v_{es}(t) \leq v_{DC}^{max,h}, \tag{2.6.3c}$$
$$v_{DC}^{min,h} \leq v_{loads}(t) \leq v_{DC}^{max,h}. \tag{2.6.3d}$$

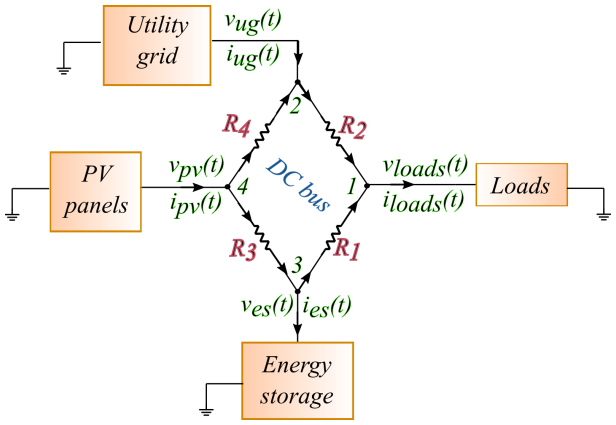

Figure 2.6.2: Central transmission network of the simplified meshed DC microgrid.

Furthermore, the duty cycles d_{1sc} and d_{2sc} of the Split-Pi converter are limited into the interval referred below:

$$0 \leq d_{1sc} \leq 1, \tag{2.6.4}$$
$$0 \leq d_{2sc} \leq 1. \tag{2.6.5}$$

Finally, the external grid cannot consume an internal amount of power. An upper and a lower limit must be defined as follows:

$$P_{ug}^{min} \leq P_{ug}(t) \leq P_{ug}^{max}, \tag{2.6.6}$$

with $P_{ug}(t) = v_{ug}(t) i_{ug}(t)$.

2.7 Conclusions

In this chapter, the meshed DC microgrid architecture of the project was presented. Afterwards, we introduced the modeling methodology used to represent the components of the system. The Bond graph and

port-Hamiltonian representations were developed proceeding to the detailed analysis of the system as a collection of electrical circuits. The global dynamics of the system was also formulated by focusing on the central transmission network.

To simplify the complexity of the system for the upcoming analysis, we established a simplified architecture of the proposed meshed DC microgrid reducing the number of transmission lines. Studying each meshgrid separately leads to a simpler PH model for the power transmission among the components. Through this representation, the explicit dynamical model of the central transmission network and the ES system are presented, important for the development of the multi-scale optimization problem.

The highlights of this chapter are enumerated below:

- development of a meshed DC microgrid using Split-Pi converters for voltage regulation and power flow direction in the network;
- development of the dynamical models using the Bond graphs and their associated port-Hamiltonian representations for each component of the DC microgrid. The dynamics for each component of the system has been introduced explicitly. A similar approach was followed for the central transmission network, thus providing the analytical framework of the power line-transmission;
- suitable cost functions and constraints have also been presented.

The next chapter will investigate the inverse dynamics of the PH models developed here. This is an important step which will provide directly the states of the system, maintaining its properties, to be used in the optimization problem. Towards this direction, two methods will be considered, differential flatness and bicausality.

Chapter 3

From port-Hamiltonian to differential flatness representation

3.1 Introduction

This chapter presents the flat representation of the PV, ES and loads components of the reduced DC microgrid model (Fig.2.5.1) detailed in chapter 2. Differential flatness was first introduced by Michel Fliess (Fliess et al., 1993) and his co-researchers in the late 1980s. It is an advantageous method, which can efficiently deal with control and optimization problems of nonlinear dynamical systems (Levine, 2009; Murray et al., 1995; Rigatos, 2015a).

There are several works in the literature in different domains that employ the differential flatness tracking control design. Many researchers use its properties in motion planning problems (Hervagault et al., 2019; Nguyen et al., 2018; Poultney et al., 2018; Prodan et al., 2013) in order to validate the system's dynamics under constraints and generate optimal profiles for velocity, acceleration, forces or torques. Other works employ B-Splines parametrization of the flat outputs to ensure continuous-time constraints validation at the trajectory generation level Stoican et al. (2017). For instance, in Pham et al. (2015) the flat representation of an electro-mechanical elevator within a DC microgrid is taken into account to generate the elevator's optimal velocity while minimizing the energy dissipation. In Thounthong and Pierfederici (2010) the authors implement an algorithm which controls the operation of a DC power source (fuel cell generator) through a power converter. The flat representation of the converter is provided and a control law is developed to study the stability of the system. In Pahlevaninezhad et al. (2011) the flatness theory is considered in order to prove controllability of an AC/DC converter and write the overall dynamical model in function of the input power which consists also the control input and flat output of the system.

As already mentioned in chapter 2, through port-Hamiltonian (PH) formulation we obtain an explicitly described and well-structured state-space representation of the system with a set of differential equations. To proceed to its supervision, it is necessary to be able to extract several physical quantities such as the voltage, the current, the power and the like. Therefore, differential flatness can be considered as a suitable tool to inverse the system dynamics generating in this way all the states and inputs in function of the flat outputs of the system and a finite number of their derivatives. It is a method closely associated to the notion of controllability, since according to Fliess et al. (1995), a nonlinear system is flat if and only if it is controllable. Due to its properties, it can be easily combined with several methods of parametrization such as the B-spline parametrization, which accounts for constraint validation in continuous-time.

Another important issue, that concerns the researchers, is the calculation of the flat outputs which can be very complex and not straightforward to find. In the literature, many useful approaches are provided, such as the algorithm for flat representation proposed in Franke and Robenack (2013). The algorithm provides an analytical computation of flat outputs for nonlinear control systems and will be described and implemented later in this chapter. Apart from the algorithm, another method was introduced in Gil et al. (1997) and Richard et al. (2002), which proves the flatness of a system after inversing the dynamics of its associated Bond graph. This method is called bicausality, firstly presented by Gawthrop (1994). Bicausality is a supplementary approach to the existing theory of the Bond graphs which inverses the system dynamics by decoupling the pairs of efforts and flows at each bond. Hence, bicausality could be an appropriate method to investigate flatness and, subsequently, develop a more straightforward way to find the possible flat outputs of the PH systems.

In this chapter, we will proceed by briefly introducing the differential flatness theory. Afterwards, we will apply the theory on the reduced DC microgrid system (section 2.5) using two sets of flat outputs, one derived from the algorithm proposed in Franke and Robenack (2013) and another considering a random flat output set. The proposed sets of flat outputs will be validated through simulations in MATLAB/Simulink. Next, we will present the bicausal Bond graph and we will demonstrate a method which can result in the generation of the possible flat outputs for a particular class of PH systems. The method will be explained through illustrative examples of electrical circuits. Fig.3.1.1 presents the methods used in this chapter which both results in the inverse dynamics of the system presenting the states and inputs in function of the flat outputs and their derivatives.

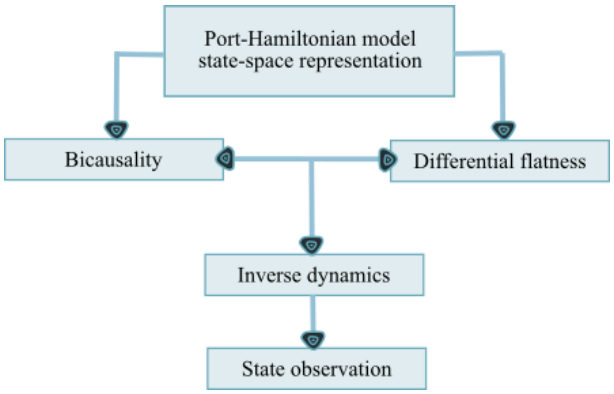

Figure 3.1.1: General idea of chapter 3 where the differential flatness and the bicausality properties will be considered for a particular class of PH systems.

3.2 Differential flatness

Differential flatness is a structural property of a class of nonlinear dynamical systems, denoting that all system variables (the states and the control inputs) can be written in terms of a set of specific variables, the so-called *flat outputs* (equal in number to the number of inputs), and their derivatives (Rigatos (2015b)).

Definition 3.2.1. *(Differential flatness (Fliess et al., 1995)): Consider the following nonlinear system:*

$$\dot{x}(t) = f(x(t), u(t)), \tag{3.2.1}$$

where the state vector $x(t) \in R^n$ *and the input vector* $u(t) \in R^m$*. In addition,* $f(0,0) = 0$ *and* $rank\dfrac{\partial f}{\partial u} = m$ *must be verified. The system can be characterized as differentially flat, if there exists a flat output vector:*

$$z(t) = [z_1(t)\ z_2(t)\ ...\ z_m(t)]^\top \tag{3.2.2}$$

which satisfies the conditions below:

- *the flat output* $z(t)$ *is represented in function of the states and the inputs of the system and their derivatives,* $z(t) = \Phi(x(t), u(t), \dot{u}(t), \ddot{u}(t), ..., u^{(k+1)}(t))$*;*
- *the states and the inputs of the system are described in terms of the flat outputs and a finite number of their derivatives,* $x(t) = \Phi_x(z(t), \dot{z}(t), \ddot{z}(t), ..., z^{(k)}(t))$ *and* $u(t) = \Phi_u(z(t), \dot{z}(t), \ddot{z}(t), ..., z^{(k+1)}(t))$*;*
- *the flat outputs* $z(t)$ *and their derivatives are differentially independent, which means that they cannot satisfy equations of the form* $\Phi(z(t), \dot{z}(t), \ddot{z}(t), ..., z^{(k+1)}(t)) = 0$*.* □

Differential flatness has many advantages due to its properties, two of them, useful for this work, are presented below:

- the number of the control inputs defines the number of the flat outputs of the system ((Lévine, 2011));

- it is commonly established that a flat system is considered as linearizable through a dynamic feedback and an appropriate change of coordinates. In general, when a system is linear and controllable, it is, consequently, flat. Therefore, a nonlinear system that can be converted into a linear, controllable system is also flat. Note that the previous statements do not prove that flatness is a method of linearization. However, when a nonlinear system is flat, its structure can be inscribed in a way to be employed in control for trajectory generation, planning, stabilization etc. (Levine, 2009; Rigatos, 2015b).

Proposition 3.2.2. *The particular class of PH systems considered in this work (sections 2.4.1.1, 2.4.1.2, 2.4.2, 2.4.3, 2.5.1, 2.5.2.2) are differentially flat.*

Proof. Consider the general state-space representation of a PH system:

$$\dot{x}(t) = [J(t) - R]Qx(t) + Gu(t), \tag{3.2.3a}$$

$$y(t) = G^{\top}Qx(t) + Du(t), \tag{3.2.3b}$$

where $x(t) \in \mathbb{R}^n$ is the state vector, $u(t) \in \mathbb{R}^m$ is the input vector and $y(t) \in \mathbb{R}^m$ is the output vector. Moreover, $J(t) \in \mathbb{R}^{n\times n}$ is the interconnection matrix, $R \in \mathbb{R}^{n\times n}$ is the dissipative matrix, $G \in \mathbb{R}^{n\times m}$ is the control matrix and $D \in \mathbb{R}^{m\times m}$ is the input matrix. For the Hamiltonian, H, and the $J(t) - R$ matrix the following are considered:

- the Hamiltonian, $H(x) = \frac{1}{2}x(t)^{\top}Qx(t)$ (2.3.2), is in quadratic form and positive definite, since Q is positive definite and invertible. Its gradient vector $\nabla H = \partial_x H(x)$ will be $\partial_x H(x) = Qx(t)$;
- $J(t) - R$ is square and invertible.

Considering as flat outputs a number of the states of the system, equal in number to the number of control inputs (see also Definition 3.2.1), the flat outputs can be written as $z_M(x) = \Phi(x_1(t), x_2(t), ..., x_n(t))$, where $M = 1, 2, .., m$, and the states can be written as $x_N(z) = \Phi(z_1(t), z_2(t), ..., z_n(t), \dot{z}_1(t), \dot{z}_2(t), ..., \dot{z}_n(t), ..., z_1^{(k)}(t), z_2^{(k)}(t), ..., z_n^{(k)}(t))$, where $N = 1, 2, .., n$. Concerning the input matrix $G \in \mathbb{R}^{n\times m}$ in (3.2.3a), it is replaced by the matrix $G_M \in \mathbb{R}^{n\times m}$ in (3.2.4) where $n = m$, i.e. the number of control inputs equals the number of flat outputs, hence the number of the corresponding states. The matrix $G_M \in \mathbb{R}^{n\times m}$, $n = m$, is constant, square and invertible. The same for matrix $Q \in \mathbb{R}^{n\times n}$ in (3.2.3a), which is replaced by the matrix $Q_M \in \mathbb{R}^{n\times n}, n = m$, since in (3.2.4) only the states representing the flat outputs of the system are included. The matrix $Q_M \in \mathbb{R}^{n\times n}, n = m$ is also square and invertible. Then, the control inputs and the states can be written in function of the flat outputs and their derivatives as follows:

$$u_M(z) = G_M^{-1}(\dot{x}_N(z) - [J(t) - R]Q_M x_N(z)), \tag{3.2.4}$$

$$x_N(z) = [J(t) - R]^{-1}Q^{-1}(\dot{x}_N(z) - Gu_M(z)). \tag{3.2.5}$$

□

Additionally, referring to the controllability of the PH systems considered here, the following remark is added:

Remark 3.2.3. (Port-controlled Hamiltonian system (Maschke and van der Schaft, 1992)): The interaction of a PH system with its environment is described defining external ports in the generalized Dirac structure (DS), similarly to the definition of the energy storing elements (see also Theorem 2.3.3). The control inputs can be represented as generalized effort or flow sources connected to the external ports of the model, with its effort or flow variables being the inputs. An external control has to act through the ports of the system, in order to change its states and, hence, its energy. Therefore, the system is port-controlled. In the network's framework an output is naturally generated, associated with each port-input control effort or flow, namely the conjugated flow or effort on the port respectively.

Consequently, from Definition 3.2.1, Proposition 3.2.2 and Remark 3.2.3, the PH systems, considered in this work, are controllable and flat.

3.3 Flat representation of the reduced DC microgrid system

Next, the differential flatness of the different components (ES, PV, loads) of the reduced DC microgrid system (section 2.5.1) will be studied taking into account their state-space representations from chapter 2. Two sets of flat outputs for each part will be considered, one set generated by the algorithm proposed in (Franke and

Robenack, 2013) and one set by randomly choosing a number of the system's states according to Proposition 3.2.2. In the following, the steps of the algorithm will be described and, afterwards, the flat representations of the ES, the PV and the loads systems will be analyzed. We highlight that the flat representation of the system will be used afterwards in chapter 4 for the optimal profile generation.

3.3.1 Algorithm description for flat output representation

The algorithm, implementing a symbolic linearization of the system and following a consecutive calculation of matrices, nullspaces and inverses, concludes to the corresponding sets of flat outputs of the system through integration. To begin, it considers control systems which are described implicitly through the implicit function theorem (Krantz and Parks, 2012) referred below.

Theorem 3.3.1. *(Implicit function theorem (David C. Royster, 1998)): Consider a point* $(x_0,\ y_0)=(x_1^0,\ x_2^0,\ \ldots,\ x_n^0,\ y_1^0,\ y_2^0,\ \ldots,\ y_m^0) \in \mathbb{R}^n \times \mathbb{R}^m$ *and on its neighborhood differentiable functions* $\mathbf{F}_1,\ \mathbf{F}_2,\ \ldots,\ \mathbf{F}_n$. *If* $\mathbf{F}_1(x_0, y_0) = \mathbf{F}_2(x_0, y_0) = \ldots = \mathbf{F}_n(x_0, y_0) = 0$ *and the* $n \times n$ *matrix at* $(x_0,\ y_0)$*:*

$$\begin{bmatrix} \frac{\partial F_1}{\partial x_1} & \frac{\partial F_1}{\partial x_2} & \cdots & \frac{\partial F_1}{\partial x_n} \\ \frac{\partial F_2}{\partial x_1} & \frac{\partial F_2}{\partial x_2} & \cdots & \frac{\partial F_2}{\partial x_n} \\ \vdots & \vdots & \ddots & \vdots \\ \frac{\partial F_n}{\partial x_1} & \frac{\partial F_n}{\partial x_2} & \cdots & \frac{\partial F_n}{\partial x_n} \end{bmatrix} \tag{3.3.1}$$

is different from 0, *then there is a neighborhood* U *of* $y_0 = (y_1^0, y_2^0, \ldots, y_m^0) \in \mathbb{R}^m$, *a neighborhood* $\mathcal{V}$ *of* $x_0 = (x_1^0, x_2^0, \ldots, x_n^0) \in \mathbb{R}^n$ *and a unique mapping* $\varphi : U \longrightarrow \mathcal{V}$ *for which* $\varphi(y_0) = x_0$ *and* $F_1(\varphi(y), y) = F_2(\varphi(y), y) = \ldots = F_n(\varphi(y), y) = 0$ *for all* $y \in U$, *where* φ *is differentiable.* □

Definition 3.3.2. *(Implicit control systems (Lévine, 2011)): For a* n*-manifold* X, *which is infinite and differentiable, its tangent space at a point* $x \in X$ *is expressed by* T_xX *and its tangent bundle* TX. *For a function* F, *which belongs to a set of* $\mathcal{C}^\infty$ *mappings* $(\mathcal{C}^\infty \in (TX; \mathbb{R}^{n-m})$, *the implicit system is considered as:*

$$F(x, \dot{x}) = 0, \tag{3.3.2}$$

for which the $rank(\frac{\partial F}{\partial \dot{x}}) = n - m$ *in a suitable open subset of* TX. □

Remark 3.3.3. According to Theorem 3.3.1, any explicit system as in (3.2.1), where $f(x, u) \in T_xX$ for every $x \in X$ and u in an open subset U of $\mathbb{R}^m$, and $rank(\frac{\partial f}{\partial u}) = m$ in a suitable subspace of $X \times U$, can be locally converted to (3.3.2) and vice versa (Lévine, 2011). □

In the following, **the steps of the algorithm for flat representation**, as used in this work, will be presented according to Franke and Robenack (2013):

Algorithm for flat representation

1. The implicit system is introduced as in (3.3.2), based on Definition 3.3.2 and Remark 3.3.3:

$$F(x, \dot{x}) = 0, \quad x \in \mathbb{R}^n, \tag{3.3.3}$$

of $n-m$ equations, where n is the number of states and m is the number of inputs. The implicit control system is obtained after the elimination of the inputs of the system (Lévine, 2004);

2. Then, a dynamic feedback linearization is applied to the system (3.3.3) as follows:

$$\sum_{i=1}^{n} \left(\frac{\partial F}{\partial x_i} dx_i + \frac{\partial F}{\partial \dot{x}_i} d\dot{x}_i \right) = dF = 0, \tag{3.3.4}$$

from which the corresponding tangent system is found. According to (Aranda-Bricaire et al., 1995; Franke and Robenack, 2013), the tangent system consists of a number of one-forms ω equal in number to the number of the inputs of the system, m:

$$\omega_j = \sum_{i=1}^{n} F_i(x) dx_i, \quad j = 1, 2, \ldots, m. \tag{3.3.5}$$

Each one-form, ω_j, is called tangent flat output of the tangent system. The goal of the proposed algorithm is to find a possible set of tangent flat outputs from which the coordinates dx can be computed through integration. In general, the algorithm for flat representation is based on an iteration process that eliminates gradually the dimensions of the tangent system proving at the same time its controllability and achieving eventually to generate the set of the tangent flat outputs.

3. For the sake of convenience, equation (3.3.4) is replaced by $(n-m)\times n$ matrices, $\boldsymbol{P}_{0,[\boldsymbol{i}]}$, $\boldsymbol{P}_{1,[\boldsymbol{i}]}$, and $n\times 1$ matrices, $\boldsymbol{u}_{[\boldsymbol{i}]}$, $\dot{\boldsymbol{u}}_{[\boldsymbol{i}]}$, where:

   - $\boldsymbol{u}_{[\boldsymbol{i}]}$ contains the $dx_{\boldsymbol{i}}$ coordinates and $\dot{\boldsymbol{u}}_{[\boldsymbol{i}]}$ the $d\dot{x}_{\boldsymbol{i}}$ coordinates of the tangent system;
   - $\boldsymbol{P}_{0,[\boldsymbol{i}]}$ is composed by $\dfrac{\partial F}{\partial x_{\boldsymbol{i}}}(x_{\boldsymbol{i}},\dot{x}_{\boldsymbol{i}})$ and $\boldsymbol{P}_{1,[\boldsymbol{i}]}$ is composed by $\dfrac{\partial F}{\partial \dot{x}_{\boldsymbol{i}}}(x_{\boldsymbol{i}},\dot{x}_{\boldsymbol{i}})$ derivatives.

   Consequently, (3.3.4) is rewritten as follows:

$$\boldsymbol{P}_{0,[i]}\boldsymbol{u}_{[i]}+\boldsymbol{P}_{1,[i]}\dot{\boldsymbol{u}}_{[i]}=0, \tag{3.3.6}$$

   where

$$\boldsymbol{u}_{[\boldsymbol{i}]}=\boldsymbol{P}^{+}_{1,[\boldsymbol{i}]}\boldsymbol{u}_{[\boldsymbol{i}+1]}+\boldsymbol{P}^{\perp}_{1,[\boldsymbol{i}]}\boldsymbol{w}_{[\boldsymbol{i}+1]}, \tag{3.3.7}$$

$$\dot{\boldsymbol{u}}_{[\boldsymbol{i}]}=\boldsymbol{P}^{+}_{1,[\boldsymbol{i}]}\dot{\boldsymbol{u}}_{[\boldsymbol{i}+1]}+\dot{\boldsymbol{P}}^{+}_{1,[\boldsymbol{i}]}\boldsymbol{u}_{[\boldsymbol{i}+1]}+\boldsymbol{P}^{\perp}_{1,[\boldsymbol{i}]}\dot{\boldsymbol{w}}_{[\boldsymbol{i}+1]}+\dot{\boldsymbol{P}}^{\perp}_{1,[\boldsymbol{i}]}\boldsymbol{w}_{[\boldsymbol{i}+1]}. \tag{3.3.8}$$

   Note that $\boldsymbol{i}$ is the step of the iteration process within the algorithm. $\boldsymbol{P}^{+}_{1,[\boldsymbol{i}]}$ matrix is the right inverse of $\boldsymbol{P}_{1,[\boldsymbol{i}]}$ and $\boldsymbol{P}^{\perp}_{1,[\boldsymbol{i}]}$ matrix is the orthogonal complement of $\boldsymbol{P}_{1,[\boldsymbol{i}]}$ which confirm:

$$\boldsymbol{P}_{1,[\boldsymbol{i}]}\boldsymbol{P}^{+}_{1,[\boldsymbol{i}]}=\mathcal{I}, \qquad\qquad \boldsymbol{P}_{1,[\boldsymbol{i}]}\boldsymbol{P}^{\perp}_{1,[\boldsymbol{i}]}=0. \tag{3.3.9}$$

4. Afterwards, substituting (3.3.7) and (3.3.8) to (3.3.6), it leads to the following:

$$\dot{\boldsymbol{u}}_{[\boldsymbol{i}+1]}+\underbrace{\left(\boldsymbol{P}_{0,[\boldsymbol{i}]}-\dot{\boldsymbol{P}}_{1,[\boldsymbol{i}]}\right)\boldsymbol{P}^{+}_{1,[\boldsymbol{i}]}}_{A_{[\boldsymbol{i}]}}\boldsymbol{u}_{[\boldsymbol{i}+1]}+\underbrace{\left(\boldsymbol{P}_{0,[\boldsymbol{i}]}-\dot{\boldsymbol{P}}_{1,[\boldsymbol{i}]}\right)\boldsymbol{P}^{\perp}_{1,[\boldsymbol{i}]}}_{B_{[\boldsymbol{i}]}}\boldsymbol{w}_{[\boldsymbol{i}+1]}=0. \tag{3.3.10}$$

   At this point, the $B_{[\boldsymbol{i}]}$ must have full column rank, otherwise another two matrices are added in (3.3.6):

$$\boldsymbol{u}_{[\boldsymbol{i}]}=\boldsymbol{P}^{+}_{1,[\boldsymbol{i}]}\boldsymbol{u}_{[\boldsymbol{i}+1]}+\widetilde{\boldsymbol{P}}^{\perp}_{1,[\boldsymbol{i}]}\boldsymbol{w}_{[\boldsymbol{i}+1]}+\boldsymbol{Z}_{[\boldsymbol{i}]}\boldsymbol{z}_{[\boldsymbol{i}+1]}. \tag{3.3.11}$$

   At this case, $B_{[\boldsymbol{i}]}$ matrix of (3.3.10) is replaced by $\widetilde{B}_{[\boldsymbol{i}]}$ which verifies $\widetilde{B}_{[\boldsymbol{i}]}=(\boldsymbol{P}_{0,[\boldsymbol{i}]}-\dot{\boldsymbol{P}}_{1,[\boldsymbol{i}]})\widetilde{\boldsymbol{P}}^{\perp}_{1,[\boldsymbol{i}]}$ and must have full column rank. Regarding matrix $\boldsymbol{Z}_{[\boldsymbol{i}]}$, it obeys to the statements written below:

   - $(\boldsymbol{P}_{0,[\boldsymbol{i}]}-\dot{\boldsymbol{P}}_{1,[\boldsymbol{i}]})\boldsymbol{Z}_{[\boldsymbol{i}]}=0$ and $\boldsymbol{P}_{1,[\boldsymbol{i}]}\boldsymbol{Z}_{[\boldsymbol{i}]}=0$;
   - the inverse of the $\boldsymbol{Z}_{[\boldsymbol{i}]}$ matrix, $\boldsymbol{Z}^{+}_{[\boldsymbol{i}]}$ is equal to $\boldsymbol{z}_{[\boldsymbol{i}+1]}=\boldsymbol{Z}^{+}_{[\boldsymbol{i}]}\boldsymbol{u}_{[\boldsymbol{i}]}$ and verifies the following conditions:

$$\boldsymbol{Z}^{+}_{[\boldsymbol{i}]}\boldsymbol{Z}_{[0]}=\mathcal{I}, \qquad \boldsymbol{Z}^{+}_{[\boldsymbol{i}]}\widetilde{\boldsymbol{P}}^{\perp}_{1,[\boldsymbol{i}]}=0, \qquad \boldsymbol{Z}^{+}_{[\boldsymbol{i}]}\boldsymbol{P}^{+}_{1,[\boldsymbol{i}]}=0. \tag{3.3.12}$$

   If the $B_{[\boldsymbol{i}]}$ matrix is equal to 0 in (3.3.10), $\boldsymbol{w}_{[\boldsymbol{i}+1]}$ coordinates disappear and (3.3.10) is replaced by a differential equation which corresponds to a non controllable system.

5. As a next step, the variables $\boldsymbol{w}_{[\boldsymbol{i}+1]}$ are eliminated from (3.3.10), using the orthogonal complement of $B_{[\boldsymbol{i}]}$ for which $B^{\perp}_{[\boldsymbol{i}]}B_{[\boldsymbol{i}]}=0$. Therefore, (3.3.10) becomes:

$$B^{\perp}_{[\boldsymbol{i}]}A_{[\boldsymbol{i}]}\boldsymbol{u}_{[\boldsymbol{i}+1]}+B^{\perp}_{[\boldsymbol{i}]}\dot{\boldsymbol{u}}_{[\boldsymbol{i}+1]}=0, \tag{3.3.13}$$

   which results in the next step $i+1$ of the iteration process where the dimensions of (3.3.6) are reduced. As a consequence, (3.3.6) is replaced by:

$$\boldsymbol{P}_{0,[i+1]}\boldsymbol{u}_{[i+1]}+\boldsymbol{P}_{1,[i+1]}\dot{\boldsymbol{u}}_{[i+1]}=0. \tag{3.3.14}$$

6. In addition, $\boldsymbol{w}_{[i+1]}$ is determined for every step of the algorithm, multiplying in (3.3.10) by the pseudo-inverse of the $B_{[i]}$, $B^{+}_{[i]}$:

$$\boldsymbol{w}_{[i+1]} = -B^{+}_{[i]} A_{[i]} \boldsymbol{u}_{[i+1]} - B^{+}_{[i]} \dot{\boldsymbol{u}}_{[i+1]}. \tag{3.3.15}$$

Concerning $\boldsymbol{u}_{[i+1]}$, multiplying (3.3.7) with $\boldsymbol{P}_{1,[i]}$, every next step of $\boldsymbol{u}_{[i+1]}$ coordinates can be computed in function of $\boldsymbol{u}_{[i]}$ as follows:

$$\boldsymbol{u}_{[i+1]} = \boldsymbol{P}_{1,[i]} \boldsymbol{u}_{[i]}. \tag{3.3.16}$$

The previously mentioned process continues until the matrix $B_{[i]}$ has full column rank, which concludes to a possible set of flat outputs, ω_j of the tangent system:

$$\omega_j = \begin{bmatrix} \boldsymbol{P}_{1,[i]} \\ \boldsymbol{Z}^{+}_{[i]} \end{bmatrix} \boldsymbol{u}_{[i]}. \tag{3.3.17}$$

Consequently, integrating (3.3.17) leads to a possible set of flat outputs for the system $\dot{x}(t) = f(x(t), u(t))$ (3.2.1).

3.3.2 Flat representation of the ES system

In this section, the ES model (the interconnected system of the battery together with the Split-Pi converter) will be considered (2.5.1, 2.5.2a, 2.5.2b, 2.5.2c). Its state-space representation is written below (Fig.3.3.1), already presented in PH form in section 2.5.1:

$$\dot{p}_{1sc}(t) = \frac{q_{1sc}(t)}{C_{1sc}} - \frac{q_{2sc}(t)}{C_{2sc}}(1 - d_{1sc}(t)), \tag{3.3.18a}$$

$$\dot{p}_{2sc}(t) = \frac{q_{2sc}(t)}{C_{2sc}}(1 - d_{2sc}(t)) - \frac{q_{3sc}(t)}{C_{3sc}}, \tag{3.3.18b}$$

$$\dot{q}_{1sc}(t) = \frac{v_s}{R_{1sc}} - \frac{q_{1sc}(t)}{C_{2sc}R_{1sc}} - \frac{p_{1sc}(t)}{I_{1sc}}, \tag{3.3.18c}$$

$$\dot{q}_{2sc}(t) = \frac{p_{1sc}(t)}{I_{1sc}}(1 - d_{1sc}(t)) - \frac{p_{2sc}(t)}{I_{2sc}}(1 - d_{2sc}(t)), \tag{3.3.18d}$$

$$\dot{q}_{3sc}(t) = \frac{p_{2sc}(t)}{I_{2sc}} - i_{R_{1b}}(t), \tag{3.3.18e}$$

$$\dot{q}_{1b}(t) = i_{R_{1b}}(t) - \frac{q_{1b}(t)}{C_{1b}R_{2b}} + \frac{q_{2b}(t)}{C_{2b}R_{2b}}, \tag{3.3.18f}$$

$$\dot{q}_{2b}(t) = \frac{q_{1b}(t)}{C_{1b}R_{2b}} - \frac{q_{2b}(t)}{C_{2b}R_{2b}}. \tag{3.3.18g}$$

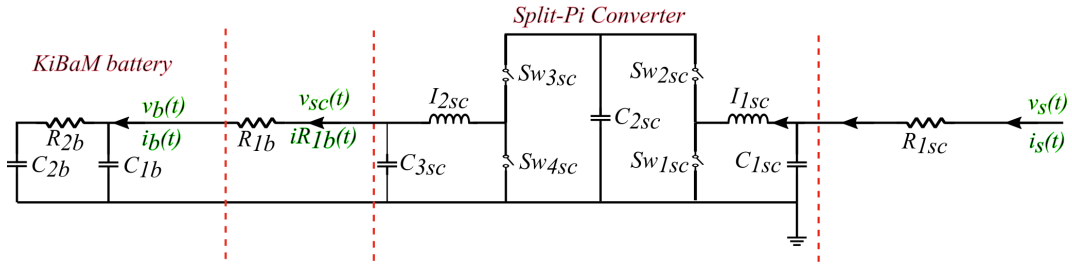

Figure 3.3.1: Electrical circuit of the ES presented in (3.3.18a)-(3.3.18g), where the input voltage v_s is equivalent to the voltage entering from the central transmission network v_{DC}. The resistor's current $i_{R_{1b}}$ equals to the battery's input current.

To proceed to the flat output calculation, we, primarily, observe that the ES system of the microgrid has:

- seven states (3.3.18a-3.3.18g); $p_{1sc}(t)$, $p_{2sc}(t)$, $q_{1sc}(t)$, $q_{2sc}(t)$, $q_{3sc}(t)$, $q_{1b}(t)$, $q_{2b}(t)$,
- four inputs (3.3.18a-3.3.18g): $d_{1sc}(t)$, $d_{2sc}(t)$, $v_s(t)$, $i_{R_{1b}}(t)$,

and the circuit's parameters and the values of the resistors are considered as constants, $1/C_{1sc} = \alpha$, $1/C_{2sc} = \beta$, $1/C_{3sc} = \gamma$, $1/C_{1b} = \delta$, $1/C_{2b} = \epsilon$, $1/I_{1sc} = \eta$, $1/I_{2sc} = \mu$, $1/R_{1sc} = \nu$, $1/R_{1b} = \sigma$, $1/R_{2b} = \psi$).

By taking into account the previously mentioned conditions, we derive the ensuing equations from the state-space representation (3.3.18a)-(3.3.18g) [1]:

$$\dot{p}_{1sc} = \alpha q_{1sc} - \beta q_{2sc}(1 - d_{1sc}), \tag{3.3.19a}$$
$$\dot{p}_{2sc} = \beta q_{2sc}(1 - d_{2sc}) - \gamma q_{3sc}, \tag{3.3.19b}$$
$$\dot{q}_{1sc} = \nu v_s - \alpha\nu q_{1sc} - \eta p_{1sc}, \tag{3.3.19c}$$
$$\dot{q}_{2sc} = \eta p_{1sc}(1 - d_{1sc}) - \mu p_{2sc}(1 - d_{2sc}), \tag{3.3.19d}$$
$$\dot{q}_{3sc} = \mu p_{2sc} - i_{R_{1b}}, \tag{3.3.19e}$$
$$\dot{q}_{1b} = i_{R_{1b}} - \delta\psi q_{1b} + \epsilon\psi q_{2b}, \tag{3.3.19f}$$
$$\dot{q}_{2b} = \delta\psi q_{1b} - \epsilon\psi q_{2b}. \tag{3.3.19g}$$

Afterwards, we will elaborate two sets of flat outputs for the ES system, one generated by the algorithm for flat representation as presented in section 3.3.1 and one chosen randomly according to the Proof 3.2. Finally, we will compare the results through simulations.

3.3.2.1 ES flat output generation using the algorithm for flat representation from Section 3.3.1

Thus, as aforementioned in section 3.3.1, we start by eliminating the system's (3.3.19a-3.3.19g) inputs and we obtain its implicit representation as in (3.3.3), which contains $n - m$ equations written below:

$$\beta q_{2sc}\dot{q}_{2sc} + \eta p_{1sc}\dot{p}_{1sc} - \alpha\eta p_{1sc}q_{1sc} + \mu p_{2sc}\dot{p}_{2sc} + \gamma\mu q_{3sc}p_{2sc} = 0, \tag{3.3.20a}$$
$$\dot{q}_{1b} + \delta\psi q_{1b} + \epsilon\psi q_{2b} - \mu p_{2sc} + \dot{q}_{3sc} = 0, \tag{3.3.20b}$$
$$\dot{q}_{2b} - \delta\psi q_{1b} + \psi\epsilon q_{2b} = 0. \tag{3.3.20c}$$

Afterwards, the linearization as in (3.3.4) of the implicit system is implemented. From equations (3.3.20a)-(3.3.20c), the following linearized system is derived:

$$\begin{aligned}\beta q_{2sc}d\dot{q}_{2sc} + \beta dq_{2sc}\dot{q}_{2sc} + \eta p_{1sc}d\dot{p}_{1sc} + \eta dp_{1sc}\dot{p}_{1sc} - \alpha\eta dp_{1sc}q_{1sc} - \alpha\eta p_{1sc}dq_{1sc} + \\ + \mu p_{2sc}d\dot{p}_{2sc} + \mu dp_{2sc}\dot{p}_{2sc} + \gamma\mu dq_{3sc}p_{2sc} + \gamma\mu q_{3sc}dp_{2sc} = 0,\end{aligned} \tag{3.3.21a}$$
$$d\dot{q}_{1b} + \delta\psi dq_{1b} + \epsilon\psi dq_{2b} - \mu dp_{2sc} + d\dot{q}_{3sc} = 0, \tag{3.3.21b}$$
$$d\dot{q}_{2b} - \delta\psi dq_{1b} + \psi\epsilon dq_{2b} = 0. \tag{3.3.21c}$$

The detailed explanation of the algorithm for flat representation procedure for the ES system is presented in Appendix A.1.1. According to (A.1.2b) and (A.1.12), we conclude to the subsequent tangent flat outputs:

$$\begin{bmatrix}\omega_1\\ \omega_2\\ \omega_3\\ \omega_4\end{bmatrix} = \begin{bmatrix}\boldsymbol{P}_{1,[0]}\\ \boldsymbol{Z}^{+}_{[0]}\end{bmatrix}\begin{bmatrix}dp_{1sc}\\ dp_{2sc}\\ dq_{1sc}\\ dq_{2sc}\\ dq_{3sc}\\ dq_{1b}\\ dq_{2b}\end{bmatrix}, \tag{3.3.22}$$

where

$$\boldsymbol{P}_{1,[0]} = \begin{bmatrix}\eta p_{1sc} & \mu p_{2sc} & 0 & \beta q_{2sc} & 0 & 0 & 0\\ 0 & 0 & 0 & 0 & 1 & 1 & 0\\ 0 & 0 & 0 & 0 & 0 & 0 & 1\end{bmatrix},$$
$$\boldsymbol{Z}^{+}_{[0]} = \begin{bmatrix}0 & 0 & 0 & 1 & 0 & 0 & 0\end{bmatrix}.$$

[1] For the sake of convenience, wherever it is straightforward implied by the text, we discard the time dependence.

More specifically, the tangent flat output is the set of one-forms $\omega_j,\ j=1,\ 2,\ 3,\ 4$ (the number of one-forms equals to the number of the control inputs of the ES system) and is written as follows:

$$\omega_1 = \eta p_{1sc} dp_{1sc} + \mu p_{2sc} dp_{2sc} + \beta q_{2sc} dq_{2sc}, \tag{3.3.24a}$$
$$\omega_2 = dq_{3sc} + dq_{1b}, \tag{3.3.24b}$$
$$\omega_3 = dq_{2b}, \tag{3.3.24c}$$
$$\omega_4 = dq_{2sc}. \tag{3.3.24d}$$

Integrating (3.3.24a)-(3.3.24d), we conclude to the following flat output set:

$$z_1 = \eta\frac{p_{1sc}^2}{2} + \mu\frac{p_{2sc}^2}{2} + \beta\frac{q_{2sc}^2}{2}, \tag{3.3.25a}$$
$$z_2 = q_{3sc} + q_{1b}, \tag{3.3.25b}$$
$$z_3 = q_{2b}, \tag{3.3.25c}$$
$$z_4 = q_{2sc}. \tag{3.3.25d}$$

In the following , the states and the control inputs of the ES system (3.3.18a-3.3.18g) are rewritten in function of the flat outputs (3.3.25a-3.3.25d) and their derivatives:

$$p_{1sc} = \sqrt{\frac{2}{\eta}(z_1 - \frac{\mu}{2}(\frac{1}{\mu}(\dot{z}_3+\dot{z}_2))^2 - \frac{\beta}{2}z_4^2)}, \tag{3.3.26a}$$
$$p_{2sc} = \frac{1}{\mu}(\dot{z}_3+\dot{z}_2), \tag{3.3.26b}$$
$$q_{1sc} = \frac{1}{a}(\frac{1}{2}\frac{1}{\sqrt{\frac{2}{g}(z_1 - \frac{h}{2}(\frac{1}{h}(\dot{z}_3+\dot{z}_2))^2 - \frac{b}{2}z_4^2)}}\frac{2}{g}(\dot{z}_1 - \frac{1}{h}(\dot{z}_2+\dot{z}_3)(\ddot{z}_2+\ddot{z}_3) - bz_4\dot{z}_4) + \tag{3.3.26c}$$
$$+\frac{b}{a}z_4\frac{\dot{z}_4 + (\dot{z}_2+\dot{z}_3) - (\dot{z}_2+\dot{z}_3)(1 - \frac{1}{hbz_4}(\ddot{z}_3+\ddot{z}_2) - \frac{c}{bz_4}(z_2 - \frac{1}{em}\dot{z}_3 - \frac{f}{e}z_3))}{g(\sqrt{\frac{2}{g}(z_1 - \frac{h}{2}(\frac{1}{h}(\dot{z}_3+\dot{z}_2))^2 - \frac{b}{2}z_4^2)})}, \tag{3.3.26d}$$
$$q_{2sc} = z_4, \tag{3.3.26e}$$
$$q_{3sc} = z_2 - \frac{1}{\delta\psi}\dot{z}_3 - \frac{\epsilon}{\delta}z_3, \tag{3.3.26f}$$
$$q_{1b} = \frac{1}{\delta\psi}\dot{z}_3 + \frac{\epsilon}{\delta}z_3, \tag{3.3.26g}$$
$$q_{2b} = z_3, \tag{3.3.26h}$$
$$d_{1sc} = 1 - \frac{\dot{z}_4 + (\dot{z}_2+\dot{z}_3) - (\dot{z}_2+\dot{z}_3)(1 - \frac{1}{\mu\beta z_4}(\ddot{z}_3+\ddot{z}_2) - \frac{\gamma}{\beta z_4}(z_2 - \frac{1}{\delta\psi}\dot{z}_3 - \frac{\epsilon}{\delta}z_3))}{\eta(\sqrt{\frac{2}{\eta}(z_1 - \frac{\mu}{2}(\frac{1}{\mu}(\dot{z}_3+\dot{z}_2))^2 - \frac{\beta}{2}z_4^2)})}, \tag{3.3.26i}$$
$$d_{2sc} = 1 - \frac{1}{\mu\beta z_4}(\ddot{z}_3+\ddot{z}_2) - \frac{\gamma}{\beta z_4}(z_2 - \frac{1}{\delta\psi}\dot{z}_3 - \frac{\epsilon}{\delta}z_3), \tag{3.3.26j}$$
$$v_s = \frac{1}{\nu}\dot{q}_{1sc} + \alpha q_{1sc} + \frac{\eta}{\nu}p_{1sc}, \tag{3.3.26k}$$
$$i_{R_{1b}} = \frac{1}{\delta\psi}\ddot{z}_3 + (\frac{\epsilon}{\delta}+1)\dot{z}_3. \tag{3.3.26l}$$

Below, the compact flat representation of the states and inputs is deduced in function of the flat outputs and their derivatives, which will be useful later for the explanation of the simulations:

$$p_{1sc} = \Phi_1(z_1, \dot{z}_2, z_3, \dot{z}_3, z_4), \tag{3.3.27a}$$
$$p_{2sc} = \Phi_2(\dot{z}_2, z_3, \dot{z}_3), \tag{3.3.27b}$$
$$q_{1sc} = \Phi_3(z_1, \dot{z}_1, z_2, \dot{z}_2, \ddot{z}_2, z_3, \dot{z}_3, \ddot{z}_3, z_4, \dot{z}_4), \tag{3.3.27c}$$
$$q_{2sc} = \Phi_4(z_4), \tag{3.3.27d}$$
$$q_{3sc} = \Phi_5(z_2, z_3, \dot{z}_3), \tag{3.3.27e}$$

$$q_{1b} = \Phi_6(z_3, \dot{z}_3), \tag{3.3.27f}$$
$$q_{2b} = \Phi_7(z_3), \tag{3.3.27g}$$
$$d_{1sc}(t) = \Phi_8(z_1, z_2, \dot{z}_2, \ddot{z}_2, z_3, \dot{z}_3, \ddot{z}_3, z_4), \tag{3.3.27h}$$
$$d_{2sc}(t) = \Phi_9(z_2, \ddot{z}_2, z_3, \dot{z}_3, \ddot{z}_3, z_4), \tag{3.3.27i}$$
$$v_s = \Phi_{10}(z_1, \dot{z}_1, \ddot{z}_1, z_2, \dot{z}_2, \ddot{z}_2, \dddot{z}_2, z_3, \dot{z}_3, \ddot{z}_3, \dddot{z}_3, z_4, \dot{z}_4, \ddot{z}_4), \tag{3.3.27j}$$
$$i_{R_{1b}} = \Phi_{11}(\dot{z}_3, \ddot{z}_3). \tag{3.3.27k}$$

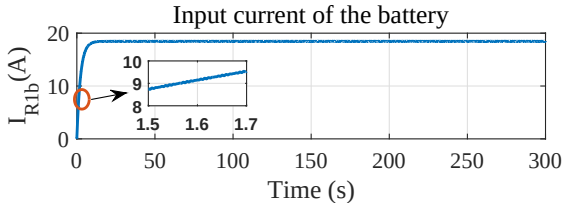

Figure 3.3.2: Battery's input current $i_{R_{1b}}$ generated by the PH system in (3.3.19a)-(3.3.19g).

For the sake of completeness, the set of flat outputs found by the algorithm for flat representation is validated through simulations, comparing the ES PH model in (3.3.18a)-(3.3.18g) and the ES flatness-based model in (3.3.26a)-(3.3.26l). To accomplish this we rewrite the model's states in (3.3.19a)-(3.3.19g) in function of the flat outputs (3.3.25a-3.3.25d). Then, the control inputs d_{1sc}, d_{2sc}, v_s, $i_{R_{1b}}$ are rewritten in function of the states as in (3.3.26i)-(3.3.26l) and we proceed with the simulations. For the simulations, we consider

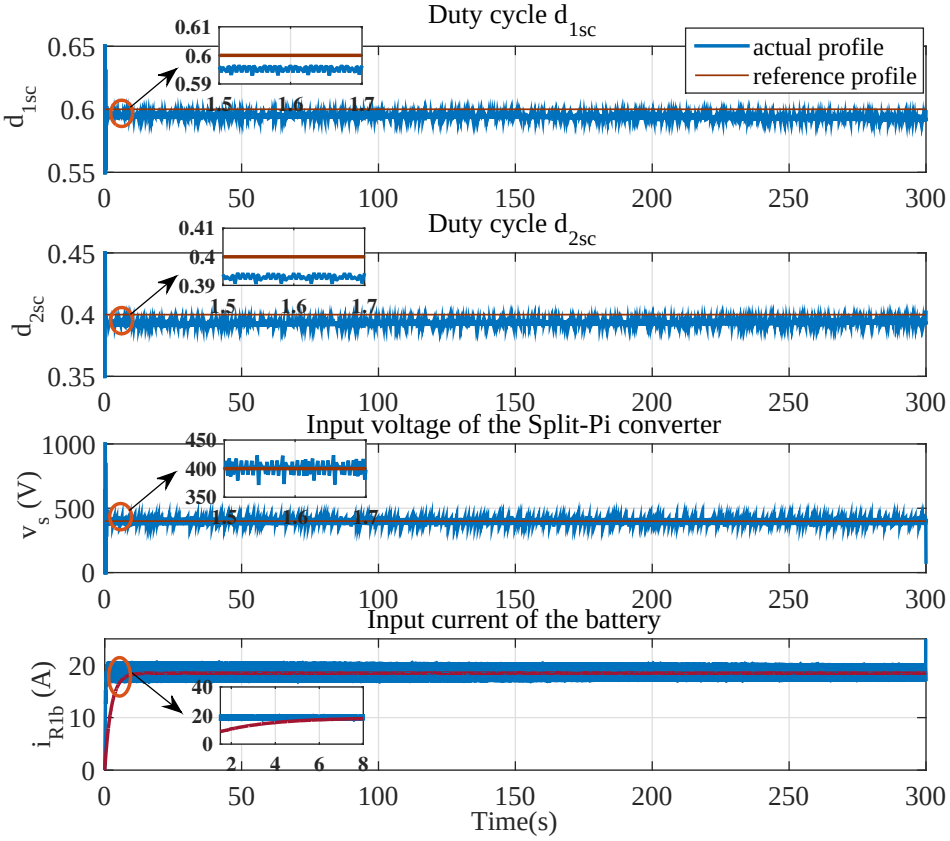

Figure 3.3.3: Control inputs of the ES in function of the states generated considering the flat output set in (3.3.25a-3.3.25d). The signals in red depict the expected value of the control inputs.

a stable input voltage equal to $v_s = 400V$ and fixed duty cycles, $d_{1sc} = 0.4$ and $d_{2sc} = 0.6$. Additionally, we present in Fig.3.3.2 the battery's input current, i_{R1b}, (where $R_{1b} = 10\ \Omega$) as has been generated by the ES PH model (3.3.19f). The duration of the simulation is 300 s, since the system's signal response stabilizes after a while and remains the same.

From the simulations, Fig.3.3.3 was generated and illustrates the control inputs (lines in blue) in function of the states written after the set of flat outputs in (3.3.25a)-(3.3.25d). We notice that the control inputs in flat representation follow very well the expected values used as inputs to the ES PH model. However, fluctuations are observed among the reference and the actual values. The noise appearing in the simulations is created because of the numerical differentiation used to estimate the flat outputs' derivatives (see also (3.3.26a)-(3.3.26l)). The more derivatives there are in the flat representation (3.3.27), the more noise-affected the data appear in the final signal. Therefore, in Fig.3.3.3, the highest noise exists in the input voltage v_s where all the flat outputs appear with their derivatives of first, second or higher order. These conjectures will be used for further comparisons with the next set of flat outputs and for analysis later in this chapter. Furthermore, in Appendix A.1.2 the simulations of the states in function of the flat outputs as in (3.3.26a)-(3.3.26l) are illustrated. In addition to this, a filter has been added after the numerical derivatives which reduces the noise and the simulation results are depicted in Fig.A.1.7a in Appendix A.1.2.

From the algorithm, we conclude to a possible set of flat outputs through the tangent system of the ES. However, according to Levine (2009), multiple flat output sets may exist for each physical system. In the following section, we consider another set of flat outputs for the ES and we compare with the preceding results.

3.3.2.2 ES flat representation through another set of flat outputs

In this section, taking into account the Proof 3.2, we suggest another set of flat outputs. According to Levine (2009), the number of control inputs equals the number of flat outputs which can be in function of the states of the system (Definition 3.2.1). Therefore, for the ES PH system of (3.3.18a)-(3.3.18g), we consider four states as flat outputs in function of which the system can be written. The selected set is the following:

$$z = \begin{bmatrix} p_{1sc} & q_{3sc} & q_{2b} & q_{2sc} \end{bmatrix}^\top . \tag{3.3.28}$$

Afterwards, considering the aforementioned set of flat outputs (3.3.28), the states and control inputs of the system are rewritten in flat representation as shown below:

$$p_{1sc} = z_1, \tag{3.3.29a}$$

$$p_{2sc} = \frac{1}{\mu}(\dot{z}_2 + \frac{1}{\delta\psi}\ddot{z}_3 + (\frac{\epsilon}{\delta}+1)\dot{z}_3), \tag{3.3.29b}$$

$$q_{1sc} = \frac{1}{a}\dot{z}_1 + \frac{\beta}{\alpha}z_4(\frac{\dot{z}_4 + \mu(\frac{1}{\mu}(\dot{z}_2 + \frac{1}{\delta\psi}\ddot{z}_3 + (\frac{\epsilon}{\delta}+1)\dot{z}_3)(\frac{\gamma z_2}{\beta z_4} + \frac{1}{\mu\beta}\frac{\ddot{z}_2}{z_4} + \frac{1}{\mu\delta\psi\beta}\frac{\dddot{z}_3}{z_4} + \frac{1}{\mu\beta}(\frac{\epsilon}{\delta}+1)\frac{\ddot{z}_3}{z_4}))}{\eta z_1}), \tag{3.3.29c}$$

$$q_{2sc} = z_4, \tag{3.3.29d}$$

$$q_{3sc} = z_2, \tag{3.3.29e}$$

$$q_{1b} = \frac{1}{\delta\psi}\dot{z}_3 + \frac{\epsilon}{\delta}z_3, \tag{3.3.29f}$$

$$q_{2b} = z_3, \tag{3.3.29g}$$

$$d_{1sc} = 1 - \frac{\dot{z}_4 + \mu(\frac{1}{\mu}(\dot{z}_2 + \frac{1}{\delta\psi}\ddot{z}_3 + (\frac{\epsilon}{\delta}+1)\dot{z}_3)(\frac{\gamma z_2}{b z_4} + \frac{1}{\mu\beta}\frac{\ddot{z}_2}{z_4} + \frac{1}{\mu\delta\psi\beta}\frac{\dddot{z}_3}{z_4} + \frac{1}{\mu\beta}(\frac{\epsilon}{\delta}+1)\frac{\ddot{z}_3}{z_4}))}{\eta z_1}, \tag{3.3.29h}$$

$$d_{2sc} = 1 - \frac{\gamma z_2}{\beta z_4} - \frac{1}{\mu\beta}\frac{\ddot{z}_2}{z_4} - \frac{1}{\mu\delta\psi\beta}\frac{\dddot{z}_3}{z_4} - \frac{1}{\mu\beta}(\frac{\epsilon}{\delta}+1)\frac{\ddot{z}_3}{z_4}, \tag{3.3.29i}$$

$$v_s = \frac{1}{n}\dot{q}_{1sc} + \alpha q_{1sc} + \frac{\eta}{\nu}p_{1sc}, \tag{3.3.29j}$$

$$i_{R_{1b}} = \frac{1}{\delta\psi}\ddot{z}_3 + (\frac{\epsilon}{\delta}+1)\dot{z}_3. \tag{3.3.29k}$$

Moreover, the compact flat representation of the states and inputs is presented in function of the flat outputs (3.3.28) and their derivatives:

$$p_{1sc} = \Phi_{12}(z_1), \tag{3.3.30a}$$

$$p_{2sc} = \Phi_{13}(\dot{z}_2, \dot{z}_3, \ddot{z}_3), \tag{3.3.30b}$$
$$q_{1sc} = \Phi_{14}(z_1, \dot{z}_1, z_2, \dot{z}_2, \ddot{z}_2, \dot{z}_3, \ddot{z}_3, \dddot{z}_3, z_4, \dot{z}_4), \tag{3.3.30c}$$
$$q_{2sc} = \Phi_{15}(z_4), \tag{3.3.30d}$$
$$q_{3sc} = \Phi_{16}(z_2), \tag{3.3.30e}$$
$$q_{1b} = \Phi_{17}(z_3, \dot{z}_3), \tag{3.3.30f}$$
$$q_{2b} = \Phi_{18}(z_3), \tag{3.3.30g}$$
$$d_{1sc} = \Phi_{19}(z_2, \dot{z}_2, \ddot{z}_2, \dot{z}_3, \ddot{z}_3, \dddot{z}_3, z_4, \dot{z}_4), \tag{3.3.30h}$$
$$d_{2sc} = \Phi_{20}(z_2, \ddot{z}_2, \ddot{z}_3, \dddot{z}_3, z_4), \tag{3.3.30i}$$
$$v_s = \Phi_{21}(z_1, \dot{z}_1, \ddot{z}_1, z_2, \dot{z}_2, \ddot{z}_2, \dddot{z}_2, \dot{z}_3, \ddot{z}_3, \dddot{z}_3, \ddddot{z}_3, z_4, \dot{z}_4, \ddot{z}_4), \tag{3.3.30j}$$
$$i_{R_{1b}} = \Phi_{22}(\dot{z}_3, \ddot{z}_3). \tag{3.3.30k}$$

Next, we proceed similarly to the simulations in order to validate the second set of flat outputs (3.3.28), considering the same reference values for the control inputs of the ES PH system, d_{1sc}, d_{2sc}, v_s, $i_{R_{1b}}$ as before. Fig.3.3.4 depicts the signal response of the control inputs which approaches very well the reference profiles. Consequently, both sets of flat outputs (3.3.25a-3.3.25d and 3.3.28) can be used to generate an equivalent flat system for the ES. However, the flat representation generated by the algorithm (3.3.26a-3.3.26l) seems to be a better choice, since in the control inputs simulations (Fig.3.3.3) less noise-affected data exist than in the control inputs generated by the secondly proposed set of flat outputs in (3.3.28) (Fig.3.3.4). This is because of the high number of derivatives that appears in the d_{1sc}, d_{2sc} and v_s flat representation, in (3.3.30h), (3.3.30i) and (3.3.30j) respectively. For i_{R1b} similar results are obtained since their values are equal for both flat representations (see (3.3.26l) and (3.3.29k)). As previously, in Appendix A.1.2 the simulations of the states in function of the second set of flat outputs (3.3.28) are also demonstrated. Additionally, the numerical derivatives are filtered to mitigate the noise and the simulation results are depicted in Fig.A.1.7b in Appendix A.1.2.

3.3.3 Flat outputs representation of the PV and the loads

In this section, the flat outputs for the PV and the loads' system (see also Fig.2.5.1) will be investigated, in the same way as previously for the ES system, by computing two different flat output sets, one with the algorithm and another through a selection among the states of the system. The PV and the loads are two different systems composed by (see also Fig.2.6.1):

- in the case of the PV, the PV is the power source which generates the input voltage, v_s, of the Split-Pi converter (Fig.3.3.5) and at the output there is the central transmission network, the common DC-bus. In Fig.3.3.5 i_R is equal to the output current of the Split-Pi converter which can be considered as input either to the load or to the central transmission network;
- in the case of the loads, the input voltage, v_s, is coming from the central transmission network and at the output the load is considered as a resistor, R (Fig.3.3.5).

For the PV system, power profiles generated by the PV model in section 2.4.1.1 are taken into account as inputs to the Split-Pi converter. On the other hand, concerning the loads, we consider profiles obtained from several open source projects as in Department of Energy Office of Energy Efficiency & Renewable Energy (2017). Therefore, it remains to study the flat representation of the Split-Pi converter PH model, with v_s the input voltage coming from source and i_R the output current, as in (2.4.10)-(2.4.11) given below, which was presented also in PH form in section 2.4.2.1:

$$\dot{p}_{1sc}(t) = \frac{q_{1sc}(t)}{C_{1sc}} - \frac{q_{2sc}(t)}{C_{2sc}}(1 - d_{1sc}(t)), \tag{3.3.31a}$$
$$\dot{p}_{2sc}(t) = \frac{q_{2sc}(t)}{C_{2sc}}(1 - d_{2sc}(t)) - \frac{q_{3sc}(t)}{C_{3sc}}, \tag{3.3.31b}$$
$$\dot{q}_{1sc}(t) = \frac{v_s}{R_{1sc}} - \frac{q_{1sc}(t)}{C_{2sc}R_{1sc}} - \frac{p_{1sc}(t)}{I_{1sc}}, \tag{3.3.31c}$$
$$\dot{q}_{2sc}(t) = \frac{p_{1sc}(t)}{I_{1sc}}(1 - d_{1sc}(t)) - \frac{p_{2sc}(t)}{I_{2sc}}(1 - d_{2sc}(t)), \tag{3.3.31d}$$
$$\dot{q}_{3sc}(t) = \frac{p_{2sc}(t)}{I_{2sc}} - i_R(t). \tag{3.3.31e}$$

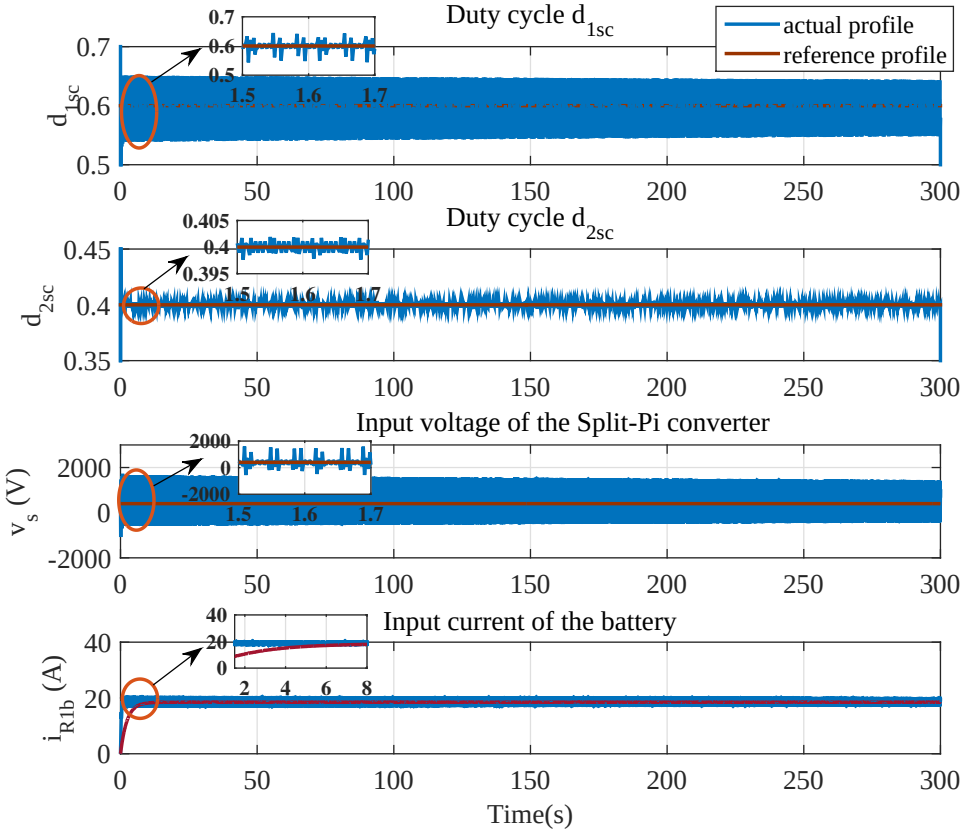

Figure 3.3.4: Control inputs of the ES in function of the second set of flat outputs as in (3.3.28).

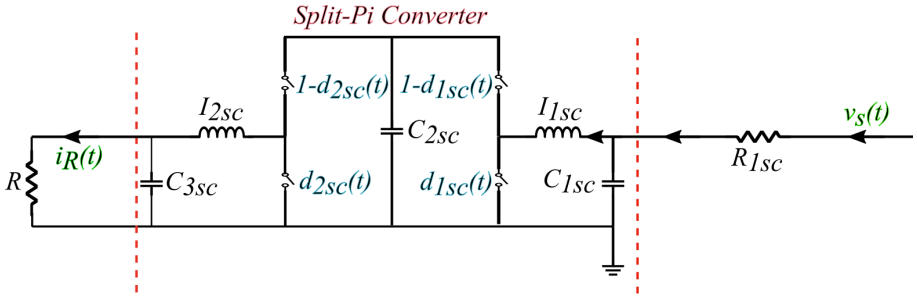

Figure 3.3.5: Electrical circuit of the Split-Pi converter presented in (3.3.31a)-(3.3.31e).

Before continuing with the flat output calculation of the Split-Pi converter, we firstly consider the following:

- five states (3.3.31a-3.3.31e); $p_{1sc}(t)$, $p_{2sc}(t)$, $q_{1sc}(t)$, $q_{2sc}(t)$, $q_{3sc}(t)$,
- four control inputs (3.3.31a-3.3.31e): $d_{1sc}(t)$, $d_{2sc}(t)$, $v_s(t)$, $i_R(t)$

and the circuit's parameters and the values of the resistors are considered as constants, $1/C_{1sc} = \alpha$, $1/C_{2sc} = \beta$, $1/C_{3sc} = \gamma$, $1/I_{1sc} = \eta$, $1/I_{2sc} = \mu$, $1/R_{1sc} = \nu$, $1/R = \zeta$.

Therefore, the equations below are deduced from the state-space representation (3.3.31a)-(3.3.31e):

$$\dot{p}_{1sc} = \alpha q_{1sc} - \beta q_{2sc}(1 - d_{1sc}), \tag{3.3.32a}$$
$$\dot{p}_{2sc} = \beta q_{2sc}(1 - d_{2sc}) - \gamma q_{3sc}, \tag{3.3.32b}$$
$$\dot{q}_{1sc} = \nu v_s - \alpha\nu q_{1sc} - \eta p_{1sc}, \tag{3.3.32c}$$
$$\dot{q}_{2sc} = \eta p_{1sc}(1 - d_{1sc}) - \mu p_{2sc}(1 - d_{2sc}), \tag{3.3.32d}$$
$$\dot{q}_{3sc} = \mu p_{2sc} - i_R, \tag{3.3.32e}$$

3.3.3.1 PV and load flat output representation using the algorithm for flat representation from Section 3.3.1

Primarily, the control inputs of the system (3.3.32a-3.3.32e) are eliminated substituting the duty cycles d_{1sc} and d_{2sc} from (3.3.32a) and (3.3.32b) in (3.3.32d). Consequently, its implicit representation is obtained as in (3.3.3), which contains $n - m$ equations written below:

$$\beta q_{2sc}\dot{q}_{2sc} + \eta p_{1sc}\dot{p}_{1sc} - \alpha\eta p_{1sc}q_{1sc} + \mu p_{2sc}\dot{p}_{2sc} + \gamma\mu q_{3sc}p_{2sc} = 0. \tag{3.3.33}$$

As a next step, the implicit system (3.3.33) is linearized as in (3.3.4). From equation (3.3.33), we obtain the following linearized system:

$$\begin{aligned}\beta q_{2sc}d\dot{q}_{2sc} + \beta dq_{2sc}\dot{q}_{2sc} + \eta p_{1sc}d\dot{p}_{1sc} + \eta dp_{1sc}\dot{p}_{1sc} - \alpha\eta dp_{1sc}q_{1sc} - \alpha\eta p_{1sc}dq_{1sc} + \mu p_{2sc}d\dot{p}_{2sc} + \\ + \mu dp_{2sc}\dot{p}_{2sc} + \gamma\mu dq_{3sc}p_{2sc} + \gamma\mu q_{3sc}dp_{2sc} = 0,\end{aligned} \tag{3.3.34}$$

Then, we proceed with the algorithm for flat representation as presented in section 3.3.1 and the detailed computation is introduced in Appendix A.2.1. According to (A.2.1b) and (A.2.10), we conclude to the subsequent tangent flat outputs:

$$\begin{bmatrix}\omega_1\\ \omega_2\\ \omega_3\\ \omega_4\end{bmatrix} = \begin{bmatrix}\boldsymbol{P}_{1,[0]}\\ \boldsymbol{Z}^{+}_{[0]}\end{bmatrix}\begin{bmatrix}dp_{1sc}\\ dp_{2sc}\\ dq_{1sc}\\ dq_{2sc}\\ dq_{3sc}\end{bmatrix}, \tag{3.3.35}$$

where

$$\boldsymbol{P}_{1,[0]} = \begin{bmatrix}\eta p_{1sc} & \mu p_{2sc} & 0 & \beta q_{2sc} & 0\end{bmatrix},$$
$$\boldsymbol{Z}^{+}_{[0]} = \begin{bmatrix}0 & 1 & 0 & 0 & 0\\ 0 & 0 & 0 & 1 & 0\\ 0 & 0 & 0 & 0 & -1\end{bmatrix}.$$

Therefore, the tangent flat outputs, $\omega_j,\ j = 1,\ 2,\ 3,\ 4$, of the Split-Pi converter are as follows:

$$\omega_1 = \eta p_{1sc}dp_{1sc} + \mu p_{2sc}dp_{2sc} + \beta q_{2sc}dq_{2sc}, \tag{3.3.37a}$$
$$\omega_2 = dq_{2sc}, \tag{3.3.37b}$$
$$\omega_3 = dp_{2sc}, \tag{3.3.37c}$$
$$\omega_4 = -dq_{3sc}. \tag{3.3.37d}$$

Consequently, after the integration of (3.3.37a)-(3.3.37d), we obtain the flat output set written below:

$$z_1 = \eta\frac{p_{1sc}^2}{2} + \mu\frac{p_{2sc}^2}{2} + \beta\frac{q_{2sc}^2}{2}, \tag{3.3.38a}$$
$$z_2 = q_{3sc} + q_{1b}, \tag{3.3.38b}$$
$$z_3 = q_{2b}, \tag{3.3.38c}$$
$$z_4 = q_{2sc}. \tag{3.3.38d}$$

In the following , we introduce the states and inputs of the Split-Pi converter in function of the flat outputs (3.3.38a-3.3.38d) and their derivatives:

$$p_{1sc} = \sqrt{\frac{2}{\eta}(z_1 - \mu\frac{{z_3}^2}{2} - \beta\frac{{z_2}^2}{2})}, \tag{3.3.39a}$$

$$p_{2sc} = z_3, \tag{3.3.39b}$$

$$q_{1sc} = \frac{1}{\alpha}\Big(\frac{1}{2}\frac{2}{\eta}(z_1 - \mu\frac{{z_3}^2}{2} - \beta\frac{{z_2}^2}{2})\frac{2}{\eta}(\dot{z}_1 - \mu z_3\dot{z}_3 - \beta z_2\dot{z}_2) + \beta z_2\frac{\dot{z}_2 + \mu z_3\frac{\dot{z}_3 - \gamma z_4}{\beta z_2}}{\eta(\sqrt{\frac{2}{\eta}(z_1 - \mu\frac{{z_3}^2}{2} - \beta\frac{{z_2}^2}{2})})}, \tag{3.3.39c}$$

$$q_{2sc} = z_2, \tag{3.3.39d}$$

$$q_{3sc} = -z_4, \tag{3.3.39e}$$

$$d_{1sc} = 1 - \frac{\dot{z}_2 + \mu z_3\frac{\dot{z}_3 - \gamma z_4}{\beta z_2}}{\eta(\sqrt{\frac{2}{\eta}(z_1 - \mu\frac{{z_3}^2}{2} - \beta\frac{{z_2}^2}{2})})}, \tag{3.3.39f}$$

$$d_{2sc} = 1 - \frac{\dot{z}_3 - \gamma z_4}{\beta z_2}, \tag{3.3.39g}$$

$$v_s = \frac{1}{\nu}\dot{q}_{1sc} + \alpha q_{1sc} + \frac{\eta}{\nu}p_{1sc}, \tag{3.3.39h}$$

$$i_R = \mu z_3 + \dot{z}_4. \tag{3.3.39i}$$

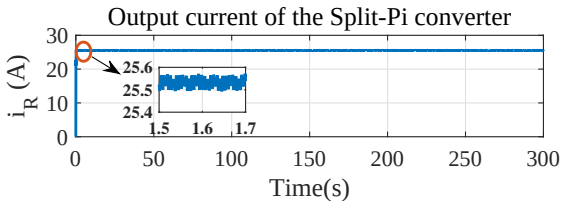

Figure 3.3.6: Output current of the Split-Pi converter generated by the PH model (3.3.31a-3.3.31e).

Furthermore, we consider the compact flat representation of the states and inputs in function of the flat outputs:

$$p_{1sc} = \Phi_{23}(z_1, z_2, z_3), \tag{3.3.40a}$$

$$p_{2sc} = \Phi_{24}(z_3), \tag{3.3.40b}$$

$$q_{1sc} = \Phi_{25}(z_1, \dot{z}_1, z_2, \dot{z}_2, z_3, \dot{z}_3, z_4), \tag{3.3.40c}$$

$$q_{2sc} = \Phi_{26}(z_2), \tag{3.3.40d}$$

$$q_{3sc} = \Phi_{27}(z_4), \tag{3.3.40e}$$

$$d_{1sc} = \Phi_{28}(z_1, z_2, \dot{z}_2, z_3, \dot{z}_3, z_4), \tag{3.3.40f}$$

$$d_{2sc} = \Phi_{29}(z_2, \dot{z}_3, z_4), \tag{3.3.40g}$$

$$v_s = \Phi_{30}(z_1, \dot{z}_1, \ddot{z}_1, z_2, \dot{z}_2, \ddot{z}_2, z_3, \dot{z}_3, \ddot{z}_3, z_4, \dot{z}_4), \tag{3.3.40h}$$

$$i_R = \Phi_{31}(z_3, \dot{z}_4). \tag{3.3.40i}$$

For validation, we replace the model's inputs in (3.3.31a)-(3.3.31e) with the inputs d_{1sc}, d_{2sc}, v_s, i_R given in function of the flat outputs in (3.3.39f)-(3.3.39i). Similarly, we consider $v_s = 400\ V$, $d_{1sc} = 0.6$ and $d_{2sc} = 0.4$. The output current of the Split-Pi converter, i_R, generated by the PH model, (3.3.31a)-(3.3.31e), is depicted in Fig.3.3.6 (where $R = 1\ \Omega$). Fig.3.3.7 shows the simulations results of the control inputs, which follow very well the reference values (lines in red). For the v_s, many fluctuations are observed because of its flat representation (3.3.40h) including all the four flat outputs (3.3.38a-3.3.38d) and their derivatives. As before, in Appendix A.2.2 the simulations of the states in function of the set of flat outputs in (3.3.38a)-(3.3.38d) are also demonstrated. Moreover, the numerical derivatives are filtered to mitigate the noise and the simulation results are depicted in Fig.A.1.7a in Appendix A.2.2.

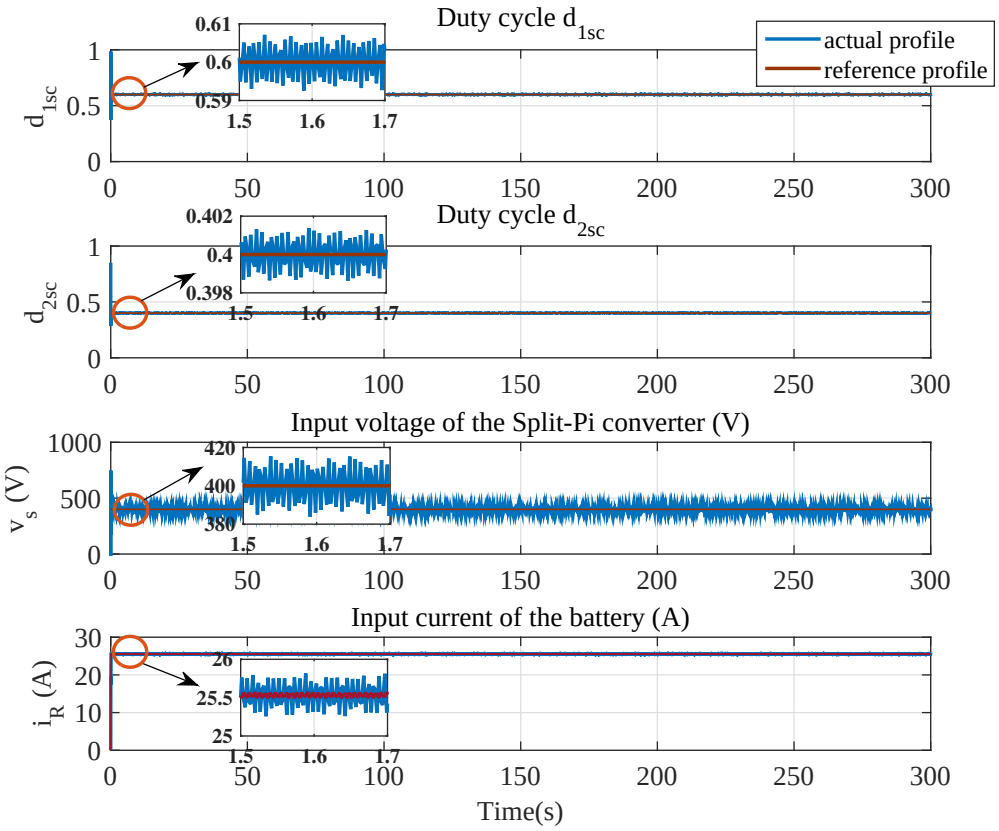

Figure 3.3.7: Control inputs in function of the flat outputs generated by the algorithm for flat representation as in (3.3.38a)-(3.3.38d).

3.3.3.2 PV and loads flat representation through another set of flat outputs

This subsection proposes another set of flat outputs, taking into account the Proof 3.2, choosing four different states of the Split-Pi converter, since we have four control inputs:

$$z = \begin{bmatrix} p_{1sc} & p_{2sc}q_{2sc} & q_{3sc} \end{bmatrix}^\top . \tag{3.3.41}$$

Consequently, through calculation, we obtain the states and the inputs in function of the aforementioned flat outputs:

$$p_{1sc} = z_1, \tag{3.3.42a}$$
$$p_{2sc} = z_2, \tag{3.3.42b}$$
$$q_{1sc} = \frac{1}{\alpha}(\dot{z}_1 + \beta z_3 \frac{\dot{z}_3 + \mu z_2 \frac{\dot{z}_2 + \gamma z_4}{\beta z_3}}{\eta z_1}), \tag{3.3.42c}$$
$$q_{2sc} = z_3, \tag{3.3.42d}$$
$$q_{3sc} = z_4, \tag{3.3.42e}$$
$$d_{1sc} = 1 - \frac{\dot{z}_3 + \mu z_2 \frac{\dot{z}_2 + \gamma z_4}{\beta z_3}}{\eta z_1}, \tag{3.3.42f}$$
$$d_{2sc} = 1 - \frac{\dot{z}_2 + \gamma z_4}{\beta z_3}, \tag{3.3.42g}$$
$$v_s = \frac{1}{\nu}\dot{q}_{1sc} + \alpha q_{1sc} + \frac{\eta}{\nu} p_{1sc}, \tag{3.3.42h}$$
$$i_R = \mu z_2 - \dot{z}_4. \tag{3.3.42i}$$

Below, the corresponding compact flat representation of the states and inputs is introduced:

$$p_{1sc} = \Phi_{32}(z_1), \tag{3.3.43a}$$
$$p_{2sc} = \Phi_{33}(z_2), \tag{3.3.43b}$$
$$q_{1sc} = \Phi_{34}(z_1, \dot{z}_1, z_2, \dot{z}_2, z_3, \dot{z}_3, z_4), \tag{3.3.43c}$$
$$q_{2sc} = \Phi_{35}(z_3), \tag{3.3.43d}$$
$$q_{3sc} = \Phi_{36}(z_4), \tag{3.3.43e}$$
$$d_{1sc} = \Phi_{37}(z_1, z_2, \dot{z}_2, z_3, \dot{z}_3, z_4), \tag{3.3.43f}$$
$$d_{2sc} = \Phi_{38}(\dot{z}_2, z_3, z_4), \tag{3.3.43g}$$
$$v_s = \Phi_{39}(z_1, \dot{z}_1, \ddot{z}_1, z_2, \dot{z}_2, \ddot{z}_2, z_3, \dot{z}_3, \ddot{z}_3, z_4, \dot{z}_4), \tag{3.3.43h}$$
$$i_R = \Phi_{40}(z_3, \dot{z}_4). \tag{3.3.43i}$$

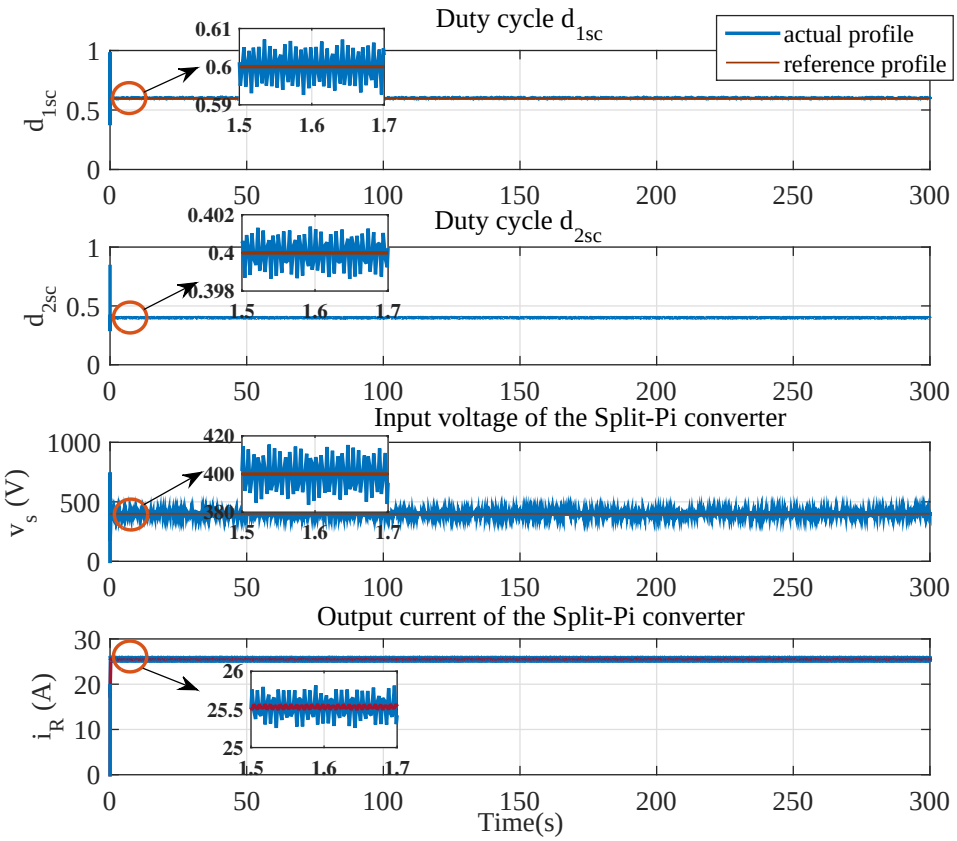

Figure 3.3.8: Control inputs in function of the flat outputs as in (3.3.41).

For validation, considering the same values as references for the control inputs d_{1sc}, d_{2sc}, v_s, i_R as before, in Fig.3.3.8 the simulation results are presented. From the simulations, similar results are observed as in Fig.3.3.7, since the flat representations obtained have similar dependence on the states and their derivatives as presented also in (3.3.40f)-(3.3.40i) and (3.3.43f)-(3.3.43i) for both set of flat outputs respectively. Appendix A.2.2 presents the simulations of the states in function of the second set of flat outputs (3.3.41). Additionally, a filter is used after the numerical differentiation to reduce the noise and in Appendix A.2.2 the corresponding simulation results are illustrated (Fig.A.1.7b).

Following the previously depicted results for the ES system and the PV and loads system, we deduce that the less derivatives are interfering in the flat representation of the system, the less disturbances will emerge. Hence, in the upcoming section, we will concentrate on the concept of finding the proper set of flat outputs of a PH system considering the less possible derivatives. Furthermore, this information is useful for

the B-spline parametrization, which will be used later in chapter 4, a method of parametrization which is strongly dependent on the order of derivatives appeared in the flat representation.

3.4 Port-Hamiltonian systems and differential flatness

Hereinafter, a connection between PH systems and differential flatness is presented. We propose a method for generating the possible sets of flat outputs for a particular class of PH systems.. The inverse dynamics of the PH systems will be described with illustrated examples considering a notion called bicausality within a Bond graph.

3.4.1 Bicausality and Bond graphs

As has been already mentioned in section 2.3.1, the causality property indicates the computational dependence among the ports characterized by pairs of effort e and flow f. Fig.3.4.3 depicts the dependence on the efforts and flows between two ports in a causal Bond graph (for further details see also section 2.3.1). The red dashed lines illustrate the power flow and the dependence among the ports created after the causality assignment.

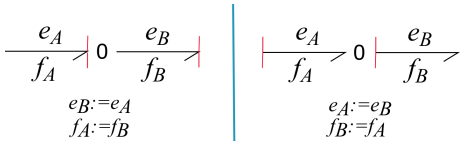

Figure 3.4.1: Causality property of the Bond graph.

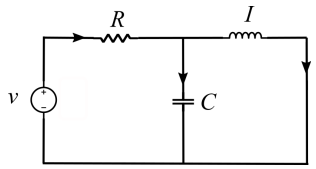

Figure 3.4.2: Electrical RLC circuit.

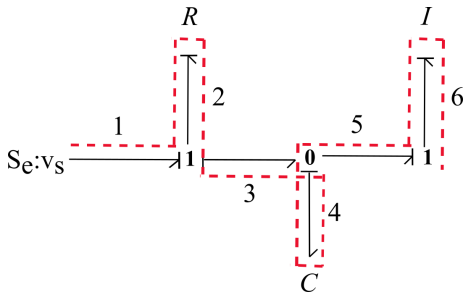

Figure 3.4.3: Causal bond graph of the electrical RLC circuit depicted in Fig.3.4.2.

Afterwards, another notion used in the Bond graph theory will be implemented. Bicausality is an extended version of causality which allows the interpretation of the inverse dynamics of a physical system (Gawthrop, 1994; Richard et al., 2002). In order to design a bicausal Bond graph, supplementary elements, such as the SS (source-sensor), should be taken into account. This elements enable the decoupling of $e - f$ pairs (Fig.3.4.5) and allow the calculation of further quantitative variables in the Bond graph model. Within a bicausal Bond graph, we can analyze explicitly the inverse dynamics of a physical system concluding to the states or parameters estimation (Ngwompo and Gawthrop, 1999). In the literature, a method exists called Sequential Causality Assignment Procedure for Inversion (SCAPI) (Ngwompo and Gawthrop, 1999), which

describes the design process of the bicausal Bond graph. According to the SCAPI method, we follow the steps mentioned below:

- firstly, we define the minimal number of causal paths or the shortest causal path between the system input and output (Fig.3.4.6);
- then, we replace each input and output element with the SS elements as in Fig.3.4.6. The SS elements contain: the effort sources, S_e, and the flow sources, S_f, as inputs to the system, and the effort detectors, D_e, and the flow detectors, D_f, representing the outputs of the system. The sources elements have specific assignment as in Fig.3.4.4, which is the opposite of the case of the causal Bond graph depicted in the previous chapter in Fig.2.3.8;
- finally, the differential causality is determined for the storing elements (C, I) and the arbitrary causality for the resistors (R) (Fig.3.4.7 and Fig.3.4.8 respectively). As previously mentioned in section 2.3.1, according to differential causality, the input's time derivative is equal to the ratio of the output as depicted in Fig.2.3.5b. Therefore, the capacitors obey to $\frac{de}{dt} = \frac{f}{C}$ and the inductors obey to $\frac{df}{dt} = \frac{e}{I}$. The resistors follow the same relations as in the causal Bond graphs: $e = f \cdot R$ and $f = \frac{e}{R}$.

Note that for the junctions 0 and 1, the same rules are applied as in the case of the causal Bond graph (see also section 2.3.1).

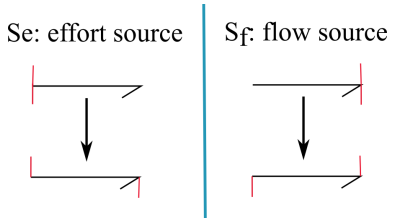

Figure 3.4.4: Bicausal assignment of the effort and flow sources.

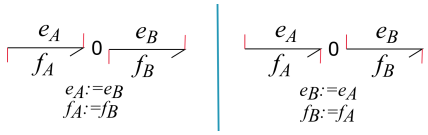

Figure 3.4.5: Relation among the $e - f$ pairs in the bicausal Bond graphs.

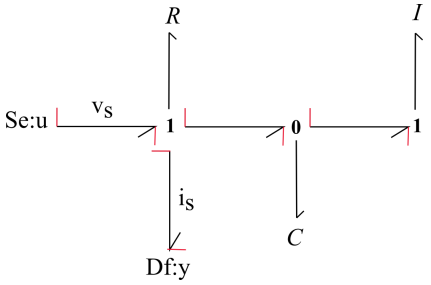

Figure 3.4.6: Definition of the shortest causal path between the system input and output.

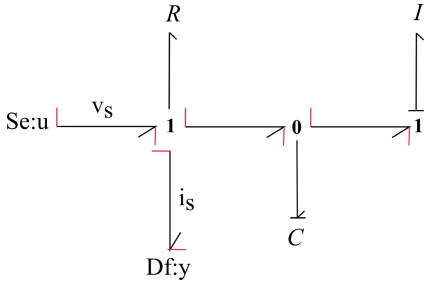

Figure 3.4.7: Assignment of the storing $(C,\ I)$ and dissipative (R) elements.

The aforementioned method, SCAPI, is considered below in order to replace the causal Bond graph of the Rlc circuit in Fig.3.4.3 with the bicausal Bond graph shown in Fig.3.4.8. From the bicausal Bond graph,

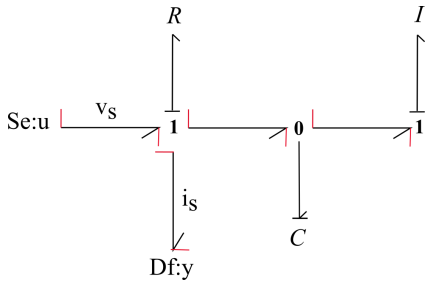

Figure 3.4.8: Final bicausal Bond graph of the electrical RLC circuit of Fig.3.4.2.

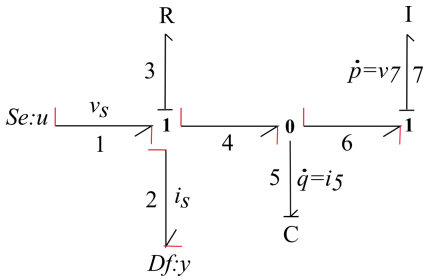

Figure 3.4.9: Corresponding bicausal Bond graph with numbers on the arrows and the differential causalities.

we conclude to the succeeding relations from the 0 and 1 junctions (Fig.3.4.9)[2]:

$$first\ 1\ junction\ from\ the\ left: \quad e_1 - e_3 - e_4 = 0, \tag{3.4.1a}$$
$$f_2 = f_3 = f_4; \tag{3.4.1b}$$
$$0\ junction: \quad e_4 = e_5 = e_6, \tag{3.4.1c}$$
$$f_4 - f_5 - f_6 = 0; \tag{3.4.1d}$$
$$second\ 1phantom..junction: \quad e_6 = e_7, \tag{3.4.1e}$$
$$f_6 = f_7. \tag{3.4.1f}$$

In the following, the differential causality of the storing and dissipative elements is defined:

$$f_5 = C\frac{de_5}{dt} = \dot{q}, \tag{3.4.2}$$
$$e_7 = I\frac{df_7}{dt} = \dot{p}, \tag{3.4.3}$$
$$e_R = f_R R = (f_5 + f_6)R = (\dot{q} + \frac{p}{I})R. \tag{3.4.4}$$

where the integral causality can be taken also into account:

$$e_5 = \frac{1}{C}\int^t f_5 dt = \frac{q}{C}, \tag{3.4.5}$$
$$f_7 = \frac{1}{I}\int^t e_7 dt = \frac{p}{I}. \tag{3.4.6}$$

From Fig.3.4.9, considering the aforementioned relations of the junctions (3.4.2) and (3.4.5), we can derive the states and inputs which represent the inverse dynamics of the RLC circuit (Fig.3.4.2):

$$p = If_7 = I(\dot{q} + \frac{p}{I} - \dot{q}) = p, \tag{3.4.7a}$$
$$q = Ce_5 = C\dot{p}, \tag{3.4.7b}$$
$$u = v_s = (\dot{q} + \frac{p}{I})R + \dot{p}. \tag{3.4.7c}$$

The state vector of the system is $x = \begin{bmatrix} p & q \end{bmatrix}^\top \in \mathbb{R}^{2\times 1}$ and the input vector is $u = v_s \in \mathbb{R}^{1\times 1}$. Regarding the relations above, (3.4.7a)-(3.4.7c), through the bicausal Bond graph, a physical representation is obtained similar to the flat representation of the system after considering the flat outputs in function of the states (Definition 3.2.1). According to Fliess et al. (1995), the number of flat outputs must be equal to the number of control inputs. The RLC system (3.4.7a-3.4.7c) has one control input, $u = v_s$. Therefore, one flat output is necessary. From the bicausal Bond graph (Fig. 3.4.9), we retrieve the state p and obtain (3.4.7a), which shows that p cannot be written in function of the other variables of the RLC circuit, the state q and the input v_s. Consequently, a straightforward choice is state p as a possible flat output for the system, $z = p$.

[2]Keep in mind that the effort e is the voltage and the flow f is the current in the case of electrical circuits, as already mentioned in section 2.3.1.

Therefore, the equations (3.4.7a)-(3.4.7c) are rewritten in function of the flat output as follows:

$$x = \begin{bmatrix} p \\ q \end{bmatrix} = \begin{bmatrix} z \\ C\dot{z} \end{bmatrix}, \tag{3.4.8a}$$

$$u = v_s = (C\ddot{z} + \frac{z}{I})R + \dot{z}, \tag{3.4.8b}$$

for which the compact flat representation (Definition 3.2.1) of the RLC circuit from (3.4.2) and (3.4.8) is:

$$p = \Phi_{41}(z), \tag{3.4.9a}$$

$$q = \Phi_{42}(z, \dot{z}), \tag{3.4.9b}$$

$$v_s = \Phi_{43}(z, \dot{z}, \ddot{z}). \tag{3.4.9c}$$

Therefore, we concluded to a flat representation of the system through the bicausal Bond graph. Consequently, the bicausal Bond graph seems to be a suitable tool to analyze differential flatness, since both methods deal with the inverse dynamics of the system.

3.4.2 Flat representation analysis of the ES system from bicausality

Hereinafter, through the ES electrical circuit, a method to derive the possible sets of flat outputs of an electrical circuit will be described. The electrical circuit of Fig.3.3.1 is divided into two circuits: i) the KiBaM circuit with the resistance R_{1b}; ii) the Split-Pi converter with the resistance R_{1sc}. The possible flat outputs of their PH representations will be generated through their bicausal Bond graphs comparing with the results of the previous sections. The idea, here, is based on the following proposition:

Remark 3.4.1. (Link between bicausal Bond graphs and Dirac structures): If effort and flow variables of the bicausal Bond graph are related with equations as in (2.5.5) of Definition 2.5.1, then the system is written in kernel representation of a DS. Hence, the overall dynamics represents a PH system. As a consequence, in the case of electrical circuits, the flat representation of their PH models can be analyzed through their bicausal Bond graphs as already presented for the RLC circuit in section 3.4.1.

Indeed taking into account the bicausal Bond graphs (Fig. 3.4.11 and Fig. 3.4.13) of the ES system (see the electrical circuit in Fig. 3.3.1), which includes the KiBaM battery and the Split-Pi converter, the relations among the efforts and flows are derived from the 0 and 1 junctions as in (3.4.1a)-(3.4.1f). Next, their kernel representations are formulated to prove that they compose a DS. Therefore, according to Definition 2.5.1, the relation $Ee + Ff = 0$ must exist, which contains the storing elements, the dissipative elements and the external ports of the system:

$$\begin{aligned} E\begin{bmatrix} e_{I_1} & e_{I_2} & \dots & e_{e_{n_I}} & e_{C_1} & e_{C_2} & \dots & e_{C_{n_C}} & e_{R_1} & e_{R_2} & \dots & e_{R_{n_R}} & u \end{bmatrix}^\top + \\ + F\begin{bmatrix} f_{I_1} & f_{I_2} & \dots & f_{I_{n_I}} & f_{C_1} & f_{C_2} & \dots & f_{C_{n_C}} & f_{R_1} & f_{R_2} & \dots & f_{R_{n_R}} & y \end{bmatrix}^\top, \end{aligned} \tag{3.4.10}$$

where n_C is the number of capacitors C, n_I is the number of inductors I (with the capacitors and inductors being the storing elements) and n_R is the number of the dissipative elements. The variable u is the input and the variable y is the output of the system. Therefore, if the kernel representation exists, it composes a DS, hence a PH system, according to Definition 2.3.3, where a PH system is expressed as noted below:

$$(-\dot{x}, \nabla H(x), f_R, e_R, f_E, e_E) \in \mathcal{D}. \tag{3.4.11}$$

$\mathcal{D}$ is the subspace $\mathcal{D} \subset \mathcal{F} \times \mathcal{E}$ of the DS regarding Definition 2.3.2. Note that the capacitors are regarded as (f_C, e_C) pairs, for which $f_C = -\dot{x}$ and $e_C = \nabla H(x)$, and the inductors as (f_I, e_I) pairs, where $e_I = -\dot{x}$ and $f_I = \nabla H(x)$. The Hamiltonian, H, is considered in its linear form, i.e. the energy storage of the electrical circuit equals to $H(x) = \frac{1}{2}\frac{q^2}{C} + \frac{1}{2}\frac{p^2}{I}$ (see also section 2.4.1). Therefore, the flat representation of the corresponding PH system can be analyzed as in section 3.4.1 for the RLC circuit.

3.4.2.1 KiBaM battery

Firstly, we concentrate on the battery (see Fig.3.4.10) of which the PH state-space representation, presented also in section 2.4.1.2 in PH form, is:

$$\dot{q}_{1b} = -\left(\frac{1}{R_{1b}} + \frac{1}{R_{2b}}\right)\frac{q_{1b}}{C_{1b}} + \frac{1}{R_{2b}}\frac{q_{2b}}{C_{2b}} + \frac{1}{R_{1b}}v_s, \tag{3.4.12a}$$

$$\dot{q}_{2b} = \frac{1}{R_{2b}}\frac{q_{1b}}{C_{1b}} - \frac{1}{R_{2b}}\frac{q_{2b}}{C_{2b}}. \tag{3.4.12b}$$

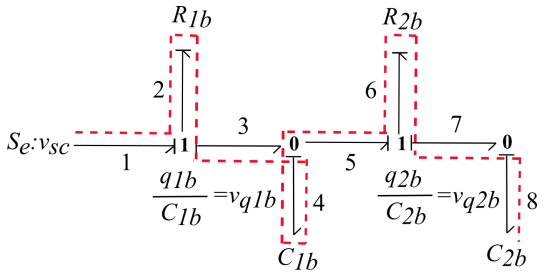

Figure 3.4.10: Causal Bond graph of the KiBaM battery.

where the state vector is $x_b = \begin{bmatrix} q_{1b} & q_{2b} \end{bmatrix}^\top \in \mathbb{R}^{2\times 1}$ and the input vector $u_b = v_{sc} \in \mathbb{R}^{1\times 1}$, with v_{sc} the voltage coming from the Split-Pi converter. According to flatness theory, since we have one input, we have to find one flat output. Developing the inverse dynamics of the battery's system through its bicausal Bond graph, we will deduce the possible flat outputs of the battery.

Fig.3.4.11 presents the bicausal Bond graph of the battery, according to the SCAPI method previously described. The graph is composed by two storing elements, the capacitors C_{1b} and C_{2b} with their differential causalities, one effort source, S_e, which is the input, and one flow detector, D_f, which is the output. Therefore, the state and input relations of the inverse system are written below:

$$q_{1b} = C_{1b} f_5 = \dot{q}_{2b} R_{2b} C_{1b} + \frac{C_{1b}}{C_{2b}} q_{2b}, \tag{3.4.13a}$$

$$q_{2b} = C_{2b} f_9 = v_s C_{2b} - \dot{q}_{1b} R_{1b} C_{2b} - \dot{q}_{2b} R_{1b} C_{2b} - \dot{q}_{2b} R_{2b} C_{2b}, \tag{3.4.13b}$$

$$v_s = \dot{q}_{1b} R_{1b} + \dot{q}_{2b} R_{1b} + \dot{q}_{2b} R_{2b} + \frac{q_{2b}}{C_{2b}}. \tag{3.4.13c}$$

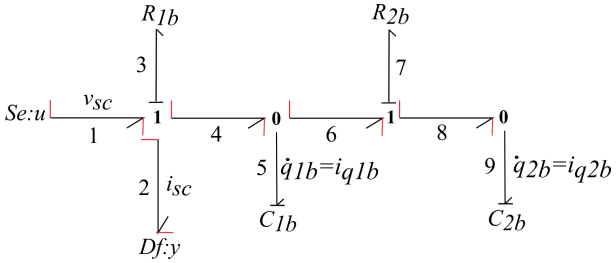

Figure 3.4.11: Bicausal bond graph of the KiBaM battery.

As a next step, we confirm if the system obtained by the bicausal Bond graph is a DS, hence a PH system. To demonstrate this, the kernel representation of the system is described which, according to Definition 2.5.1 ($Ee + Ff = 0$), if present (verifying the conditions $EF^\top + FE^\top = 0$ and $rank(F + E) = dimF$), then the system composes a DS. Therefore, the kernel representation of the bicausal Bond graph in Fig.3.4.11 is presented below:

$$\underbrace{\begin{bmatrix} 1 & -1 & 0 & 1 & 0 \\ -1 & 0 & 1 & 0 & 1 \\ 0 & 0 & 0 & 0 & 0 \\ 0 & 0 & 0 & 0 & 0 \\ 0 & 0 & 0 & 0 & 0 \end{bmatrix}}_{E} \underbrace{\begin{bmatrix} v_{q_{1b}} \\ v_{q_{2b}} \\ v_{R_{1b}} \\ v_{R_{2b}} \\ v_{sc} \end{bmatrix}}_{e} + \underbrace{\begin{bmatrix} 0 & 0 & 0 & 0 & 0 \\ 0 & 0 & 0 & 0 & 0 \\ 1 & 1 & 0 & 0 & 1 \\ 0 & 0 & 1 & 0 & -1 \\ 0 & 1 & 0 & 1 & 0 \end{bmatrix}}_{F} \underbrace{\begin{bmatrix} i_{q_{1b}} \\ i_{q_{2b}} \\ i_{R_{1b}} \\ i_{R_{2b}} \\ i_s \end{bmatrix}}_{f} = \begin{bmatrix} 0 \\ 0 \\ 0 \\ 0 \\ 0 \end{bmatrix}, \tag{3.4.14}$$

Therefore, the bicausal Bond graph of the battery is also a PH system. By isolating the derivatives of the state on the left side of the equations in (3.4.13a)-(3.4.13c), we result in the primary PH state-space representation as in (3.4.12a)-(3.4.12a). The equation (3.4.14) gives one combination among the efforts and flows from the bicausal Bond graph. However, more combinations exist derived by the 0 and 1 junctions.

Considering Definition 2.3.3, the capacitors are regarded as (f_C, e_C), for which $f_C = -\dot{x}$ and $e_C = \nabla H(x)$, and the Hamiltonian, H, is considered in the linear case, i.e. the energy storage of the electrical circuit, equal

to $H(x) = \frac{1}{2}\frac{q^2}{C} + \frac{1}{2}\frac{p^2}{I}$. Consequently, all the possible relations among the efforts and flows, derived from the 0 and 1 junctions (Fig.3.4.11), are presented below:

$$\begin{bmatrix} q_{1b} \\ q_{1b} \\ q_{2b} \\ q_{2b} \\ v_{sc} \\ v_{sc} \end{bmatrix} = \begin{bmatrix} 0 & 0 & \frac{C_{1b}}{C_{2b}} & R_{2b}C_{1b} & 0 \\ 0 & -R_{1b}C_{1b} & 0 & -R_{1b}C_{1b} & C_{1b} \\ 0 & 0 & 1 & 0 & 0 \\ 0 & 0 & 0 & 0 & 0 \\ 0 & R_{1b} & \frac{1}{C_{2b}} & R_{1b}+R_{2b} & 0 \\ 0 & 0 & 0 & 0 & 0 \end{bmatrix} \begin{bmatrix} q_{1b} \\ \dot{q}_{1b} \\ q_{2b} \\ \dot{q}_{2b} \\ v_{sc} \end{bmatrix}. \tag{3.4.15}$$

From the latter matrix representation, in the left part the states and the inputs are illustrated, which, concerning flatness theory, can be written in function of the flat outputs and their derivatives. Since we have one control input, v_{sc}, we expect only one flat output (Levine, 2009). Taking into account Proof 3.2, where the flat output can be written in function of the states, we assume that the only possible flat output for the battery is $z = q_{2b}$ from (3.4.15). This conclusion comes from the fact that it is the only state not written in function of the inputs, the other states or their derivatives. In order to look at the result more carefully, we separate the matrices extracting the circuit parameters, C_{1b}, C_{2b}, and the dissipation, R_{1b}, R_{2b}, as follows:

$$\begin{bmatrix} q_{1b} \\ \frac{q_{1b}}{C_{1b}} \\ \frac{q_{2b}}{C_{2b}} \\ \frac{q_{2b}}{C_{2b}} \\ u_s \\ u_s \end{bmatrix} = \left(\underbrace{\begin{bmatrix} 0 & 0 & 1 & 0 & 0 \\ 0 & 0 & 0 & 0 & 1 \\ 0 & 0 & 1 & 0 & 0 \\ 0 & 0 & 1 & 0 & 0 \\ 0 & 0 & 1 & 0 & 0 \\ 0 & 0 & 0 & 0 & 1 \end{bmatrix}}_{V} + \underbrace{\begin{bmatrix} 0 & 0 & 0 & R_{2b} & 0 \\ 0 & -R_{1b} & 0 & -R_{1b} & 0 \\ 0 & 0 & 0 & 0 & 0 \\ 0 & 0 & 0 & 0 & 0 \\ 0 & R_{1b} & 0 & R_{1b}+R_{2b} & 0 \\ 0 & 0 & 0 & 0 & 0 \end{bmatrix}}_{W} \right) \begin{bmatrix} \frac{q_{1b}}{C_{1b}} \\ \dot{q}_{1b} \\ \frac{q_{2b}}{C_{2b}} \\ \dot{q}_{2b} \\ v_{sc} \end{bmatrix}. \tag{3.4.16}$$

Therefore, from matrix V we can derive the states and control inputs which are structurally required for the flat representation. The state q_{2b} is included, in function of which q_{1b} and v_{sc} can be derived (third column of matrix V). In W matrix, the dissipative elements are presented and are involved only with the derivatives of the states, which are not taken into consideration for the flat outputs selection. The flat representation of the battery is written below from (3.4.13a)-(3.4.13c):

$$x_b = \begin{bmatrix} q_{1b} \\ q_{2b} \end{bmatrix} = \begin{bmatrix} R_{2b}C_{1b}\dot{z} + \frac{C_{1b}}{C_{2b}}z \\ z \end{bmatrix}, \tag{3.4.17a}$$

$$u = v_{sc} = R_{2b}R_{1b}C_{1b}\ddot{z} + (R_{1b}\frac{C_{1b}}{C_{2b}} + R_{1b} + R_{2b})\dot{z} + \frac{1}{C_{2b}}z. \tag{3.4.17b}$$

The compact flat representation, as in Definition 3.2.1, of the KiBaM battery circuit deriving from (3.4.17a) and (3.4.17b) is:

$$q_{1b} = \Phi_{44}(z, \dot{z}), \tag{3.4.18a}$$

$$q_{2b} = \Phi_{45}(z), \tag{3.4.18b}$$

$$v_{sc} = \Phi_{46}(z, \dot{z}, \ddot{z}). \tag{3.4.18c}$$

This approach can be extended for the nonlinear cases of constitutive equations.

3.4.2.2 Split-Pi converter

Afterwards, following the same steps as for the KiBaM battery, the flat representation of the Split-Pi converter will be analyzed through its bicausal Bond graph. At first, its PH state-space representation is presented

(see Fig.3.4.10) below, introduced also before:

$$\dot{p}_{1sc} = \frac{q_{1sc}}{C_{1sc}} - \frac{q_{2sc}}{C_{2sc}}(1 - d_{1sc}), \tag{3.4.19a}$$

$$\dot{p}_{2sc} = \frac{q_{2sc}}{C_{2sc}}(1 - d_{2sc}) - \frac{q_{3sc}}{C_{3sc}}, \tag{3.4.19b}$$

$$\dot{q}_{1sc} = \frac{v_s}{R_{1sc}} - \frac{q_{1sc}}{C_{1sc}R_{1sc}} - \frac{p_{1sc}}{I_{1sc}}, \tag{3.4.19c}$$

$$\dot{q}_{2sc} = \frac{p_{1sc}}{I_{1sc}}(1 - d_{1sc}) - \frac{p_{2sc}}{I_{2sc}}(1 - d_{2sc}), \tag{3.4.19d}$$

$$\dot{q}_{3sc} = \frac{p_{2sc}}{I_{2sc}} - i_R. \tag{3.4.19e}$$

where the state vector is $x_{sc} = \begin{bmatrix} p_{1sc} & p_{2sc} & q_{1sc} & q_{2sc} & q_{3sc} \end{bmatrix}^\top \in \mathbb{R}^{5\times 1}$ and the input vector $u_{sc} = \begin{bmatrix} v_s & i_b \end{bmatrix}^\top \in \mathbb{R}^{2\times 1}$, where v_s is the voltage coming from the source and i_b is the current of the resistor R. Furthermore, the converter's duty cycles, d_{1sc}, d_{2sc} are considered also as control inputs to the system (see also Fig.3.3.1). Since we have four control inputs in total, we have to find four flat outputs. Developing the inverse dynamics of the system through its bicausal Bond graph, the four possible states considered as flat outputs will be deduced.

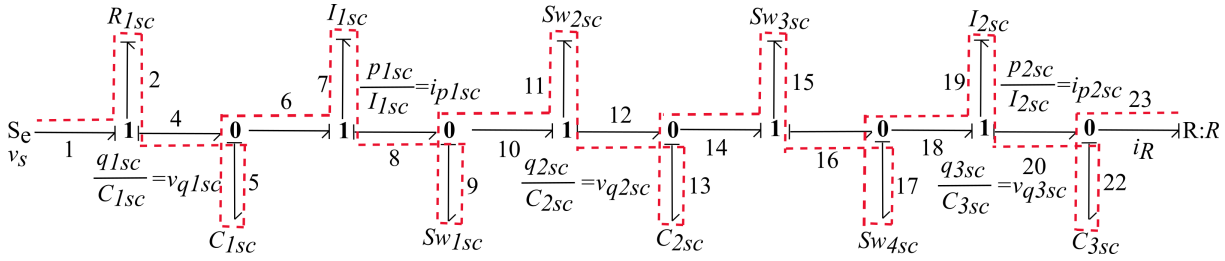

Figure 3.4.12: Causal Bond graph of the Split-Pi converter.

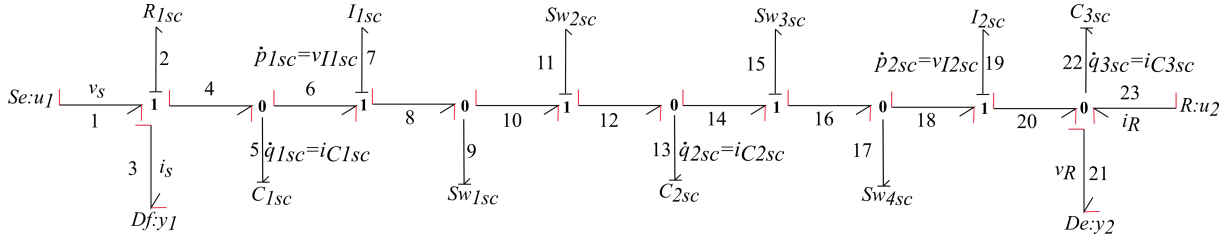

Figure 3.4.13: Bicausal Bond graph of the Split-Pi converter.

Fig.3.4.13 presents the bicausal Bond graph of the Split-Pi converter, composed by five storing elements, the capacitors C_{1sc}, C_{2sc}, C_{3sc} and the inductors I_{1sc}, I_{2sc} with their differential causalities, one effort source, S_e, and the resistor R which contain the inputs, one flow detector, D_f, which is the first output and one effort detector, D_e, which is the second output of the system. Furthermore, the duty cycles, d_{1sc} and d_{2sc}, correspond to the activity of the switches, Sw_{1sc}, Sw_{2sc}, Sw_{3sc}, Sw_{4sc}. Therefore, the states of the inverse system are derived below:

$$p_{1sc} = I_{1sc}\left(\frac{u_s}{R_{1sc}} - \frac{q_{1sc}}{C_{1sc}R_{1sc}} - \dot{q}_{1sc}\right), \tag{3.4.20a}$$

$$p_{2sc} = I_{2sc}\left[\dot{q}_{3sc} + i_R\right], \tag{3.4.20b}$$

$$q_{1sc} = C_{1sc}\left[\dot{p}_{1sc} + \frac{q_{2sc}}{C_{2sc}}(1 - d_{1sc})\right], \tag{3.4.20c}$$

$$q_{2sc} = q_{2sc}, \tag{3.4.20d}$$

$$q_{3sc} = C_{3sc}\left[\frac{q_{2sc}}{C_{2sc}}(1 - d_{2sc}) - \dot{p}_{2sc}\right]. \tag{3.4.20e}$$

Moreover, the control inputs are deduced also in function of the states and their derivatives from the bicausal Bond graph as follows:

$$v_s = \left(\frac{p_{1sc}}{I_{1sc}} + \frac{q_{1sc}}{C_{1sc}R_{1sc}} + \dot{q}_{1sc}\right) R_{1sc}, \tag{3.4.21a}$$

$$i_R = \frac{q_{3sc}}{C_{3sc}R}, \tag{3.4.21b}$$

$$d_{1sc} = \frac{C_{2sc}}{q_{2sc}}\left(\dot{p}_{1sc} - \frac{q_{1sc}}{C_{1sc}} + \frac{q_{2sc}}{C_{2sc}}\right), \tag{3.4.21c}$$

$$d_{2sc} = \frac{C_{2sc}}{q_{2sc}}\left(-\dot{p}_{2sc} + \frac{q_{2sc}}{C_{2sc}} - \frac{q_{3sc}}{C_{3sc}}\right). \tag{3.4.21d}$$

Next, the kernel representation of the bicausal Bond graph of the Split-Pi converter is presented (Definition 2.5.1), which proves that it composes a DS:

$$\underbrace{\begin{bmatrix} -1 & 0 & -1 & 1-d_{1sc} & 0 & 0 & 0 & 0 \\ 0 & 1 & 0 & 1-d_{2sc} & -1 & 0 & 0 & 0 \\ 0 & 0 & 0 & 0 & 0 & 0 & 0 & 0 \\ 0 & 0 & 0 & 0 & 0 & 0 & 0 & 0 \\ 0 & 0 & 0 & 0 & 0 & 0 & 0 & 0 \\ 0 & 0 & -1 & 0 & 0 & -1 & 0 & 1 \\ 0 & 0 & 0 & 0 & -1 & 0 & -1 & 0 \\ 0 & 0 & 0 & 0 & 0 & 0 & 0 & 0 \end{bmatrix}}_{E} \underbrace{\begin{bmatrix} e_{p_{1sc}} \\ e_{p_{2sc}} \\ e_{q_{1sc}} \\ e_{q_{2sc}} \\ e_{q_{3sc}} \\ e_{R_{1sc}} \\ e_R \\ v_s \end{bmatrix}}_{e} + \tag{3.4.22a}$$

$$+ \underbrace{\begin{bmatrix} 0 & 0 & 0 & 0 & 0 & 0 & 0 & 0 \\ 0 & 0 & 0 & 0 & 0 & 0 & 0 & 0 \\ -1 & 0 & 1 & 0 & 0 & 0 & 0 & 1 \\ 1-d_{1sc} & -(1-d_{2sc}) & 0 & 1 & 0 & 0 & 0 & 0 \\ 0 & -1 & 0 & 0 & -1 & 0 & 1 & 0 \\ 0 & 0 & 0 & 0 & 0 & 0 & 0 & 0 \\ 0 & 0 & 0 & 0 & 0 & 0 & 0 & 0 \\ 0 & 0 & 0 & 0 & 0 & 1 & 0 & 1 \end{bmatrix}}_{F} \underbrace{\begin{bmatrix} f_{p_{1sc}} \\ f_{p_{2sc}} \\ f_{q_{1sc}} \\ f_{q_{2sc}} \\ f_{q_{3sc}} \\ f_{R_{1sc}} \\ f_R \\ i_s \end{bmatrix}}_{f} = \begin{bmatrix} 0 \\ 0 \\ 0 \\ 0 \\ 0 \\ 0 \\ 0 \\ 0 \end{bmatrix},$$

Consequently, the bicausal Bond graph of the Split-Pi converter is also a PH system. By placing the state derivatives on the left side of the equations in (3.4.20a)-(3.4.20e) (considering also the control inputs in (3.4.21a)-(3.4.21d)), we conclude to the primary PH state-space representation as in (3.4.19a)-(3.4.19e).

Then, we consider likewise Definition 2.3.3, with the storing elements regarded as (f_C, e_C) and (f_I, e_I), where $f_C = -\dot{x}$ and $e_C = \nabla H(x)$ and $e_I = -\dot{x}$ and $f_I = \nabla H(x)$ respectively, and the Hamiltonian in the linear case ($H(x) = \frac{1}{2}\frac{q^2}{C} + \frac{1}{2}\frac{p^2}{I}$). Subsequently, all the relations among the flow and the effort variables from

the 0 and 1 junctions (Fig.3.4.13) are introduced below:

$$\begin{bmatrix} p_{1sc} & p_{1sc} & p_{2sc} & p_{2sc} & q_{1sc} & q_{1sc} & q_{2sc} & q_{3sc} & q_{3sc} & q_{3sc} & v_s & i_R \end{bmatrix}^\top =$$

$$= \begin{bmatrix} 1 & 0 & 0 & 0 & 0 & 0 & 0 & 0 & 0 & 0 & 0 & 0 & 0 \\ 0 & 0 & 0 & 0 & -\frac{I_{1sc}}{C_{1sc}R_{1sc}} & -I_{1sc} & 0 & 0 & 0 & \frac{I_{1sc}}{R_{1sc}} & 0 & 0 & 0 \\ 0 & 0 & 1 & 0 & 0 & 0 & 0 & 0 & 0 & 0 & 0 & 0 & 0 \\ 0 & 0 & 0 & 0 & 0 & 0 & 0 & 0 & I_{2sc} & 0 & I_{2sc} & 0 & 0 \\ 0 & 0 & 0 & 0 & 1 & 0 & 0 & 0 & 0 & 0 & 0 & 0 & 0 \\ 0 & C_{1sc} & 0 & 0 & 0 & 0 & \frac{C_{1sc}}{C_{2sc}} & 0 & 0 & 0 & 0 & -C_{1sc} & 0 \\ 0 & 0 & 0 & 0 & 0 & 0 & 1 & 0 & 0 & 0 & 0 & 0 & 0 \\ 0 & 0 & 0 & 0 & 0 & 0 & 0 & 1 & 0 & 0 & 0 & 0 & 0 \\ 0 & 0 & 0 & -C_{3sc} & 0 & 0 & \frac{C_{3sc}}{C_{2sc}} & 0 & 0 & 0 & 0 & 0 & -C_{3sc} \\ 0 & 0 & 0 & 0 & 0 & 0 & 0 & 0 & 0 & 0 & C_{3sc}R & 0 & 0 \\ \frac{R_{1sc}}{I_{1sc}} & 0 & 0 & 0 & \frac{1}{C_{1sc}} & R_{1sc} & 0 & 0 & 0 & 0 & 0 & 0 & 0 \\ 0 & 0 & 0 & 0 & 0 & 0 & 0 & \frac{1}{C_{1sc}R} & 0 & 0 & 0 & 0 & 0 \end{bmatrix} \cdot$$

$$\cdot \begin{bmatrix} p_{1sc} & \dot{p}_{1sc} & p_{2sc} & \dot{p}_{2sc} & q_{1sc} & \dot{q}_{1sc} & q_{2sc} & q_{3sc} & \dot{q}_{3sc} & v_s & i_R & d_{1sc} & d_{2sc} \end{bmatrix}^\top . \tag{3.4.23}$$

At this point, four additional relations are obtained for the states p_{1sc}, p_{2sc} and q_{2sc} which include the duty cycles of the converter, d_{1sc} and d_{2sc}:

$$\frac{p_{1sc}}{I_{1sc}} d_{1sc} = \frac{p_{1sc}}{I_{1sc}} - \dot{q}_{2sc} - \frac{p_{2sc}}{I_{2sc}}(1 - d_{2sc}), \tag{3.4.24a}$$

$$\frac{p_{2sc}}{I_{2sc}} d_{2sc} = \frac{p_{2sc}}{I_{2sc}} - \dot{q}_{2sc} - \frac{p_{1sc}}{I_{1sc}}(1 - d_{1sc}), \tag{3.4.24b}$$

$$\frac{q_{2sc}}{C_{2sc}} d_{1sc} = \frac{q_{2sc}}{C_{2sc}} - \frac{q_{1sc}}{C_{1sc}} + \dot{p}_{1sc}, \tag{3.4.24c}$$

$$\frac{q_{2sc}}{C_{2sc}} d_{2sc} = \frac{q_{2sc}}{C_{2sc}} - \frac{q_{3sc}}{C_{3sc}} - \dot{p}_{2sc}. \tag{3.4.24d}$$

These four equations will be considered in the analysis of the flat outputs under restrictions. This is because of the fact that during the operation of the converter the states p_{1sc}, p_{2sc}, q_{2sc} are different from 0. Contrariwise, the duty cycles, d_{1sc} and d_{2sc}, can be equal to 0. Therefore, the duty cycles cannot be placed in the denominator's position and cannot be included in the flat outputs selection.

Afterwards, the circuit's parameters and the dissipative elements are divided into two matrices as in (3.4.16), V and W and (3.4.23) becomes:

$$\begin{bmatrix} p_{1sc} & \frac{p_{1sc}}{I_{1sc}} & p_{2sc} & \frac{p_{2sc}}{I_{2sc}} & q_{1sc} & \frac{q_{1sc}}{C_{1sc}} & q_{2sc} & q_{3sc} & \frac{q_{3sc}}{C_{3sc}} & \frac{q_{3sc}}{C_{3sc}} & v_s & i_R \end{bmatrix}^\top =$$

$$= (V + W) \begin{bmatrix} p_{1sc} & \dot{p}_{1sc} & p_{2sc} & \dot{p}_{2sc} & q_{1sc} & \dot{q}_{1sc} & q_{2sc} & q_{3sc} & \dot{q}_{3sc} & v_s & i_R & d_{1sc} & d_{2sc} \end{bmatrix}^\top , \tag{3.4.25}$$

where

$$V = \begin{bmatrix} 1 & 0 & 0 & 0 & 0 & 0 & 0 & 0 & 0 & 0 & 0 & 0 & 0 \\ 0 & 0 & 0 & 0 & 0 & -1 & 0 & 0 & 0 & 0 & 0 & 0 & 0 \\ 0 & 0 & 1 & 0 & 0 & 0 & 0 & 0 & 0 & 0 & 0 & 0 & 0 \\ 0 & 0 & 0 & 0 & 0 & 0 & 0 & 0 & 1 & 0 & 1 & 0 & 0 \\ 0 & 0 & 0 & 0 & 1 & 0 & 0 & 0 & 0 & 0 & 0 & 0 & 0 \\ 0 & 1 & 0 & 0 & 0 & 0 & 1 & 0 & 0 & 0 & 0 & -1 & 0 \\ 0 & 0 & 0 & 0 & 0 & 0 & 1 & 0 & 0 & 0 & 0 & 0 & 0 \\ 0 & 0 & 0 & 0 & 0 & 0 & 0 & 1 & 0 & 0 & 0 & 0 & 0 \\ 0 & 0 & 0 & -1 & 0 & 0 & 1 & 0 & 0 & 0 & 0 & 0 & -1 \\ 0 & 0 & 0 & 0 & 0 & 0 & 0 & 0 & 0 & 0 & 0 & 0 & 0 \\ 0 & 0 & 0 & 0 & 1 & 0 & 0 & 0 & 0 & 0 & 0 & 0 & 0 \\ 0 & 0 & 0 & 0 & 0 & 0 & 0 & 0 & 0 & 0 & 0 & 0 & 0 \end{bmatrix} \tag{3.4.26}$$

and

$$W = \begin{bmatrix} 0 & 0 & 0 & 0 & 0 & 0 & 0 & 0 & 0 & 0 & 0 & 0 & 0 \\ 0 & 0 & 0 & 0 & -\frac{1}{R_{1sc}} & 0 & 0 & 0 & 0 & \frac{1}{R_{1sc}} & 0 & 0 & 0 \\ 0 & 0 & 0 & 0 & 0 & 0 & 0 & 0 & 0 & 0 & 0 & 0 & 0 \\ 0 & 0 & 0 & 0 & 0 & 0 & 0 & 0 & 0 & 0 & 0 & 0 & 0 \\ 0 & 0 & 0 & 0 & 0 & 0 & 0 & 0 & 0 & 0 & 0 & 0 & 0 \\ 0 & 0 & 0 & 0 & 0 & 0 & 0 & 0 & 0 & 0 & 0 & 0 & 0 \\ 0 & 0 & 0 & 0 & 0 & 0 & 0 & 0 & 0 & 0 & 0 & 0 & 0 \\ 0 & 0 & 0 & 0 & 0 & 0 & 0 & 0 & 0 & 0 & 0 & 0 & 0 \\ 0 & 0 & 0 & 0 & 0 & 0 & 0 & 0 & 0 & 0 & 0 & 0 & 0 \\ 0 & 0 & 0 & 0 & 0 & 0 & 0 & 0 & 0 & 0 & R & 0 & 0 \\ R_{1sc} & 0 & 0 & 0 & & R_{1sc} & 0 & 0 & 0 & 0 & 0 & 0 & 0 \\ 0 & 0 & 0 & 0 & 0 & 0 & 0 & \frac{1}{R} & 0 & 0 & 0 & 0 & 0 \end{bmatrix}. \tag{3.4.27}$$

From (3.4.23), we assume that the set of flat outputs for the Split-Pi converter system contains the states p_{1sc}, p_{2sc}, q_{1sc}, q_{2sc}, q_{3sc}. Concerning the state q_{2sc}, it must be regarded as one of the flat outputs (seventh row of matrix V). Since it cannot be expressed in function of the other states and inputs, it is necessary for the flat representation. Additionally, because of (3.4.24a)-(3.4.24d), it is indispensable to consider states p_{1sc}, p_{2sc}, q_{2sc} as part of the flat outputs since they are linked to the switching activity of the converter. Moreover, the d_{1sc} and d_{2sc} are given only from (3.4.24a)-3.4.24d and they cannot be taken into account as flat outputs for the system. The control inputs, v_s and i_R, similarly cannot be considered, since they are written in function of the states and their derivatives, but not all the states can be written in function of v_s and i_R (eleventh and twelfth column of matrices V and W).

Thereupon, referring to the noise that the derivatives of the states create in the results, we need to select the states appropriate from (3.4.25), (3.4.26), (3.4.27) and (3.4.23) (less derivatives create less deviations among the reference and the actual values), so that the less possible derivatives appear in the flat representation. If we look into (3.4.23), the state q_{1sc} is in function of more than one derivatives, while the state q_{3sc} can be replaced from an equation with no derivatives included. However, neither can be excluded and we conclude to the following possible flat outputs sets:

$$z_1 = \begin{bmatrix} p_{1sc} & p_{2sc} & q_{2sc} & q_{1sc} \end{bmatrix}^\top, \tag{3.4.28}$$

$$z_2 = \begin{bmatrix} p_{1sc} & p_{2sc} & q_{2sc} & q_{3sc} \end{bmatrix}^\top. \tag{3.4.29}$$

The flat representation of the Split-Pi converter is written below from (3.4.20a)-(3.4.20e), (3.4.21a)-(3.4.21d) and (3.4.24a)[3]:

- for the first flat output $z_1 = \begin{bmatrix} p_{1sc} & p_{2sc} & q_{2sc} & q_{1sc} \end{bmatrix}^\top$, the flat representation of the states and the inputs is introduced:

$$p_{1sc} = z_1, \tag{3.4.30a}$$

$$p_{2sc} = z_2, \tag{3.4.30b}$$

$$q_{1sc} = z_4, \tag{3.4.30c}$$

$$q_{2sc} = z_3, \tag{3.4.30d}$$

$$q_{3sc} = \frac{1}{\gamma}\left[\beta z_3\big(\frac{\dot{z}_3}{\mu z_2} + \frac{\eta\alpha}{\beta}\frac{z_1 z_4}{z_3} + \eta z_1 \dot{z}_1\big) - \dot{z}_2\right], \tag{3.4.30e}$$

$$d_{1sc} = 1 - \frac{\mu \dot{z}_3 z_2}{\eta^2 z_1^2}\left(\frac{\gamma}{\beta}\frac{q_{3sc}}{z_3} - \dot{z}_2\right), \tag{3.4.30f}$$

$$d_{2sc} = 1 - \frac{\dot{z}_3}{z_2}\mu - \eta z_1\left(\frac{\alpha}{\beta}\frac{z_4}{z_3} + \dot{z}_1\right), \tag{3.4.30g}$$

$$v_s = \frac{1}{\nu}\big(\eta z_1 + \nu\alpha z_4 + \dot{z}_4\big), \tag{3.4.30h}$$

$$i_R = \mu z_2 - \dot{q}_{3sc}. \tag{3.4.30i}$$

[3]The circuit's parameters and the values of the resistors are considered as in section 3.3.3: $1/C_{1sc} = \alpha$, $1/C_{2sc} = \beta$, $1/C_{3sc} = \gamma$, $1/I_{1sc} = \eta$, $1/I_{2sc} = \mu$, $1/R_{1sc} = \nu$, $1/R = \zeta$.

Below, the compact flat representation, as in Definition 3.2.1, of the states and inputs is written:

$$p_{1sc} = \Phi_{44}(z_1), \tag{3.4.31a}$$
$$p_{2sc} = \Phi_{45}(z_2), \tag{3.4.31b}$$
$$q_{1sc} = \Phi_{46}(z_1, \dot{z}_1, z_2, \dot{z}_2, z_3, \dot{z}_3, z_4), \tag{3.4.31c}$$
$$q_{2sc} = \Phi_{47}(z_3), \tag{3.4.31d}$$
$$q_{3sc} = \Phi_{48}(z_1, \dot{z}_1, z_2, \dot{z}_2, z_3, \dot{z}_3, z_4), \tag{3.4.31e}$$
$$d_{1sc} = \Phi_{49}(z_1, \dot{z}_1, z_2, \dot{z}_2, z_3, \dot{z}_3, z_4), \tag{3.4.31f}$$
$$d_{2sc} = \Phi_{50}(z_1, \dot{z}_1, z_2, z_3, \dot{z}_3, z_4), \tag{3.4.31g}$$
$$v_s = \Phi_{51}(z_1, z_4, \dot{z}_4), \tag{3.4.31h}$$
$$i_R = \Phi_{52}(z_1, \dot{z}_1, \ddot{z}_1, z_2, \dot{z}_2, \ddot{z}_2, z_3, \dot{z}_3, \ddot{z}_3, z_4, \dot{z}_4). \tag{3.4.31i}$$

- for the second flat output $z_2 = \begin{bmatrix} p_{1sc} & p_{2sc} & q_{2sc} & q_{3sc} \end{bmatrix}^\top$, the flat representation of the states and the inputs is written below:

$$p_{1sc} = z_1, \tag{3.4.32a}$$
$$p_{2sc} = z_2, \tag{3.4.32b}$$
$$q_{1sc} = \frac{1}{\alpha}(\dot{z}_1 + \beta z_3 \frac{\dot{z}_3 + \mu z_2 \frac{\dot{z}_2 + \gamma z_4}{\beta z_3}}{\eta z_1}), \tag{3.4.32c}$$
$$q_{2sc} = z_3, \tag{3.4.32d}$$
$$q_{3sc} = z_4, \tag{3.4.32e}$$
$$d_{1sc} = 1 - \frac{\dot{z}_3 + \mu z_2 \frac{\dot{z}_2 + \gamma z_4}{\beta z_3}}{\eta z_1}, \tag{3.4.32f}$$
$$d_{2sc} = 1 - \frac{\dot{z}_2 + \gamma z_4}{\beta z_3}, \tag{3.4.32g}$$
$$v_s = \frac{1}{\nu}\dot{q}_{1sc} + \alpha q_{1sc} + \frac{\eta}{\nu} z_1, \tag{3.4.32h}$$
$$i_R = \mu z_2 - \dot{z}_4. \tag{3.4.32i}$$

Below, the corresponding compact flat representation of the states and inputs is introduced:

$$p_{1sc} = \Phi_{53}(z_1), \tag{3.4.33a}$$
$$p_{2sc} = \Phi_{54}(z_2), \tag{3.4.33b}$$
$$q_{1sc} = \Phi_{55}(z_1, \dot{z}_1, z_2, \dot{z}_2, z_3, \dot{z}_3, z_4), \tag{3.4.33c}$$
$$q_{2sc} = \Phi_{56}(z_3), \tag{3.4.33d}$$
$$q_{3sc} = \Phi_{57}(z_4), \tag{3.4.33e}$$
$$d_{1sc} = \Phi_{58}(z_1, z_2, \dot{z}_2, z_3, \dot{z}_3, z_4), \tag{3.4.33f}$$
$$d_{2sc} = \Phi_{59}(\dot{z}_2, z_3, z_4), \tag{3.4.33g}$$
$$v_s = \Phi_{60}(z_1, \dot{z}_1, \ddot{z}_1, z_2, \dot{z}_2, \ddot{z}_2, z_3, \dot{z}_3, \ddot{z}_3, z_4, \dot{z}_4), \tag{3.4.33h}$$
$$i_R = \Phi_{61}(z_2, \dot{z}_4). \tag{3.4.33i}$$

For the second flat output set, the same representation was obtained by the bicausal Bond graph as in (3.3.42a)-(3.3.42i).

In Fig.3.4.15 and Fig.3.4.14, the control inputs were written in function of the two sets of flat outputs (3.4.28-3.4.29). Developing the Split-Pi model in Matlab/Simulink both in PH form and in flat representation, the simulation results are obtained respectively. The same reference values are considered as before in section 3.3.39a, $v_s = 400\ V$, $d_{1sc} = 0.6$, $d_{2sc} = 0.4$ and i_R as in Fig.3.3.6. Analyzing the two figures, Fig.3.4.15 and Fig.3.4.14, we observe that regarding (3.4.28) we have more convergent to the reference value and less noise-affected results for v_s. Contrariwise, i_b signal contains more oscillations. In the duty cycles, though, slight disturbances appear for both cases. In general, both sets of flat outputs can be considered for the flat

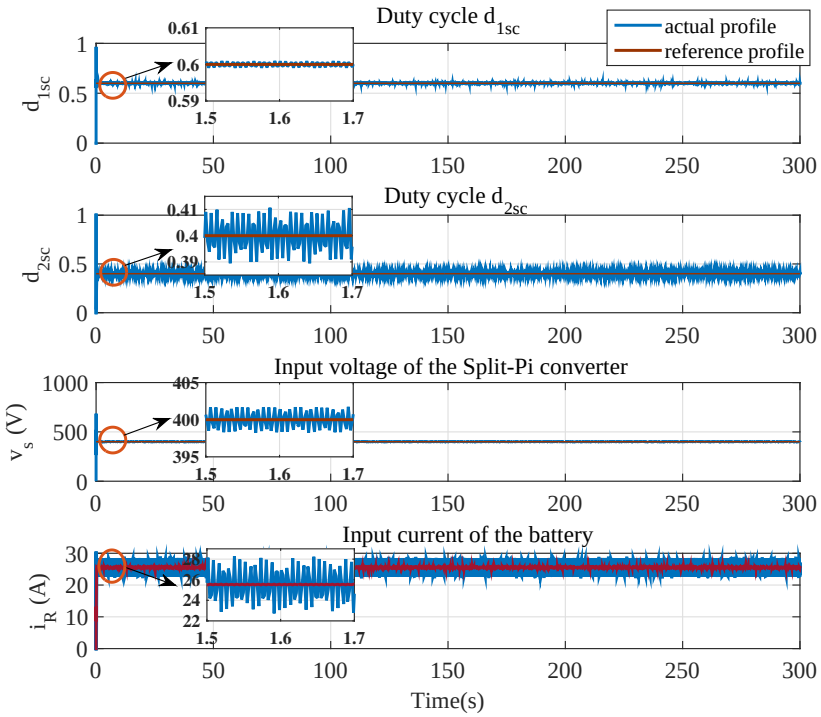

Figure 3.4.14: Control inputs in function of the first flat output set in (3.4.28).

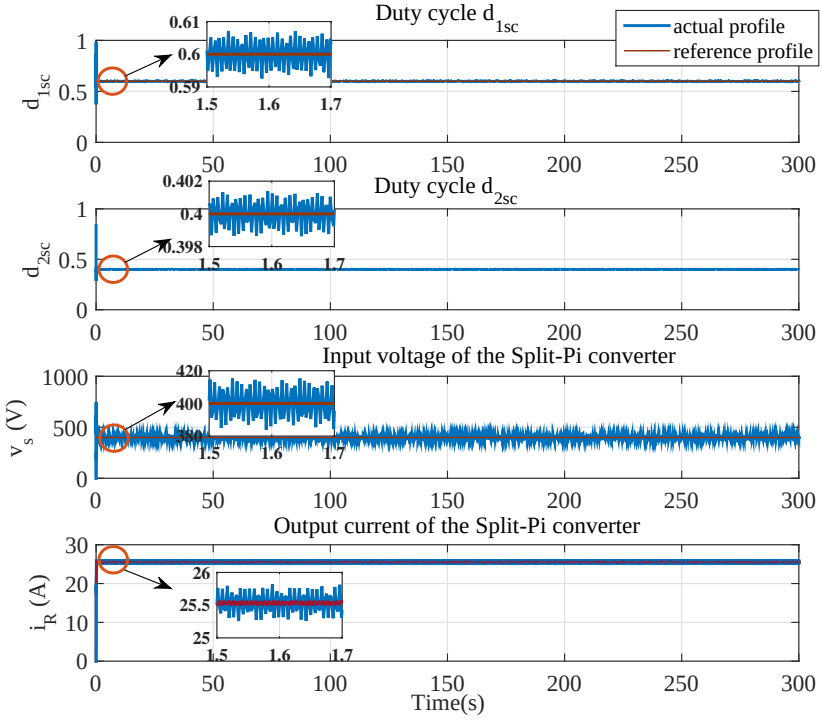

Figure 3.4.15: Control inputs in function of the second flat output set in (3.4.29).

representation of the Split-Pi converter. Although, in DC microgrids, the voltage regulation of the central transmission network is one of the principal factors to investigate. Here, the input voltage, v_s of the Split-Pi

converter is considered in the optimization problem chapter 4, where the flat representation is combined with the B-spline parametrization, strongly dependent on the number of derivatives included. Consequently, to simplify the calculations at this case (see also (3.4.21a)), the first set of flat outputs (3.4.28) would be the appropriate choice.

3.5 Conclusion

In this chapter, the differential flatness method was introduced and implemented for PH systems. The flat representation was investigated for the various components (ES, PV, loads) of the reduced DC microgrid presented in PH form in chapter 2. The flat outputs were, primarily, generated through an algorithm proposed in (Franke and Robenack, 2013) which provides the flat representation of the tangent system. However, since multiple sets of flat outputs can exist for each physical system, to compare and be able to decide what is the best choice, another flat output was found according to Proof 3.2, where the flat outputs can be written in function of the states of the system. The sets of flat outputs were validated through simulations, where the noise appeared in the flat system, created by the numerical differentiation, affects the signals response. The conclusion was that the more derivatives exist in the flat representation of the states and control inputs, the more noise-affected the results are.

Afterwards, the concept of bicausality in the Bond graphs was described which considers the inverse dynamics of physical systems. Through several examples, it was shown that bicausality is an appropriate tool to study flat representation. This was further extended in PH systems proving through the kernel representation that the bicausal Bond graphs compose a Dirac structure. Afterwards taking into account all the possible relations among the pairs of efforts and flows, a primary procedure was described which generated in a straightforward way the possible flat outputs of the illustrated examples.

In the succeeding chapter, the flat representation of the system will be employed in the energy management problem considered for the DC microgrid and will be combined with B-spline parametrization for continuous-time constraint validation.

Chapter 4

Multilevel supervision of a DC microgrid

4.1 Introduction

In the previous chapters, the proposed DC microgrid system was built stepwise, describing its detailed dynamical model using PH modeling. Next, through differential flatness and bicausality properties, the inverse dynamics of the system components (PV, ES, loads) were provided. In this chapter, the global and local supervision of the system will be investigated. To select a suitable control approach, various issues need to be taken into consideration, as for example the multiple timescales or the islanding and grid-connecting modes. As already mentioned in chapter 1, a variety of control approaches was developed according to the different requirements appearing in the energy management problem.

In general, the energy management problem of a microgrid is considered as a constrained optimization-based control problem not straightforward to solve. Considering that fast (converters) and slow (DERs) dynamics components which are composing the system, a control system in many levels needs to be implemented. The higher level with longer planning intervals and global supervision tasks will account for the lower level with smaller time intervals and local supervision. The most suitable control architecture to deal with these problems is, consequently, the hierarchical control. Its design framework is organized as a 'tree', as already introduced in chapter 1 in Fig. 1.1.1, from the higher level up to the lower level. In the literature, various control strategies were proposed to date, where the hierarchy presides (Bouzid et al., 2015; Fallahzadeh-Abarghouei et al., 2018; Parisio et al., 2014; Vandoorn et al., 2013). Hereinafter, various methods used at each level of the hierarchical control architecture are introduced:

- the tertiary control (high level) deals with power flow and optimization and, in parallel, takes into consideration different economical aspects. At this level, the power flow is regulated among the different parts of the microgrid succeeding the load balancing within the transmission network and providing the most economical solution. Several methods for optimization have been developed including constraints, energy storage or uncertainties. Such a method was presented in Parisio et al. (2015); Prodan and Zio (2014), where they combine Model Preditive Control (MPC) with mixed integer programming for battery scheduling. In Farina et al. (2016); Velarde et al. (2017), the authors use MPC with chance constraints to deal with profile uncertainties. In Drgoňa et al. (2018), they present a combination of MPC with machine learning, using MPC for the optimal profile generation and machine learning for system adjustment to the consumer's demand;

- the secondary control (middle level) enforces the amelioration of power quality. It targets the internal processes of the system under voltage and frequency disturbances. Both centralized (Shafiee et al., 2014) and distributed (Lou et al., 2017) secondary controllers have been investigated and various control methods have been proposed. In Shafiee et al. (2014), a phase controller is used which regulates the phase angle of the distributed generators instead of the frequency to decrease frequency and amplitude discrepancies. In Wang et al. (2015), the authors aim at reducing the voltage deviations caused by droop control method in a distributed control framework for accuracy in current sharing. Baghaee et al. (2016) improves the performance of a microgrid by controlling the reactive power under disturbances caused by power outages, short circuits and the like. In Simpson-Porco et al. (2015), frequency and voltage controllers are designed, enabling the possibility for the system to achieve either frequency or

voltage regulation while maintaining reactive power sharing. Predictive controllers are used such as MPC (Mayne, 2014). For instance, Ahumada et al. (2015) implements MPC in combination with a PI controller in order to decrease the discrepancies between the nominal and the actual frequency, to increase the stability of the system and to counteract communication delays;

- the primary control (low level) includes a localized supervision of the power distribution and the voltage/current adjustment among the DERs and converters. This control level defines the proper operation of the converters in order to ensure stability. The converters contain an internal switching activity that obeys to an external power loop based on a management strategy (Hadjeras et al., 2017; Wang et al., 2019). Such strategies are for instance the maximum power point tracking (Liu et al., 2016), which contains controllers that extract the maximum available power from energy sources, like wind turbines or PVs. Another approach is the master/slave control (Mazumder et al., 2008), where a device is selected as the master controller over one or more devices that act as slaves. Additionally, there is also droop control (Guerrero et al., 2011), that allows balance of load sharing during parallel generators operation. Moreover, inner voltage and current control loops are further considered to study the stability of the system (Gavagsaz-Ghoachani et al., 2016).

Another important aspect which influences the operation of microgrids is the power loss. Optimal power flow accounts for the effective and reliable functioning of the system with either minimizing the electricity cost or the energy dissipation. Power losses in the DC-bus network can significantly affect the power quality during transmission. Hence, their mitigation constitutes a very important factor for the improvement of the power transmission. Different approaches have been proposed recently for the power loss reduction, concentrating either on the components connected to the microgrid or on the central transmission network (Gamarra and Guerrero, 2015). Some works focus on topological issues or optimal scheduling of the energy storage (ES) and the renewable sources, as in Iovine et al. (2017) and Wei et al. (2014). Others concentrate on the existing power losses in the transmission lines, which are inherent to the electrical network and they cannot be prevented or eliminated. In the literature, researchers have proposed several methods for optimal power distribution including power loss minimization. In Nahata et al. (2019), the authors propose a three-layer hierarchical control approach to solve the energy management problem in islanded microgrids. More specifically, at the higher level, taking into account topological and stability issues, optimal power profiles are generated, within a MPC framework. At the middle level, using the upper level references, a voltage regulation problem is solved taking into account the power losses of the transmission network and the converters. Furthermore, a two-level hierarchical control based on plug and play method has been proposed in Vazquez et al. (2018) where at a low level load sharing is achieved through droop control and at a higher level adaptive droop controllers are developed for power losses minimization. Sanseverino et al. (2015) introduce an optimal power flow algorithm for islanded microgrids to cope with central power dissipation under a centralized three-layer supervision controller.

In the methods and techniques previously described, the dynamical models are mostly considered as sets of differential equations (Parisio et al., 2016). Consequently, the models are described as sets of constitutive equations which do not explicitly represent the structure of the power−preserving functions or maintain the energy conservation within the system. Next, concerning the generation of the optimal profiles, constrained optimization−based control methods are often employed such as MPC (Mayne, 2014), a popular method to generate on−line optimal profiles for discrete−time systems. Depending on the type of MPC, the cost function penalizes the cost, the dissipation or the error among the actual and reference signal profiles. However, the microgrids are convoluted networks where numerous factors need to be examined and considered at the same time, such as power optimization, cost minimization, stability, robustness and the like. Consequently, no definitive microgrid models and control methods exist and many aspects remain still open for investigation. In this work, a different approach is developed in a hierarchical control framework. The models already introduced in chapter 2 will be considered in PH formulation, which always respects the power conservation among the physical elements and describes the dynamics of the system explicitly. Furthermore, differential flatness for continuous-time optimal profile generation will be used, combined with B-spline approximation for continuous-time constraint validation.

This chapter presents the power balancing problem and aims at reducing the electricity cost and the power dissipation exploiting the energy storage and the meshed topology of the system. The contributions of this chapter are summarized below:

- the use of differential flatness and B-splines parametrization at the high level to obtain optimal reference profiles for the UG, ES power and for the battery's voltage and current. In contrast to the previously referenced publications, which concentrate more on obtaining optimal profiles for the source power

generation, in here a further analysis with optimal profiles in continuous time is provided not only for the power but also for the current and voltage of the battery, which will be used at the middle level as reference. Through B-spline approximation of the flat representations, the continuous-time constraint validation will be ensured;

- the multi-level control structure which provides at each level (high, middle and low) optimal profiles to be followed by the lower level. For instance, power balancing requirements at the high level lead to an optimal battery usage profile, to be tracked at the middle level; the middle level provides voltage and current references for the battery which are tracked at the low level by an explicit switching law for the DC/DC converters. In all cases bottom to top information in the power flow is exploited for a reliable profile generation (e.g., tracking errors are accounted for);
- the validation of the proposed hierarchical control through extensive simulations based on realistic load, renewable power and electricity price profiles. The behavior of the scheme is analyzed at the high, middle and low levels over the meshed DC microgrid benchmark previously introduced.

This chapter is organized as follows. Firstly, the basic tools used to build the hierarchical control problem are introduced. Then, the energy management problem will be presented defining, primarily, the objectives, the reference profiles and the set of constraints. Afterwards, the multi-layer supervision problem is analyzed explicitly. Finally, the simulation results and conclusions are presented.

4.2 Constrained optimization-based problem formulation

Optimal control theory deals with systems which can be controlled under a specific optimal criterion with given inputs, boundary conditions and a set of constraints for the states. It's a method that defines the evolution of a dynamical system generating state trajectories over a period of time. This section recalls the basic tools important to construct the multi-scale supervision problem for the system presented in chapters chapter 2 and chapter 3. The notions of optimal control theory, B-spline parametrization and MPC tracking are presented (Rawlings and Mayne, 2009; Suryawan, 2012).

4.2.1 Constrained optimization-based control

A constrained optimization problem for a control system as in (3.2.1) contains an objective function and a set of constraints as follows (Bertsekas, 2014). The general constrained minimization problem is written as follows:

$$\min_{u} \ \mathcal{J}(x(t),u(t)) \tag{4.2.1}$$

$$\textit{subject to} \quad \dot{x}(t) = f(x(t),u(t)), \ \ x(t_0)=x_0 \ \ \forall t\in[t_0,t_f], \tag{4.2.2}$$

$$c_{eq}(x(t),u(t))=0, \ eq=1,\dots,N_{c_{eq}}, \ \forall t\in[t_0,t_f], \tag{4.2.3}$$

$$c_{neq}(x(t),u(t))\leq 0, \ neq=1,\dots,N_{neq}, \ \forall t\in[t_0,t_f], \tag{4.2.4}$$

$$(t_f,x(t_f))\in\mathbb{S}_f. \tag{4.2.5}$$

The objective function (otherwise called cost function) $\mathcal{J}$ is defined as:

$$\mathcal{J}(x(t),u(t)) = \phi_1(x_{t_f}) + \int_{t_0}^{t_f} \phi_2(x(t),u(t))dt, \tag{4.2.6}$$

with $[t_0,t_f]$ the time interval of interest, $\phi_1(x_{t_f})$ and $\phi_2(x(t),u(t))$ are given functions, the terminal and the running cost, respectively, and x_{t_f} is the final state vector. The cost function is chosen based on different objectives, as the electricity cost minimization or the power dissipation. In addition to this, the states and control variables obey to a set of equality and inequality constraints referred below:

$$\begin{cases} c_{eq}(x(t),u(t))=0, \ eq=1,\dots,N_{c_{eq}}, \ \forall t\in[t_0,t_f], \\ c_{neq}(x(t),u(t))\leq 0, \ neq=1,\dots,N_{neq}, \ \forall t\in[t_0,t_f], \end{cases} \tag{4.2.7}$$

with c_{eq} the equality constraints, c_{neq} the inequality constraints and N_{eq}, N_{neq} the number of equality and inequality constraints correspondingly. These relations arise from the system requirements, parameters and

some general physical restrictions. Furthermore, there is another set of constraints, $\mathbb{S}_{t_f}$, which defines the endpoints of the final time t_f and the final state x_{t_f} which may vary depending on the optimization problem. Consequently, the final time and final state must additionally fulfill the constraint below:

$$(t_f, x(t_f)) \in \mathbb{S}_f. \tag{4.2.8}$$

In general, a constrained optimization-based control problem is not straightforward to solve, especially when there are nonlinearities in the objective functions and the constraints. Usually the solution to these problems is given through methods which require system discretization. Contrarily to the classical methods, in here the optimization problem (4.2.1) is maintained in continuous time, applying the notions of differential flatness from chapter 3 and B-spline parametrization, described below.

4.2.2 B-spline parametrization

In this section, the B-spline parametrization and some of its basic properties will be presented. The flat output will be projected over a finite set of basis functions, called B-splines, in function of which the cost and constraints will be written later in this chapter. The idea of B-spline parametrization is based on the construction of a curve defined by a number of points. These points are connected successively representing the polynomials which characterize and form the B-splines (see also Fig. 4.2.1). The polynomials, connected together, constitute the control polyline of the B-spline curve as shown in Fig. 4.2.1.

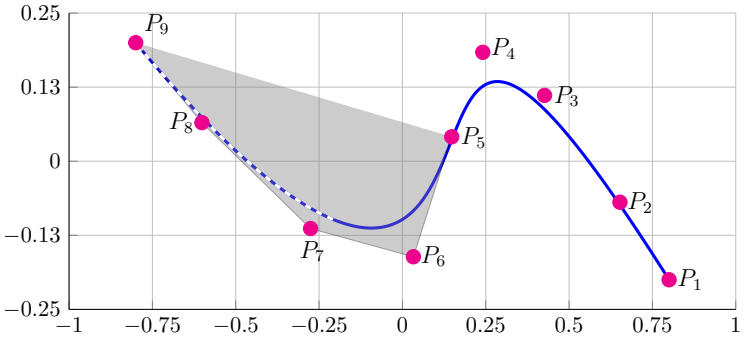

Figure 4.2.1: B-spline curve (blue), its control polyline (dark grey) and convex hull (light grey) (Prodan et al., 2019).

Definition 4.2.1. *(B-spline parametrization (Lyche et al., 2018)): A B-spline function of order d is expressed by* $\mathbf{b}_{i,\mathbf{d}}(t)$ *following the relation defined below:*

$$\begin{aligned} \mathbf{b}_{i,1}(t) &= \begin{cases} 1, & \tau_i \leq t < \tau_{i+1}, \\ 0, & \textit{otherwise}, \end{cases} \\ \mathbf{b}_{i,\mathbf{d}}(t) &= \frac{t-\tau_i}{\tau_{i+\mathbf{d}-1}-\tau_i}\mathbf{b}_{i,\mathbf{d}\text{-}1}(t) + \frac{\tau_{i+\mathbf{d}}-t}{\tau_{i+\mathbf{d}}-\tau_{i+1}}\mathbf{b}_{i+1,\mathbf{d}}(t). \end{aligned} \tag{4.2.9}$$

The b-splines are defined by a knot-vector $T \in R^{N+\mathbf{d}}$ *which is a set of non-decreasing time instants equal to* $T = \{\tau_0 \leq \tau_1 \leq ... \leq \tau_\kappa\}$*, where* $\tau_\kappa = N + \mathbf{d} + 1$*:*

$$T = \{\tau_0, \tau_1, \ldots, \tau_{\kappa-1}, \tau_\kappa\} = \{\underbrace{t_0, \ldots, t_0}_{\mathbf{d}}, \tau_{\mathbf{d}}, \ldots, \tau_{\kappa-\mathbf{d}-1}, \underbrace{t_f, \ldots, t_f}_{\mathbf{d}}\}, \tag{4.2.10}$$

where $\tau_0 = t_0,\ \tau_\kappa = t_f$. □

Definition 4.2.2. *(B-spline parametrization of a flat output (Lyche et al., 2018)): The flat output* $z(t)$ *is projected over N B-splines of order* $\mathbf{d}$ *as follows (Suryawan, 2012):*

$$z(t) = \sum_{i=1}^{N} \mathbf{p}_i \cdot \mathbf{b}_{i,\mathbf{d}}(t) = \mathcal{P}\mathcal{B}_{\mathbf{d}}(t), \tag{4.2.11}$$

where $\mathbf{p}_i$ *is the* i^{th} *control point, to which it corresponds the matrix* $\mathcal{P}$ *of* N *control points equal to* $\mathcal{P} = \begin{bmatrix}\mathbf{p}_1 & \mathbf{p}_2 & \dots & \mathbf{p}_N\end{bmatrix}^\top \in \mathbb{R}^{N\times 1}$. *Moreover,* $\mathcal{B}_{\mathbf{d}}(t) = \begin{bmatrix}\mathbf{b}_{1,\mathbf{d}}(t) & \mathbf{b}_{2,\mathbf{d}}(t) & \dots & \mathbf{b}_{N,\mathbf{d}}(t)\end{bmatrix}^\top \in \mathbb{R}^{N\times \mathrm{d}}$ *is the B-spline vector.* □

B-spline parametrization seems appropriate due to its numerous properties such as convexity, continuity, ease on derivatives computation and so on. The B-splines are used because they can easily enforce continuity across the control points. This accounts for continuous-time constraint validation considering the control points as decision variables (Stoican et al., 2017). Furthermore, they facilitate the computation of the derivatives existing from the flat representation. Below, some of the most significant properties of B-splines are enumerated (Stoican et al., 2017):

P1. A B-spline curve of order $\boldsymbol{d}$ is $\mathcal{C}^{\boldsymbol{d}-1}$-continuous at any time instant included in the knot vector T and $\mathcal{C}^{\infty}$-continuous at any other point (Stoican et al., 2017).

P2. The r-order derivatives of $\boldsymbol{d}$-order B-splines can be expressed as linear combinations of $\boldsymbol{d}-r$ order B-splines which, in turn, can be expressed as $\boldsymbol{d}$-order B-splines over each knot sub-interval:

$$\mathcal{B}_{\boldsymbol{d}}^{(r)}(t) = \mathcal{M}_{\boldsymbol{d},\boldsymbol{d}-r}\mathcal{B}_{\boldsymbol{d}-r}(t) = \mathcal{M}_{\boldsymbol{d},\boldsymbol{d}-r}\mathcal{S}_{\kappa,\boldsymbol{d}-r,\boldsymbol{d}}\mathcal{B}_{\boldsymbol{d}}(t), \quad \forall t \in [\tau_\kappa, \tau_{\kappa+1}), \tag{4.2.12}$$

with $\mathcal{S}_{\kappa,\boldsymbol{d}-r,\boldsymbol{d}}$ denoting the translation matrix from higher to lower degree basis functions and $\mathcal{M}_{\boldsymbol{d},\boldsymbol{d}-r}$ the matrix performing the linear combinations of the lower-degree basis functions.

P3. The sum of the B-splines basis functions $\boldsymbol{b}_{i,\boldsymbol{d}}(t)$ is equal to 1 for the time interval $[\tau_0, \tau_\kappa]$ and the B-splines themselves are either equal or greater than 0 (Stoican et al., 2017; Suryawan, 2012).

P4. Every B-spline function depends on its order r and its degree $\boldsymbol{d}$. The degree of B-splines depends on the derivative order where the continuity is ensured. Each B-spline may be locally treated without influencing the rest of the curve.

P5. From the third property, we have that for the interval $[\tau_\kappa, \tau_{\kappa+1}]$ the sum of B-splines basis functions $\boldsymbol{b}_{i,\boldsymbol{d}}(t)$ is equal to 1. Therefore, from (4.2.11)and (4.2.9), $z(t)$ can be written also as:

$$z(t) = \bigcup_{i:t\in[\tau_\kappa,\tau_{\kappa+1}]} \sum_{j=i-\boldsymbol{d}+1}^{i} \boldsymbol{p}_j \cdot \boldsymbol{b}_{i,\boldsymbol{d}}(t) \tag{4.2.13}$$

and exists in the following unity of all convex hulls formulated by the control points (Stoican et al., 2017; Suryawan, 2012):

$$z(t) \quad \in \quad \bigcup_{i=\boldsymbol{d}-1}^{\boldsymbol{n}} \quad \mathrm{conv}\{\boldsymbol{p}_{i-\boldsymbol{d}+1}, \dots, \boldsymbol{p}_i\}, \tag{4.2.14}$$

where n is the total number of convex hulls.

4.2.3 Model Predictive Control

An important optimization-based control method on which this thesis builds its results is Model Predictive Control (MPC). We will consider two types of MPC, tracking MPC and economic MPC. The tracking MPC will be taken into account in the middle level for reference tracking and the economic MPC will be considered as a comparison tool for generating optimal profiles at the high level.

MPC is an on-line optimal control technique which optimizes a cost function while satisfying a set of constraints. The tracking MPC significantly reduces the deviations among the real and reference profiles, while the economic MPC penalizes a general cost depending on the objective, such as electricity cost or power loss mitigation (Ellis et al., 2014; Rawlings and Mayne, 2009). In general, MPC algorithms take into account discretized dynamical systems, the current state and a cost function over a receding prediction horizon in order to compute the future evolution of the system.

The MPC controller solves an open-loop optimization problem at each time step k over a prediction horizon (see also the proof of concept illustration given in Fig. 4.2.2). Next, it applies the first value of the obtained control sequence to the system dynamics, updates the system's states and repeats the procedure at the next step. Receding horizon control (RHC) was one of the first attempts done by researchers (Kamel et al., 2017; Mayne and Michalska, 1990; Rawlings and Muske, 1993) to approach more closely problems with fixed horizon and allowed the computation of a complete control sequence by sending only the first step to the system in order to recompute and restart the process.

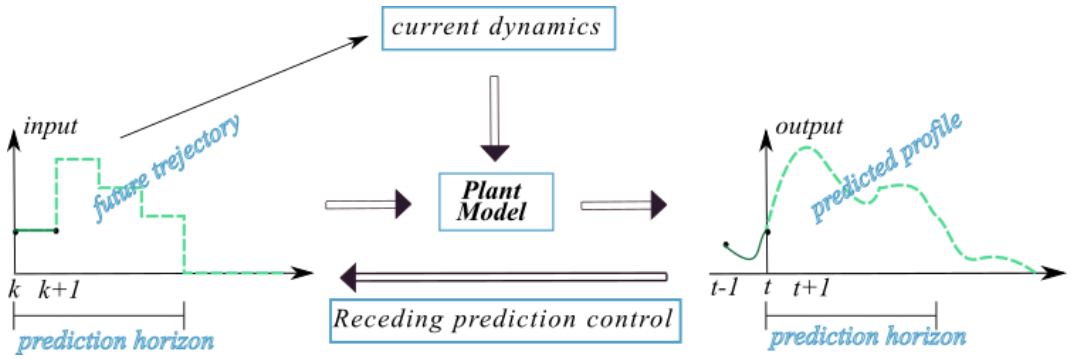

Figure 4.2.2: General MPC control scheme.

Consider the following nonlinear discrete-time system:

$$\tilde{x}(k+1) = f_d(\tilde{x}(k), \tilde{u}(k)), \quad x(t) = \tilde{x}, \quad k \geq t, \tag{4.2.15}$$

with the state vector $x(k) \in \mathbb{R}^n$ and the control input $u(k) \in \mathbb{R}^m$. For the considered optimization problem, the cost function to minimize is defined as follows (Allgöwer and Zheng, 2012):

$$\begin{aligned} \mathcal{J}_{MPC} = & \sum_{k=t}^{t+N_p-1} (\tilde{x}(k)^\top Q_{\tilde{x}} \tilde{x}(k) + \tilde{u}(k)^\top R_{\tilde{u}} \tilde{u}(k)) + \tilde{V}_f(x(t+N)), \\ subject\ \ to: \ & \tilde{x}(k+1) = f_d(\tilde{x}(k), \tilde{u}(k)), \\ & \tilde{x}(k) \in \tilde{\mathcal{X}}, \\ & \tilde{u}(k) \in \tilde{\mathcal{U}}, \\ & \tilde{x}(t+N_p) \in \tilde{\mathcal{X}}_f \ \ (terminal\ \ constraint), \end{aligned}$$

where $Q_{\tilde{x}}$ and $R_{\tilde{u}}$ are matrices of appropriate dimensions, $\tilde{\mathcal{X}}$ is the set of state constraints and $\mathcal{U}$ the set of input constraints. Furthermore, the term $\tilde{V}_f(x(t+N))$ plays an important role for the system's stability, since it forces the states to always exist in a particular set.

4.2.4 Control objectives, reference profiles and general constraints

This subsection presents the ingredients necessary for the formulation of the flatness-based optimization control problem of the reduced meshed DC microgrid introduced in Fig. 2.5.1.

4.2.4.1 Control objectives

The energy management problem for the meshed DC microgird system (Fig. 2.5.1) addresses the following control objectives:

- energy management, load balancing in the common DC-bus among the nodes;
- cost minimization exploiting the PV power generation and the energy storing devices;
- reduction of the power losses during distribution within the central transmission network;
- satisfaction of a set of constraints for several variables of the system, such as current, voltage, charge etc.
- continuity in the operation of the system in case of a line under fault.

4.2.4.2 Reference profiles

Fig. 4.2.3 presents the reference profiles of the electricity price, the PV panel and the loads which will be used later in the simulations:

- a variable cost is considered: 0.147 $[euros/kWh]$ from $4p.m.$ to $10p.m.$ and 0.116 $[euros/kWh]$ for the rest of the day, with equal selling and buying values for the UG;

- for the renewable source, 28 PV modules of DS-100M PV model (180 W peak PV generation of 72 cells) are taken into account. The PV power profile were obtained after simulations based on the PV model presented in section 2.4.1.1. External temperature and irradiation data were gathered for a whole day in June (CIAT company, 2014). A profile with high power generation is selected to observe the controller response regarding the power sold to the UG or stored to the ES system;
- for the consumer's demand, real historical data gathered from National Renewable Energy Laboratory (2016) and Department of Energy Office of Energy Efficiency & Renewable Energy (2017) are used, one for commercial usage (CU) (4308 W peak demand) (National Renewable Energy Laboratory, 2016), where the demand is higher during the day, and one for domestic usage (DU) (3901 W peak demand) (Department of Energy Office of Energy Efficiency & Renewable Energy, 2017), where the demand increases after $4p.m.$ in the afternoon.

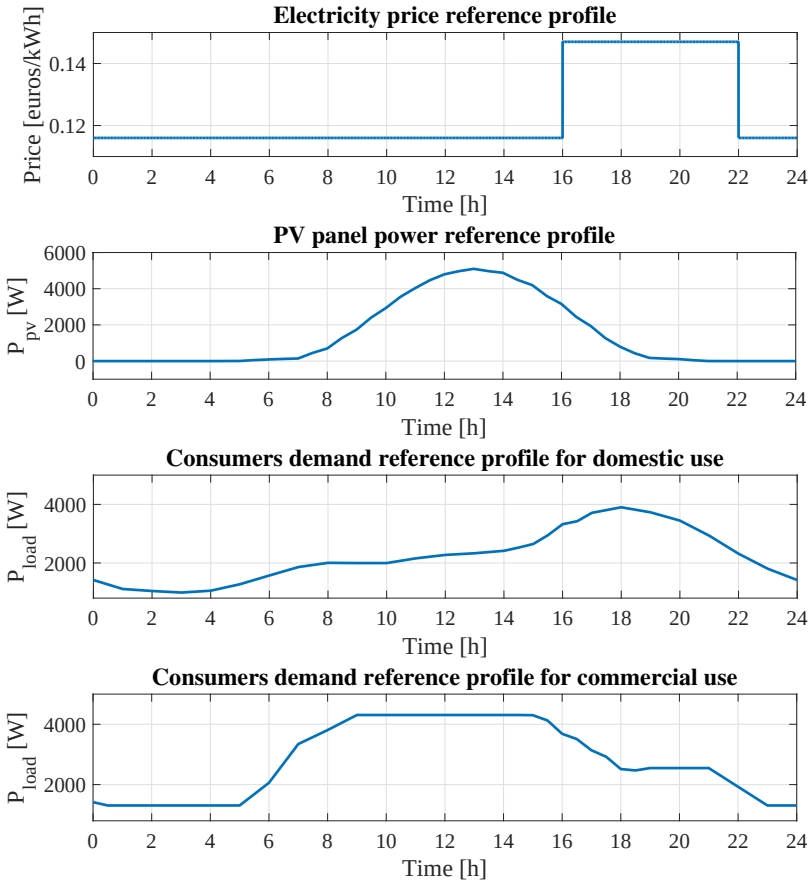

Figure 4.2.3: Profiles of electricity price, renewable power from the PV panel and loads for domestic and CU.

4.2.4.3 Constraints

In this section, we will describe the necessary constraints and restrictions for the system as previously described in section 2.6.2. As already emphasized, the ES system is of high importance and its long lifetime and maintenance are significant factors. Because of the fact that the ES stores and conserves energy, it ensures the safe and continuous operation of the DC microgrid when other resources (PV and UG) are unable to generate power. Priority on the battery's optimal operation will be given and the dynamics of the ES system will be analytically described in the optimization problem. Therefore, setting constraints for the battery's proper operation is indispensable.

Firstly, since the battery can store a finite amount of energy, boundaries concerning the charge must be considered. The charge of the battery has to be between a minimum q_b^{min} and a maximum q_b^{max} value (both states, $q_{1b}(t)$ and $q_{2b}(t)$ as in (2.4.8), have positive values and $q_b^{max} = q_{1b}^{max} + q_{2b}^{max}$. Additionally, q_b^{min} and q_b^{max} depends on the depth of discharge (DOD), which describes the battery's discharging possibilities.

Table 4.2.1: Number of discharge cycles of the battery.

Number of cycles	DOD
400	20%
600	50%
1500	70%

Table 4.2.2: Boundaries of the battery's variables.

Variables	Values
q_b^{min}	15Ah
q_b^{max}	168Ah
$v_{b,charging}^{min}$	13.5V
$v_{b,charging}^{max}$	13.8V
$i_{b,charging}^{min}$	0A
$i_{b,charging}^{max}$	20A
$v_{b,dicharging}^{min}$	11.9V
$v_{b,dicharging}^{max}$	12.7V

According to the characteristics of the AGM 12-165 lead acid batteries (Victron Energy, 2015), they are fully charged at 92%. Therefore, the DOD is equal to 8%. The maximum capacity of the battery is equal to $165Ah$. By respecting the DOD of the battery, the battery will keep its rated capacity for a limited number of charge/discharge cycles, which are shown in Table 4.2.1.

Furthermore, another important factor is the charging and discharging rate. A quick discharge can reduce the amount of generated power and can influence the battery's capacity. This is because of the limited time remaining for the battery's chemical elements to move to their necessary positions, which leads to the decrease of the available power inside the battery. In the contrary, a slow discharge rate contributes to the amelioration of the capacity and the generated power. The rate of charge is defined by the current of the battery which is also bounded between a maximum, i_b^{min}, and a minimum, i_b^{max}, value. Similar constraints exist for the voltage of the battery.

All the aforementioned constraints for the proper operation of the battery are expressed below (see also Table 4.2.2:

$$q_b^{min} \leq q_b(t) \leq q_b^{max}, \tag{4.2.17a}$$

$$Charging\ \ mode: \tag{4.2.17b}$$

$$v_{b,charging}^{min} \leq v_{b,charging}(t) \leq v_{b,charging}^{max}, \tag{4.2.17c}$$

$$i_{b,charging}^{min} \leq i_{b,charging}(t) \leq i_{b,charging}^{max}, \tag{4.2.17d}$$

$$Dischaging\ \ mode: \tag{4.2.17e}$$

$$v_{b,dicharging}^{min} \leq v_{b,dicharging}(t) \leq v_{b,dicharging}^{max}, \tag{4.2.17f}$$

$$I_{b,dicharging}(t) \simeq 15A. \tag{4.2.17g}$$

In addition, boundaries are defined for the voltage in the central transmission network (Fig. 2.6.2), which maintain the voltage on the connecting nodes close to 400 V, as already presented in chapter 2:

$$v_{DC}^{min,h} \leq v_{ug}(t), v_{pv}(t), v_{es}(t), v_{loads}(t) \leq v_{DC}^{max,h}, \tag{4.2.18}$$

where $v_{DC}^{min,h}$ is equal to 380 V and $v_{DC}^{max,h}$ is equal to 430 V.

Furthermore, limitations for the duty cycles d_{1sc} and d_{2sc} of the Split-Pi converter are considered:

$$0 \leq d_{1sc} \leq 1,$$
$$0 \leq d_{2sc} \leq 1.$$

Finally, an upper and lower limit for the UG is necessary as follows:

$$P_{ug}^{min} \leq P_{ug}(t) \leq P_{ug}^{max},$$

with P_{ug}^{min} is $-2100\ W$ and P_{ug}^{max} is $4200\ W$. Since we aim the cost minimization, it is necessary to confine the power consumption from the UG, guaranteeing the full exploitation of the renewable sources and the energy storing devices.

4.3 Hierarchical constrained optimization-based control

In the previous sections, the system's characteristics, the control objectives and the different scenarios, which will be included in the optimization problem, were introduced. The combination of renewable sources, storing elements, variable consumers' demands and DC/DC converters lead to the multi-timescale dynamics. Hence, a hierarchical control problem divided in three levels will be proposed for the cost minimization with and without power losses in the central transmission network. At the high level, we deal with the slow dynamics, which, in this case, concludes to the power balancing in the central network. Then, at the lower level, the fast dynamics is introduced controlling the switches of the converters. The main goal is to reduce the electricity cost by minimizing the power generated by the UG, hence taking advantage of the PV power production and the ES system capacity. Considering all the above, the proposed hierarchical control approach is (Fig. 4.3.1 and Fig. 4.3.3):

- *high level* (power flow optimization): optimal profiles for the battery current i_b and voltage v_b are provided to use at the middle level. Differential flatness and B-spline parametrization are combined for continuous-time constraint validation;
- *middle level* (battery scheduling): a tube-MPC tracking controller (Langson et al., 2004) is employed to mitigate the discrepancies among the reference and actual profiles under perturbation;
- *low level* (switching activity in the converter): an explicit control law for the duty cycles of the converter is provided to follow the tracking profiles obtained at the middle level.

In the following, each level is described in detail exploring two scenarios: i) the absence of power losses within the transmission lines; ii) the existence of power losses in the central transmission network.

4.3.1 High level control

The principal objective of the high level problem is the generation of reference trajectories in continuous time, exploiting the flat output representations provided in section 3. Therefore, an optimal scheduling for the battery charging and discharging is obtained and, in the meantime, the electrical power purchase from the UG is minimized. The general cost function considered at the high level is the following:

$$\mathcal{J} = \int_{t_0}^{t_f} ep(t) P_{ug} dt, \tag{4.3.1}$$

where $ep(t)$ is the electricity price. Depending on the scenario, the form of the cost function changes, as it will be observed later in the detailed analysis.

4.3.1.1 Transmission line network without power losses

To determine the objective function at the high level for the reduced DC microgrid (Fig. 2.5.1) without power losses in the common DC bus, the dissipative elements will be erased from the power conservation equation (2.5.14). Therefore, considering that $P_{R1}(t) = P_{R2}(t) = P_{R3}(t) = P_{R4}(t) = 0$, (2.5.14) becomes:

$$P_{ug}(t) + P_{pv}(t) - P_{es}(t) - P_{loads}(t) = 0, \tag{4.3.2a}$$

$$P_{ug}(t) = P_{es}(t) + P_{loads}(t) - P_{pv}(t) \ \ or \ \ P_{es}(t) = P_{ug}(t) - P_{loads}(t) + P_{pv}(t). \tag{4.3.2b}$$

Hereinafter, we consider the minimization of the power coming from the UG while satisfying the ES system dynamics (2.5.1, 2.5.2a, 2.5.2b, 2.5.2c) and the constraints (4.2.17):

$$\min_{i_b, v_b} \int_{t_0}^{t_f} ep(t) \Big(\underbrace{P_{es}(t)}_{i_b(t) v_b(t)} + P_{loads}(t) - P_{pv}(t) \Big) dt, \tag{4.3.3a}$$

$$subject\ \ to:\ the\ system\ dynamics\ (2.5.1)-(2.5.2b), \tag{4.3.3b}$$
$$v_b^{min,h} \leq v_b(t) \leq v_b^{max,h}, \tag{4.3.3c}$$
$$i_b^{min,h} \leq i_b(t) \leq i_b^{max,h}, \tag{4.3.3d}$$
$$q_{2b}^{min,h} \leq q_{2b}(t) \leq q_{2b}^{max,h}, \tag{4.3.3e}$$
$$P_{ug}^{min,h} - P_{loads}(t) + P_{pv}(t) \leq P_{es}(t) \leq P_{ug}^{max,h} + P_{loads}(t) - P_{pv}(t). \tag{4.3.3f}$$

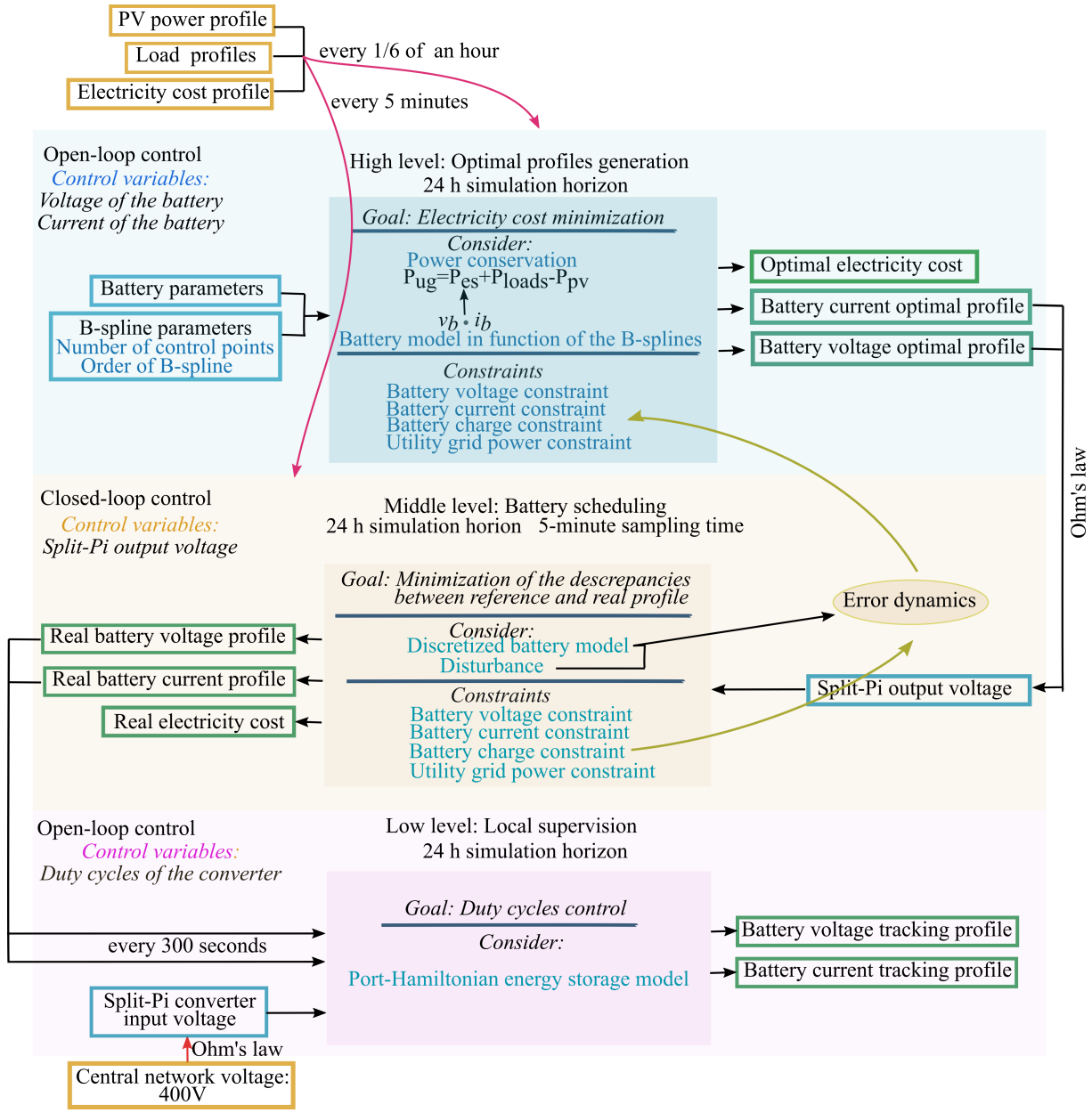

Figure 4.3.1: Flowchart of the proposed hierarchical control strategy of the DC microgrid without considering the power losses in the central transmission network.

The control variables of the optimization problem are the voltage, v_b, and the current, i_b of the battery. They are written in function of the flat output $z(t) = q_{2b}(t)$ (3.3.26h) and, then, the B-spline parametrization is applied to obtain continuous-time optimal profiles for the charge, $q_{2b}(t)$, hence, the voltage, v_b, and the current, i_b, of the battery. The main objective is the minimization of the electricity cost, ept, providing the optimal power generation from the ES, P_{es}, and the UG, P_{ug}, after considering the energy conservation

equation (4.3.2a). Therefore, replacing in (4.3.3a) the power of the ES, P_{es}, from (4.3.2b) with the control variables, a nonlinear optimization problem is obtained, since P_{es} is in quadratic form.

In Fig. 4.3.1, the control scheme of the energy management problem, in the absence of power losses in the central transmission network, is presented. At each level, the control variables are illustrated. At the high level, the battery model and the constraints are presented in function of the B-splines. As aforementioned, the control variables are the voltage, v_b, and the current, i_b, of the battery. Optimal profiles are generated to use them at the middle level, where MPC tracking is applied and disturbances are considered. The control variable at this level is the output voltage of the Split-Pi converter, v_{sc_out}, which is linked to the voltage, v_b, of the battery through Ohm's law. The discretized model of the battery is taken into account with its corresponding constraints in discrete-time. At this level, the main objective is the minimization of the discrepancies among the reference and the actual values. Afterwards, at the low level, the tracking profiles of the voltage, v_b, and the current , i_b, of the battery are applied to the ES PH system, as previously presented in section 2.5.1, in order to regulate the operation of the switches characterized by their duty cycles, d_{1sc} and d_{2sc}.

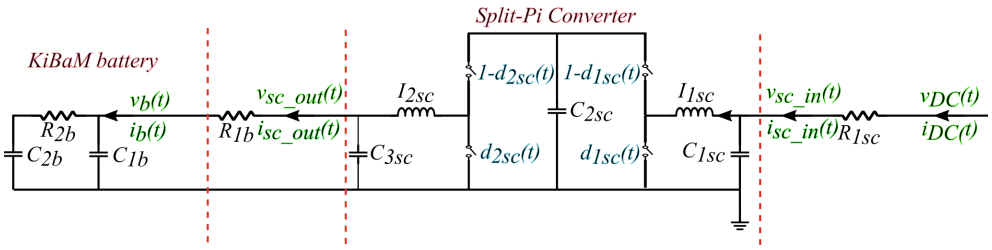

Figure 4.3.2: Electrical network of the battery connected to the Split-Pi converter during charging mode, where $v_{DC}(t) = 400\ V$.

Continuing with the high level problem formulation, the cost function and the constraints of (4.3.3a)-(4.3.3f) will be rewritten in function of the flat representation of the ES system generated by the algorithm for flat representation in section A.1.1 (3.3.26a-3.3.26l). From the ES state-space representation (2.5.1)-(2.5.2b) and, also, the ES electrical circuit (Fig. 4.3.2), we obtain:

$$i_b(t) = i_{R_{1b}}(t), \tag{4.3.4a}$$

$$v_b(t) = \frac{q_{1b}(t)}{C_{1b}}, \tag{4.3.4b}$$

$$i_b(t) = i_{R_{1b}}(t) = i_{R2b}(t) + i_{C1b}(t) = i_{2b}(t) + \dot{q}_{1b} = \dot{q}_{1b}(t) + \dot{q}_{2b}(t), \tag{4.3.4c}$$

$$v_b(t) = v_{1b}(t) = \frac{q_{1b}(t)}{C_{1b}}, \tag{4.3.4d}$$

where $q_{2b}(t)$ considered to be the flat output of the battery as already introduced in sections 3.3.2.1 (3.3.26h) and also from the bicausal Bond graph in section 3.4.2.1 (3.4.17a). Therefore, considering also the flat representation of q_{1b} in (3.3.26g) and (3.4.17a):

$$q_{1b}(t) = R_{2b}C_{1b}\dot{z}(t) + \frac{C_{1b}}{C_{2b}}z(t), \tag{4.3.5a}$$

$$q_{2b}(t) = z(t), \tag{4.3.5b}$$

we obtain the battery's voltage and current profile references expressed as:

$$v_b(t) = \frac{1}{C_{2b}}z(t) + R_{2b}\dot{z}(t), \tag{4.3.6a}$$

$$i_b(t) = (1 + \frac{C_{1b}}{C_{2b}})\dot{z}(t) + C_{1b}R_{2b}\ddot{z}(t). \tag{4.3.6b}$$

Next in order is the B-spline approximation which ensures the continuous-time constraints validation. This will facilitate also the middle level controller to similarly respect them. Therefore, we replace $z(t)$ with the B-splines approximation as in Definition 4.2.2:

$$z_3(t) = \sum_{i=1}^{N} \boldsymbol{p}_i \cdot \mathcal{B}_{i,\boldsymbol{d}}(t) = \mathcal{P}\mathcal{B}_{\boldsymbol{d}}(t). \tag{4.3.7}$$

with control points $\mathcal{P} = [\boldsymbol{p}_1 ... \boldsymbol{p}_N]$ and basic functions of order $\boldsymbol{d}$ $\mathcal{B}_{\boldsymbol{d}}(t) = [\mathcal{B}_{1,\boldsymbol{d}}(t) ... \mathcal{B}_{N,\boldsymbol{d}}(t)]$. From (4.3.6a) and (4.3.6b), the control variables are expressed in function of the B-splines as follows:

$$v_b(t) = \sum_{i=1}^{N} \left(\frac{1}{C_{2b}} \mathcal{P} + R_{2b} \mathcal{P} \right) \mathcal{B}_{\boldsymbol{d}}^{(r)}(t), \tag{4.3.8a}$$

$$i_b(t) = \sum_{i=1}^{N} \left[\left(1 + \frac{C_{1b}}{C_{2b}} \right) \mathcal{P} + C_{1b} R_{2b} \mathcal{P} \right] \mathcal{B}_{\boldsymbol{d}}^{(r)}(t). \tag{4.3.8b}$$

Then, employing the differentiation property of the B-splines (second property from section 4.2.2 (4.2.12)), the control points for voltage,v_b, and the current, i_b, are equal to:

$$\boldsymbol{p}_{\kappa_i}^{v_b} = \frac{1}{C_{2b}} p_i + R_{2b} \left(\mathcal{P} M_{\boldsymbol{d},\boldsymbol{d}-1} S_{\kappa,\boldsymbol{d}-1,\boldsymbol{d}} \right)_i, \tag{4.3.9a}$$

$$\boldsymbol{p}_{\kappa_i}^{i_b} = \left(1 + \frac{C_{1b}}{C_{2b}} \right) \left(\mathcal{P} M_{\boldsymbol{d},\boldsymbol{d}-1} S_{\kappa,\boldsymbol{d}-1,\boldsymbol{d}} \right)_i + C_{1b} R_{2b} \cdot \left(\mathcal{P} M_{\boldsymbol{d},\boldsymbol{d}-2} S_{\kappa,\boldsymbol{d}-2,\boldsymbol{d}} \right)_i. \tag{4.3.9b}$$

Next, for $v_b(t)$ and $i_b(t)$ in (4.3.8a)-(4.3.8b), we have:

$$v_b(t) = \sum_{i=1}^{N} \left[\frac{1}{C_{2b}} p_i + R_{2b} \left(\mathcal{P} M_{\boldsymbol{d},\boldsymbol{d}-1} S_{\kappa,\boldsymbol{d}-1,\boldsymbol{d}} \right)_i \right] \boldsymbol{b}_{i,\boldsymbol{d}}(t), \tag{4.3.10a}$$

$$i_b(t) = \sum_{i=1}^{N} \left[\left(1 + \frac{C_{1b}}{C_{2b}} \right) \left(\mathcal{P} M_{\boldsymbol{d},\boldsymbol{d}-1} S_{\kappa,\boldsymbol{d}-1,\boldsymbol{d}} \right)_i + C_{1b} R_{2b} \cdot \left(\mathcal{P} \mathcal{M}_{\boldsymbol{d},\boldsymbol{d}-2} \mathcal{S}_{\kappa,\boldsymbol{d}-2,\boldsymbol{d}} \right)_i \right] \cdot \boldsymbol{b}_{i,\boldsymbol{d}}(t), \quad \forall t \in [\tau_\kappa, \tau_{\kappa+1}). \tag{4.3.10b}$$

Thus, the a priori optimization problem (4.3.3a-4.3.3f) is rewritten as follows:

$$\min_{i_b, v_b} \int_{t_0}^{t_f} \underbrace{P_{es}(t)}_{i_b(t) v_b(t)} + P_{loads}(t) - P_{pv}(t)) dt = \underbrace{\int_{t_0}^{t_f} ep(t)(i_b(t) v_b(t)) \mathrm{d}t}_{J_{es}} + \int_{t_0}^{t_f} ep(t)(P_{loads}(t) - P_{pv}(t)) \mathrm{d}t \tag{4.3.11a}$$

$$subject\ to: \ the\ system\ dynamics\ (2.5.1) - (2.5.2b), (4.3.6a), (4.3.6b), \tag{4.3.11b}$$

$$v_b^{min,h} \leq \sum_{i=1}^{N} \boldsymbol{p}_{\kappa_i}^{v_b} \boldsymbol{b}_{i,\boldsymbol{d}}(t) \leq v_b^{max,h}, \tag{4.3.11c}$$

$$i_b^{min,h} \leq \sum_{i=1}^{N} \boldsymbol{p}_{\kappa_i}^{i_b} \boldsymbol{b}_{i,\boldsymbol{d}}(t) \leq i_b^{max,h}, \tag{4.3.11d}$$

$$q_{2b}^{min,h} \leq \sum_{i=1}^{N} \boldsymbol{p}_i \boldsymbol{b}_{i,\boldsymbol{d}}(t) \leq q_{2b}^{max,h}, \tag{4.3.11e}$$

$$P_{ug}^{min,h} \leq P_{ug} \leq P_{ug}^{max,h}. \tag{4.3.11f}$$

The matrices S change across the knot sub-intervals $[\tau_\kappa, \tau_{\kappa+1}]$. Thus, constraints are also considered for each interval. For the P_{es} constraint in (4.3.11f), we follow the power conservation equation (4.3.2a):

$$P_{ug}^{min,h} - P_{loads}(t) + P_{pv}(t) \leq P_{es}(t) \leq P_{ug}^{max,h} - P_{loads}(t) + P_{pv}(t), \tag{4.3.12}$$

where $P_{es}(t) = i_b(t) v_b(t)$ as aforementioned. Appendix B.1 demonstrates the detailed calculation of $\mathcal{J}_{es}$ of (4.3.11a).

In this section, optimal profiles were obtained for the voltage, v_b, and the current, i_b, of the battery. Furthermore, the optimal power profiles for the ES and the UG were generated providing the optimal electricity cost. In the next section, we go further and consider in the optimization problem the power losses within the transmission network. The main idea is to find the optimal power routing while minimizing the power dissipation in the transmission lines and the electricity cost.

4.3.1.2 Transmission line network with power losses

In this section, the aforementioned flatness-based optimization approach is reformulated adding the power losses within the central network as in Fig. 4.3.4. Therefore, the dynamics of the system changes and the problem becomes more complicated because of the relations among the voltage, the current and the power of the DERs, the consumers' demand and the power losses. At this point, the dynamics of the central network, analyzed through its Bond graph in section 2.5.2.2 (see also Fig. 4.3.4), is considered. In Fig. 4.3.4, we observe that the notation on each connecting node has changed and, instead of v_{DC} or i_{DC} at the input of the ES, we have v_{es} or i_{es}. Since the power losses in the central transmission lines are considered, the voltage in the common DC-bus will not be stable. On each connecting node[1] a different voltage value will appear, because of the voltage drop created by the resistors. Therefore, a different notation for the voltage and the current on each connecting node is necessary.

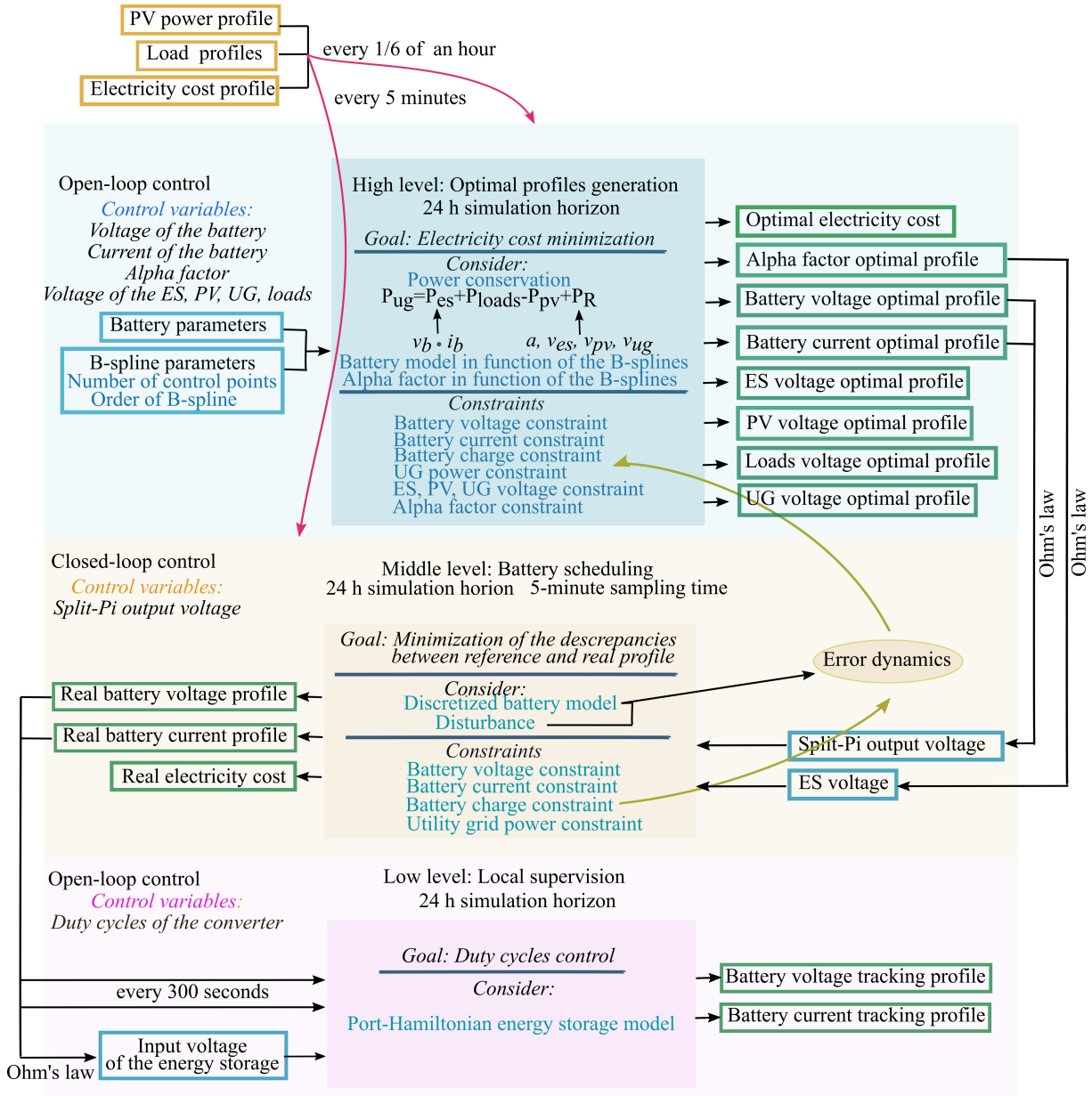

Figure 4.3.3: Flowchart of the proposed hierarchical control strategy of the DC microgrid considering the power losses in the central transmission network.

[1]Connecting node is the point where a source or a load is linked to the central network as in Fig. 4.3.4 for the connecting nodes $n:1$, $n:2$, $n:3$, $n:4$.

In Fig. 4.3.3, the control scheme of the energy management problem, in the existence of power losses in the central transmission network, is illustrated. At the high level, the battery model and the constraints previously presented in section 4.3.1.1 in function of the B-splines are employed to the new objective function. The control variables are the voltage, v_b, and the current, i_b, of the battery, the voltages on the connecting nodes of the ES, v_{es}, the PV, v_{pv}, the UG, v_ug, and the loads, v_{loads}, and the α factor, which defines the relations among the duty cycles, d_{1sc} and d_{2sc}, in the Split-Pi converter, as already presented in section 2.4.2.1. The concept is similar to the previous case where the power losses in the common DC-bus are not considered. Optimal profiles are generated for the ES system, the duty cycles through the α factor and the voltages on the connecting nodes. The optimal power profiles for the ES, P_{es}, and the UG, P_{ug}, are provided minimizing the electricity cost and the power dissipation. At the high and the middle level, the whole dynamics of the ES system is taken into account, as it will be shown later, in order to link the power losses of the central transmission network to the battery dynamics. Afterwards, the optimal profiles obtained at the high level are used as references at the middle level for tracking under perturbation, where the control variable is the output voltage of the Split-Pi converter, v_{sc_out}. The discretized model of the battery is considered again and the main objective is the reduction of the deviations among the reference and the actual values. Finally, at the low level, the tracking profiles of the voltage and the current of the battery, as well as the input voltage of the ES system, v_{es}, are applied to the ES PH model, as already described in section 2.5.1, to control the switching activity within the Split-Pi converter.

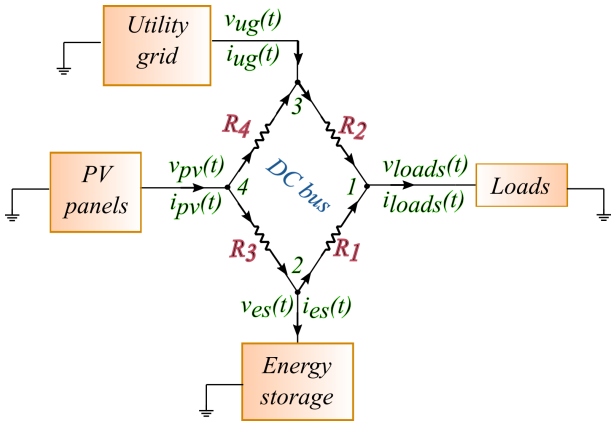

Figure 4.3.4: Central electrical network of the meshed DC microgrid system under the existence of power losses.

At first, the power losses are taken into consideration in (2.5.14) and the $P_{ug}(t)$ is equal to:

$$P_{ug}(t) = P_{es}(t) + P_{loads}(t) - P_{pv}(t) + P_R(t) \;\; or \tag{4.3.13a}$$

$$P_{es}(t) = P_{ug}(t) - P_{loads}(t) + P_{pv}(t) - P_R(t), \tag{4.3.13b}$$

where $P_{es}(t) = v_{es}(t)i_{es}(t)$ is the input power on the third connecting node, $P_{ug}(t) = v_{ug}(t)i_{ug}(t)$ is the output power on the second connecting node, $P_{pv}(t) = v_{pv}(t)i_{pv}(t)$ is the output power on the fourth connecting node and $P_{loads}(t) = v_{loads}(t)i_{loads}(t)$ is the input power on the first connecting node of the central transmission network (see also Fig. 4.3.4 and Fig. 4.3.2). $P_R(t) = P_{R1}(t) + P_{R2}(t) + P_{R3}(t) + P_{R4}(t)$ is the total power loss created by the four resistors existing in the central network.

Hereinafter,the new objective function is analytically calculated, which will be in the following form:

$$\mathcal{J} = \int_{t_0}^{t_f} ep(t)\big(P_{es}(t) + P_{loads}(t) - P_{pv}(t) + P_R(t)\big)dt \tag{4.3.14}$$

and the restored optimization problem will be:

$$\min_{i_b, v_b, \alpha, v_{es}, v_{pv}, v_{ug}} \int_{t_0}^{t_f} ep(t)\big[\underbrace{P_{es}(t)}_{i_b(t)v_b(t)}(t) + P_{loads}(t) - P_{pv}(t) + P_R(t)\big]dt, \tag{4.3.15a}$$

$$subject\ \ to:\ \ the\ system\ dynamics\ (section 2.5.2.2) and (2.5.1) - (2.5.2b), \tag{4.3.15b}$$

$$the\ power\ conservation\ (4.3.13a), \tag{4.3.15c}$$

$$v_{DC}^{min,h} \leq v_{ug}(t), v_{pv}(t), v_{es}(t), v_{loads}(t) \leq v_{DC}^{max,h}, \tag{4.3.15d}$$

$$v_b^{min,h} \leq v_b(t) \leq v_b^{max,h}, \tag{4.3.15e}$$

$$i_b^{min,h} \leq i_b(t) \leq i_b^{max,h}, \tag{4.3.15f}$$

$$q_{2b}^{min,h} \leq q_{2b}(t) \leq q_{2b}^{max,h}, \tag{4.3.15g}$$

$$P_{ug}^{min,h} - P_{loads}(t) + P_{pv}(t) - P_R(t) \leq P_{es}(t) \leq P_{ug}^{max,h} + P_{loads}(t) - P_{pv}(t) - P_R(t). \tag{4.3.15h}$$

Next, the optimization problem in (4.3.15a)-(4.3.15h) is rewritten in function of the flat outputs as in (4.3.6a) and (4.3.6b).

As a first step, the cost function is expressed in terms of the relations below, as they have been introduced in section 2.5.2.2:

$$P_{R_1}(t) = \frac{[v_{es}(t) - v_{loads}(t)]^2}{R_1} \tag{4.3.16a}$$

$$P_{R_2}(t) = \frac{[v_{loads}(t) - v_{ug}(t)]^2}{R_2} \tag{4.3.16b}$$

$$P_{R_3}(t) = \frac{[v_{pv}(t) - v_{es}(t)]^2}{R_3} \tag{4.3.16c}$$

$$P_{R_4}(t) = \frac{[v_{ug}(t) - v_{pv}(t)]^2}{R_4} \tag{4.3.16d}$$

where $v_{es}(t)$ and $i_{es}(t)$, $v_{pv}(t)$ and $i_{pv}(t)$, $v_{ug}(t)$ and $i_{ug}(t)$, $v_{loads}(t)$ and $i_{loads}(t)$ denote the voltage and the current on the connecting nodes of the ES, PV, UG and loads system respectively, as in Fig. 4.3.4. The

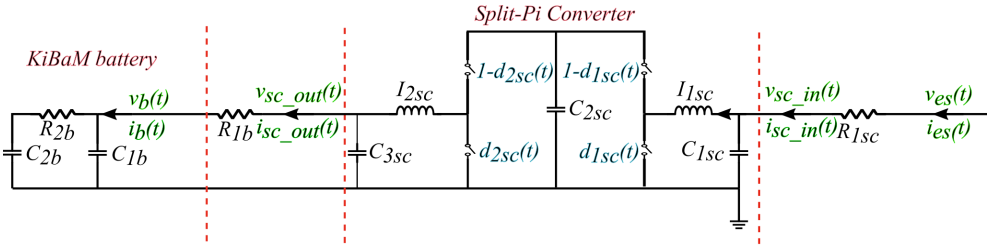

Figure 4.3.5: Electrical network of the battery connected to the Split-Pi converter during charging mode, where $v_{es}(t)$ varies according to the power losses in the central transmission network.

flat representation of the ES system generated by the algorithm in section 3.3.2.1 will be considered. The variable $v_{es}(t)$ can be written in function of the flat outputs as in (3.3.26k). However, this relation is too complicated to be integrated in the optimization problem and written in function of the B-splines. Therefore, an alternative solution will be presented. Taking into account that the converters considered in the model are ideal as already introduced in section 2.4.2.1, the input power of the converter, $P_{sc\_in}(t)$, is equal to the output power of the converter, $P_{sc\_out}(t)$, as in (2.4.18), which leads to:

$$v_{sc\_in} i_{sc\_in} = v_{sc\_out} i_{sc\_out}. \tag{4.3.17}$$

Moreover, the input voltage v_{sc_in} of the Split-Pi is always close to 400 V meaning higher than the expecting output voltage, v_{sc_out}, coming from the battery. Therefore, the Split-Pi converter will continually operates in down-conversion towards the positive direction and in up-conversion otherwise, which means that d_{1sc} is equal to 0 and only d_{2sc} will change values in the $(0, 1)$ interval (for further explanation see also section 4.3.3). Hence, from (2.4.17):

$$\alpha = \frac{i_{sc\_in}}{i_{sc\_out}} = \frac{u_{sc\_out}}{u_{sc\_in}} = \frac{1 - d_{2sc}}{1 - d_{1sc}} = 1 - d_{2sc}. \tag{4.3.18a}$$

Additionally, through Ohm's law, a connection among the input and output voltage, $v_{sc\_in}(t)$ and $v_{sc\_out}(t)$ and current, $i_{sc\_in}(t)$ and $i_{sc\_out}(t)$, of the Split-Pi converter and the input voltage, $v_{es}(t)$, and current, $i_{es}(t)$,

of the ES system and the input voltage, $v_b(t)$, and current, $i_b(t)$, of the battery are obtained below:

$$v_{sc\_in}(t) = v_{es}(t) - R_{1sc} i_{es}(t) \tag{4.3.19a}$$
$$v_{sc\_out}(t) = v_b(t) + i_b(t) R_{1b} \tag{4.3.19b}$$
$$i_{sc\_in}(t) = i_{es}(t) \tag{4.3.19c}$$
$$i_{sc\_out}(t) = i_b(t) \tag{4.3.19d}$$

Therefore, combining the above equations in (4.3.19) and in (4.3.18), we conclude to the relations below:

$$v_{es}(t) = \frac{v_b(t) + i_b(t) R_{1b}}{\alpha(t)} + R_{1sc} \alpha(t) i_b(t) \tag{4.3.20a}$$
$$i_{es}(t) = \alpha(t) i_b(t) \tag{4.3.20b}$$

and the ES power is deduced as follows:

$$P_{es}(t) = v_{es}(t) i_{es}(t) = (v_b(t) + i_b(t) R_{1b}) i_b(t) + R_{1sc} (\alpha(t) i_b(t))^2 \tag{4.3.21}$$

Substituting (4.3.16) in the cost function in (4.3.14), the cost function becomes:

$$\mathcal{J} = \int_{t_0}^{t_f} ep(t) \Big[Q_{cost} \big[\underbrace{P_{es}(t)}_{v_{es}(t) i_{es}(t)} - P_{pv}(t) + P_{loads}(t) \big] + Q_{loss} \big[\frac{(v_{es}(t) - v_{loads}(t))^2}{R_1} + \frac{(v_{loads}(t) - v_{ug}(t))^2}{R_2} + \frac{(v_{ug}(t) - v_{pv}(t))^2}{R_4} + \frac{(v_{pv}(t) - v_{es}(t))^2}{R_3} \big] \Big] \mathrm{d}t. \tag{4.3.22a}$$

where $v_{es}(t), i_{es}(t), P_{es}(t)$ are defined by (4.3.20a), (4.3.20b), (4.3.21) respectively. Since the variables $v_{es}(t)$ and $i_{es}(t)$ are written in function of the voltage and the current of the battery, v_b and i_b, they can be written also in function of the B-splines according to (4.3.10a) and (4.3.10b).

Additionally , the following are also considered before writing the final form of the objective function of (4.3.15a):

- from (2.5.13), the voltage, v_{loads}, on the connecting node $n : 1$ is written in function of the input voltage, v_{es}, and the input current, i_{es}, of the ES system:

$$v_{loads}(t) = R_1 i_{es}(t) + (1 + \frac{R_1}{R_3}) v_{es}(t) - \frac{R_1}{R_3} v_{pv}(t); \tag{4.3.23}$$

- from (2.3.4) and (2.5.17) the generated power from the PV system is written also in function of the voltages on the connecting nodes, v_{es}, v_{pv}, v_{ug}:

$$P_{pv}(t) = v_{pv}(t) i_{pv}(t) = v_{pv}(t) \Big[\frac{v_{pv}(t) - v_{es}(t)}{R_3} - \frac{v_{ug}(t) - v_{pv}(t)}{R_4} \Big]; \tag{4.3.24}$$

- from (2.3.4) and (2.5.16), the constraint for the consumer's demand is considered as follows:

$$P_{loads}(t) - \epsilon_{loads} \leq v_{loads}(t) \Big[\frac{v_{es}(t) - v_{loads}(t)}{R_1} - \frac{v_{loads}(t) - v_{ug}(t)}{R_2} \Big] \leq P_{loads}(t) + \epsilon_{loads}, \tag{4.3.25}$$

  where ϵ_{loads} is the soft constraint to relax the load's demand in order to ensure the feasibility of the optimization problem.

The voltages on the connecting nodes, v_{es}, v_{ug}, v_{loads} and v_{pv}, obey to (4.2.18). The v_{loads} and i_{loads} are also written in function of the B-splines, since they are in function of v_{es} and i_{es} as in (4.3.23). Two last constraints remain to be found for the $\alpha(t)$ factor and the $P_{ug}(t)$ in (4.3.15h) (taking into account also (4.3.13a)):

$$\alpha(t)^{-1} > 1, \tag{4.3.26a}$$
$$P_{ug}^{min,h} \leq P_{ug}(t) \leq P_{ug}^{max,h}. \tag{4.3.26b}$$
$$P_{ug}^{min,h} \leq P_{es}(t) - P_{pv}(t) + P_{loads}(t) + P_{R_1}(t) + P_{R_2}(t) + P_{R_3}(t) + P_{R_4}(t) \leq P_{ug}^{max,h}. \tag{4.3.26c}$$

To ensure constraint validation in continuous-time, (4.3.26a) and (4.3.26b) must be deduced in function of the B-splines. The α factor is, firstly, parametrized considering $\frac{1}{\alpha(t)} \in (1, +\infty)$ and a set of B-splines basis functions of order d_α as follows:

$$\frac{1}{\alpha(t)} = \sum_{j=1}^{N_\alpha} p_j^\alpha \boldsymbol{b}_{i,\boldsymbol{d}_\alpha}(t) \tag{4.3.27}$$

where N_α is the number of control points $\boldsymbol{p}_i^\alpha$. Then, applying Theorem B.2.1 from Appendix B, the constraint of the α factor will be as follows:

$$\boldsymbol{p}_i^\alpha > 1, \forall i = 1, \dots, N_\alpha. \tag{4.3.28}$$

Since α lies in the interval of $(0, 1)$, meaning that is positive, the following can be considered for the second part of (4.3.20a):

$$-R_{1sc}|i_b(t)| \leq R_{1sc}\alpha(t)i_b(t) \leq R_{1sc}|i_b(t)|. \tag{4.3.29}$$

Therefore, the constraint $v_{DC}^{min,h} \leq v_{es}(t) \leq v_{DC}^{max,h}$, where v_es is considered as in (4.3.20a), is valid if and only if:

$$\frac{v_b(t) + i_b(t)R_{1b}}{\alpha(t)} - R_{1sc}|i_b(t)| \geq v_{DC}^{min,h}, \tag{4.3.30a}$$

$$\frac{v_b(t) + i_b(t)R_{1b}}{\alpha(t)} + R_{1sc}|i_b(t)| \leq v_{DC}^{max,h}. \tag{4.3.30b}$$

Then, for (4.2.18) and (4.3.26b), (4.3.20a), (4.3.20b) and (4.3.21) are combined to conclude to the following:

$$\big(\boldsymbol{p}_{\kappa,i}^{v_b} + R_{1b}\boldsymbol{p}_{\kappa,i}^{i_b}\big)\boldsymbol{p}_j^\alpha - R_{1sc}|\boldsymbol{p}_{\kappa,i}^{i_b}| \geq v_{DC}^{min,h}, \tag{4.3.31a}$$

$$\big(\boldsymbol{p}_{\kappa,i}^{v_b} + R_{1b}p_{\kappa,i}^{i_b}\big)\boldsymbol{p}_j^\alpha + R_{1sc}|\boldsymbol{p}_{\kappa,i}^{i_b}| \leq v_{DC}^{max,h}, \tag{4.3.31b}$$

where $\boldsymbol{p}_{\kappa,i}^{v_b}$ and $\boldsymbol{p}_{\kappa,i}^{i_b}$ are defined by (4.3.9) and κ, i and $j \in \mathbb{N}$ satisfy $\boldsymbol{d}-1 \leq \kappa \leq n-1$, $\kappa - \boldsymbol{d}+2 \leq i \leq \kappa+1$ and $1 \leq j \leq N_\alpha$. After calculation, which is given explicitly in Appendix B.3, the previous inequalities are rewritten as:

$$\begin{aligned} v_{DC}^{min,h} &\leq \sum_{i=1}^{N}\sum_{j=1}^{N_\alpha}(\boldsymbol{p}_{\kappa,i}^{v_b} + R_{1b}\boldsymbol{p}_{\kappa,i}^{i_b})\boldsymbol{p}_j^\alpha \boldsymbol{b}_{i,j,\boldsymbol{d}}(t) - \sum_{i=1}^{N}\sum_{j=1}^{N_\alpha} R_{1sc}|\boldsymbol{p}_{\kappa,i}^{i_b}|\boldsymbol{p}_j^\alpha \boldsymbol{b}_{i,j,\boldsymbol{d}}(t) \leq \\ &\leq \sum_{i=1}^{N}\sum_{j=1}^{N_\alpha}\big[\boldsymbol{p}_{\kappa,i}^{v_b} + R_{1b}\boldsymbol{p}_{\kappa,i}^{i_b} - R_{1sc}|\boldsymbol{p}_{\kappa,i}^{i_b}|\big]\boldsymbol{p}_j^\alpha \boldsymbol{b}_{i,j,\boldsymbol{d}}(t), \end{aligned} \tag{4.3.32a}$$

$$\begin{aligned} v_{DC}^{max,h} &\geq \sum_{i=1}^{N}\sum_{j=1}^{N_\alpha}(\boldsymbol{p}_{\kappa,i}^{v_b} + R_{1b}\boldsymbol{p}_{\kappa,i}^{i_b})\boldsymbol{p}_j^\alpha \boldsymbol{b}_{i,j,\boldsymbol{d}}(t) + \sum_{i=1}^{N}\sum_{j=1}^{N_\alpha} R_{1sc}|\boldsymbol{p}_{\kappa,i}^{i_b}|\boldsymbol{p}_j^\alpha \boldsymbol{b}_{i,j,\boldsymbol{d}}(t) \geq \\ &\geq \sum_{i=1}^{N}\sum_{j=1}^{N_\alpha}\big[(\boldsymbol{p}_{\kappa,i}^{v_b} + R_{1b}\boldsymbol{p}_{\kappa,i}^{i_b}) + R_{1sc}|\boldsymbol{p}_{\kappa,i}^{i_b}|\big]\boldsymbol{p}_j^\alpha \boldsymbol{b}_{i,j,\boldsymbol{d}}(t). \end{aligned} \tag{4.3.32b}$$

Concerning the constraint of the $P_{ug}(t)$, from (2.5.18), it is defined below:

$$\begin{aligned} P_{ug}(t) = v_{ug}(t)i_{ug}(t) = v_{ug}(t)[i_{R_4}(t) - i_{R_2}(t)] &= v_{ug}(t)\left[\frac{v_{ug}(t) - v_{pv}(t)}{R_4} - \frac{v_{loads}(t) - v_{ug}(t)}{R_2}\right] = \\ &= v_{ug}^2(t)(\frac{1}{R_4} + \frac{1}{R_2}) - v_{ug}(t)\big[\frac{v_{pv}(t)}{R_4} + \frac{v_{loads}(t)}{R_2}\big]. \end{aligned} \tag{4.3.33}$$

Replacing $v_{loads}(t)$ with (4.3.23) leads to:

$$P_{ug}(t) = v_{ug}^2(t)(\frac{1}{R_4} + \frac{1}{R_2}) - \frac{1}{R_4}v_{ug}(t)v_{pv}(t) - v_{ug}(t)\big[R_1 i_{es}(t) + (1 + \frac{R_1}{R_3})v_{es}(t) - \frac{R_1}{R_3}v_{pv}(t)\big]. \tag{4.3.34}$$

Including also (4.3.20a) and (4.3.20b), $P_{ug}(t)$ is denoted as:

$$\begin{aligned} P_{ug}(t) &= v_{ug}^2(t)(\frac{1}{R_4}+\frac{1}{R_2}) + v_{ug}(t)v_{pv}(t)(\frac{R_1}{R_2R_3}-\frac{1}{R_4}) \\ &\quad - \frac{1}{R_2}v_{ug}(t)\big[R_1\alpha(t)i_b(t) + (1+\frac{R_1}{R_3})\frac{v_b(t)+R_{1b}i_b(t)}{\alpha(t)} + R_{1sc}\alpha(t)i_b(t)\big] \\ &= v_{ug}^2(t)(\frac{1}{R_4}+\frac{1}{R_2}) + v_{ug}(t)v_{pv}(t)(\frac{R_1}{R_2R_3}-\frac{1}{R_4}) \\ &\quad - \frac{1}{R_2}v_{ug}(t)\big[(1+\frac{R_1}{R_3})\frac{v_b(t)+R_{1b}i_b(t)}{\alpha(t)} + (R_1+R_{1sc}+\frac{R_1R_{1sc}}{R_3})\alpha(t)i_b(t)\big]. \end{aligned} \tag{4.3.35}$$

Therefore, finally, the constraint (4.3.26b) is defined as:

$$\begin{aligned} P_{ug}^{max,h} &\geq v_{ug}^2(t)(\frac{1}{R_4}+\frac{1}{R_2}) + v_{ug}(t)v_{pv}(t)(\frac{R_1}{R_2R_3}-\frac{1}{R_4}) \\ &\quad - \frac{1}{R_2}v_{ug}(t)\big[(1+\frac{R_1}{R_3})\frac{v_b(t)+R_{1b}i_b(t)}{\alpha(t)} - (R_1+R_{1sc}+\frac{R_1R_{1sc}}{R_3})|i_b(t)|\big], \end{aligned} \tag{4.3.36a}$$

$$\begin{aligned} P_{ug}^{min,h} &\leq v_{ug}^2(t)(\frac{1}{R_4}+\frac{1}{R_2}) + v_{ug}(t)v_{pv}(t)(\frac{R_1}{R_2R_3}-\frac{1}{R_4}) \\ &\quad - \frac{1}{R_2}v_{ug}(t)\big[(1+\frac{R_1}{R_3})\frac{v_b(t)+R_{1b}i_b(t)}{\alpha(t)} + (R_1+R_{1sc}+\frac{R_1R_{1sc}}{R_3})|i_b(t)|\big]. \end{aligned} \tag{4.3.36b}$$

Additionally, considering that $-|i_b(t)| \leq \alpha(t)i_b(t) \leq |i_b(t)|$ and $\frac{v_b(t)+R_{1b}i_b(t)}{\alpha(t)} > 0$ we can rewrite the two previous constraints, (4.3.36a) and (4.3.36b), as follows:

$$\begin{aligned} (1+\frac{R_1}{R_3})\frac{v_b(t)+R_{1b}i_b(t)}{\alpha(t)} - (R_1+R_{1sc}+\frac{R_1R_{1sc}}{R_3})|i_b(t)| \geq -\frac{R_2}{v_{ug}(t)}\big[P_{ug}^{max,h} - v_{ug}^2(t)(\frac{1}{R_4}+\frac{1}{R_2}) \\ - v_{ug}(t)v_{pv}(t)(\frac{R_1}{R_2R_3}-\frac{1}{R_4})\big], \end{aligned} \tag{4.3.37a}$$

$$\begin{aligned} (1+\frac{R_1}{R_3})\frac{v_b(t)+R_{1b}i_b(t)}{\alpha(t)} + (R_1+R_{1sc}+\frac{R_1R_{1sc}}{R_3})|i_b(t)| \leq -\frac{R_2}{v_{ug}(t)}\big[P_{ug}^{min,h} - v_{ug}^2(t)(\frac{1}{R_4}+\frac{1}{R_2}) \\ - v_{ug}(t)v_{pv}(t)(\frac{R_1}{R_2R_3}-\frac{1}{R_4})\big]. \end{aligned} \tag{4.3.37b}$$

Next, through (B.3.1a) and (B.3.1b) in Appendix B.3, the left part of (4.3.37a) and (4.3.37b) is defined in function of the B-splines:

$$\begin{aligned} &(1+\frac{R_1}{R_3})\frac{v_b(t)+R_{1b}i_b(t)}{\alpha(t)} \pm (R_1+R_{1sc}+\frac{R_1R_{1sc}}{R_3})|i_b(t)| \\ &= (1+\frac{R_1}{R_3})\sum_{i=1}^{N}\sum_{j=1}^{N_\alpha}(\boldsymbol{p}_{\kappa,i}^{v_b}+R_{1b}\boldsymbol{p}_{\kappa,i}^{i_b})\boldsymbol{p}_j^\alpha \boldsymbol{b}_{i,j,\boldsymbol{d}}(t) \pm (R_1+R_{1sc}+\frac{R_1R_{1sc}}{R_3})\sum_{i=1}^{N}\sum_{j=1}^{N_\alpha}\left|\boldsymbol{p}_{\kappa,i}^{i_b}\right|\boldsymbol{b}_{i,j,\boldsymbol{d}}(t), \end{aligned} \tag{4.3.38}$$

which is proven similarly as in (B.3.2a) and (B.3.2b).

Hence, the optimization problem of (4.3.15a)-(4.3.15h) becomes:

$$\begin{aligned} \min_{\boldsymbol{p},\boldsymbol{p}^\alpha,v_{pv}(t),v_{ug}(t)} \int_{t_0}^{t_f} ep(t)\Big[&Q_{cost}\big[(v_b(t)+i_b(t)R_{1b})i_b(t)+R_{1sc}(\alpha(t)i_b(t))^2 - P_{pv}(t)+P_{loads}(t)\big] + \\ &+Q_{loss}\big[\frac{(\frac{v_b(t)+i_b(t)R_{1b}}{\alpha(t)}+R_{1sc}\alpha(t)i_b(t)-v_{loads}(t))^2}{R_1} + \frac{(v_{loads}(t)-v_{ug}(t))^2}{R_2} + \\ &+\frac{(v_{pv}(t)-\frac{v_b(t)+i_b(t)R_{1b}}{\alpha(t)}+R_{1sc}\alpha(t)i_b(t))^2}{R_3} + \frac{(v_{ug}(t)-v_{pv}(t))^2}{R_4}\big]\Big]\mathrm{d}t \end{aligned} \tag{4.3.39a}$$

$$\textit{subject to}: \textit{ the system dynamics } (2.5.1)-(2.5.2b), \tag{4.3.39b}$$

$$\textit{the power conservation } (4.3.13a), \tag{4.3.39c}$$

$$\textit{the voltage constraints on the connecting nodes } (4.2.18) \tag{4.3.39d}$$

$$v_b^{min,h} \leq \sum_{i=1}^{N} \boldsymbol{p}_{\kappa_i}^{v_b} \boldsymbol{b}_{i,\boldsymbol{d}}(t) \leq v_b^{max,h},$$

$$i_b^{min,h} \leq \sum_{i=1}^{N} \boldsymbol{p}_{\kappa_i}^{i_b} \boldsymbol{b}_{i,\boldsymbol{d}}(t) \leq i_b^{max,h}, \tag{4.3.39e}$$

$$q_{2b}^{min,h} \leq \sum_{i=1}^{N} \boldsymbol{p}_i \boldsymbol{b}_{i,\boldsymbol{d}}(t) \leq q_{2b}^{max,h}, \tag{4.3.39f}$$

$$\textit{the } P_{ug} \textit{ constraints } (4.3.36a), (4.3.36b), \tag{4.3.39g}$$

$$\textit{the central network relations constraints } (4.3.23), (4.3.24), (4.3.25), \tag{4.3.39h}$$

where $v_b(t)$ and $i_b(t)$ are written in terms of the B-splines as in(4.3.10a) and (4.3.10b) respectively.

Then, in the next subsection, the middle level of the hierarchical problem is described. Note that the reference profiles obtained at the high level for the battery current, i_b, battery voltage, v_b, and input voltage of the ES system v_{es} will be denoted in the middle level as i_b^{ref}, v_b^{ref} and v_{es}^{ref}, respectively. Similarly for the α factor reference profile which is also mentioned at the middle level as α^{ref}.

4.3.2 Middle level control

In here, a tube-MPC controller is introduced to track the output voltage reference profile, $v_{sc\_out}^{ref}$, of the Split-Pi converter under perturbation. Consider that the output voltage reference of the converter can be written in function of the battery current and voltage reference profiles obtained at the high level by solving (4.3.3a)-(4.3.3f):

$$v_{sc\_out}^{ref}(t) = v_b^{ref}(t) + i_b^{ref}(t) R_{1b}, \tag{4.3.40}$$

according to Ohm's law obtained from the electrical circuit (Fig. 4.3.2). At this level, the system of the battery will be discretized through Euler explicit as presented below:

$$\dot{\tilde{x}}(t = kT_s) \approx \frac{\tilde{x}(k+1) - \tilde{x}(k)}{T_s}, \tag{4.3.41}$$

where T_s is the discretization sampling time. Consequently, using the Euler explicit method, the battery's dynamics is discretized having as state variables the charges of the battery, q_{1b} and q_{2b}, as input variable the output voltage from the Split-Pi converter, v_{sc_out}, and as output variables the current and voltage of the battery, v_b and i_b, denoted as:

$$\tilde{x}(k) = \begin{bmatrix} \tilde{q}_{1b}(k) & \tilde{q}_{2b}(k) \end{bmatrix}^\top, \quad \tilde{u}(k) = \tilde{v}_{sc\_out}(k), \quad \tilde{y}(k) = \begin{bmatrix} \tilde{i}_b(k) & \tilde{v}_b(k) \end{bmatrix}^\top, \tag{4.3.42}$$

where we have the state vector $\tilde{x}(k) \in \mathbb{R}^2$, the input $\tilde{u}(k) \in \mathbb{R}$ and the output vector $\tilde{y}(k) \in \mathbb{R}^2$. From the ES electrical circuit, we obtain some additional information according to which $\tilde{i}_b(k) = \tilde{i}_{sc}(k)$ and $\tilde{v}_b(k) = \dfrac{\tilde{q}_{1b}(k)}{C_{1b}}$. Therefore, we obtain the discretized system as follows:

$$\begin{cases} \tilde{x}_b(k+1) & = A\tilde{x}_b(k) + B\tilde{u}_b(k), \\ \tilde{y}(k) & = C\tilde{x}_b(k) + D\tilde{u}_b(k), \end{cases} \tag{4.3.43}$$

with $A \in \mathbb{R}^{2\times 2}$, $B \in \mathbb{R}^2$, $C \in \mathbb{R}^{2\times 2}$ and $D \in \mathbb{R}^2$ equal to:

$$A = \begin{bmatrix} 1 - \dfrac{T_s}{C_{1b}}\left(\dfrac{1}{R_{1b}} + \dfrac{1}{R_{2b}}\right) & \dfrac{T_s}{C_{2b}R_{2b}} \\ \dfrac{T_s}{C_{1b}R_{2b}} & 1 - \dfrac{T_s}{C_{2b}R_{2b}} \end{bmatrix}, \quad B = \begin{bmatrix} \dfrac{T_s}{R_{1b}} \\ 0 \end{bmatrix},$$

$$C = \begin{bmatrix} -\dfrac{1}{C_{1b}R_{1b}} & 0 \\ \dfrac{1}{C_{1b}} & 0 \end{bmatrix}, \quad D = \begin{bmatrix} \dfrac{1}{R_{1b}} \\ 0 \end{bmatrix}.$$

4.3.2.1 Transmission line network in the absence of power losses

Next a tracking MPC controller is proposed in which the cost penalizes the tracking error (the difference between the actual and the reference output profiles) over a finite prediction horizon N_p:

$$\min_{\tilde{u}(k)} \sum_{i=k}^{k+N_p-1} (\tilde{y}(i)-\tilde{y}^{ref}(i))^\top Q_{\tilde{y}}(\tilde{y}(i)-\tilde{y}^{ref}(i))+(\tilde{u}(i)-\tilde{u}^{ref}(i))^\top R_{\tilde{u}}\left(\tilde{u}(i)-\tilde{u}^{ref}(i)\right) \tag{4.3.44a}$$

$$subject\ to:\ the\ system\ dynamics\ (4.3.43), \tag{4.3.44b}$$

$$\tilde{v}_b^{min,m} \leq \tilde{v}_b(k) \leq \tilde{v}_b^{max,m}, \tag{4.3.44c}$$

$$\tilde{i}_b^{min,m} \leq \tilde{i}_b(k) \leq \tilde{i}_b^{max,m}, \tag{4.3.44d}$$

$$\tilde{q}_{2b}^{min,m} \leq \tilde{q}_{2b}(k) \leq \tilde{q}_{2b}^{max,m}, \tag{4.3.44e}$$

$$\tilde{P}_{ug}^{min,m} \leq \tilde{P}_{ug}(k) \leq \tilde{P}_{ug}^{max,m}, \tag{4.3.44f}$$

with $\tilde{y}^{ref}(k) = \begin{bmatrix}\tilde{i}_b^{ref}(k) & \tilde{v}_b^{ref}(k)\end{bmatrix}^\top$, the current and voltage references of the battery, and $\tilde{u}^{ref}(k) = \tilde{v}_{sc\_out}^{ref}(k)$, the output voltage reference of the Split-Pi converter, taken with a sampling time, T_s. The last constraint $P_{ug}(t)$, it is rewritten as shown below (4.3.2a):

$$\tilde{P}_{ug}^{min,m} - \tilde{P}_{loads}(k) + \tilde{P}_{pv}(k) \leq \tilde{P}_{es}(k) \leq \tilde{P}_{ug}^{max,m} - \tilde{P}_{loads}(k) + \tilde{P}_{pv}(k), \tag{4.3.45}$$

where $\tilde{P}_{es}(k) = \tilde{i}_b(k)\tilde{v}_b(k)$ as aforementioned. The above objective function is in quadratic form with non-linear constraints and a variable electricity cost. Additionally, the profiles of the PV, the loads demand and the electricity price are employed as in Fig. 4.3.1.

4.3.2.2 Error dynamics

At the high level, a desired profile is generated for the voltage v_b and the current i_b of the battery. The dynamics considered at the middle level has to follow these profiles (replaced by the output voltage of the Split-Pi converter v_{sc_out}) in the best possible way. This approach is the so-called *tube-MPC* (Langson et al., 2004) where an MPC law provides the nominal input (based on the nominal, noise-free dynamics) and the actual input adds to the nominal value a corrective term which counteracts the noise.

Definition 4.3.1. *(Robust positively invariant set (Yu et al., 2013)): Let us consider a nominal system* $\dot{\tilde{x}}(t) = f(\tilde{x}(t),\tilde{u}(t),0)$ *and an actual system* $\dot{\tilde{x}}_w(t) = f_w(\tilde{x}_w(t),\tilde{u}_w(t),\tilde{w}(t))$. *The error between them is denoted as* $s(t) = \tilde{x}_w(t) - \tilde{x}(t)$ *and the error system is given as follows:*

$$\dot{s}(t) = f_w(\tilde{x}_w(t),\tilde{u}_w(t),\tilde{w}(t)) - f(\tilde{x}(t),\tilde{u}(t),0), \tag{4.3.46}$$

where $\tilde{x}(t) \in \tilde{\mathcal{X}}$. *Furthermore, a control signal is designed which is composed by a nominal input and a state feedback control as follows:*

$$\tilde{u}_w(t) = \tilde{u}(t) + K(\tilde{x}_w(t),\tilde{x}(t)), \tag{4.3.47}$$

where $\tilde{u}(t) \in \tilde{\mathcal{U}}$ *and* $K(\tilde{x}_w(t),\tilde{x}(t)) : \tilde{\mathcal{X}} \times \tilde{\mathcal{X}} \longrightarrow \mathbb{R}^m$, *where min is the number of inputs. A set* $\mathcal{S} \subset \tilde{\mathcal{X}} \subset \mathbb{R}^n$ *(n is the number of states) is called robust invariant for the error system in* (4.3.46), *if a feedback controller* K *exists for which* $\tilde{u}(t) + K(\tilde{x}_w(t),\tilde{x}(t)) \subseteq \tilde{\mathcal{U}} \in \mathbb{R}^m$ *such that for all* $= e(t_0) \in \mathcal{S}$ *and for all* $w \in \mathcal{W}$, $s(t) \in \mathcal{S}$ *for* $t \geq t_0$. $\mathcal{S}$ *is the robust positively invariant (RPI) set of the error system* (4.3.46) *under a feedback control law* K.

The tracking error, under certain assumptions, can be bounded by a RPI set. Since the profile to be tracked is generated at the high level, we can tighten the constraints considered in its design in order to guarantee reliability under noises (with the tightening factor being defined by the aforementioned RPI set). The pair of nominal input and nominal state $(\tilde{u}_b(k),\tilde{x}_b(k)$ is generated by the application of the MPC law over the nominal dynamics of the battery (4.3.48b). Furthermore, the real dynamics (4.3.48a) is affected by the bounded noise $\tilde{w}_b(k)$:

$$\tilde{x}_{w_b}(k+1) = A\tilde{x}_{w_b}(k) + B\tilde{u}_{w_b}(k) + \tilde{w}_b(k), \tag{4.3.48a}$$

$$\tilde{x}_b(k+1) = A\tilde{x}_b(k) + B\tilde{u}_b(k), \tag{4.3.48b}$$

where $\tilde{w}_b(k)$ is the perturbation, $\tilde{x}_b(k)$ is the nominal state and $\tilde{x}_{w_b}(k)$ is the real, noise-affected, state. Linking the nominal and actual inputs through the relation $\tilde{u}_{w_b}(k) = \tilde{u}_b(k) + K(\tilde{x}_b(k) - \tilde{x}_{w_b}(k))$ allows us to write the tracking error dynamics:

$$s_b(k+1) = (A + BK)s_b(k) + \tilde{w}_b(k), \tag{4.3.49}$$

where $s_b(k) = \tilde{x}_{w_b}(k) - \tilde{x}_b(k)$. For any pair $(A,\ B)$ in (4.3.48b) controllable there exists a static feedback K such that $(A+BK)$ is stable which means that there exists an RPI set $\mathcal{S}_b$ for which $s_b(k) \in \mathcal{S}_b\ \forall\ k \geq k_0$ holds. Such a set can be computed with the *ultimate bounds* method (Kofman et al., 2007) or iterative procedures (Olaru et al., 2010).

Having $s_b(k) \in \mathcal{S}_b$, it is equivalent with $\tilde{x}_{w_b}(k) \in \{\tilde{x}_b(k) \oplus \mathcal{S}\}$ (note that $\oplus$ is the Minkowski sum[2]). In other words, the nominal $\tilde{x}_b(k)$ has to be chosen more conservatively than $\tilde{x}_{w_b}(k)$. Thus, to ensure that $\tilde{x}_{w_b}(k) \in \tilde{\mathcal{X}}_b = \{\tilde{x}_b^{min,m} \leq \tilde{x}_b(k) \leq \tilde{x}_b^{max,m}\}$, $\tilde{x}_b(k)$ must be confined as follows:

$$\tilde{x}_b(k) \in \tilde{\mathcal{X}}_b \ominus \mathcal{S} \tag{4.3.50}$$

Note that the restriction on $\tilde{x}(k)$ translates to a similar restriction on $\tilde{y}(k)$:

$$\tilde{y}_b(k) \in \tilde{\mathcal{Y}}_b \ominus C\mathcal{S}_b, \tag{4.3.51}$$

where $\tilde{\mathcal{Y}}_b$ is a shorthand notation for constraints (4.3.44c),(4.3.44d) and (4.3.44f). The $\ominus$ symbol refers to the Pontryagin difference[3]. This tightening term $C\mathcal{S}_b$ is considered in the profile generation at the high level at (4.3.10a)-(4.3.10b).

4.3.2.3 Transmission line network with power losses

At this point, similarly to the case of the transmission central network without the power losses in section 4.3.2.1, we continue using the tube-MPC controller and the discrete dynamics of the system 4.3.43. However, since the power losses are taken into account, the MPC tracking problem is reformulated as follows:

$$\min_{\tilde{u}(k)} \sum_{i=k}^{k+N_p-1} (\tilde{v}_{es}(i) - \tilde{v}_{es}^{ref}(i))^\top Q_{\tilde{v}_{es}} (\tilde{v}_{es}(i) - \tilde{v}_{es}^{ref}(i)) + (\tilde{u}(i) - \tilde{u}^{ref}(i))^\top R_{\tilde{u}} \left(\tilde{u}(i) - \tilde{u}^{ref}(i)\right) \tag{4.3.52a}$$

$$subject\ \ to: \ the\ system\ dynamics\ (4.3.43), \tag{4.3.52b}$$

$$\tilde{v}_b^{min,m} \leq \tilde{v}_b(k) \leq \tilde{v}_b^{max,m}, \tag{4.3.52c}$$

$$\tilde{i}_b^{min,m} \leq \tilde{i}_b(k) \leq \tilde{i}_b^{max,m}, \tag{4.3.52d}$$

$$\tilde{q}_{2b}^{min,m} \leq \tilde{q}_{2b}(k) \leq \tilde{q}_{2b}^{max,m}, \tag{4.3.52e}$$

$$\tilde{v}_{es}^{min,m} \leq \tilde{v}_{es}(k) \leq \tilde{v}_{es}^{max,m}, \tag{4.3.52f}$$

$$\tilde{P}_{ug}^{min,m} \leq \tilde{P}_{ug}(k) \leq \tilde{P}_{ug}^{max,m}. \tag{4.3.52g}$$

In the last constraint $P_{ug}(t)$, the power losses must be considered in the power conservation equation as in (4.3.13a) in section 4.3.1.2. Therefore, (4.3.52g) is replaced by:

$$\tilde{P}_{ug}^{min,m} - \tilde{P}_{loads}(k) + \tilde{P}_{pv}(k) - \tilde{P}_{R_1}(k) - \tilde{P}_{R_2}(k) - \tilde{P}_{R_3}(k) - \tilde{P}_{R_4}(k) \leq \tilde{P}_{es}(k), \tag{4.3.53a}$$

$$\tilde{P}_{ug}^{max,m} - \tilde{P}_{loads}(k) + \tilde{P}_{pv}(k) - \tilde{P}_{R_1}(k) - \tilde{P}_{R_2}(k) - \tilde{P}_{R_3}(k) - \tilde{P}_{R_4}(k) \geq \tilde{P}_{es}(k), \tag{4.3.53b}$$

where $\tilde{P}_{es}(k) = \tilde{i}_{es}(k)\tilde{v}_{es}(k)$. $\tilde{i}_{es}(k)$ and $\tilde{v}_{es}(k)$ are calculated with respect to the α factor reference profile, α^{ref}, obtained at the high level as in (4.3.20a) and (4.3.20b):

$$v_{es}(k) = \frac{v_b(k) + i_b(k)R_{1b}}{\alpha^{ref,h}(k)} + R_{1sc}\alpha^{ref}(k), \tag{4.3.54a}$$

$$i_{es}(k) = \alpha^{ref}(k) i_b(k). \tag{4.3.54b}$$

[2]It is the sum of two position vectors X_1 and X_2 which results from the addition of each vector in X_1 to each vector in X_2.

[3]It is the difference between two position vectors X_1 and X_2. More precisely, it describes the difference between each vector in X_1 and each vector in X_2 resulting in another vector $X_3 : X_3 + X_2 \subseteq X_1$.

4.3.3 Low level control

In the low level control, the fast dynamics of the system is considered caused by the switching activity within the Split-Pi converter. Here, the duty cycles of the switches are supervised according to the tracking profiles we obtained in the middle level, that we will use as references.

In order to proceed to the analysis of the Split-Pi converter system, we follow the patent of United States Patent and Trademark Office No: US 6914420 B2 published on July 2005 (Crocker, 2005) as already described in section 2.2.1.3. The patent provides the relations among the input and output voltage, v_{sc_in} and v_{sc_out}, and the duty cycles, d_{1sc} and d_{2sc}, of the converter. As already mentioned, the Split-Pi always operates in down-conversion towards the positive direction and in up-conversion otherwise. This means that only the duty cycle d_{2sc} will function and change values from 0 to 1 (on/off switching between Sw_3 and Sw_4 as shown in section 2.2.1.3). Therefore, the duty cycle d_{1sc} is always equal to 0 (Sw_2 is always off and Sw_1 is always on as shown in section 2.2.1.3). Consequently, the control variable is d_{2sc} and through (2.4.20) and Ohm's law the following are deduced (also previously described in (4.3.18), (4.3.19), (4.3.20a), (4.3.20b)):

$$\alpha = \frac{v_{sc\_out}(t)}{v_{sc\_in}(t)} = 1 - d_{2sc}(t), \tag{4.3.55}$$

where

$$v_{sc\_in}(t) = v_{DC}(t) - i_{DC}(t)R_{1sc}, \tag{4.3.56}$$
$$v_{sc\_out}(t) = v_b(t) + i_b(t)R_{1b}. \tag{4.3.57}$$

Moreover, since there is no dissipation within the converter, the total power contained in the capacitors and inductors is preserved:

$$i_{DC}(t)v_{DC}(t) = i_b(t)v_{sc\_out}(t). \tag{4.3.58}$$

Taking into account the equations (4.3.55), (4.3.56), (4.3.57), (4.3.58), d_{2sc} is equal to:

$$d_{2sc}(t) = 1 - \frac{v_{DC}(t) - \sqrt{v_{DC}^2(t) - 4(v_{sc\_out}(t) - v_b(t))(v_{sc\_out})}}{2(v_{sc\_out}(t) - v_b(t))}. \tag{4.3.59}$$

The last equation (4.3.59) can be valid only if $v_{sc\_out}(t) \neq v_b(t)$.

In the case of the transmission network with power loss existence, the same procedure is followed at the low level since it concerns the internal supervision of the ES system.

4.4 Simulation results

In this section, the simulation results of the three levels of the hierarchical control design are presented. Table 4.4.1 depicts the parameters of the DC microgrid used for the simulations. To proceed, the reference profiles are taken into account, as presented in section 4.2.4.2. Furthermore, a collection of AGM 12-165 lead acid batteries is considered (165 Ah battery capacity) for the ES system. The DC microgrid is connected to the UG (4200 W maximum UG generation) through a DC breaker, as shown also in Fig. 2.5.1. For the simulations we use MATLAB 2015a. Furthermore, YALMIP optimization toolbox (Löfberg, 2004) was chosen for both high and middle level which allows the use of the IPOPT solver (Biegler and Zavala, 2009) capable to handle nonlinear optimization problems. For the low level, we design and implement the PH ES system (section 2.5.1) in MATLAB/Simulink in order to validate the proper operation of the switching activity within the Split-Pi converter.

4.4.1 Error dynamics

Firstly, the constraints of the current and the voltage of the battery should be adjusted at the high level according to the RPI set (4.3.50, 4.3.51) as presented before in section 4.3.2.2. At this point, we mention that disturbances are added at the nominal input variable of the discretized system (4.3.43, 4.3.2), the output voltage of the Split-Pi converter $\tilde{v}_{sc\_out}$, equivalent to 5% of the difference between the minimum and the maximum value of the $\tilde{v}_{sc\_out}^{ref}$ in (4.3.44a). In Table 4.4.4, the constraints of the high level are depicted. These are confined according to the constraints chosen at the middle level and the defined RPI set below (4.4.1).

In Fig. 4.4.1 and Fig. 4.4.2 we present the RPI set $\mathcal{S}_b$ and the nominal and noise-affected variables, respectively. At several time instants, the set was illustrated to highlight that the profiles are robust under

Table 4.4.1: Parameters of the variables.

Variable	Values	Units
R_{1sc}, R_{1b}, R_{2b}	1, 0.025, 0.088	$[\Omega]$
I_{1sc}, I_{2sc}	0.25, 0.25	$[H]$
C_{1sc}, C_{2sc}, C_{3sc}	0.0008, 0.0008, 0.0008	$[F]$
C_{1b}, C_{2b}	86400, 21600	$[F]$
R_1, R_2, R_3, R_4	1	$[\Omega]$

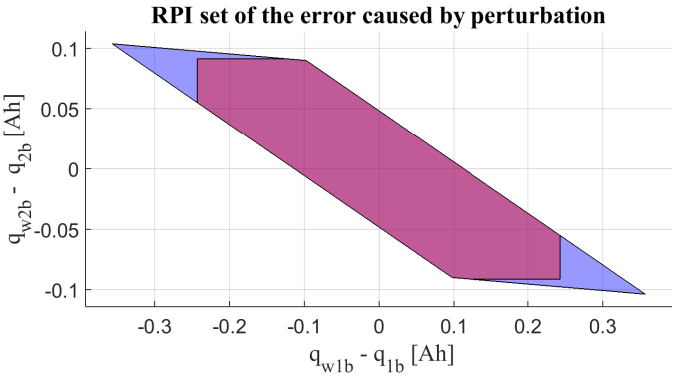

(a) RPI set $\mathcal{S}_b$ of the model states under perturbation.

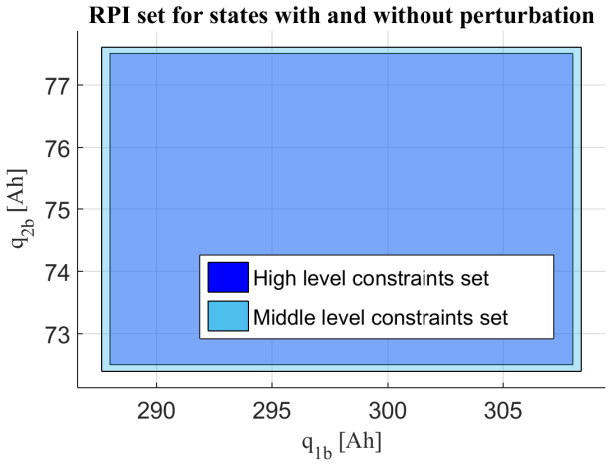

(b) RPI set of the battery's states constraints.

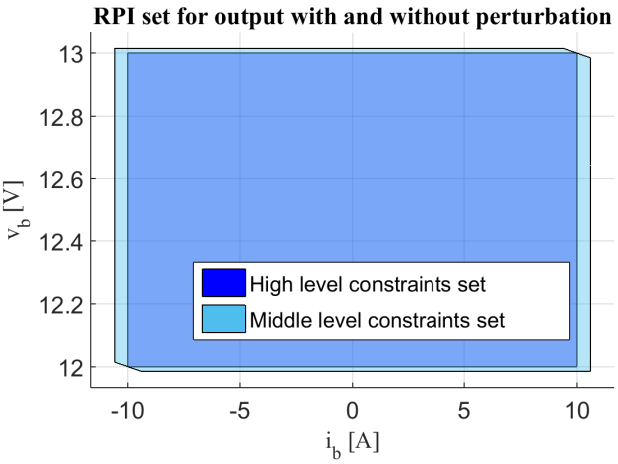

(c) RPI set of the battery's voltage and current constraints.

Figure 4.4.1: RPI sets for defining the constraints of high and middle level.

bounded noise (i.e., the real trajectory lies in a tube centered around the nominal trajectory). The corresponding RPI set is given below, which actually depicts the set where the error among the nominal and actual values can be. Therefore, the error is bounded as follows (see also Fig. 4.4.1a):

$$\mathcal{S}_b \triangleq \left\{ \begin{bmatrix} -0.38\ [Ah] \\ -0.11\ [Ah] \end{bmatrix} \leqslant \begin{bmatrix} \tilde{q}_{w_{1b}} - \tilde{q}_{1b} \\ \tilde{q}_{w_{2b}} - \tilde{q}_{2b} \end{bmatrix} \leqslant \begin{bmatrix} 0.38\ [Ah] \\ 0.11\ [Ah] \end{bmatrix} \right\} \tag{4.4.1}$$

and the associated static feedback $K = \begin{bmatrix} 0.685 \cdot 10^{-4} & 0.139 \cdot 10^{-4} \end{bmatrix}$ as in (4.3.48b). Hence, the constraints are restricted at the high level according to (4.4.1), (4.3.50) and (4.3.51), as illustrated also in Fig. 4.4.1b and Fig. 4.4.1c. Furthermore, from Fig. 4.4.2, we can verify that the states, $\tilde{q}_{1b}$ and $\tilde{q}_{2b}$ lie in the RPI set.

4.4.2 Simulation results of the high level without power losses

First, the simulation results of the high level are introduced under the absence of power losses in the central transmission network (as in (4.3.11a)-(4.3.11f)) following Table 4.4.2 simulation parameters. Fig. 4.4.4

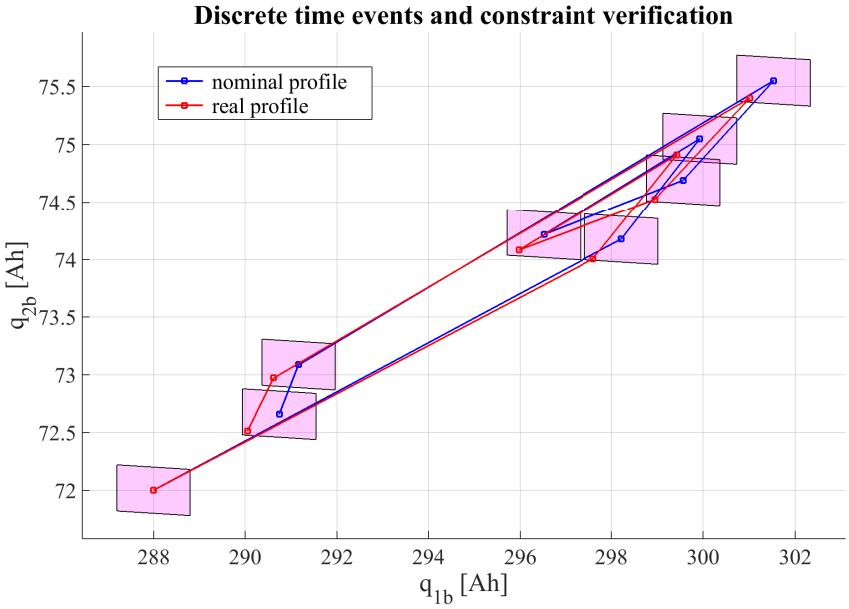

Figure 4.4.2: Ultimate bounds for discrete time events of the model states, $\tilde{q}_{1b}$ and $\tilde{q}_{2b}$ following the CU load profile.

portrays the simulation for both the commercial use (CU) (Fig. 4.4.4a) and the domestic use (DU) (Fig. 4.4.4b) profiles. The figure showing the *Power Balancing* (see Fig. 4.4.3a, 4.4.3b) contains the power generation coming from the ES and the *UG* within 24 hours taking into account the PV and the CU and DU consumers demand. For the CU, the demand is high during the day from $6a.m.$ to $4p.m.$. On the other hand, the DU demand increases during the afternoon after $4p.m.$. According to this two load profiles, the continuous-time reference trajectories for the P_{ug} and the P_{es} by solving the optimization problem expressed in function of the control points and B-splines without power losses (4.3.11a-4.3.11f). Afterwards, the reference profiles for the battery current, i_b, voltage, v_b, and charge, q_{2b}, are also generated in Fig. 4.4.3, where the constraints are satisfied. Note that the power positive sign indicates the power supplied to the microgrid.

Table 4.4.2: Variables and constraints for the high level.

	Variable	Values	Units
High level	Without power losses		
	N as in (4.3.11a)	18	
	d as in (4.3.11a)	4	
	With power losses		
	N as in (4.3.32a) (4.3.32b), (4.3.38)	27	
	N_a as in (4.3.32a) (4.3.32b), (4.3.38)	18	
	d=d_a as in (4.3.11a)	4	
Constraints	$v_b^{min,h} \leq v_b(t) \leq v_b^{max,h}$	$12 \leq v_b(t) \leq 13$	$[V]$
	$i_b^{min,h} \leq i_b \leq i_b^{max,h}$	$-9 \leq i_b(t) \leq 9$	$[A]$
	$q_{1b}^{min,m} \leq q_{1b}(t) \leq q_{1b}^{max,m}$	$288.3 \leq q_{1b}(t) \leq 307.7$	$[Ah]$
	$q_{2b}^{min,h} \leq q_{2b}(t) \leq q_{2b}^{max,h}$	$72.5 \leq q_{2b}(t) \leq 77.5$	$[Ah]$
	$P_{ug}^{min,h} \leq P_{ug}(t) \leq P_{ug}^{max,h}$	$-2100 \leq P_{ug}(t) \leq 4200$	$[W]$
additional constraint (with power losses)	$v_{DC}^{min,h} \leq v_{ug,pv,es,loads}(t) \leq v_{DC}^{max,h}$	$380 \leq v_{ug,pv,es,loads}(t) \leq 430$	$[V]$

Table 4.4.3 presents the percentages of the power produced or consumed by the sources and loads, UG,

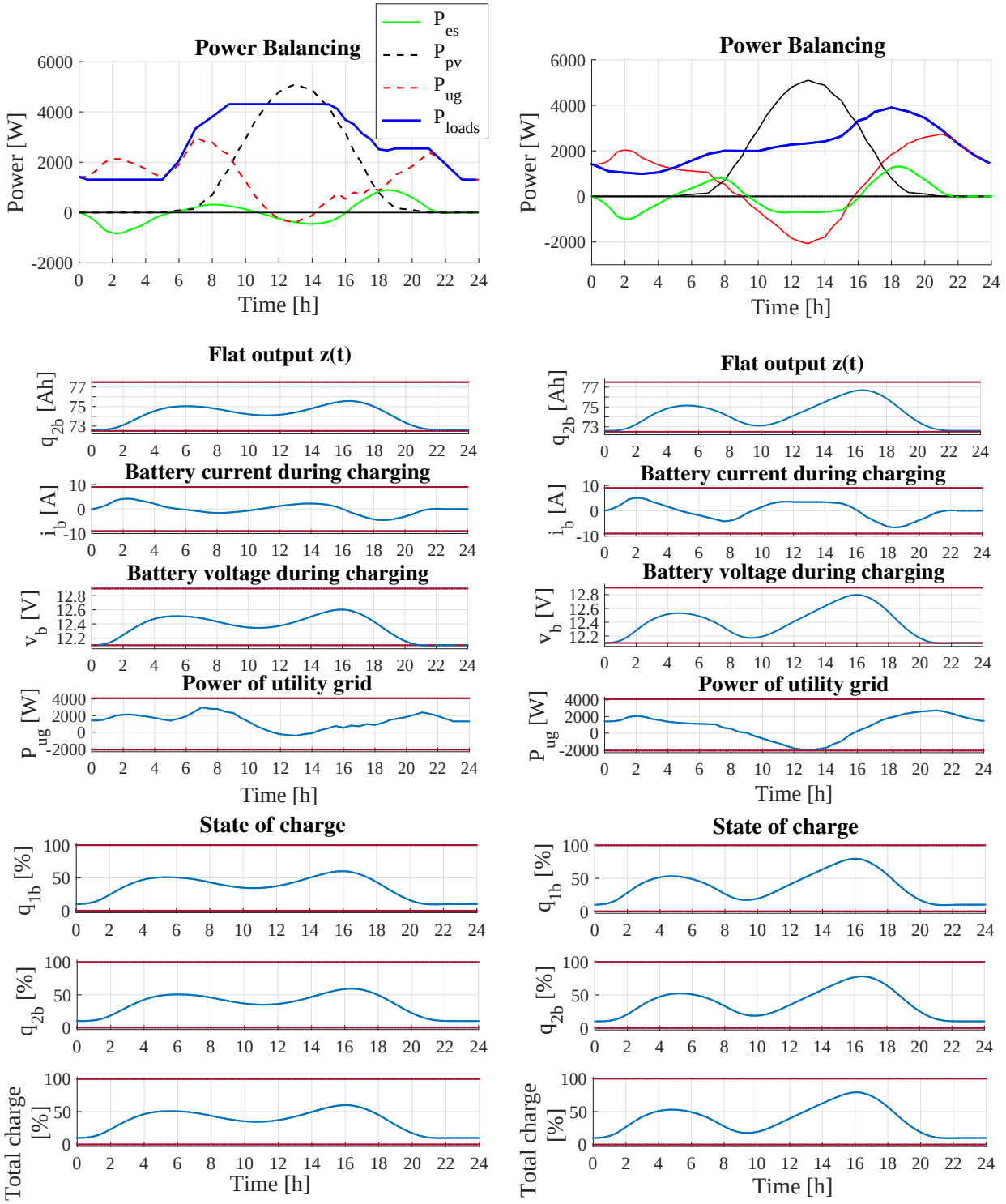

Figure 4.4.3: (a) Power balancing, optimal reference profiles and state of charge of the ES system of the CU. (b) Power balancing, optimal reference profiles and state of charge of the ES system of the domestic load profile. The red lines at the upper and lower part represent the corresponding constraints. (Transmission line network without power losses)

PV, ES, in respect to the total generated power. The UG and and the PV source are producing the highest amount of the total power. In correlation with Fig. 4.4.3, in the case of the CU demand which is high during the day, the PV, generating 47% of the total energy, tries to satisfy the consumers demand and the rest is sold to the UG. While in the afternoon, both the UG and the ES contribute to the loads' supply especially

after $4p.m.$ when the energy generated from the PV is decreasing. Overall, only 1% of the ES power is sold to the UG and 93% of the total energy produced is addressed to the consumers. On the other hand, for DU, when the electricity price is high during the day the demand is low. The spare of the PV power is sold to the UG, almost 12% of the total power consumed. Additionally the batteries are charged during the night, when the electricity costs less, and during the day, when the PV power is at its peak (9% for charging of the total power consumed). In general, we notice that in both cases whenever the PV power fully covers the consumer demand, the difference is stored to the ES system or sold to the UG. Additionally, the electricity cost was calculated for both cases being equal to 4.052 *euros* for the CU profile and 2.462 *euros* for the DU profile. The cost without using the ES system is equal to 4.737 *euros* for the CU profile and 2.644 *euros* for the DU profile, which clearly shows its importance. In general, the simulation results are as expected, where for the CU case, where the demand is high during the day, the PV mostly supports the consumers' demand. While, in the DU case, where the demand is high during the afternoon, the power generated by the PV is either stored to the ES or sold to the UG. The power stored is used later in the afternoon together with the UG to satisfy the consumers' demand.

Table 4.4.3: Percentage of power in respect to the total power produced or consumed without power losses in the central network.

Load profile	Power	Power produced [%]	Power consumed [%]	Electricity cost [euros]
Commercial	P_{ug}	46%	1% sold to the UG	4.052
	P_{es}	7%	6% for ES charging	-
	P_{pv}	47%	-	-
	P_{loads}	-	93% for load usage	-
Domestic	P_{ug}	40%	12% sold to the UG	2.462
	P_{es}	9%	9% for ES charging	-
	P_{pv}	51%	-	-
	P_{loads}	-	79% for load usage	-

Table 4.4.4: Results for different numbers of control points.

Load profile	N as in (4.3.11a)	Electricity cost [euros]	Computation time [s]	ES discharges
Commercial	18	4.052	157	2
	27	3.991	268	3
	36	3.576	525	7
	45	3.409	865	9
	54	3.188	1333	11
Domestic	18	2.462	136	2
	27	2.505	248	2
	36	2.193	482	7
	45	2.002	699	8
	54	1.797	916	9

At this point, the lifetime of the battery is considered. For this reason, after carrying out several simulations for different number of control points, N, as in (4.3.11a)-(4.3.11f), we obtain Table 4.4.4 which shows the electricity cost, the computation time and the number of discharges of the battery for both load profiles. We observe that as the number of control points grows, the computation time and the number of battery discharges increase, whereas the electricity cost decreases. From the number of discharges, the lifetime of the battery can be defined. Although notice that a large number of discharges leads to a decrease of battery's

capacitance. This results in a reduced life for the battery and, thus to higher operational costs (necessitated by its premature replacement). Therefore, the number of control points in the optimization problem needs to be kept as low as possible to extend the lifetime of the battery and increase the electricity cost savings.

4.4.3 Simulation results of the high level with power losses

In this section, the simulation results of the high level are introduced according to (4.3.39a)-(4.3.39h), including the transmission network with power losses. For the simulation, we follow similarly Table 4.4.2 with the added constraints for this case. The profiles generated at the high level for the CU (Fig. 4.4.4a) and the DU load (Fig. 4.4.4b) are illustrated. Moreover, the constraints of the system are considered as previously according to the RPI set found in section 4.4.1.

Table 4.4.5: Percentage of power in respect to the total power produced or consumed with power losses in the central network.

Load profile	Power	Power produced [%]	Power consumed [%]	Electricity cost [euros]
Commercial	P_{ug}	49.91%	1.78% sold to the UG	4.318
	P_{es}	0.79%	0.76% for ES charging	-
	P_{pv}	49.30%	-	-
	P_{loads}	-	96.9% for load usage	-
	P_{loss}	-	Total: 0.56% R_1: 0.12% R_2: 0.24% R_3: 0.11% R_4: 0.09%	-
Domestic	P_{ug}	42.14%	13% sold to the UG	2.713
	P_{es}	6.58%	6.7% for ES charging	-
	P_{pv}	51.28%	-	-
	P_{loads}	-	79.66% for load usage	-
	P_{loss}	-	Total: 0.64% R_1: 0.12% R_2: 0.21% R_3: 0.13% R_4: 0.18%	-

Concerning the simulations, in the CU case there is a large difference between the *Power Balancing* profiles generated from the network without losses (Fig. 4.4.3a) when compared to the network with losses (Fig. 4.4.4a). This happens because in a commercial environment, the consuming hours are during the day. Furthermore, the UG is unable to charge completely the batteries during the night, when the electricity cost is lower, because of the losses that exist in the transmission line (only 0.8% for battery charging). After, during the day, UG and PV sources collaborate (in total 99% power production) to satisfy the consumers' demand (97% consumed from the total power). This is possible considering that we keep same resistor values in the transmission lines, $R = 1\ \Omega$. In the case where the batteries are closer to the renewable sources, then the losses among them are lower and the batteries could be more effectively charged. Also, when the distance among the external grid and the microgrid is higher (meaning higher power loss), then the controller gives priority to the parts that are less affected by the power losses. On the other hand, in DU case (Fig. 4.4.3a) where there is no high demand from $12p.m.$ to $12a.m.$, the UG and the PV charge the batteries. In general, for the DU profile, similar profiles are obtained in both cases (Fig. 4.4.4b and Fig. 4.4.3b). The consumers' demand in the afternoon, while during the day until $3p.m.$ is more or less stable. As aforementioned, there

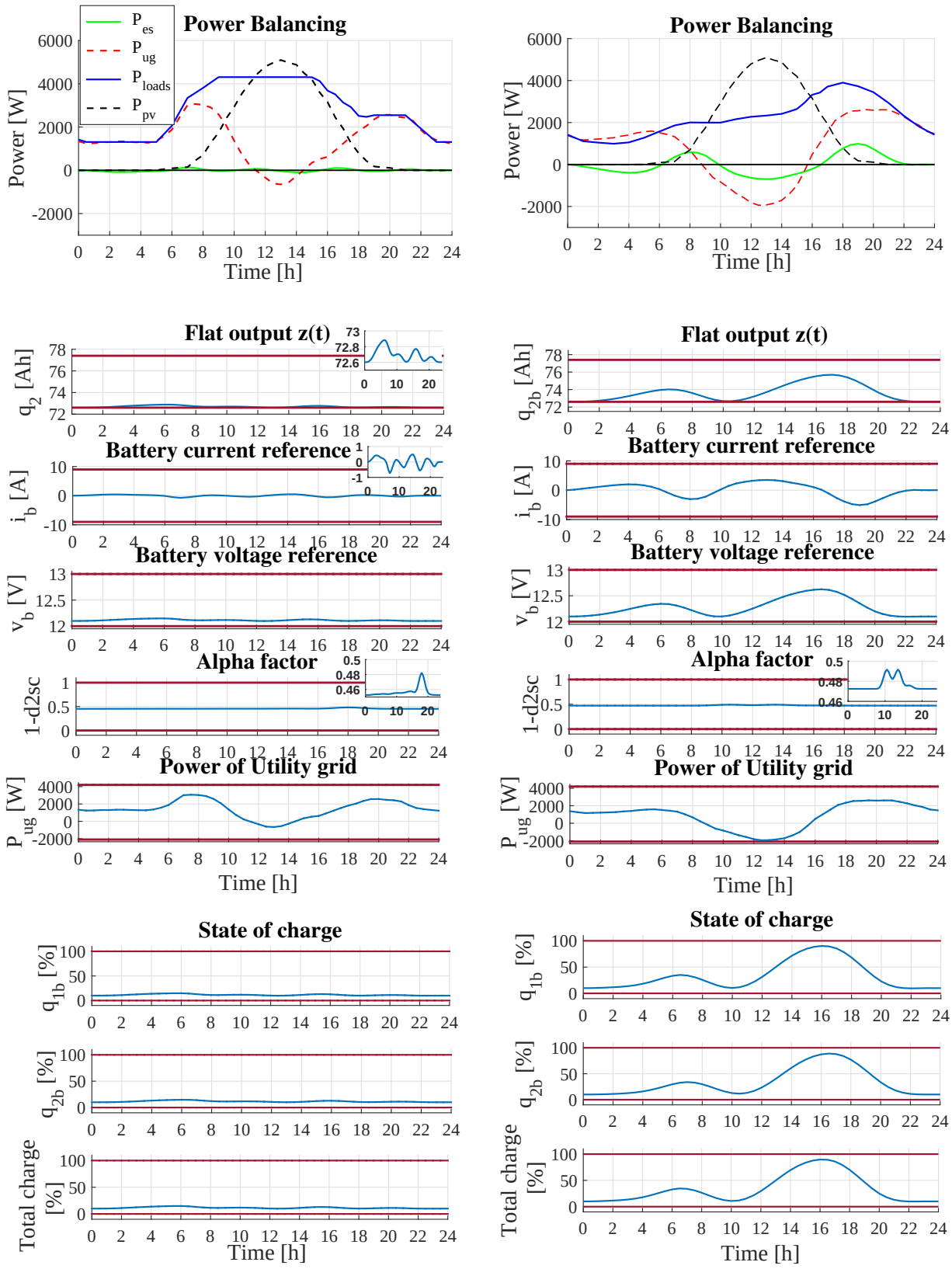

Figure 4.4.4: (a) Power balancing, optimal reference profiles and state of charge of the ES system of the commercial load profile. (b) Power balancing in the absence of power losses in the the transmission line network, optimal reference profiles and state of charge of the ES system of the domestic load profile. The red lines at the upper and lower part represent the corresponding constraints. (Transmission line network with power losses)

is, also, enough energy to sell to the UG (approximately 13% of the total power consumed). Hence, to make profit in a commercial environment, the use of larger installations for the renewable resources is important.

Likewise, the batteries' reference profiles for the current, voltage, state of charge are introduced where the constraints are verified. The electricity cost is also calculated which is 4.318 *euros* for the CUs and 2.713 *euros* for the DU. The cost without using the ES system is equal to 4.737 *euros* for the CU profile and 4.732 *euros* for the DU profile, where we observe that in the first case remains the same since the ES system usage is almost negligible. Although, in the case of the DU profile, the cost without the battery existence is a lot higher, since its usage is exploited in the best possible way.

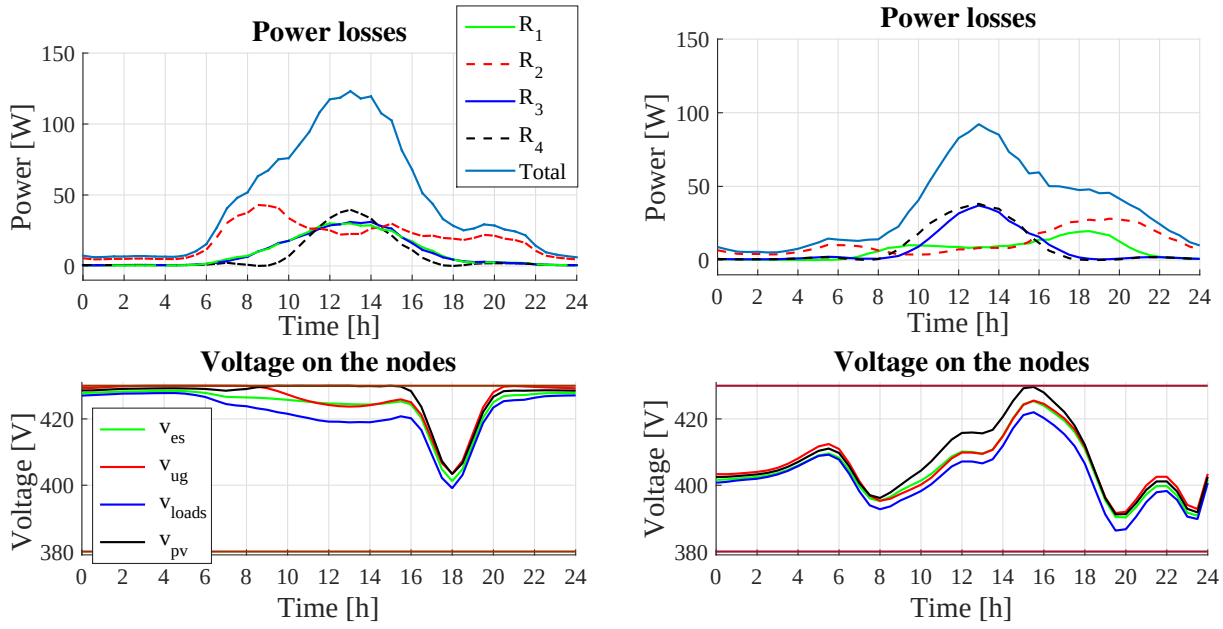

Figure 4.4.5: (a) Power losses and voltage on the transmission network nodes for CU profile. (b) Power losses and voltage on the transmission network nodes for DU profile. The red lines at the upper and lower part represent the corresponding constraints.

Afterwards, the power losses are depicted in Fig. 4.4.5 together with the constraint validation for the voltage on the four different nodes where the sources and the loads' systems stand. In the CU profile (Fig. 4.4.5a), the power losses are higher mostly because of the UG power purchase towards the loads during the day (transmission line R_2: 0.24% of the total power loss), while in the DU is less (Fig. 4.4.5b). Furthermore, we observe that the power losses in lines R_3 and R_4 are similar for both cases because of the PV purchase towards the UG or the ES system. For transmission line R_1, with the CU profile, the loss is around 0.12% of the total loss and higher than the DU case since a large amount of power is transmitted from the UG to the loads during the day. While, for the DU, the total loss of R_1 and R_2, about 0.33%, mostly exists due to the fact that the load demand increases during the afternoon. It is visible from Table 4.4.5 that, finally, the power loss is higher in the CU scenario since also the total power produced is higher than in the case of the DU load profile. The calculation time of the simulation is 12 *min* for the DU load and 6 *min* for the CU load.

As previously, the simulations correspond to the expected results. Since, the CU is high during the day, considering also the power losses existing in the transmission line network, the UG is unable to charge the batteries, since it must generate power for the consumers in cooperation with the PV source. In the DU case, since the consumers' demand is low during the day, similar results are expected as before without including the power losses in the central transmission network. The PV power is able to charge the batteries and sell power to the UG. However, because of the power losses, the power weakens while passing through the transmission lines.

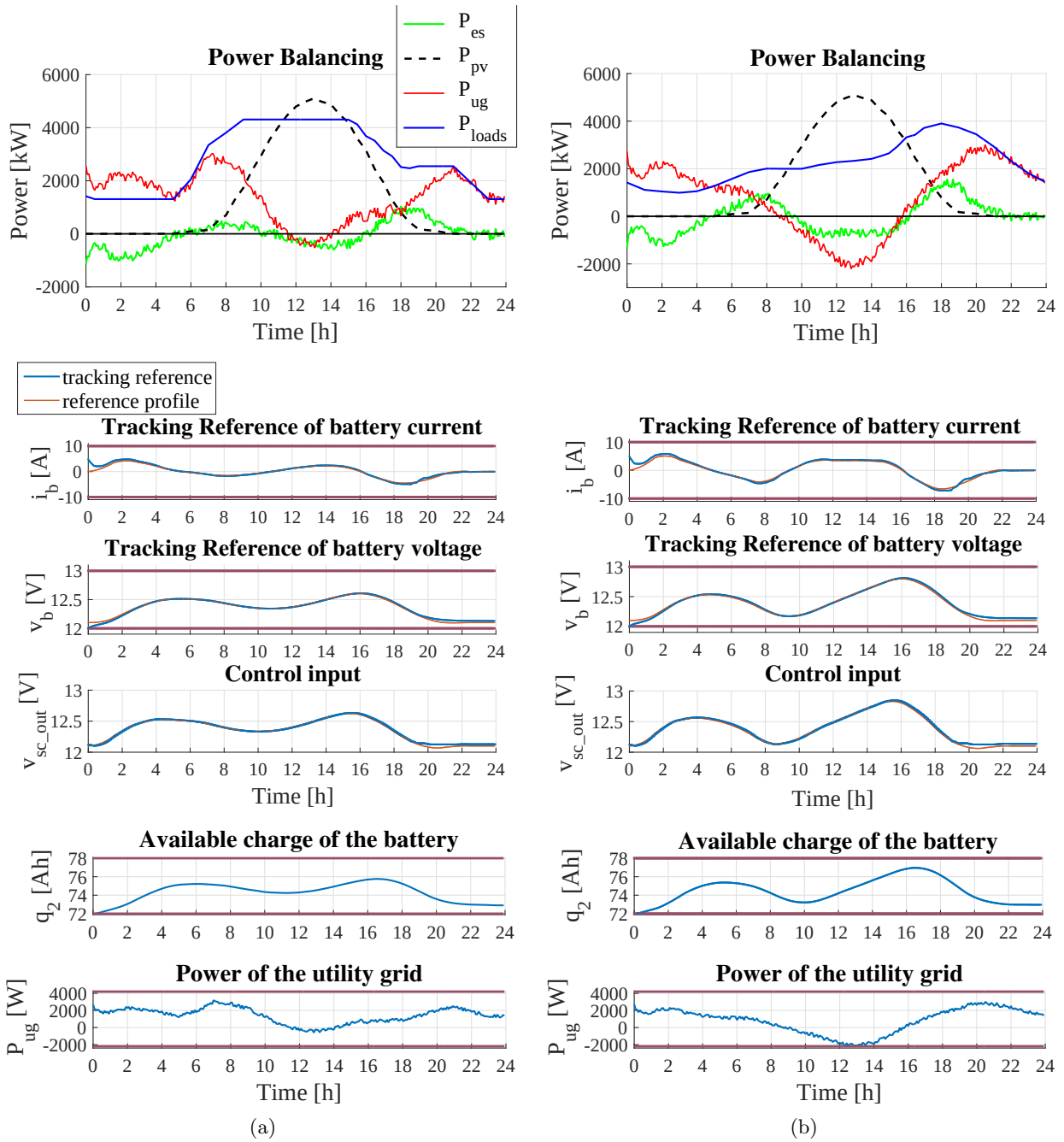

Figure 4.4.6: (a) Power balancing, tracking references, available charge and UG power of the commercial load profile. (b) Power balancing, tracking references, available charge and UG power of the domestic load profile. The red lines represent the corresponding constraints. (Transmission-line network without power losses)

4.4.4 Simulation results of the middle level

This section introduces the results of the middle level using as reference the optimal profiles generated at the high level for the battery current, i_b, and the voltage, v_b as in Fig. 4.4.3. Firstly, in Table 4.4.6, the parameters are set for the middle level simulations. As previously mentioned, in the middle level, we use MPC for reference tracking with a prediction horizon N_p equal to 5 and a sampling time T_s equal to 5 *min*. The system, at this point, is discretized as in (4.3.48a) and (4.3.48b) and it follows the optimization problem under constraints as in (4.3.44a)-(4.3.44f) without losses or as in (4.3.52a)-(4.3.52g) with losses in the transmission network. Additionally, a perturbation is added to the system that is always lower than the difference between the maximum and minimum state value defined previously by the RPI set.

In Fig. 4.4.6 and 4.4.7, we observe the tracking profiles of the *Power Balancing*, and the control input, v_{sc_out} (the output voltage of the Split-Pi converter), which is in function of the current, i_b, and the voltage,

Table 4.4.6: Variables and constraints for the middle level.

	Variable	Values	Units
Middle level	N_p as in (4.3.44a)	5	$[h]$
	T_s as in (4.3.43)	300	$[s]$
	Q_y as in (4.3.44a)	$diag(1,1)$	
	R_u as in (4.3.44a)	800	
Constraints	$v_b^{min,m} \leq \tilde{v}_b(k) \leq v_b^{max,m}$	$11.9 \leq \tilde{v}_b(k) \leq 13.1$	$[V]$
	$i_b^{min,m} \leq \tilde{i}_b(k) \leq i_b^{max,m}$	$-10.6 \leq \tilde{i}_b(k) \leq 10.6$	$[A]$
	$q_{1b}^{min,m} \leq \tilde{q}_{1b}(k) \leq q_{1b}^{max,m}$	$287.6 \leq \tilde{q}_{1b}(k) \leq 308.4$	$[Ah]$
	$q_{2b}^{min,m} \leq \tilde{q}_{2b}(k) \leq q_{2b}^{max,m}$	$72.3 \leq \tilde{q}_{2b}(k) \leq 77.7$	$[Ah]$
	$P_{ug}^{min,m} \leq \tilde{P}_{ug}(k) \leq P_{ug}^{max,m}$	$-2100 \leq \tilde{P}_{ug}(k) \leq 4200$	$[W]$
additional constraint (with power losses)	$v_{DC}^{min,h} \leq v_{ug,pv,es,loads}(t) \leq v_{DC}^{max,h}$	$370 \leq v_{ug,pv,es,loads}(t) \leq 430$	$[V]$

v_b of the battery as in (4.3.40). From the figures and the tables, Table 4.4.7 and Table 4.4.8, where the power produced and the power consumed are illustrated in respect to the total power, we observe that the optimal profiles obtained at the high level are very closely followed.

In the transmission network without power losses (Table 4.4.7), for the CU profile, a slight difference of 1% in charging and discharging of the battery is observed as well as for the power production by the UG. The cost of the electricity increases at this case about 2% and from 4.052 raises to 4.140 for the real profile. The same situation is noticed also for the DU demand regarding the discharging of the battery, but since there is no difference in the UG power production, the electricity cost remains the same. Therefore, for both the CU and the DU profile, the reference profiles are closely followed. The calculation time of the simulation lasts around 3 *min* for both the CU and the DU demands.

Table 4.4.7: Percentage of power in respect to the total power produced by the sources or consumed by the sources and the loads without power losses in the transmission lines.

Load profile	Power	Power produced [%]	Power consumed [%]	Power production difference from high level [%]	Power consumption difference with high level [%]
Commercial	P_{ug}	47%	1% sold to the UG	1%	0%
	P_{es}	6%	7% for ES charging	-1%	1%
	P_{pv}	47%	-	0%	-
	P_{loads}	-	92% for load usage	-	-1%
Domestic	P_{ug}	40%	12% sold to the UG	0%	0%
	P_{es}	9%	11% for ES charging	0%	-2%
	P_{pv}	51%	-	0%	-
	P_{loads}	-	77% for load usage	-	-2%

Similarly, for the transmission network with power losses, the same behavior is observed. There is small dissimilarities (less than 1%) between the UG power production/consumption reference and the real profiles as well as the battery's charging/discharging. The cost shortly changes, from 2.713 to 2.708 *euros* for the DU demand and from 4.318 to 4.308 *euros* . The electricity cost decreases slightly, approximately 0.2%, since the UG power production decreases and, in parallel, the power sold to the UG increases. Furthermore, the power

loss is higher by 1% for the real profiles because of the slight raise of power generated and transmitted from and to the ES system. Although, in general the errors are low and the reference profiles are well followed. The simulations time endure around 14 *min* for the CU demand and 9 *min* for the DU demand.

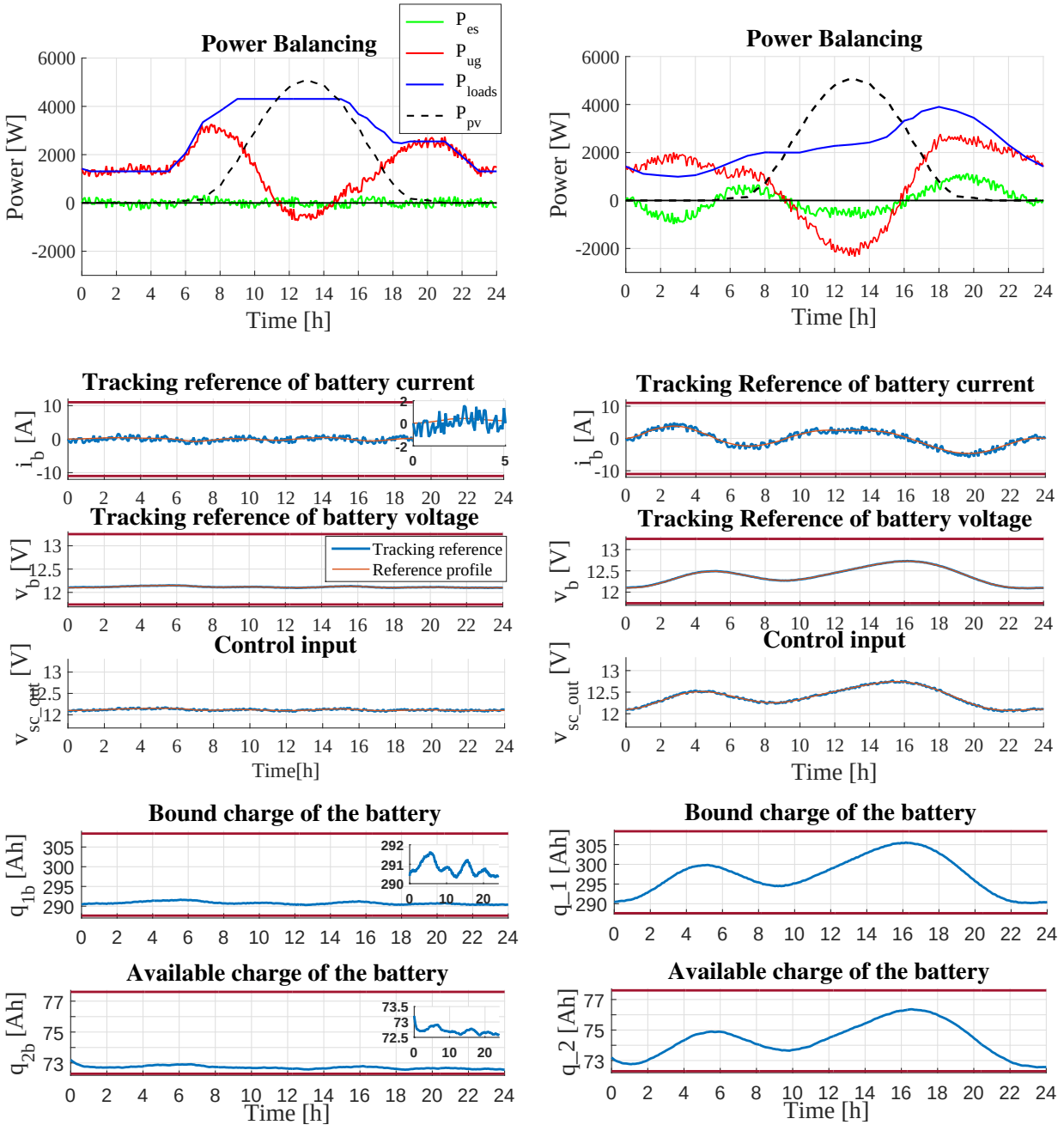

Figure 4.4.7: (a) Power balancing, tracking references, available charge and UG power of the commercial load profile. (b) Power balancing, tracking references, available charge and UG power of the domestic load profile. The red lines represent the corresponding constraints. (Transmission-line network with power losses)

Table 4.4.8: Percentage of power in respect to the total power produced or consumed with power losses in the central transmission network.

Load profile	Power	Power produced [%]	Power consumed [%]	Power production difference from high level [%]	Power consumption difference with high level [%]
Commercial	P_{ug}	49.24%	1.85% sold to the UG	-0.62%	0.07%
	P_{es}	2.08%	1.84% for ES charging	1.29%	1.05%
	P_{pv}	48.68%	-	-0.62%	-
	P_{loads}	-	94.74% for load usage	-	0.75%
	P_{loss}	-	1.57%	-	1.01%
Domestic	P_{ug}	41.27%	13.15% sold to the UG	-0.87%	0.08%
	P_{es}	7.95%	7.73% for ES charging	1.37%	0.97%
	P_{pv}	50.78%	-	-0.5%	-
	P_{loads}	-	77.71% for load usage	-	-1.05%
	P_{loss}	-	1.41%	-	0.77%

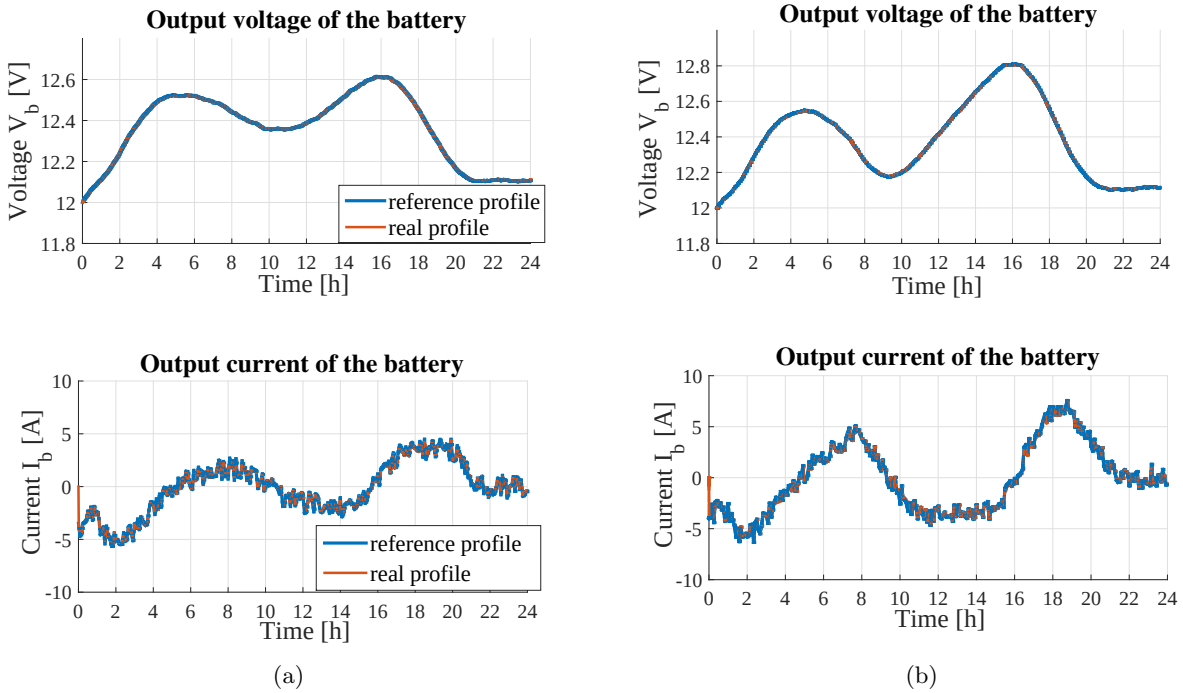

(a) (b)

Figure 4.4.8: (a) Voltage and current tracking profiles for CU. (b) Voltage and current tracking profiles for DU. (Transmission-line network without power losses)

4.4.5 Simulation results of the low level

In the following, we present the results obtained for the low level following the tracking profiles of the middle level for the battery current, i_b, and the voltage, v_b, under perturbation from Fig. 4.3.52a and Fig. 4.4.7. For both central transmission networks with or without power losses, the ES PH model (section 2.5.1) is considered, designed in MATLAB/Simulink. Afterwards, in the case of the powerlossless transmission network, the current, i_b, and the voltage, v_b, of the battery are considered as the reference profiles to follow, taking into account the control law developed in section 4.3.3 (4.3.59). The voltage coming from the central transmission network is stable equal to 400 V. For the transmission network with power losses, apart from the voltage and current reference profiles of the battery, the reference profile of the voltage, v_{es}, entering from the central transmission network is also considered.

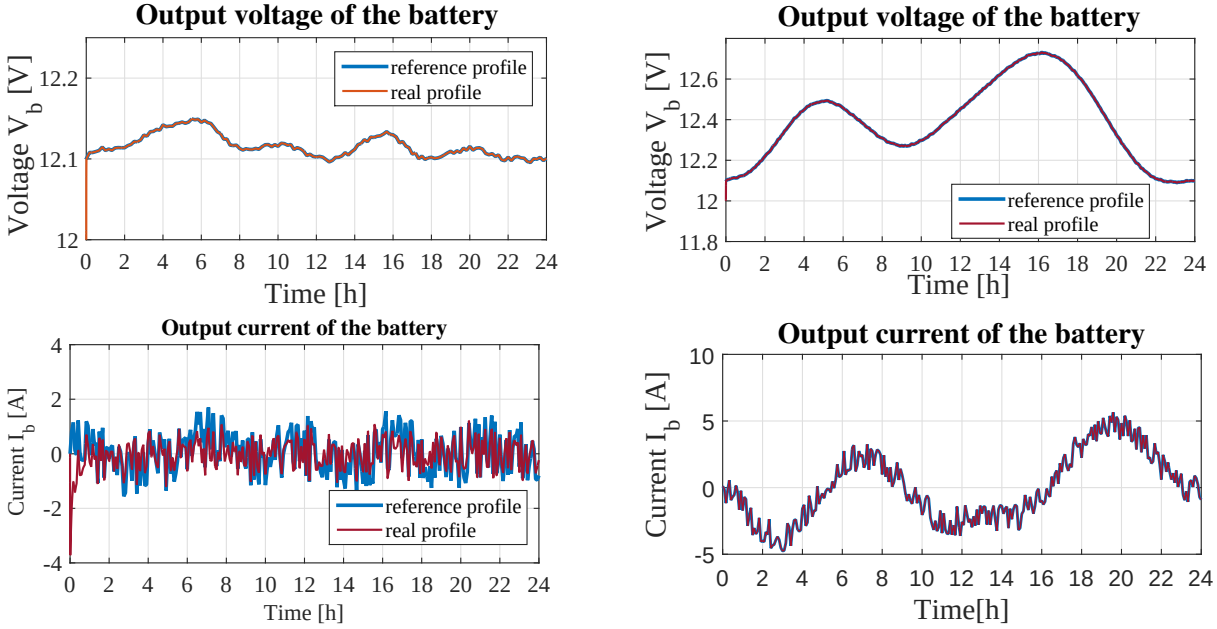

(a) (b)

Figure 4.4.9: (a) Voltage and current tracking profiles using the commercial load profile. (b) Voltage and current tracking profiles using the domestic load profile. (Transmission-line network with power losses)

The continuous-time simulation lasts for around 10 s and demonstrates the proper operation of the converter which regulates very well the current and the voltage according to the reference profiles as we can see in Fig. 4.4.8a and Fig. 4.4.8b for the powerlossless transmission line framework and in Fig. 4.4.9a and Fig. 4.4.9b for the network with losses. The reference profiles are very well followed by the low level controller and the operation of the switches of the Split-Pi converter is regulated.

4.4.6 Comparisons with MPC for optimal profiles generation

As it has been previously described, the reference trajectories were obtained through differential flatness and B-spline parametrization. As a next step, we compare the reference trajectories generation obtained through differential flatness and B-spline parametrization with MPC, as presented also in (Parisio et al., 2014) and (Iovine et al., 2018). For the simulation, the system with the power losses is considered (section 4.4.3). The simulation results are presented for the reference profiles obtained with MPC in Fig. 4.4.10 and Fig. 4.4.11. Similar trajectories are observed with a slight difference in the cost as it is depicted also in Table 4.4.9 of about $0.2 - 3\%$ for the DU and $2 - 5\%$ for the CU.

Because of the electricity cost difference between the optimal profiles obtained with MPC and flatness, we proceed to several simulations using MPC at the high level with different prediction horizons N_p and sampling times T_s. In Table 4.4.9, we notice that with MPC and a prediction horizon equal to 24 and a sampling time equal to 1200 s, more than 1000 s are needed to perform a simulation, approximately twice of the differential flatness calculation time for a $24h$ simulation. Furthermore, we observe that because of the discretization in MPC, the value of the sampling time greatly influences (for better or worse) the simulation's

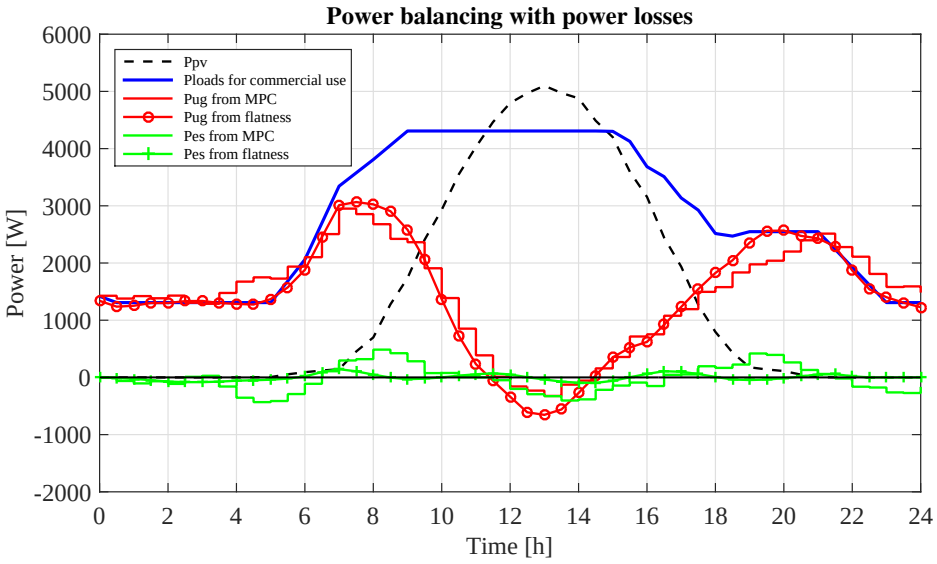

Figure 4.4.10: figure/Power balancing using commercial load profile. Comparisons of P_{es} and P_{ug} with optimal profiles obtained by MPC.

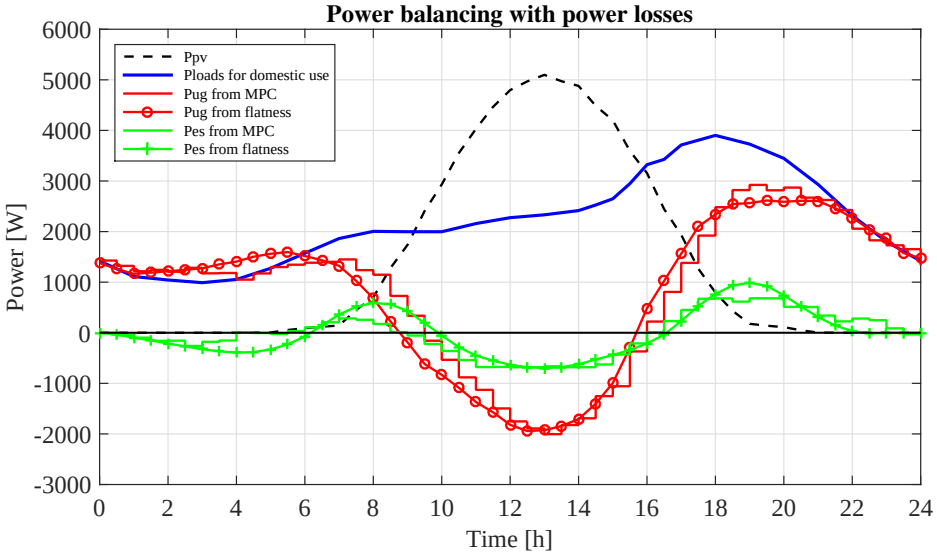

Figure 4.4.11: figure/Power balancing using domestic load profile. Comparisons of P_{es} and P_{ug} with optimal profiles obtained by MPC.

performance (note in particular the variation of the electricity cost). Therefore, we cannot ensure which case from Table 4.4.9 is the most effective in order to obtain the optimal profiles for the optimization problem. On the other hand with differential flatness, apart from the complexity of the flat outputs' calculation to construct the objective function and constraints, we have significant advantages:

- we avoid discretization since we solve an optimization problem in continuous time;
- since the simulations generated from differential flatness with B-spline parametrization are generated in continuous-time, the results are not affected by discretization approximations or under-sampling. Moreover, the profile is generated in its entirety for the full simulation horizon (and not piece by piece, as would be the case for a discrete optimization problem like MPC);
- practically, we observed that the total economic cost and required computational resources are lower when exploiting the flat representation;

Table 4.4.9: Simulation results obtained for optimal profiles with MPC.

Load	Prediction horizon N_p [h]	Sampling time T_s [s]	Electricity cost [euros]	Power loss [%]	Calculation time [s]
Commercial	24	1800	4.569	1.72%	1094
	24	1200	4.433	1.73%	522
	15	1800	4.418	1.74%	262
	15	1200	4.377	1.74%	251
	10	1800	4.441	1.74%	329
	10	1200	4.361	1.76%	310
	10	600	4.379	1.77%	763
Domestic	24	1200	2.801	1.63%	1315
	15	1800	2.747	1.65%	475
	15	1200	2.763	1.64%	400
	15	600	2.719	1.63%	751
	10	1800	2.788	1.64%	420
	10	1200	2.734	1.65%	452

- off-line simulations can predict system's behavior for different scenarios as in the case of lines under fault or long-time period simulations.

4.4.7 Optimal profile generation of different scenarios

Scenario 1: (One week optimal profiles generation) In here, we perform a simulation for one week considering the system without power losses as in section 4.4.2. The simulation lasts approximately 3 h and is performed under $N = 164$ control points. In Fig. 4.4.12, the *Power Balancing* and the constraints validation of the optimization problem are illustrated. For the reference profiles, the PV generated power holds the same profile every day, contrary to the load profile which varies and concerns a domestic environment. During the simulations, the battery is discharged 14 times (see also Fig. 4.4.12). Table 4.4.10 depicts the percentages of power produced and consumed by the sources and loads in respect to the total power. For the simulation, the same parameters as in Table 4.4.2 are considered.

Table 4.4.10: Simulation results of Scenario 1.

Power	Power produced [%]	Power consumed [%]	Electricity cost [euros]
P_{ug}	43.5%	13.4% sold to the UG	21.169
P_{es}	8.2%	8.2% for ES charging	-
P_{loads}	-	78.4% for load usage	-
P_{pv}	48.3%	-	-

Scenario 2: (Different values on the central lines resistors) In here, we consider two different scenarios as in Table 4.4.11:

- for the CU profile, the transmission lines R_1 and R_4 are with different values lower than the R_2 and R_3 considering a greater distance between the UG and the consumers, the PV and the ES than in the previous case;
- for the DU profile, the transmission lines R_1 and R_4 are equal to 1 Ω (as in section 4.4.3) and R_2 and R_3 are equal to 3 Ω keeping this way the renewable resource closer to the UG and the ES closer to the loads.

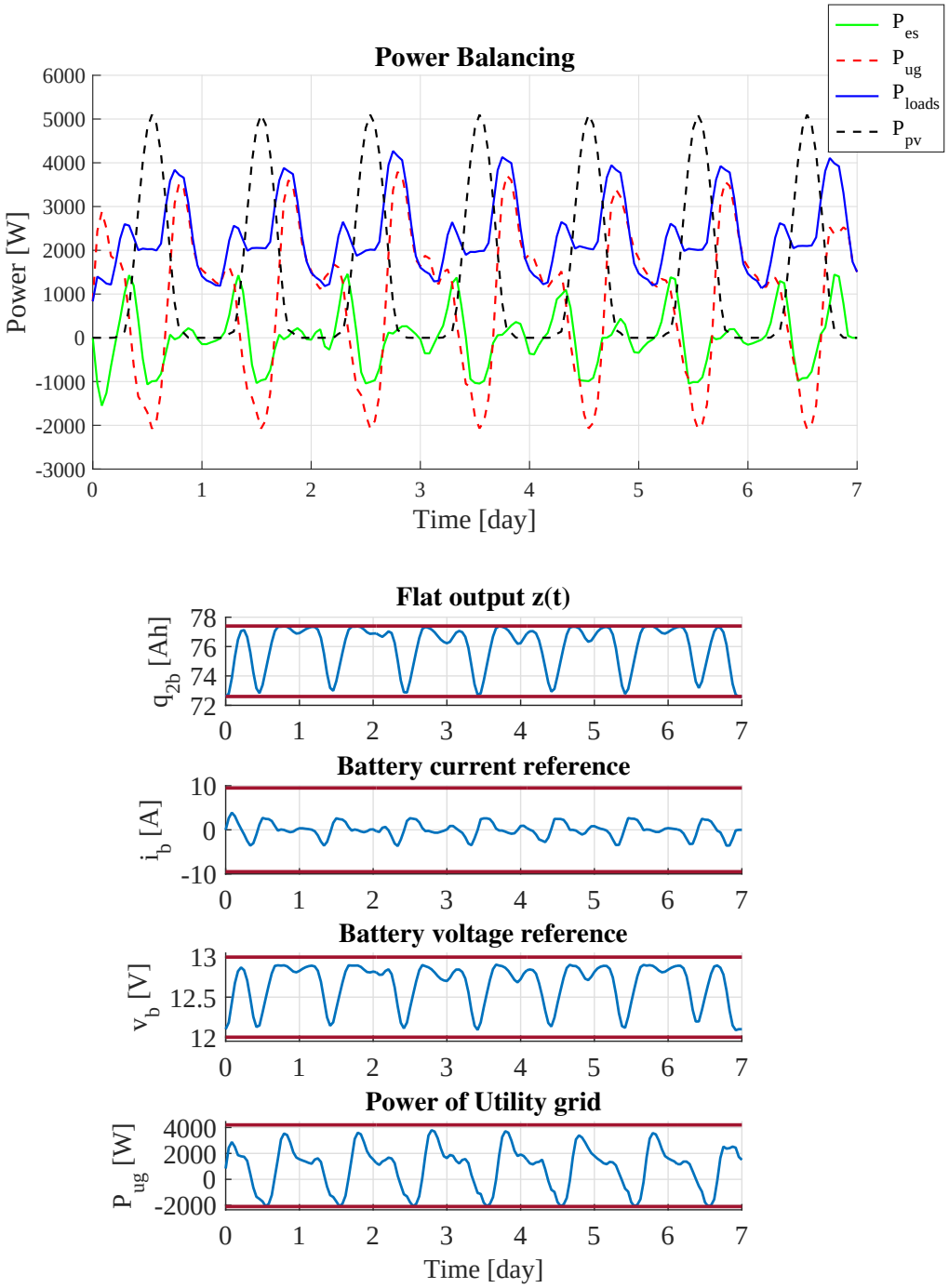

Figure 4.4.12: Power balancing and reference profiles within one week.

In the first case, the electricity cost increases for about 30 *cents* compared to the results obtained in section 4.4.3 for the CU profile, since the power loss among the loads and the UG is higher and, as a result, the external grid generates more power to satisfy the consumers' demand. Furthermore, the PV gives priority to the battery. Since the power loss is less from the battery to the loads, the battery discharges and transmit power towards the consumers. Equal behavior is observed also for the second scenario, where similarly the external grid needs to generate more power because of the loss that exists in R_2, while the profile of the ES power remains almost the same as in Fig. 4.4.4b. Therefore, from the aforementioned results, the number of PVs and batteries close to the load play an important role for the consumers' profit. The power generated from the renewable resources and the batteries must be able to overcome the power losses caused by the UG, reducing this way the UG power generation towards the microgrid.

Scenario 3: (Faulted lines in the transmission network) In here, considering the DU profile, optimal

Table 4.4.11: Resistor values for Scenario 2.

Load	Resistors	Value	Unit
Commercial	R_1	0.5	[Ω]
	R_2	5	[Ω]
	R_3	5	[Ω]
	R_4	0.2	[Ω]
Domestic	R_1, R_4	1	[Ω]
	R_2, R_3	3	[Ω]

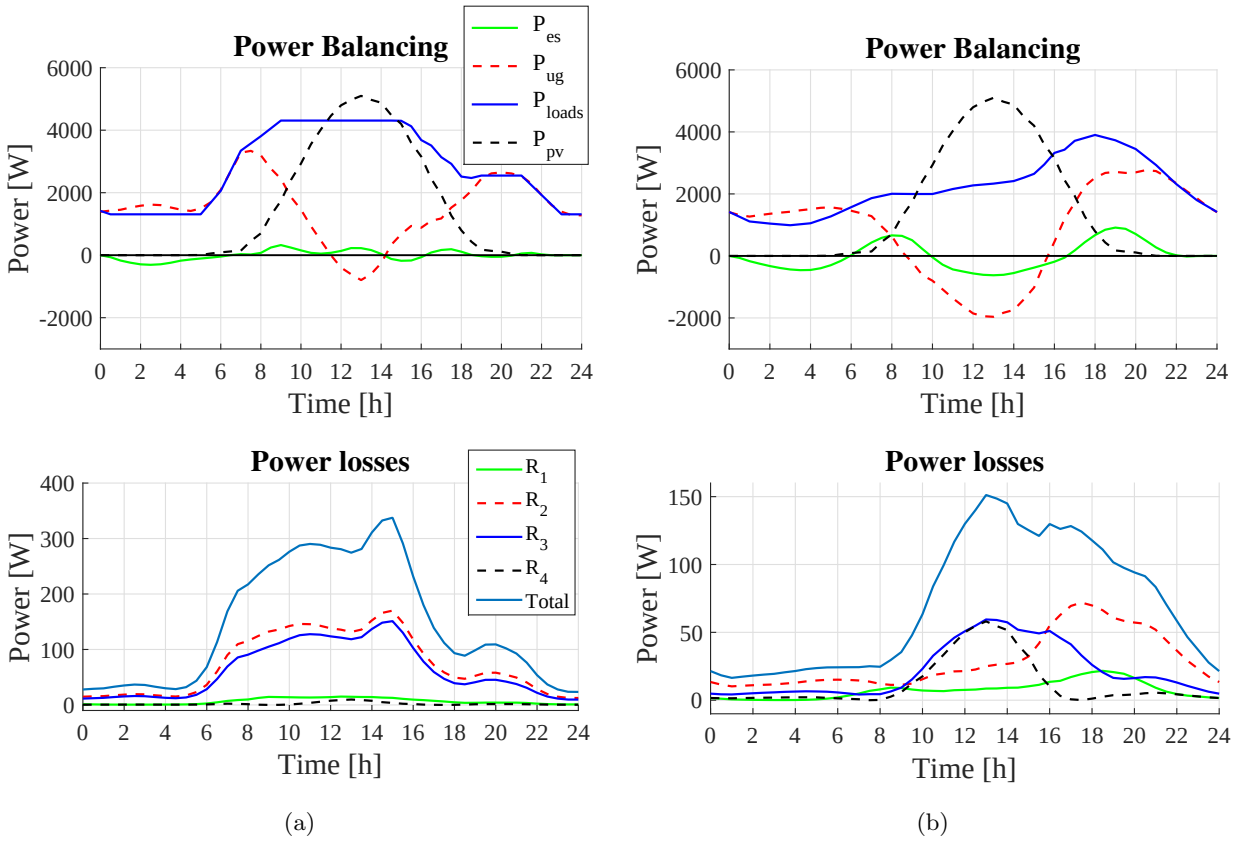

(a) (b)

Figure 4.4.13: (a) Power balancing and power losses profiles for DU load demand. (b) Power balancing and power losses profiles for CU load demand.

profiles are generated in case of faulted line events. We consider two scenarios with one faulted line each:

- $R_2 = 0$, the transmission line among the loads and the UG;
- $R_4 = 0$, the transmission line between the PV and the UG system.

In the first case, where the transmission line among the loads and the external grid doesn't work, the loss caused by the rest functional lines is higher than in the case of Fig. 4.4.4b. The UG generated power is distributed through three lines, hence the loss increases as does the electricity cost. Similar situation is observed in the case of line under fault between the PV and the UG system. The power loss is higher towards the UG system from the PV for selling power than in the case of Fig. 4.4.4b. This is because of the interruption of the direct connection among the UG and the PV and, as a result, the power passes through the remaining lines. In general, we observe in both cases, that, finally, the demand is fully satisfied. Therefore, the results validate the meshed topology of the network. In case of a line under fault, the optimization-based controller can meet the consumers' demand through the remaining transmission lines.

Table 4.4.12: Simulation results obtained of Scenario 3.

Load	Power	Power produced [%]	Power consumed [%]	Electricity cost [euros]
Commercial	P_{ug}	51.2%	1.9% sold to the UG	4.623
	P_{es}	1.9%	2% for ES charging	-
	P_{loads}	-	92% for load usage	-
	P_{pv}	46.9%	-	-
	P_{loss}	-	Total: 4.1% R_1: 0.19%, R_2: 2.1%, R_3: 1.76%, R_4: 0.05%	-
Domestic	P_{ug}	44%	13.1% sold to the UG	2.857
	P_{es}	6%	6.7% for ES charging	-
	P_{loads}	-	78.1% for load usage	-
	P_{pv}	50%	-	-
	P_{loss}	-	Total: 2.1% R_1: 0.2%, R_2: 0.9%, R_3: 0.6%, R_4: 0.4%	-

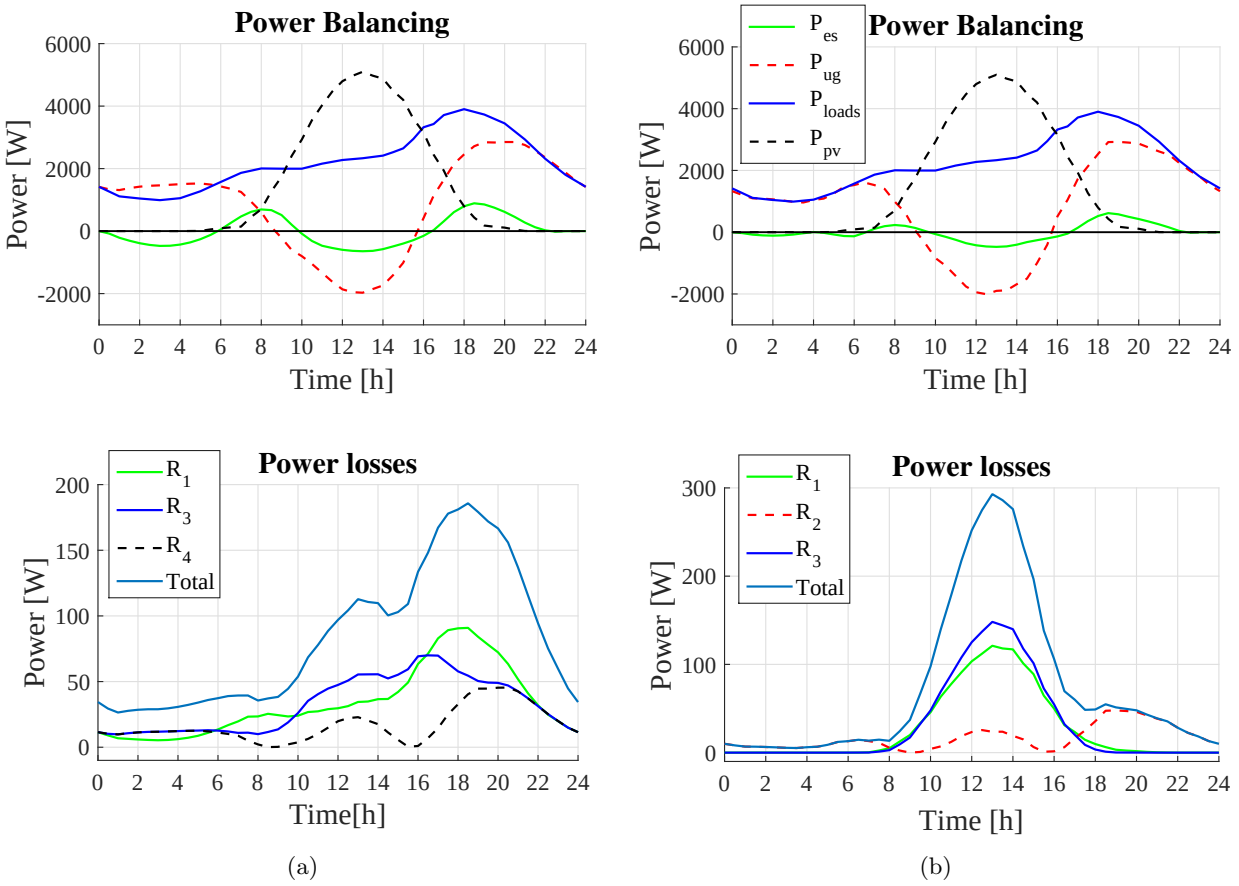

(a) (b)

Figure 4.4.14: (a) Power balancing and power losses profile generation with R_2 equal to 0. (b) Power balancing and power losses profile generation with R_4 equal to 0.

Table 4.4.13: Simulation results obtained of Scenario 3.

Load	Power	Power produced [%]	Power consumed [%]	Electricity cost [euros]
R_2=0	P_{ug}	43%	13.1% sold to the UG	2.881
	P_{es}	6.8%	6.8% for ES charging	-
	P_{loads}	-	77.5% for load usage	-
	P_{pv}	50.2%	-	-
	P_{loss}	-	Total: 2.6% R_1: 1.09%, R_2: 0%, R_3: 0.98%, R_4: 0.53%	-
R_4=0	P_{ug}	43.7%	13.6% sold to the UG	2.765
	P_{es}	3.7%	3.7% for ES charging	-
	P_{loads}	-	80% for load usage	-
	P_{pv}	52.6%	-	-
	P_{loss}	-	Total: 2.7% R_1: 0.98%, R_2: 0.61%, R_3: 1.11%, R_4: 0%	-

4.5 Conclusion

In this chapter, a multilevel supervision for a meshed DC microgrid was introduced. A constrained optimization-based control approach was presented which solves the power balancing problem with or without power losses in the network. The three control levels were analyzed: the high, the middle and the low level. In a meshed topology, the optimization problem to solve becomes complicated since a model consists of multiple sources, different timescales, nonlinearities and constraint satisfaction at the same time. Therefore, we built a controller which could manage and take into consideration all the aforementioned factors.

Afterwards, the reference profiles obtained by differential flatness and B-spline approximations were compared with the optimal profiles deduced by MPC proving that differential flatness represents an accurate and straightforward way to generate optimal profiles generation for power balancing optimization. Furthermore, considering different kind of scenarios, we analyzed the response of the system, verifying the operation of the meshed topology in the DC microgrid.

The main contributions of this chapter are summarized below:

- the differential flatness and the associated B−splines approximations were used for optimal profile generation. The method handles successfully continuous-time constraints (validated not only at each sampling time, but for the entire sampling interval) and integral costs (along the entire simulation horizon);
- a multi-scale approach was implemented in the control architecture. Most of the works presented in the introduction of this chapter concentrate on a single aspect of microgrid control due to the large disparities in sampling times (from hours for load balancing to tenths of seconds for DC/DC converter switching). Here, each level is analyzed and an appropriate control law is given (which takes into account computation time limitations);
- overall, we may conclude that the PH implementation and the avoidance of discretization at the load balancing level provide significant improvements in comparison with standard approaches which discretize the dynamics and apply, e.g., MPC to solve the problem.

In the following chapter, the conclusions of this thesis are drawn.

Chapter 5

Conclusion and future research

5.1 Conclusions

In the present manuscript, a hierarchical control strategy under constraints was studied to generate the optimal power distribution within a meshed DC microgrid architecture (Fig.2.2.1) composed by a renewable source (PV), an ES system, a collection of DC loads (e.g. EVs, LED lighting, printers, computers and the like) and DC/DC converters. To obtain its dynamical model, the DC microgrid was analyzed interpreting all its components as electrical circuits. Each component was studied separately, deriving its mathematical model from the associated Bond graph (Duindam et al., 2009; Karnopp et al., 2012) in chapter 2. From the Bond graphs, the PH state-space representation (van der Schaft et al., 2014) of every element was presented including the central transmission network. This approach was selected because it preserves the constitutive laws for the components together with the Kirchoff's law and the associated power continuity. Then, the hierarchical control approach was analyzed, divided into three levels, the high, the middle and the low level. An optimization-based approach under constraints was proposed at the high level under the combination of differential flatness and B-spline parametrizations for the PH model. Afterwards, at the middle level, a tracking MPC was developed to follow the optimal profiles obtained at the high level. Finally, the tracking profiles were used at the low level for the local supervision of the ES system.

More precisely, at first, the PH state-space representation for the sources was introduced. The PH model of the solar cell and the KiBaM battery were derived from their Bond graphs. Afterwards, the DC/DC converters, the Split-Pi converter and the Ćuk converter, were analytically described and their PH representations were validated through simulations, considering as control variables their duty cycles. Next, the PH dynamical model of the overall central transmission network was provided replacing the transmission lines with RL circuits. The complexity of the resulted system led us to simplify the mathematical models according to the control objectives. In this work, the main goals were to develop an optimization problem capable to ensure power balancing in the central transmission network while simultaneously minimizing the power dissipation and the electricity cost. Therefore, high importance was given to the ES system and the central transmission-line network. A simplified version of the system was introduced, thus reducing the transmission lines model but still preserving the detailed dynamical model of the ES.

Before integrating the DC microgrid model into the optimization problem, a flatness-based representation (Fliess et al., 1995; Levine, 2009) was proposed which maintains the power-preserving interconnections and the power conservation properties of the PH system. Through the flatness representation, the states and inputs of the PH model were reformulated in function of the derived flat outputs. A significant advantage of this approach and its combination with the B-spline parametrization (Suryawan, 2012) is the continuous-time constraints validation. Despite the fact that flat representation is an advantageous method for system analysis, the calculation of the flat outputs remains to date a challenging problem. In this work, the computation of the flat outputs was studied, primarily, implementing the algorithm for flat representation proposed in (Franke and Robenack, 2013) for the PH models of the different components of the reduced microgrid model introduced in this work (Fig. 2.5.1). Through this algorithm the flat representation of each component was provided. In the sequel, the flat outputs resulting from the algorithm were compared with another set of flat outputs, proposed for each part of the system by selecting a number of states as flat outputs equal to the number of control inputs according to Levine (2009). Comparisons among the flat output sets were realized to find the most appropriate set for the system's flat representation. From theory, it is known that the states and the control inputs are deduced through the flat outputs and a finite number of their derivatives. However, the simulations indicated that the more derivatives there are in the flat representation of the states

and inputs of the system, the more noise-affected the states and the control inputs are. Therefore, a suitable flat output set is the one requiring fewer derivatives.

Because of the complexity in the flat outputs' calculation, another method was investigated in order to develop a more straightforward way to derive the possible flat outputs for the PH systems. This method is called bicausality which was proposed to inverse the dynamics of the Bond graphs. Since flat representation and bicausality are both based on the notion of reversibility of the dynamics of the system, bicausality seems an appropriate tool to generate the possible flat outputs of the PH systems. The proposed method was elaborated through the electrical circuits of the battery and the Split-Pi converter, for which the flat outputs were found. Through simulations, the flat outputs were analyzed to decide which set is the best choice.

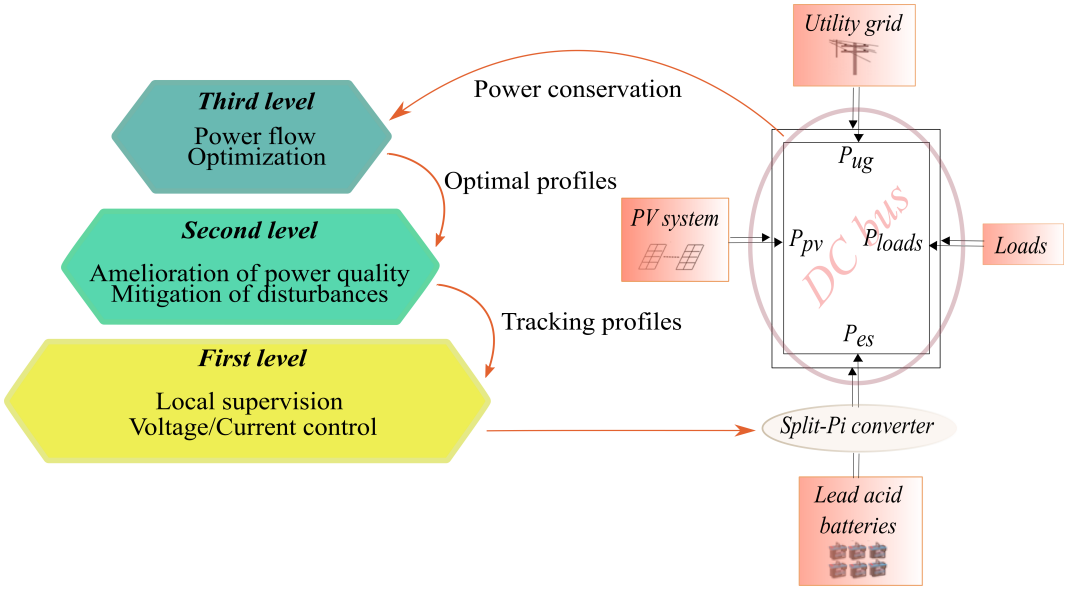

Figure 5.1.1: General hierarchical control scheme of the DC microgrid.

Finally, we dealt with the fast and the slow dynamics of the system separating the control problem into smaller sub-problems. The hierarchical control strategy was developed and the three composing levels have been detailed (Fig.5.1.1):

- the high level, where the flat representation of the ES system was integrated into the optimization problem. The flat model and its corresponding constraints were rewritten using B-spline parametrization for continuous-time constraint validation. Two cases were investigated: i) the cost minimization generating profiles for the utility grid (UG) and the energy storage (ES) power as well as the voltage and the current of the battery during charging and discharging; ii) the power dissipation was also added to the optimization problem cost to generate the optimal power distribution among the DC microgrid's components. Optimal profiles were produced for the UG and the ES power, the power losses, the voltages on the connecting nodes, the voltage and the current of the battery;

- the middle level, where a MPC tracking controller was developed to track the optimal profiles computed at the high level under perturbation. The error dynamics of the system was also analyzed. The objective function was introduced with and without power losses in the central transmission network;

- the low level, where the tracking profiles of the middle level were taken into account to be followed by the PH model of the ES system in order to supervise the switching activity inside the Split-Pi converter.

Furthermore, the high level flatness-based approach was compared with an economic MPC scheme. This comparison showed slight differences in the electricity cost among the power profiles generated by the flatness-based approach and MPC. Noteworthy, the overall cost value was shown to depend on the sampling time and the length of the prediction horizon. This is the result of discretization which can affect the performance of the simulation. Other optimal profiles were generated for different scenarios such as in the case of fault events or for different distances among the components. In the case of a line under fault, it was proved that the meshed topology is reliable satisfying the consumers' demand even under faults. On the other hand, the

relative distance between components was shown to be relevant. In particular, the renewable sources and the ES system benefit being close to the loads, thus avoiding power losses, ameliorating the operation of the microgrid, while also minimizing the electricity cost.

In the field of microgrids, many questions remain open. This work focused only on some particular modeling and control approaches. The control objectives include the power balancing of the DC microgrid and the scheduling of the energy storing elements. However, we firmly believe that the detailed PH models together with their flat representations and the hierarchical control approach developed in this work could further be used to cope with other challenging problems arising in this domain, as discussed in the following section.

5.2 Future improvements

Henceforward, the **short term future work** (Fig.5.2.1) will be described. Since a modeling and an optimization approach were developed for the central transmission network, the operation of the system in case of unexpected events or power outages could be further studied. With the mathematical model developed for the central transmission network, fault mitigation is possible, improving the performance and the reliability of the system.

The reconfiguration of the system may be accomplished at the high level. The optimization problem developed including the power losses in the central transmission network could be used to predict the behavior of the system in case of unexpected events as has been already started in this work in section 4.4.7. Generating profiles in case of a line under fault, the corresponding line can be isolated by forecasting the new behavior of the remaining transmission lines. In such a way, the operation of the system continues taking into account the updated optimal profiles. Furthermore, these tools will help in storage sizing for functioning in islanded mode.

The stability of the system can be studied thorough Nonlinear Model Predictive Control (NMPC) which considers the PH models. Recall that, PH formalism is a useful approach to analyze the stability of the system, due to its properties related to power-preserving interconnections, the dissipative and the storing elements. According to (van der Schaft et al., 2014), the Hamiltonian, H, i.e. the energy stored in the physical systems, is regarded as a candidate Lyapunov function. Therefore, the stability of the PH system can be investigated over a MPC controller which handles constraints and nonlinearities in an improvement to other control methods used in PH systems, such as Energy-balancing passivity-based control or Interconnection and damping assignment passivity-based control (Macchelli, 2014; van der Schaft et al., 2014). For instance, a passivity-based controller could enforce locally the stability of the PH system and be used as a local controller for the terminal region used to formally prove the recursive feasibility in an NMPC framework (Nguyen et al., 2019). Apart from this, at the middle level, the error dynamics can be further studied for the overall system, as was already started with the battery in section 4.3.2.2, defining the upper limits of the states.

In addition, the flat representation of the Split-Pi converter, presented in chapter 3, could be added, taking into account its input and output voltage with their flat representations and not only through the battery's flat model. This would be useful also to further analyze the switching activity within the converters. Optimal profiles for the states of the Split-Pi converter could be provided, considering power loss minimization. Further constraints could be considered for the states of the Split-Pi converter, thus ensuring a better regulation in the converters.

Finally, the system could be developed in its primary form by adding back the transmission lines which were discarded in the reduced model. Not in the least, the transmission line model can consider inductors, relevant for the transitional behavior of the grid.

A variable sized storage component may also be considered. That is, we may consider electrical vehicles connected to the grid which temporarily can act as storage elements.

As a **long term future work** (Fig.5.2.1), the bicausality notion, presented in section 3.4, should be further analyzed in order to develop a general methodology which could provide the flat outputs of the PH systems. In here, a first attempt was realized concerning the electrical circuits employed in this work and a first idea was developed on how we can proceed towards a more general solution which may cover not only the electrical circuits but also other physical systems. This information is essential and will facilitate the use of differential flatness in order to be able to exploit its advantages (e.g. preservation of the system properties) before incorporating the control part.

Another important issue which might be further analyzed is the correct topology and design of the proposed meshed DC microgrid to further reduce the power losses and the electricity cost, but also ameliorate the power quality. The number of batteries, the proper sizing, the number of PV panels, the type of renewable

sources are some of the factors on which the performance of the system strongly depends. For example, the PV panels are a trustworthy choice to be part of a DC microgrid, since it is a DC source. However, when the solar irradiation is very low, its power generation is negligible. Therefore, other sources must be taken into consideration, e.g. air turbines, geothermal sources and the like.

A further aspect which may ameliorate the operation of the system is the distance among the sources and the consumers, which should be considered in the optimization problem, defined by the power loss in the transmission lines. Finally, the importance of the batteries' existence in such systems makes necessary the investigation of their lifetime. Improving the battery model, its lifetime could be considered, hence avoiding a fast deterioration of the energy storing element and, as a consequence, decreasing its cost and increasing the safe operation of the system.

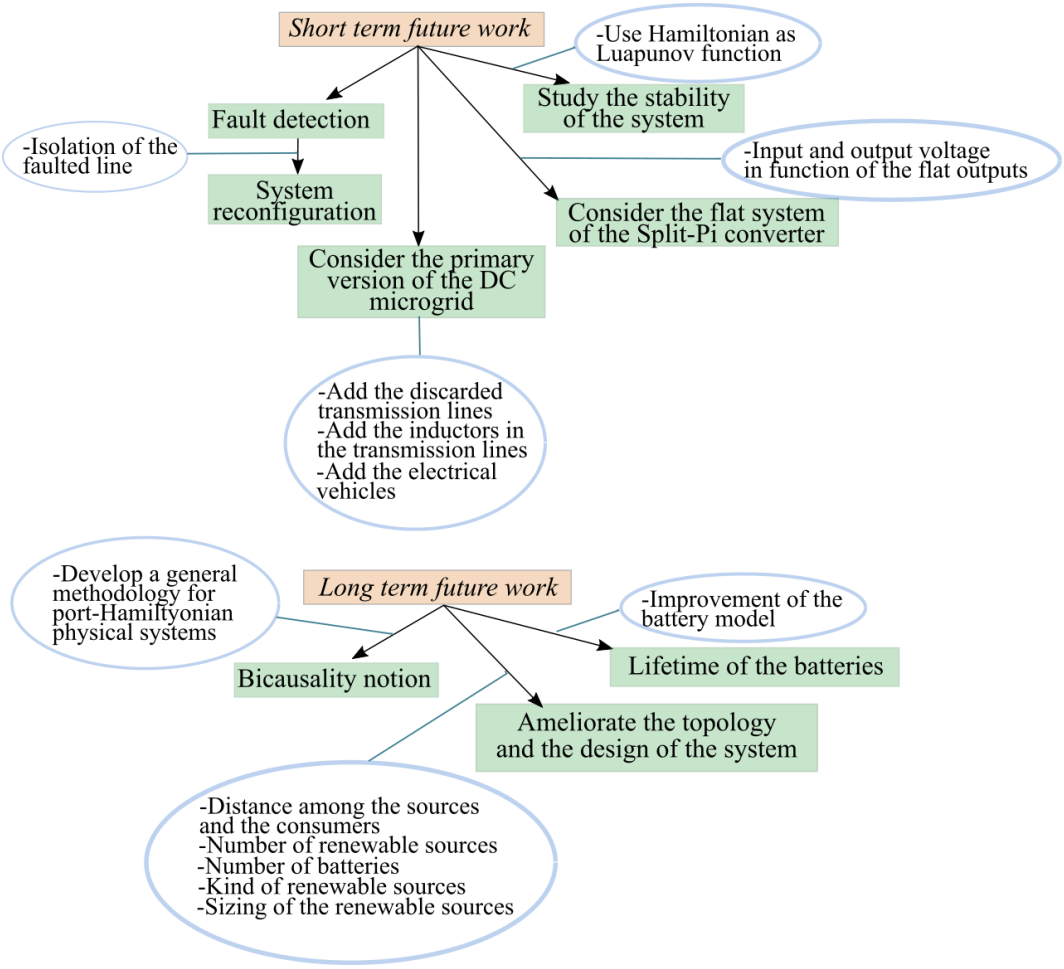

Figure 5.2.1: Short and long term future work.

Appendix A

Detailed explanation of the algorithm for the ES, PV and loads systems

A.1 ES system

A.1.1 Implementation of the algorithm for the ES system

As already indicated in section 3.3.1, the computation hinges on an iteration process that starts from $i = 0$ and continues step by step, if necessary. Initially, from the linearized system in (3.3.21a)-(3.3.21c), we will introduce the $(n - m) \times n$ matrices below:

$$\boldsymbol{P}_{0,[\boldsymbol{i}]} = \frac{\partial \boldsymbol{F}}{\partial x_{\boldsymbol{i}}}(x_{\boldsymbol{i}}, \dot{x}_{\boldsymbol{i}}), \qquad \boldsymbol{P}_{1,[\boldsymbol{i}]} = \frac{\partial \boldsymbol{F}}{\partial \dot{x}_{\boldsymbol{i}}}(x_{\boldsymbol{i}}, \dot{x}_{\boldsymbol{i}}), \tag{A.1.1}$$

The corresponding matrices of (A.1.1), $\boldsymbol{P}_{0,[\boldsymbol{i}]}$ and $\boldsymbol{P}_{1,[\boldsymbol{i}]}$, at the first step of the algorithm, where $i = 0$, are equal to[1]:

$$\boldsymbol{P}_{0,[0]} = \begin{bmatrix} \eta\dot{p}_{1sc} - \alpha\eta q_{1sc} & \mu\dot{p}_{2sc} + \gamma\mu q_{3sc} & -\alpha\eta p_{1sc} & \beta\dot{q}_{2sc} & \gamma\mu p_{2sc} & 0 & 0 \\ 0 & -\mu & 0 & 0 & 0 & -\delta\psi & \epsilon\psi \\ 0 & 0 & 0 & 0 & 0 & -\delta\psi & \epsilon\psi \end{bmatrix}, \tag{A.1.2a}$$

$$\boldsymbol{P}_{1,[0]} = \begin{bmatrix} \eta p_{1sc} & \mu p_{2sc} & 0 & \beta q_{2sc} & 0 & 0 & 0 \\ 0 & 0 & 0 & 0 & 1 & 1 & 0 \\ 0 & 0 & 0 & 0 & 0 & 0 & 1 \end{bmatrix}. \tag{A.1.2b}$$

Then, the dx coordinates are presented through (3.3.21a), (3.3.21b) and (3.3.21c) for $i = 0$, as shown below:

$$\boldsymbol{u}_{[0]} = \begin{bmatrix} dp_{1sc} & dp_{2sc} & dq_{1sc} & dq_{2sc} & dq_{3sc} & dq_{1b} & dq_{2b} \end{bmatrix}^T \in R^{7\times 1}. \tag{A.1.3}$$

The time derivative of $\boldsymbol{u}_{[0]}$ will be:

$$\dot{\boldsymbol{u}}_{[0]} = \begin{bmatrix} d\dot{p}_{1sc} & d\dot{p}_{2sc} & d\dot{q}_{1sc} & d\dot{q}_{2sc} & d\dot{q}_{3sc} & d\dot{q}_{1b} & d\dot{q}_{2b} \end{bmatrix}^T \in R^{7\times 1}. \tag{A.1.4}$$

[1]The circuit's parameters and the values of the resistors are considered as in section 3.3.2: $1/C_{1sc} = \alpha$, $1/C_{2sc} = \beta$, $1/C_{3sc} = \gamma$, $1/C_{1b} = \delta$, $1/C_{2b} = \epsilon$, $1/I_{1sc} = \eta$, $1/I_{2sc} = \mu$, $1/R_{1sc} = \nu$, $1/R_{1b} = \sigma$, $1/R_{2b} = \psi$).

Next, the matrices $\boldsymbol{P}^{+}_{1,[0]}$ and $\boldsymbol{P}^{\perp}_{1,[0]}$ through (3.3.9) are described below:

$$\boldsymbol{P}^{+}_{1,[0]} = \begin{bmatrix} \frac{1}{\eta p_{1sc}} & 0 & 0 \\ 0 & 0 & 0 \\ 0 & 0 & 0 \\ 0 & 0 & 0 \\ 0 & 1 & 0 \\ 0 & 0 & 0 \\ 0 & 0 & 1 \end{bmatrix}, \tag{A.1.5a}$$

$$\boldsymbol{P}^{\perp}_{1,[0]} = \begin{bmatrix} \frac{-\mu p_{2sc}}{\eta p_{1sc}} & 0 & \frac{-\beta q_{2sc}}{\eta p_{1sc}} & 0 \\ 1 & 0 & 0 & 0 \\ 0 & 1 & -\frac{\beta q_{1sc} q_{2sc}}{\eta p^2_{1sc}} & 0 \\ 0 & 0 & 1 & 0 \\ 0 & 0 & 0 & -1 \\ 0 & 0 & 0 & 1 \\ 0 & 0 & 0 & 0 \end{bmatrix}. \tag{A.1.5b}$$

Furthermore, from (3.3.10), the matrices $A_{[0]}$ and $B_{[0]}$ are equal to:

$$A_{[0]} = \begin{bmatrix} -\frac{a q_{1sc}}{p_{1sc}} & \gamma h p_{2sc} & 0 \\ 0 & 0 & -\epsilon\psi \\ 0 & 0 & \epsilon\psi \end{bmatrix}, \tag{A.1.6a}$$

$$B_{[0]} = \begin{bmatrix} \gamma\mu q_{3sc} + \frac{\alpha\mu p_{2sc} q_{1sc}}{p_{1sc}} & -\alpha\eta p_{1sc} & 0 & -\gamma\mu p_{2sc} \\ -\mu & 0 & 0 & \delta\psi \\ 0 & 0 & 0 & -\delta\psi \end{bmatrix}. \tag{A.1.6b}$$

The matrix $B_{[0]}$ is different from 0 which means that the system is controllable. From (3.3.16) and (3.3.15), $\boldsymbol{u}_1$ and $\boldsymbol{w}_1$ are equal to:

$$\boldsymbol{u}_{[1]} = \begin{bmatrix} \eta p_{1sc} dp_{1sc} + \mu p_{2sc} dp_{2sc} + \beta q_{2sc} dq_{2sc} \\ dq_{3sc} + dq_{1b} \\ dq_{2b} \end{bmatrix}, \tag{A.1.7a}$$

$$\boldsymbol{w}_{[1]} = \begin{bmatrix} dp_{2sc} \\ dq_{1sc} - \frac{\beta q_{1sc} q_{2sc}}{\eta p^2_{1sc}} dq_{2sc} \\ dq_{2sc} \\ dq_{1b} \end{bmatrix}. \tag{A.1.7b}$$

As a next step, we observe the rank of matrix $B_{[0]}$ has full row rank but not full column rank. Since this matrix has linear dependent columns, the equation $\boldsymbol{u}_{[0]} = \boldsymbol{P}^{+}_{1,[0]}\boldsymbol{u}_{[1]} + \boldsymbol{P}^{\perp}_{1,[0]}\boldsymbol{w}_{[1]}$ as in (3.3.7) is replaced by (3.3.11):

$$\boldsymbol{u}_{[0]} = \boldsymbol{P}^{+}_{1,[0]}\boldsymbol{u}_{[1]} + \widetilde{\boldsymbol{P}}^{\perp}_{1,[0]}\boldsymbol{w}_{[1]} + \boldsymbol{Z}_{[0]}\boldsymbol{z}_{[1]}, \tag{A.1.8}$$

where $\boldsymbol{Z}_{[0]}$ and $\boldsymbol{z}_{[1]}$ are equal to:

$$\boldsymbol{Z}_{[0]} = \begin{bmatrix} \frac{-\beta q_{2sc}}{\eta p_{1sc}} \\ 0 \\ 0 \\ -\frac{\beta q_{1sc} q_{2sc}}{\eta p^2_{1sc}} \\ 1 \\ 0 \\ 0 \\ 0 \end{bmatrix}, \tag{A.1.9a}$$

$$\boldsymbol{z}_{[1]} = \begin{bmatrix} dq_{2sc} \end{bmatrix}. \tag{A.1.9b}$$

The matrices $\widetilde{\boldsymbol{P}}^{\perp}_{1,[0]}$ and $\boldsymbol{w}_{[1]}$ are presented below:

$$\widetilde{\boldsymbol{P}}^{\perp}_{1,[0]} = \begin{bmatrix} \frac{-\mu p_{2sc}}{\eta p_{1sc}} & 0 & 0 \\ 1 & 0 & 0 \\ 0 & 1 & 0 \\ 0 & 0 & 0 \\ 0 & 0 & -1 \\ 0 & 0 & 1 \\ 0 & 0 & 0 \end{bmatrix}, \tag{A.1.10a}$$

$$\boldsymbol{w}_{[1]} = \begin{bmatrix} dp_{2sc} \\ dp_{1sc} - \frac{bq_{1sc}q_{2sc}}{\eta p^2_{1sc}} dq_{2sc} \\ dq_{1b} \end{bmatrix}. \tag{A.1.10b}$$

Consequently, the matrix $\widetilde{B}_{[0]}$, considering also (A.1.10a), is as follows:

$$\widetilde{B}_{[0]} = (\boldsymbol{P}_{0,[0]} - \dot{\boldsymbol{P}}_{1,[0]})\widetilde{\boldsymbol{P}}^{\perp}_{1,[0]} => \tag{A.1.11a}$$

$$=> \widetilde{B}_{[0]} = \begin{bmatrix} \gamma a - \alpha\eta p_{1sc} & -\gamma\mu p_{2sc} & 0 \\ -\mu & 0 & \delta\psi \\ 0 & 0 & -\delta\psi \end{bmatrix}. \tag{A.1.11b}$$

At this point, the matrix $\widetilde{B}_{[0]}$ has full column rank and replaces the previously mentioned matrix $B_{[0]}$ (A.1.6b). Therefore, the iteration process stops. Next, the pseudo-inverse matrix, $\boldsymbol{Z}^{+}_{[0]}$, is calculated and is equal to:

$$\boldsymbol{Z}^{+}_{[0]} = \begin{bmatrix} 0 & 0 & 0 & 1 & 0 & 0 & 0 \end{bmatrix}. \tag{A.1.12}$$

Therefore, according to (3.3.17), the tangent flat output of the ES system is:

$$\omega_1 = \eta p_{1sc} dp_{1sc} + \mu p_{2sc} dp_{2sc} + \beta q_{2sc} dq_{2sc}, \tag{A.1.13a}$$

$$\omega_2 = dq_{3sc} + dq_{1b}, \tag{A.1.13b}$$

$$\omega_3 = dq_{2b}, \tag{A.1.13c}$$

$$\omega_4 = dq_{2sc}. \tag{A.1.13d}$$

A.1.2 Supplementary results regarding the ES flat representation

Fig. A.1.1, A.1.2, A.1.3 compare the states generated by the ES PH model in (3.3.18a)-(3.3.18g) and the ES flat model in (3.3.26a)-(3.3.26i) in order to verify the set of the flat outputs (3.3.25a-3.3.25d) found by the algorithm. From the simulations, we observe that the flat representation of the system follows very well the response of the principal ES PH model, since the error is negligible. The error is created because of the noise caused by the numerical derivation during the simulation. The more derivatives we obtain, the more noisy data we will have in the final signal.

Furthermore, in Fig. A.1.1, A.1.2, A.1.3 the states from the ES flat representation in (3.3.29a)-(3.3.29g) are introduced generated by the random set of flat outputs as in (3.3.28). The figures verify the corresponding flat representation of the system, since the error among the states of the ES flat and PH model is very low. The duration of the simulations is 300 s.

Next, we observe the differences in the signal response among the states of the two proposed sets of flat outputs (3.3.25a-3.3.25d) and (3.3.28), depending on the number of derivatives that each state has in its flat representation (see also (3.3.27) and (3.3.30)). For instance, no error exist for the states p_{1sc} (Fig. A.1.4) and q_{3sc} (Fig. A.1.5) in the case of the second flat output (3.3.28) in contrary to the corresponding states generated with the first set (3.3.26a-3.3.26b). On the other hand, for the states p_{2sc} (Fig. A.1.4) and q_{1sc} (Fig. A.1.5), the error is higher with the second set of flat outputs (3.3.28), considering the compact flat representations of the ES system (3.3.27) and (3.3.30) and the number of derivatives included.

For further validation, an approximation of the derivatives is realized by adding a continuous transfer function block after the numerical differentiation in order to filter the signal's response for both sets of flat outputs and avoid the noise created in the data (Fig. A.1.7). We observe that the actual values of the control inputs, v_s, d_{1sc}, d_{1sc}, i_{R1b}, approximate closely the reference values.

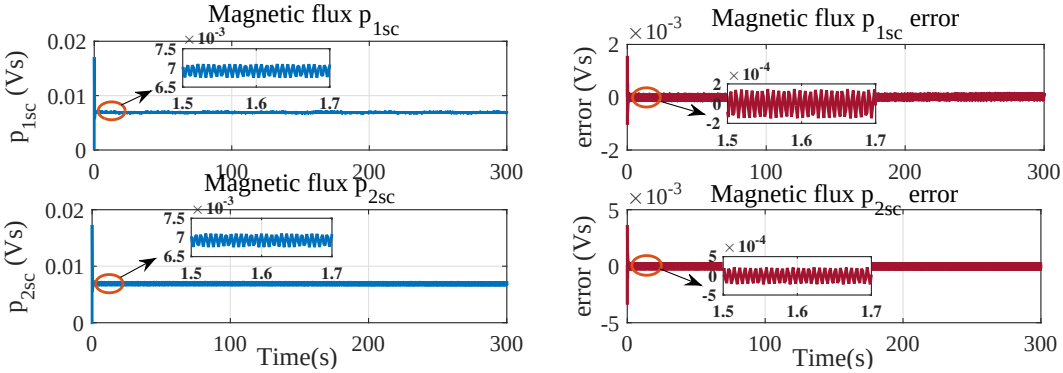

Figure A.1.1: Magnetic flux states of the inductors I_{1sc} and I_{2sc} of the Split-Pi converter in function of the flat outputs generated by the algorithm as in (3.3.25a)-(3.3.25d). The error between the magnetic flux states of (3.3.26a)-(3.3.26b) and (3.3.19a)-(3.3.19b) is depicted.

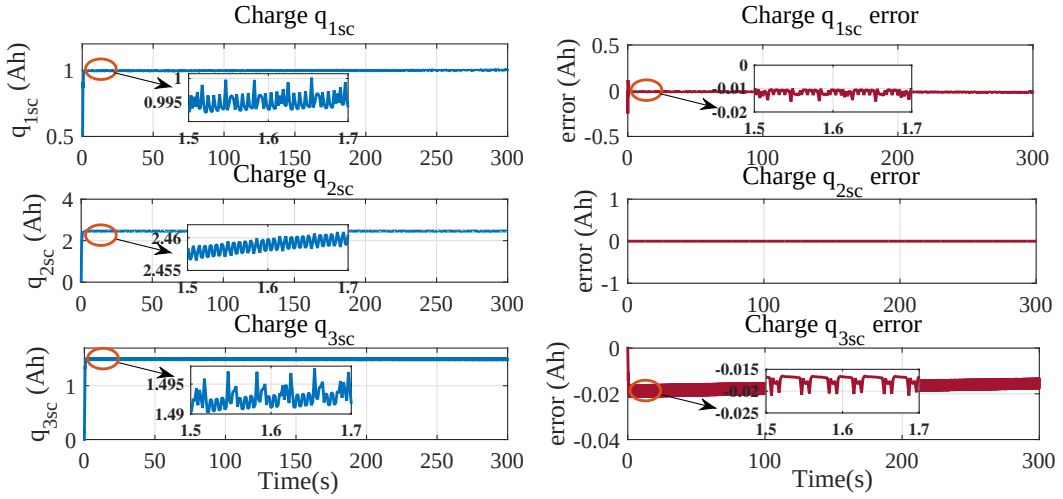

Figure A.1.2: Charge states of the capacitors C_{1b} and C_{2b} of the battery written in function of the flat outputs generated by the algorithm as in (3.3.25a)-(3.3.25d). The error between the charge states of (3.3.26g)-(3.3.26h) and (3.3.19f)-(3.3.19g) is depicted.

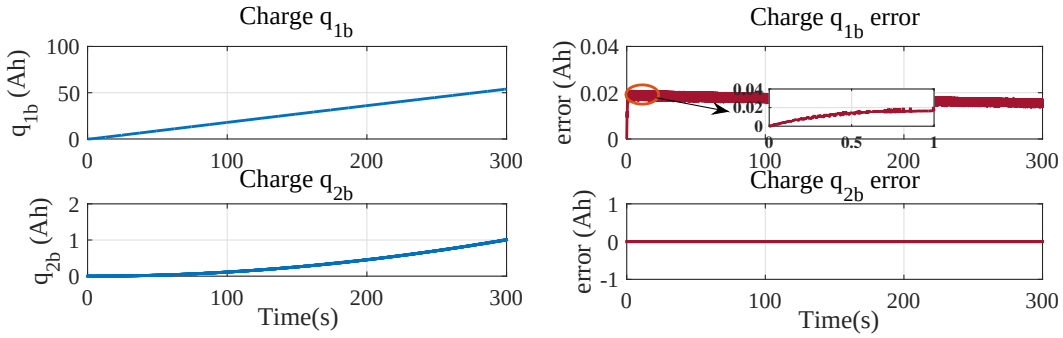

Figure A.1.3: Charge states of the capacitors C_{1sc}, C_{2sc} and C_{3sc} of the Split-Pi converter in function of the flat outputs generated by the algorithm as in (3.3.25a)-(3.3.25d). The error between the charge states of (3.3.26c), (3.3.26e), (3.3.26f) and (3.3.19c), (3.3.19d), (3.3.19e) is depicted.

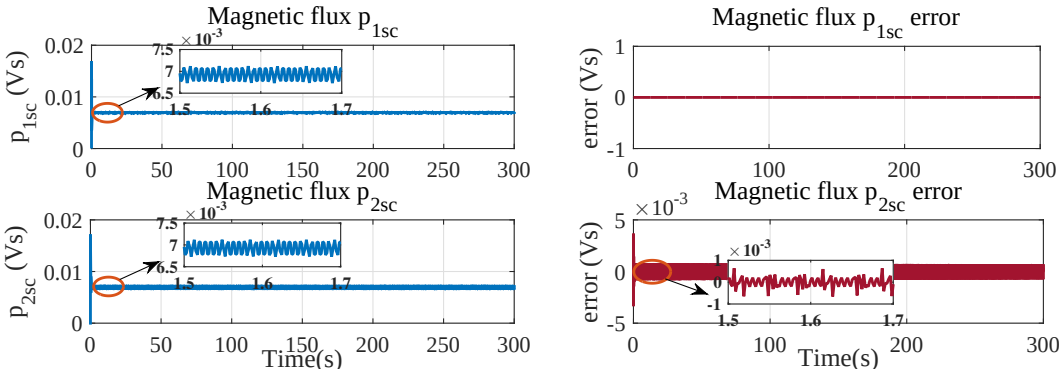

Figure A.1.4: Magnetic flux states of the inductors I_{1sc} and I_{2sc} of the Split-Pi converter in function of the second set of flat outputs as in (3.3.28). The error between the magnetic flux states of (3.3.29a)-(3.3.29b) and (3.3.19a)-(3.3.19b) is depicted.

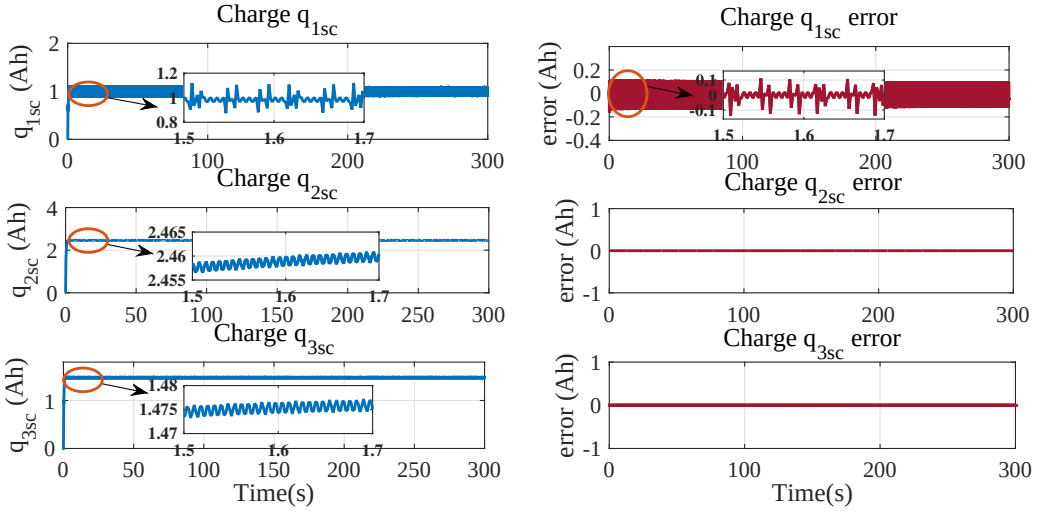

Figure A.1.5: Charge states of the capacitors C_{1sc}, C_{2sc} and C_{3sc} of the Split-Pi converter in function of the flat outputs generated by the algorithm in (3.3.28). The error between the charge states of (3.3.29c), (3.3.29d), (3.3.29e) and of (3.3.19c), (3.3.19d) and (3.3.19e) is depicted.

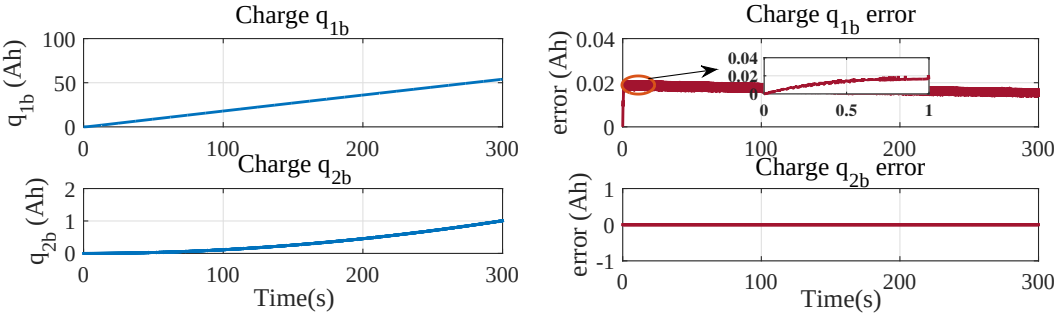

Figure A.1.6: Charge states of the capacitors C_{1b} and C_{2b} of the battery written in function of the flat outputs generated by the algorithm in (3.3.28). The error between the charge states in function of the flat outputs (3.3.29f)-(3.3.29g)) and of (3.3.19f) and (3.3.19g) is depicted.

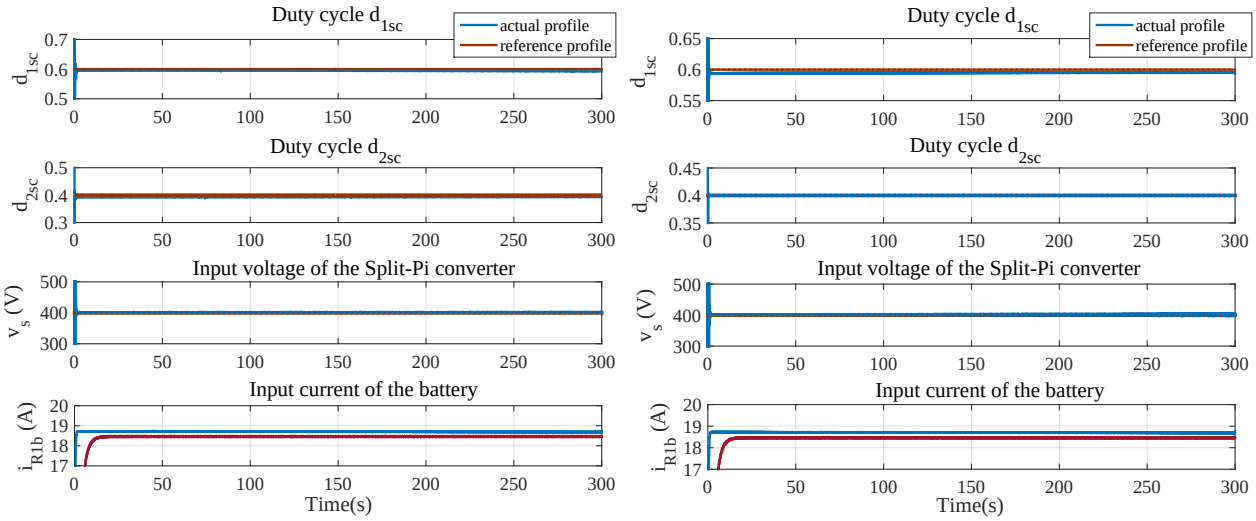

(a) (b)

Figure A.1.7: (a) Signal response of the control inputs after filtering the derivatives shown in the ES system flat representation in (3.3.26i)-(3.3.26l). (b) Signal response of the control inputs after filtering the derivatives shown in the ES system flat representation with the set of random flat outputs (3.3.29h-3.3.29k) is depicted.

A.2 PV and loads system

A.2.1 Implementation of the algorithm for the Split-pi converter

In this section, we follow the same steps as in Appendix A.1.1 introducing below the corresponding matrices of the algorithm for the Split-Pi converter[2]:

1. The matrices $\boldsymbol{P}_{0,[0]}$ and $\boldsymbol{P}_{1,[0]}$ are introduced below:

$$\boldsymbol{P}_{0,[0]} = \begin{bmatrix} \eta\dot{p}_{1sc} - \alpha\eta q_{1sc} & \mu\dot{p}_{2sc} + \gamma\mu q_{3sc} & -\alpha\eta p_{1sc} & \beta\dot{q}_{2sc} & \gamma\mu p_{2sc} \end{bmatrix}, \tag{A.2.1a}$$

$$\boldsymbol{P}_{1,[0]} = \begin{bmatrix} \eta p_{1sc} & \mu p_{2sc} & 0 & \beta q_{2sc} & 0 \end{bmatrix}. \tag{A.2.1b}$$

2. Next, the dx coordinates are introduced as in (3.3.34) for $i = 0$, as follows:

$$\boldsymbol{u}_{[0]} = \begin{bmatrix} dp_{1sc} & dp_{2sc} & dq_{1sc} & dq_{2sc} & dq_{3sc} \end{bmatrix}^T \in R^{5\times 1} \tag{A.2.2}$$

with their time derivatives in matrix $\boldsymbol{u}_{[0]}$ presented below:

$$\dot{\boldsymbol{u}}_{[0]} = \begin{bmatrix} d\dot{p}_{1sc} & d\dot{p}_{2sc} & d\dot{q}_{1sc} & d\dot{q}_{2sc} & d\dot{q}_{3sc} \end{bmatrix}^T \in R^{5\times 1}. \tag{A.2.3}$$

[2]The circuit's parameters and the values of the resistors are considered as in section 3.3.3: $1/C_{1sc} = \alpha$, $1/C_{2sc} = \beta$, $1/C_{3sc} = \gamma$, $1/I_{1sc} = \eta$, $1/I_{2sc} = \mu$, $1/R_{1sc} = \nu$, $1/R = \zeta$.

3. Afterwards, the matrices $\boldsymbol{P}^{+}_{1,[0]}$ and $\boldsymbol{P}^{\perp}_{1,[0]}$ as in (3.3.9) are described:

$$\boldsymbol{P}^{+}_{1,[0]} = \begin{bmatrix} \frac{1}{\eta p_{1sc}} \\ 0 \\ 0 \\ 0 \\ 0 \end{bmatrix}, \tag{A.2.4a}$$

$$\boldsymbol{P}^{\perp}_{1,[0]} = \begin{bmatrix} \frac{-\mu p_{2sc}}{\eta p_{1sc}} & 0 & \frac{-\beta q_{2sc}}{\eta p_{1sc}} & 0 \\ 1 & 0 & 0 & 0 \\ 0 & 1 & -\frac{\beta q_{1sc} q_{2sc}}{\eta p^2_{1sc}} & 0 \\ 0 & 0 & 1 & 0 \\ 0 & 0 & 0 & -1 \end{bmatrix}. \tag{A.2.4b}$$

4. Additionally, from (3.3.10), the matrices $A_{[0]}$ and $B_{[0]}$ are introduced below:

$$A_{[0]} = \left[-\frac{a q_{1sc}}{p_{1sc}} \right], \tag{A.2.5a}$$

$$B_{[0]} = \begin{bmatrix} \gamma \mu q_{3sc} + \frac{\alpha \mu p_{2sc} q_{1sc}}{p_{1sc}} & -\alpha \eta p_{1sc} & 0 & -\gamma \mu p_{2sc} \end{bmatrix}. \tag{A.2.5b}$$

The matrix $B_{[0]}$ is different from 0 which proves the controllability of the system.

5. Then, from (3.3.16) and (3.3.15), the $\boldsymbol{u}_1$ and $\boldsymbol{w}_1$ matrices are presented below:

$$\boldsymbol{u}_{[1]} = \left[\eta p_{1sc} dp_{1sc} + \mu p_{2sc} dp_{2sc} + \beta q_{2sc} dq_{2sc} \right], \tag{A.2.6a}$$

$$\boldsymbol{w}_{[1]} = \begin{bmatrix} dp_{2sc} \\ dq_{1sc} - \frac{\beta q_{1sc} q_{2sc}}{\eta p^2_{1sc}} dq_{2sc} \\ dq_{2sc} \\ -dq_{3sc} \end{bmatrix}. \tag{A.2.6b}$$

6. Afterwards, since the rank of matrix $B_{[0]}$ is not of full column rank, we proceed as in Appendix A.1.1 with (3.3.11). Therefore, the matrices $\boldsymbol{Z}_{[0]}$ and $\boldsymbol{z}_{[1]}$ are equal to:

$$\boldsymbol{Z}_{[0]} = \begin{bmatrix} \frac{-\mu p_{2sc}}{\eta p_{1sc}} & \frac{-\beta q_{2sc}}{\eta p_{1sc}} & 0 \\ 1 & 0 & 0 \\ 0 & 0 & 0 \\ 0 & -\frac{\beta q_{1sc} q_{2sc}}{\eta p^2_{1sc}} & 0 \\ 0 & 1 & 0 \\ 0 & 0 & -1 \end{bmatrix}, \tag{A.2.7a}$$

$$\boldsymbol{z}_{[1]} = \begin{bmatrix} dp_{2sc} \\ dq_{2sc} \\ -dq_{3sc} \end{bmatrix}. \tag{A.2.7b}$$

7. Thus, the matrices $\widetilde{\boldsymbol{P}}^{\perp}_{1,[0]}$ and $\boldsymbol{w}_{[1]}$ are presented below:

$$\widetilde{\boldsymbol{P}}^{\perp}_{1,[0]} = \begin{bmatrix} 0 \\ 0 \\ 1 \\ 0 \\ 0 \\ 0 \\ 0 \end{bmatrix}, \tag{A.2.8a}$$

$$\boldsymbol{w}_{[1]} = \left[dq_{1sc} - \frac{b q_{1sc} q_{2sc}}{\eta p^2_{1sc}} dq_{2sc} \right]. \tag{A.2.8b}$$

8. As a consequence, the matrix $\widetilde{B}_{[0]}$, considering also (A.1.11a), is as follows:

$$\widetilde{B}_{[0]} = \left[-\alpha\eta p_{1sc}\right], \tag{A.2.9}$$

which has full column rank, hence the iteration process within the algorithm stops.

9. Next, the pseudo-inverse matrix, $Z^{+}_{[0]}$, is calculated and is equal to:

$$\boldsymbol{Z}^{+}_{[0]} = \begin{bmatrix} 0 & 1 & 0 & 0 & 0 \\ 0 & 0 & 0 & 1 & 0 \\ 0 & 0 & 0 & 0 & -1 \end{bmatrix}. \tag{A.2.10}$$

10. Therefore, according to (3.3.17), the tangent flat output of the Split-Pi converter is:

$$\omega_1 = \eta p_{1sc} dp_{1sc} + \mu p_{2sc} dp_{2sc} + \beta q_{2sc} dq_{2sc}, \tag{A.2.11a}$$
$$\omega_2 = dq_{2sc}, \tag{A.2.11b}$$
$$\omega_3 = dp_{2sc}, \tag{A.2.11c}$$
$$\omega_4 = -dq_{3sc}. \tag{A.2.11d}$$

A.2.2 Supplementary results regarding the PV and loads system flat representation

In Fig. A.1.1 and A.1.2, the simulation results of the states of the Split-Pi converter in function of the flat outputs as in (3.3.39a)-(3.3.39e) are presented. Additionally, the error among the states generated by the Split-Pi flat model in (3.3.39a)-(3.3.39e) and the Split-Pi PH model in (3.3.31a)-(3.3.31e) is depicted. For all the states the error is negligible or equal to 0, which verifies the flat representation of the states in function of the flat outputs generated by the algorithm. As for the ES system, the oscillations appeared in the simulations is because of the noise caused by the numerical differentiation during the simulation. Additionally, Fig. A.2.1 and A.1.2 illustrate the states generated by the Split-Pi converter flat representation in (3.3.42a)-(3.3.42i) considering the second set of flat outputs as in (3.3.41). The figures validate the corresponding flat representation of the system, since the error among the states of the Split-Pi flat and PH model is very low. The duration of the simulations is 300 s.

At this point, we analyze the difference in the signals among the states of the two proposed sets of flat outputs (3.3.38a-3.3.38d) and (3.3.38), taking also into account the number of derivatives that each state has in its flat representation (see also (3.3.40) and (3.3.43)). A slight error is observed in the state p_{1sc} (Fig. A.2.1), generated considering the flat outputs provided by the algorithm as in (3.3.38a)- (3.3.38d). The state q_{1sc} (Fig. A.2.2 and Fig. A.2.4) for both flat representations (3.3.39c and 3.3.42c) is almost the same, considering also the derivatives included in its general flat representations in (3.3.40c) and (3.3.43c) respectively. Moreover, for the states p_{2sc}, q_{2sc} and q_{3sc} (Fig. A.2.1, A.2.2, A.2.3, A.2.4) no errors exist since there are no additive flat outputs or derivatives in their general representations in (3.3.40b), (3.3.40d), (3.3.40e) , (3.3.43b) , (3.3.43d) and (3.3.43e).

For further validation, the derivatives are approximated by adding a continuous transfer function block after the numerical differentiation as a filter for both sets of flat outputs in order to mitigate the noise created in the data (Fig. A.2.5). Below the simulations of the control inputs, v_s, d_{1sc}, d_{1sc}, i_{R1b}, are depicted and we observe that the results (lines in blue) approximate closely the reference values.

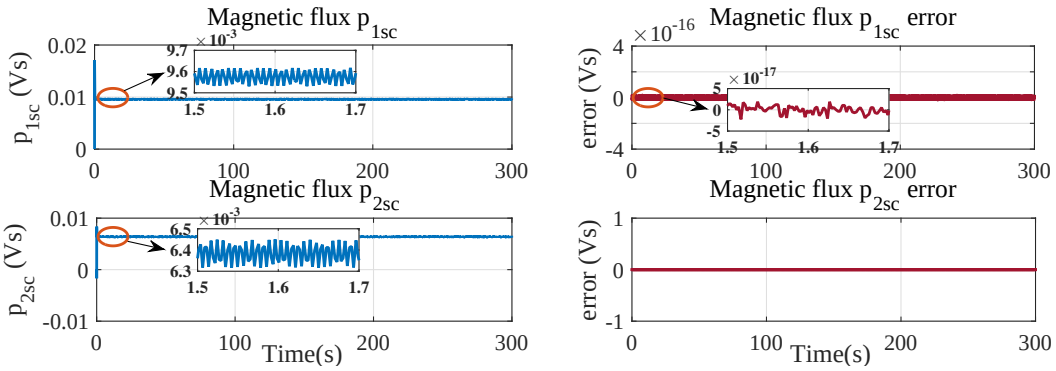

Figure A.2.1: Magnetic flux states of the inductors I_{1sc} and I_{2sc} of the Split-Pi converter in function of the flat outputs generated by the algorithm as in (3.3.38a)- (3.3.38d). The error between the magnetic flux states of (3.3.39a)-(3.3.39b) and (3.3.32a)-(3.3.32b) is presented.

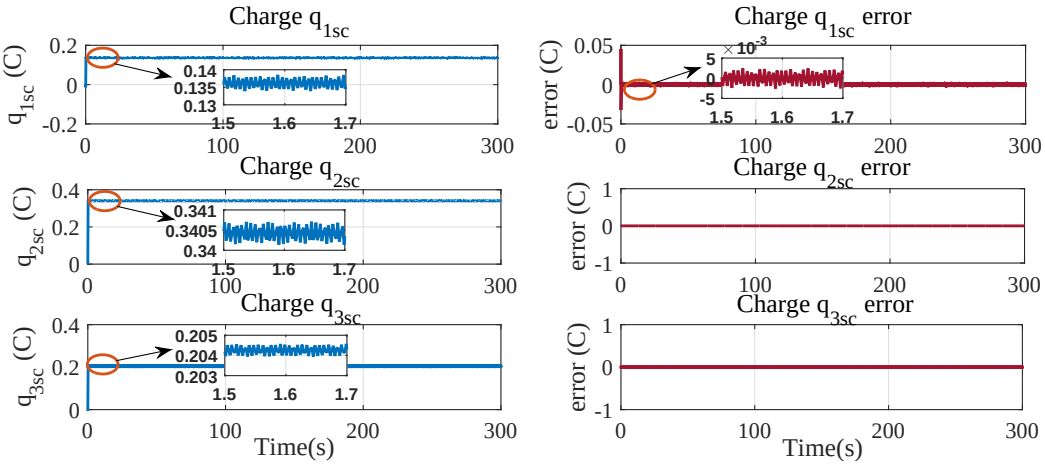

Figure A.2.2: Charge states of the capacitors C_{1sc}, C_{2sc} and C_{3sc} of the Split-Pi converter written in function of the flat outputs generated by the algorithm as in (3.3.38a)- (3.3.38d). The error between the charge states of (3.3.39c)- (3.3.39e)) and (3.3.32c)-(3.3.32e) is depicted.

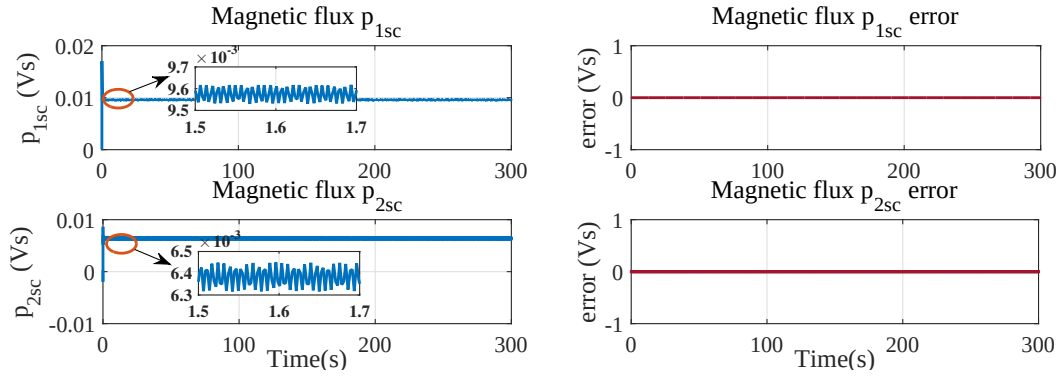

Figure A.2.3: Magnetic flux states of the inductors I_{1sc} and I_{2sc} of the Split-Pi converter in function of the second set of flat outputs as in (3.3.38). The error between the magnetic flux states of (3.3.42a)-(3.3.42b) and (3.3.32a)-(3.3.32b) is depicted.

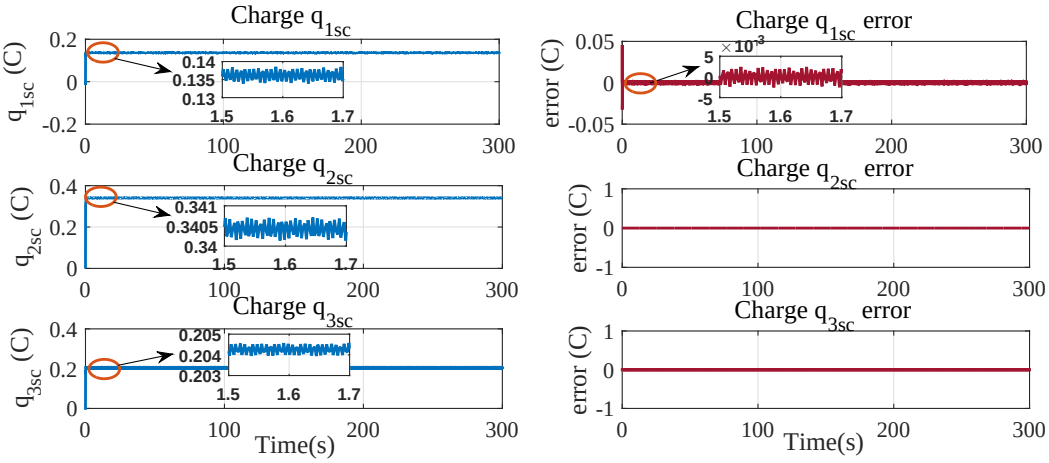

Figure A.2.4: Charge states of the capacitors C_{1sc}, C_{2sc} and C_{3sc} of the Split-Pi converter in function of the flat outputs generated by the algorithm in (3.3.28). The error between the charge states of (3.3.29c), (3.3.42c), (3.3.42d), (3.3.42e) and of (3.3.32c), (3.3.32d), (3.3.32e) is depicted.

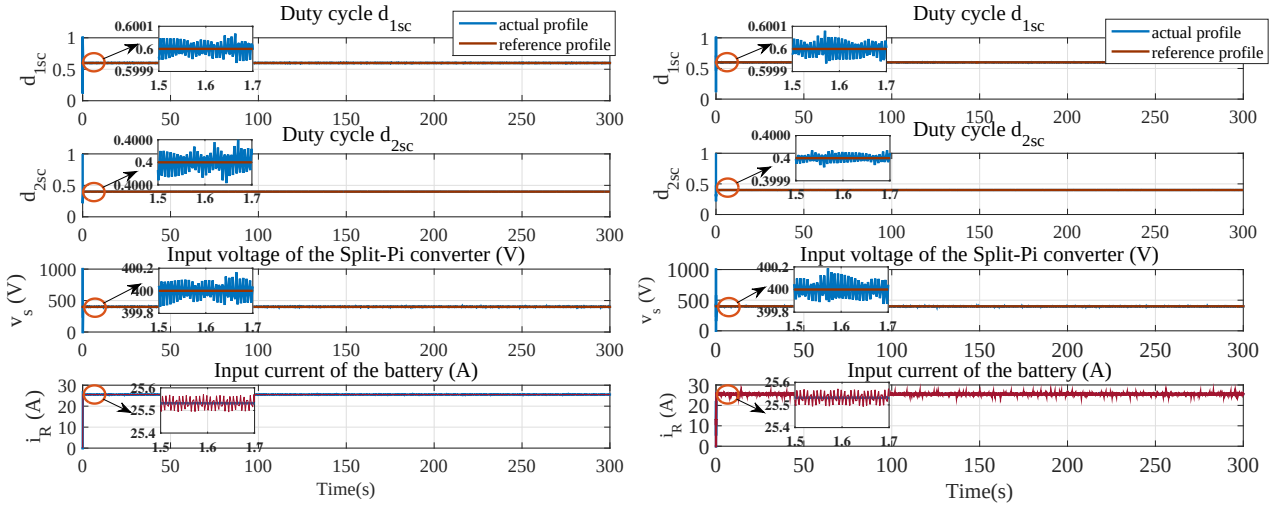

(a) (b)

Figure A.2.5: (a) Signal response of the control inputs after filtering the derivatives shown in the Split-Pi converter system flat representation in (3.3.39f)-(3.3.39i). (b) Signal response of the control inputs after filtering the derivatives shown in the ES system flat representation with the set of random flat outputs (3.3.42f-3.3.42i) is depicted.

Appendix B

Supplementary calculations for the cost functions and the constraints

B.1 Detailed calculation of the J_{es}

In the following, the detailed calculation of the J_{es} of the cost function in (4.3.11a) is presented:

$$\mathcal{J}_{es} = \int_{t_0}^{t_f} e(t) \left[\frac{1}{C_{2b}} \left(\sum_{i=1}^{N} \boldsymbol{p}_i \boldsymbol{b}_{i,\boldsymbol{d}}(t) \right) + R_{2b} \left(\sum_{i=1}^{N} \boldsymbol{p}_i \mathcal{M}_{\boldsymbol{d},\boldsymbol{d}-1} \boldsymbol{b}_{i,\boldsymbol{d}-1}(t) \right) \right] \cdot \tag{B.1.1}$$
$$\cdot \left[\left(\frac{C_{1b}}{C_{2b}} + 1 \right) \left(\sum_{i=1}^{N} \boldsymbol{p}_i \mathcal{M}_{\boldsymbol{d},\boldsymbol{d}-1} \boldsymbol{b}_{i,\boldsymbol{d}-1}(t) \right) + C_{1b} R_{2b} \left(\sum_{i=1}^{N} \boldsymbol{p}_i . \mathcal{M}_{\boldsymbol{d},\boldsymbol{d}-2} . \boldsymbol{b}_{i,\boldsymbol{d}-2}(t) \right) \right] \mathrm{d}t$$

The previous multiplication in (B.1.1) concludes in a 4-term relation and we proceed to the calculation of each term separately:

$$Term_1 = \left(\frac{C_{1b}}{C_{2b}^2} + \frac{1}{C_{2b}} \right) \int_{t_0}^{t_f} e(t) \left(\sum_{i=1}^{N} \boldsymbol{p}_i \boldsymbol{b}_{i,\boldsymbol{d}}(t) \right)^T \left(\sum_{j=1}^{N} \left(\mathcal{P} M_{\boldsymbol{d},\boldsymbol{d}-1} \right)_j \boldsymbol{b}_{j,\boldsymbol{d}-1}(t) \right) \mathrm{d}t =$$
$$= \left(\frac{C_{1b}}{C_{2b}^2} + \frac{1}{C_{2b}} \right) \sum_{i=1}^{N} \sum_{j=1}^{N} \boldsymbol{p}_i \left(\mathcal{P} M_{\boldsymbol{d},\boldsymbol{d}-1} \right)_j \int_{t_0}^{t_f} e(t) \boldsymbol{b}_{i,\boldsymbol{d}}(t) \boldsymbol{b}_{j,\boldsymbol{d}-1}(t) \mathrm{d}t.$$

Since the $Term_1$ results in scalar values, the obtained objective function will be in quadratic form. Similarly, we continue with the calculation of the other terms:

$$Term_2 = \frac{C_{1b} R_{2b}}{C_{2b}} \sum_{i=1}^{N} \sum_{j=1}^{N} \mathcal{P}_i \left(\mathcal{P} \mathcal{M}_{\boldsymbol{d},\boldsymbol{d}-2} \right)_j \int_{t_0}^{t_f} e(t) \cdot \boldsymbol{b}_{i,\boldsymbol{d}}(t) \boldsymbol{b}_{j,\boldsymbol{d}-2}(t) \mathrm{d}t,$$

$$Term_3 = C_{1b} R_{2b} \left(\frac{1}{C_{2b}} + \frac{1}{C_{1b}} \right) \sum_{i=1}^{N} \sum_{j=1}^{N} \left(\mathcal{P} \mathcal{M}_{\boldsymbol{d},\boldsymbol{d}-1} \right)_i \left(\mathcal{P} \mathcal{M}_{\boldsymbol{d},\boldsymbol{d}-1} \right)_j \int_{t_0}^{t_f} e(t) \boldsymbol{b}_{i,\boldsymbol{d}-1}(t) \cdot \boldsymbol{b}_{j,\boldsymbol{d}-1}(t) \mathrm{d}t,$$

$$Term_4 = C_{1b} R_{2b}^2 \sum_{i=1}^{N} \sum_{j=1}^{N} \left(\mathcal{P} \mathcal{M}_{\boldsymbol{d},\boldsymbol{d}-1} \right)_i \left(\mathcal{P} \mathcal{M}_{\boldsymbol{d},\boldsymbol{d}-2} \right)_j \cdot \int_{t_0}^{t_f} e(t) \boldsymbol{b}_{i,\boldsymbol{d}-1}(t) \boldsymbol{b}_{j,\boldsymbol{d}-2}(t) \mathrm{d}t.$$

B.2 Theorem from B-splines theory

Below a theorem of the B-splines is presented considered for the B-spline parametrization of the α factor in (4.3.26a).

Theorem B.2.1. *(Stoican et al., 2017): Given scalars $\underline{z}, \overline{z} \in \mathbb{R}$ and a B-spline curve define by $z(t) = \sum_{i=1}^{n} \mathbf{p}_i \mathbf{b}_{i,\mathbf{d}}(t)$ and a knot vector T, a sufficient condition for the validation of*

$$\underline{z} \leq z(t) \leq \overline{z}$$

for any $t \in [\tau_\kappa, \tau_{\kappa+1}] \in T$ is that:

$$\underline{z} \leq p_i \leq \overline{z}, \qquad \kappa - \mathbf{d} + 1 \leq i \leq \kappa$$

B.3 Supplementary calculation for the B-splines

For the constraints (4.3.30a,4.3.30b), we give explicitly the calculations for their B-spline parametrization. From (4.3.10a), (4.3.10b), (4.3.27) and the B-splines properties from section 4.2.2, we continue as follows (Consider that $\boldsymbol{b}_{i,j,\boldsymbol{d}}(t) = \boldsymbol{b}_{i,\boldsymbol{d}}(t)\boldsymbol{b}_{j,\boldsymbol{d}}(t)$ where $1 \leq i$ and $j \leq n$ and $\boldsymbol{d} = \boldsymbol{d}_\alpha$):

$$\begin{aligned}
\frac{v_b(t) + i_b(t)R_{1b}}{\alpha(t)} &= \left[\sum_{i=1}^{n} \boldsymbol{p}_{k,i}^{v_b} \boldsymbol{b}_{i,\boldsymbol{d}}(t) + R_{1b} \sum_{i=1}^{n} \boldsymbol{p}_{\kappa,i}^{i_b} \boldsymbol{b}_{i,\boldsymbol{d}}(t)\right] \sum_{j=1}^{n_\alpha} \boldsymbol{p}_j^\alpha \boldsymbol{b}_{j,\boldsymbol{d}_\alpha}(t) = \\
&= \sum_{i=1}^{n} \sum_{j=1}^{n_\alpha} (\boldsymbol{p}_{\kappa,i}^{v_b} + R_{1b} \boldsymbol{p}_{k,i}^{i_b}) \boldsymbol{p}_j^\alpha \boldsymbol{b}_{i,j,\boldsymbol{d}}(t)
\end{aligned} \tag{B.3.1a}$$

$$\begin{aligned}
R_{1sc}|i_b(t)| &= R_{1sc} \left| \sum_{i=1}^{n} \boldsymbol{p}_{\kappa,i}^{i_b} \boldsymbol{b}_{i,\boldsymbol{d}}(t) \right| \leq R_{1sc} \left| \sum_{i=1}^{n} \boldsymbol{p}_{\kappa,i}^{i_b} \boldsymbol{b}_{i,\boldsymbol{d}}(t) \right| \sum_{j=1}^{n_\alpha} \boldsymbol{p}_j^\alpha \boldsymbol{b}_{j,\boldsymbol{d}_\alpha}(t) \leq \\
&\leq R_{1sc} \sum_{i=1}^{n} \left| \boldsymbol{p}_{\kappa,i}^{i_b} \right| \left| \boldsymbol{b}_{i,\boldsymbol{d}}(t) \right| \sum_{j=1}^{n_\alpha} \boldsymbol{p}_j^\alpha \boldsymbol{b}_{j,\boldsymbol{d}_\alpha}(t) \leq R_{1sc} \sum_{i=1}^{n} \left| \boldsymbol{p}_{\kappa,i}^{i_b} \right| \boldsymbol{b}_{i,\boldsymbol{d}}(t) \sum_{j=1}^{n_\alpha} \boldsymbol{p}_j^\alpha \boldsymbol{b}_{j,\boldsymbol{d}_\alpha}(t) = \\
&= \sum_{i=1}^{n} \sum_{j=1}^{n_\alpha} R_{1sc} \left| \boldsymbol{p}_{\kappa,i}^{i_b} \right| \boldsymbol{p}_j^\alpha \boldsymbol{b}_{i,j,\boldsymbol{d}}(t)
\end{aligned} \tag{B.3.1b}$$

Afterwards, placing (B.3.1a), (B.3.1b) in (4.3.31a) and 4.3.31b) we obtain:

$$\begin{aligned}
v_{DC}^{min,h} &\leq \sum_{i=1}^{n} \sum_{j=1}^{n_\alpha} (\boldsymbol{p}_{\kappa,i}^{v_b} + R_{1b} \boldsymbol{p}_{\kappa,i}^{i_b}) \boldsymbol{p}_j^\alpha \boldsymbol{b}_{i,j,\boldsymbol{d}}(t) - \sum_{i=1}^{n} \sum_{j=1}^{n_\alpha} R_{1sc} |\boldsymbol{p}_{\kappa,i}^{i_b}| \boldsymbol{p}_j^\alpha \boldsymbol{b}_{i,j,\boldsymbol{d}}(t) \leq \\
&\leq \sum_{i=1}^{n} \sum_{j=1}^{n_\alpha} \left[\boldsymbol{p}_{\kappa,i}^{v_b} + R_{1b} \boldsymbol{p}_{\kappa,i}^{i_b} - R_{1sc} |\boldsymbol{p}_{\kappa,i}^{i_b}|\right] \boldsymbol{p}_j^\alpha \boldsymbol{b}_{i,j,\boldsymbol{d}}(t),
\end{aligned} \tag{B.3.2a}$$

$$\begin{aligned}
v_{DC}^{max,h} &\geq \sum_{i=1}^{n} \sum_{j=1}^{n_\alpha} (\boldsymbol{p}_{\kappa,i}^{v_b} + R_{1b} \boldsymbol{p}_{\kappa,i}^{i_b}) \boldsymbol{p}_j^\alpha \boldsymbol{b}_{i,j,\boldsymbol{d}}(t) + \sum_{i=1}^{n} \sum_{j=1}^{n_\alpha} R_{1sc} |\boldsymbol{p}_{\kappa,i}^{i_b}| \boldsymbol{p}_j^\alpha \boldsymbol{b}_{i,j,\boldsymbol{d}}(t) \geq \\
&\geq \sum_{i=1}^{n} \sum_{j=1}^{n_\alpha} \left[(\boldsymbol{p}_{\kappa,i}^{v_b} + R_{1b} \boldsymbol{p}_{\kappa,i}^{i_b}) + R_{1sc} |\boldsymbol{p}_{\kappa,i}^{i_b}|\right] \boldsymbol{p}_j^\alpha \boldsymbol{b}_{i,j,\boldsymbol{d}}(t).
\end{aligned} \tag{B.3.2b}$$

where $\kappa - \boldsymbol{d} + 1 \leq i, j \leq \kappa$.

Bibliography

Adibi, M., van der Woude, J. W., and Jeltsema, D. (2017). A port-hamiltonian approach to secondary voltage control of microgrids. In *2017 IEEE PES Innovative Smart Grid Technologies Conference Europe (ISGT-Europe)*, pages 1–6. IEEE. 14

Agence Nationale de la Recherche, A. N. R. (2016). Components control communication for DC microgrid – $C^3\mu$. 8

Ahumada, C., Cárdenas, R., Saez, D., and Guerrero, J. M. (2015). Secondary control strategies for frequency restoration in islanded microgrids with consideration of communication delays. *IEEE Transactions on Smart Grid*, 7(3):1430–1441. 76

Allgöwer, F. and Zheng, A. (2012). *Nonlinear model predictive control*, volume 26. Birkhäuser. 80

Aranda-Bricaire, E., Moog, C., and Pomet, J.-B. (1995). A linear algebraic framework for dynamic feedback linearization. *IEEE Transactions on Automatic Control*, 40(1):127–132. 48

Atia, R. and Yamada, N. (2016). Sizing and analysis of renewable energy and battery systems in residential microgrids. *IEEE Transactions on Smart Grid*, 7(3):1204–1213. 3

Baghaee, H. R., Mirsalim, M., and Gharehpetian, G. B. (2016). Performance improvement of multi-der microgrid for small-and large-signal disturbances and nonlinear loads: novel complementary control loop and fuzzy controller in a hierarchical droop-based control scheme. *IEEE Systems Journal*, 12(1):444–451. 75

Berger, M. and Gostiaux, B. (2012). *Differential Geometry: Manifolds, Curves, and Surfaces: Manifolds, Curves, and Surfaces*, volume 115. Springer Science & Business Media. v

Bergna-Diaz, G., Zonetti, D., Sanchez, S., Tedeschi, E., and Ortega, R. (2017). Pi passivity-based control of modular multilevel converters for multi-terminal hvdc systems. In *2017 IEEE 18th Workshop on Control and Modeling for Power Electronics (COMPEL)*, pages 1–8. IEEE. 14

Bertsekas, D. P. (2014). *Constrained optimization and Lagrange multiplier methods*. Academic press. 77

Biegler, L. T. and Zavala, V. M. (2009). Large-scale nonlinear programming using ipopt: An integrating framework for enterprise-wide dynamic optimization. *Computers & Chemical Engineering*, 33(3):575–582. 96

Borutzky, W. (2010). Bond graph based physical systems modelling. *Bond Graph Methodology: Development and Analysis of Multidisciplinary Dynamic System Models*, pages 17–88. 19

Bourbaki, N. (2003). *Elements of mathematics: Algebra*. Springer. v

Bouzid, A. M., Guerrero, J. M., Cheriti, A., Bouhamida, M., Sicard, P., and Benghanem, M. (2015). A survey on control of electric power distributed generation systems for microgrid applications. *Renewable and Sustainable Energy Reviews*, 44:751–766. 75

Braunschweig, B. and Gani, R. (2002). *Software architectures and tools for computer aided process engineering*, volume 11. Elsevier. 6

Cairoli, P. and Dougal, R. A. (2017). Fault detection and isolation in medium-voltage dc microgrids: Coordination between supply power converters and bus contactors. *IEEE Transactions on Power Electronics*, 33(5):4535–4546. 4

Cannon, J. W. et al. (1978). The recognition problem: what is a topological manifold? *Bulletin of the American Mathematical Society*, 84(5):832–866. v

CIAT company, U. T. C. (2014). Temperature and irradiation data. http://www.ciat.fr/. 81

Crocker, T. R. (2005). Power converter and method for power conversion. US Patent 6,914,420. 5, 14, 17, 29, 96

David C. Royster, D. C. R. (1998). Implicit function therorem. http://www.ms.uky.edu/~droyster/courses/fall98/math4080/classnotes/implfuncthm.pdf. Department of Mathematics, University of Kentucky. 48

Department of Energy Office of Energy Efficiency & Renewable Energy, E. E. R. E. (2017). Commercial and residential hourly load profiles. https://openei.org/datasets/files/961/pub/. 55, 81

Dragičević, T. (2017). Model predictive control of power converters for robust and fast operation of ac microgrids. *IEEE Transactions on Power Electronics*, 33(7):6304–6317. 7

Drgoňa, J., Picard, D., Kvasnica, M., and Helsen, L. (2018). Approximate model predictive building control via machine learning. *Applied Energy*, 218:199–216. 75

Duindam, V., Macchelli, A., Stramigioli, S., and Bruyninckx, H. (2009). *Modeling and control of complex physical systems: the port-Hamiltonian approach*. Springer Science & Business Media. 6, 23, 24, 115

Ellis, M., Durand, H., and Christofides, P. D. (2014). A tutorial review of economic model predictive control methods. *Journal of Process Control*, 24(8):1156–1178. 79

Elsayed, A. T., Mohamed, A. A., and Mohammed, O. A. (2015). Dc microgrids and distribution systems: An overview. *Electric Power Systems Research*, 119:407–417. 40

Enrique, J., Duran, E., Sidrach-de Cardona, M., and Andujar, J. (2007). Theoretical assessment of the maximum power point tracking efficiency of photovoltaic facilities with different converter topologies. *Solar Energy*, 81(1):31–38. 26

Escobar, G., van der Schaft, J., and Ortega, R. (2015). A hamiltonian viewpoint in the modeling of switching power converters. *Automatica*, 35:445–45. 1, 17, 23, 31

Fallahzadeh-Abarghouei, H., Hasanvand, S., Nikoobakht, A., and Doostizadeh, M. (2018). Decentralized and hierarchical voltage management of renewable energy resources in distribution smart grid. *International Journal of Electrical Power & Energy Systems*, 100:117–128. 75

Farina, M., Giulioni, L., and Scattolini, R. (2016). Stochastic linear model predictive control with chance constraints–a review. *Journal of Process Control*, 44:53–67. 75

Fiaz, S., Zonetti, D., Ortega, R., Scherpen, J. M., and Van der Schaft, A. (2013). A port-hamiltonian approach to power network modeling and analysis. *European Journal of Control*, 19(6):477–485. 14

Flick, T. and Morehouse, J., editors (2011). *Securing the Smart Grid: Next Generation Power Grid Security*. Elsevier. 2, 3

Fliess, M., Lévine, J., Martin, P., and Rouchon, P. (1993). Differential flatness and defect: an overview. In *Workshop on Geometry in Nonlinear Control, Banach Center Publications, Warsaw*. 45

Fliess, M., Lévine, J., Martin, P., and Rouchon, P. (1995). Flatness and defect of non-linear systems: introductory theory and examples. *International journal of control*, 61(6):1327–1361. 7, 45, 46, 63, 115

Fossati, J. P., Galarza, A., Martín-Villate, A., and Fontan, L. (2015). A method for optimal sizing energy storage systems for microgrids. *Renewable Energy*, 77:539–549. 3, 6

Franke, M. and Robenack, K. (2013). On the computation of flat outputs for nonlinear control systems. In *Control Conference (ECC), 2013 European*, pages 167–172. IEEE. 8, 9, 45, 46, 47, 48, 73, 115

Gamarra, C. and Guerrero, J. M. (2015). Computational optimization techniques applied to microgrids planning: A review. *Renewable and Sustainable Energy Reviews*, 48:413–424. 76

Gavagsaz-Ghoachani, R., Saublet, L.-M., Martin, J.-P., Nahid-Mobarakeh, B., and Pierfederici, S. (2016). Stability analysis and active stabilization of dc power systems for electrified transportation systems, taking into account the load dynamics. *IEEE Transactions on Transportation Electrification*, 3(1):3–12. 76

Gavriluta, C., Candela, I., Luna, A., Gomez-Exposito, A., and Rodriguez, P. (2015). Hierarchical control of hv-mtdc systems with droop-based primary and opf-based secondary. *IEEE Transactions on Smart Grid*, 6(3):1502–1510. 32

Gawthrop, P. (1994). Bicausal bond graphs. *SIMULATION SERIES*, 27:83–83. 45, 61

Gil, J. C., Pedraza, A., Delgado, M., and Sira-Ramirez, H. (1997). Flatness and passivity from a bond graph. In *1997 IEEE International Conference on Systems, Man, and Cybernetics. Computational Cybernetics and Simulation*, volume 2, pages 1516–1521. IEEE. 45

Guerrero, J. M., Chandorkar, M., Lee, T.-L., and Loh, P. C. (2012). Advanced control architectures for intelligent microgrids—part i: Decentralized and hierarchical control. *IEEE Transactions on Industrial Electronics*, 60(4):1254–1262. 7

Guerrero, J. M., Chandorkar, M., Lee, T. L., and Loh, P. C. (2013). Advanced control architectures for intelligent microgrids, part i: decentralized and hierarchical control. *IEEE Transactions on Industrial Electronics*, 60:1254–1262. 3

Guerrero, J. M., Vasquez, J. C., Matas, J., De Vicuña, L. G., and Castilla, M. (2011). Hierarchical control of droop-controlled ac and dc microgrids—a general approach toward standardization. *IEEE Transactions on industrial electronics*, 58(1):158–172. 76

Guo, L., Zhang, S., Li, X., Li, Y. W., Wang, C., and Feng, Y. (2016). Stability analysis and damping enhancement based on frequency-dependent virtual impedance for dc microgrids. *IEEE Journal of emerging and selected topics in power electronics*, 5(1):338–350. 4

Hadjeras, S., Sanchez, C. A., and Garcia, G. (2017). Hybrid adaptive control of the boost converter. In *2017 IEEE 56th Annual Conference on Decision and Control (CDC)*, pages 5720–5725. IEEE. 76

Haileselassie, T. M. and Uhlen, K. (2013). Power system security in a meshed north sea hvdc grid. *Proceedings of the IEEE*, 101:978–990. 3

Hatziargyriou, N., Jenkins, N., Strbac, G., Lopes, J. P., Ruela, J., Engler, A., Oyarzabal, J., Kariniotakis, G., Amorim, A., et al. (2006). Microgrids–large scale integration of microgeneration to low voltage grids. *CIGRE C6-309*. 1

Herrera, L., Zhang, W., and Wang, J. (2015). Stability analysis and controller design of dc microgrids with constant power loads. *IEEE Transactions on Smart Grid*, 8(2):881–888. 4

Hervagault, Y., Prodan, I., and Lefèvre, L. (2019). Motion planning for usvs with communication guarantees: an experimental setup. In *2019 18th European Control Conference (ECC)*, pages 3984–3989. IEEE. 45

Hirsch, A., Parag, Y., and Guerrero, J. (2018). Microgrids: A review of technologies, key drivers, and outstanding issues. *Renewable and Sustainable Energy Reviews*, 90:402–411. 1

Hughes, T. P. (1993). *Networks of power: electrification in Western society, 1880-1930*. JHU Press. 1

Iovine, A., Rigaut, T., Damm, G., De Santis, E., and Di Benedetto, M. D. (2018). Power management for a dc microgrid integrating renewables and storages. *Control Engineering Practice*. 108

Iovine, A., Siad, S. B., Damm, G., De Santis, E., and Di Benedetto, M. D. (2017). Nonlinear control of a dc microgrid for the integration of photovoltaic panels. *IEEE Transactions on automation science and engineering*, 14(2):524–535. 3, 4, 76

Jin, Z., Sulligoi, G., Cuzner, R., Meng, L., Vasquez, J. C., and Guerrero, J. M. (2016). Next-generation shipboard dc power system: Introduction smart grid and dc microgrid technologies into maritime electrical netowrks. *IEEE Electrification Magazine*, 4(2):45–57. 2

Jongerden, M. R. and Haverkort, B. R. (2017). Battery aging, battery charging and the kinetic battery model: A first exploration. In *International Conference on Quantitative Evaluation of Systems*, pages 88–103. Springer. 16

Kamel, M., Stastny, T., Alexis, K., and Siegwart, R. (2017). Model predictive control for trajectory tracking of unmanned aerial vehicles using robot operating system. In *Robot operating system (ROS)*, pages 3–39. Springer. 79

Kanchev, H., Lu, D., Colas, F., Lazarov, V., and Francois, B. (2011). Energy management and operational planning of a microgrid with a pv-based active generator for smart grid applications. *IEEE transactions on industrial electronics*, 58(10):4583–4592. 2, 5

Karavas, C.-S., Kyriakarakos, G., Arvanitis, K. G., and Papadakis, G. (2015). A multi-agent decentralized energy management system based on distributed intelligence for the design and control of autonomous polygeneration microgrids. *Energy Conversion and Management*, 103:166–179. 6

Karnopp, D. C., Margolis, D. L., and Rosenberg, R. C. (2012). *System dynamics: modeling, simulation, and control of mechatronic systems*. John Wiley & Sons. v, 14, 19, 115

Katiraei, F., Iravani, R., Hatziargyriou, N., and Dimeas, A. (2008). Microgrids management. *IEEE power and energy magazine*, 6(3). 2

Khan, M. R. B., Jidin, R., and Pasupuleti, J. (2016). Multi-agent based distributed control architecture for microgrid energy management and optimization. *Energy Conversion and Management*, 112:288–307. 6

Khorramdel, H., Aghaei, J., Khorramdel, B., and Siano, P. (2015). Optimal battery sizing in microgrids using probabilistic unit commitment. *IEEE Transactions on Industrial Informatics*, 12(2):834–843. 3

Kofman, E., Haimovich, H., and Seron, M. M. (2007). A systematic method to obtain ultimate bounds for perturbed systems. *International Journal of Control*, 80(2):167–178. 95

Krantz, S. G. and Parks, H. R. (2012). *The implicit function theorem: history, theory, and applications*. Springer Science & Business Media. 48

Kumar, Y. P. and Bhimasingu, R. (2015). Renewable energy based microgrid system sizing and energy management for green buildings. *Journal of Modern Power Systems and Clean Energy*, 3(1):1–13. 3

Langson, W., Chryssochoos, I., Raković, S., and Mayne, D. Q. (2004). Robust model predictive control using tubes. *Automatica*, 40(1):125–133. 83, 94

Lasseter, R., Akhil, A., Marnay, C., Stephens, J., Dagle, J., Guttromson, R., Meliopoulous, A. S., Yinger, R., and Eto, J. (2002). Integration of distributed energy resources. the certs microgrid concept. 1

Lauritzen, N. (2009). Lectures on convex sets. *Notas de aula, Aarhus University: http://home. imf. au. dk/niels/lecconset. pdf*. vi

Legry, M., Colas, F., Saudemont, C., Dieulot, J.-Y., and Ducarme, O. (2018). A two-layer model predictive control based secondary control with economic performance tracking for islanded microgrids. In *IECON 2018-44th Annual Conference of the IEEE Industrial Electronics Society*, pages 77–82. IEEE. 7

Lévine, J. (2004). On flatness necessary and sufficient conditions. *IFAC Proceedings Volumes*, 37(13):123–128. 48

Levine, J. (2009). *Analysis and control of nonlinear systems: A flatness-based approach*. Springer Science & Business Media. 45, 47, 54, 66, 115

Lévine, J. (2011). On necessary and sufficient conditions for differential flatness. *Applicable Algebra in Engineering, Communication and Computing*, 22(1):47–90. 46, 48

Li, Q., Chen, F., Chen, M., Guerrero, J. M., and Abbott, D. (2015). Agent-based decentralized control method for islanded microgrids. *IEEE Transactions on Smart Grid*, 7(2):637–649. 7

Liu, L., Meng, X., and Liu, C. (2016). A review of maximum power point tracking methods of pv power system at uniform and partial shading. *Renewable and Sustainable Energy Reviews*, 53:1500–1507. 76

Locment, F. and Sechilariu, M. (2015). Modeling and simulation of dc microgrids for electric vehicle charging stations. *Energies*, 8(5):4335–4356. 5

Löfberg, J. (2004). Yalmip: A toolbox for modeling and optimization in matlab. In *Proceedings of the CACSD Conference*, volume 3. Taipei, Taiwan. 96

Lotfi, H. and Khodaei, A. (2015). Ac versus dc microgrid planning. *IEEE Transactions on Smart Grid*, 8(1):296–304. 40

Lotfi, H. and Khodaei, A. (2017a). Ac versus dc microgrid planning. *IEEE Transactions on Smart Grid*, 8(1):296–304. 2

Lotfi, H. and Khodaei, A. (2017b). Hybrid ac/dc microgrid planning. *Energy*, 118:37–46. 1

Lou, G., Gu, W., Xu, Y., Cheng, M., and Liu, W. (2017). Distributed mpc-based secondary voltage control scheme for autonomous droop-controlled microgrids. *IEEE Transactions on Sustainable Energy*, 8(2):792–804. 75

Lu, X., Guerrero, J. M., Sun, K., and Vasquez, J. C. (2013). An improved droop control method for dc microgrids based on low bandwidth communication with dc bus voltage restoration and enhanced current sharing accuracy. *IEEE Transactions on Power Electronics*, 29(4):1800–1812. 7

Lyche, T., Manni, C., and Speleers, H. (2018). Foundations of spline theory: B-splines, spline approximation, and hierarchical refinement. In *Splines and PDEs: From Approximation Theory to Numerical Linear Algebra*, pages 1–76. Springer. 78

Ma, T., Cintuglu, M. H., and Mohammed, O. A. (2016). Control of a hybrid ac/dc microgrid involving energy storage and pulsed loads. *IEEE Transactions on Industry Applications*, 53(1):567–575. 5

Macchelli, A. (2013). Port-hamiltonian formulation of simple macro-economic systems. In *52nd IEEE Conference on Decision and Control*, pages 3888–3893. IEEE. 14

Macchelli, A. (2014). Passivity-based control of implicit port-hamiltonian systems. *SIAM Journal on Control and Optimization*, 52(4):2422–2448. 117

Machado, J. T. and Mata, M. E. (2015). A fractional perspective to the bond graph modelling of world economies. *Nonlinear Dynamics*, 80(4):1839–1852. 14

Mackiw, G. (1995). A note on the equality of the columr, and row rank of a matrix. *Mathematics Magazine*, 68(4):285. v

Mahmoud, M. S., Hussain, S. A., and Abido, M. A. (2014). Modeling and control of microgrid: An overview. *Journal of the Franklin Institute*, 351(5):2822–2859. 6

Manwell, J. F. and McGowan, J. G. (1993). Lead acid battery storage model for hybrid energy systems. *Solar Energy*, 50(5):399–405. 16, 28

Mariam, L., Basu, M., and Conlon, M. F. (2016). Microgrid: Architecture, policy and future trends. *Renewable and Sustainable Energy Reviews*, 64:477–489. 4

Maschke, B. M. and van der Schaft, A. J. (1992). Port-controlled hamiltonian systems: modelling origins and systemtheoretic properties. *IFAC Proceedings Volumes*, 25(13):359–365. 47

Mayne, D. Q. (2014). Model predictive control: Recent developments and future promise. *Automatica*, 50(12):2967–2986. 76

Mayne, D. Q. and Michalska, H. (1990). Receding horizon control of nonlinear systems. *IEEE Transactions on automatic control*, 35(7):814–824. 79

Mazumder, S. K., Tahir, M., and Acharya, K. (2008). Master-slave current-sharing control of a parallel dc-dc converter system over an rf communication interface. *IEEE transactions on industrial electronics (1982)*, 55(1):59. 76

Meng, L., Sanseverino, E. R., Luna, A., Dragicevic, T., Vasquez, J. C., and Guerrero, J. M. (2016). Microgrid supervisory controllers and energy management systems: A literature review. *Renewable and Sustainable Energy Reviews*, 60:1263–1273. 3

Meng, L., Shafiee, Q., Trecate, G. F., Karimi, H., Fulwani, D., Lu, X., and Guerrero, J. M. (2017). Review on control of dc microgrids and multiple microgrid clusters. *IEEE Journal of Emerging and Selected Topics in Power Electronics*, 5(3):928–948. 8

Meshram, R. V., Bhagwat, M., Khade, S., Wagh, S. R., Stanković, A. M., and Singh, N. M. (2017). Port-controlled phasor hamiltonian modeling and ida-pbc control of solid-state transformer. *IEEE Transactions on Control Systems Technology*, 27(1):161–174. 14

Mike Boyle, M. M. B. (2012). Open subset. https://www.math.umd.edu/~mboyle/courses/410f12/open.pdf. Department of Mathematics, University of Maryland. v

Misner, C. W., Thorne, K. S., and Wheeler, J. A. (1973). *Gravitation*. W.H. Freeman & Co. v

Moehrke, F. and Myrzik, J. (2014). Control methods for microgrids. In *Power Engineering Conference (UPEC), 2014 49th International Universities*, pages 1–6. IEEE. 2

Moghimi, M., Leskarac, D., Bennett, C., Lu, J., and Stegen, S. (2016). Rule-based energy management system in an experimental microgrid with the presence of time of use tariffs. In *MATEC Web of Conferences*, volume 70, page 10011. EDP Sciences. 6

Morstyn, T., Hredzak, B., and Agelidis, V. G. (2015). Cooperative multi-agent control of heterogeneous storage devices distributed in a dc microgrid. *IEEE Transactions on Power Systems*, 31(4):2974–2986. 5

Murray, R. M., Rathinam, M., and Sluis, W. (1995). Differential flatness of mechanical control systems: A catalog of prototype systems. In *ASME international mechanical engineering congress and exposition*. Citeseer. 45

Mutarraf, M., Terriche, Y., Niazi, K., Vasquez, J., and Guerrero, J. (2018). Energy storage systems for shipboard microgrids—a review. *Energies*, 11(12):3492. 4

Nahata, P., La Bella, A., Scattolini, R., and Ferrari-Trecate, G. (2019). Hierarchical control in islanded dc microgrids with flexible structures. *arXiv preprint arXiv:1910.05107*. 76

National Renewable Energy Laboratory, N. R. E. L. (2016). Rural african commercial load profile. https://www.google.com/url?sa=t&rct=j&q=&esrc=s&source=web&cd=6&ved=2ahUKEwi50M7SzMrhAhUIqxoKHX2zCg4QFjAFegQIABAC&url=https%3A%2F%2Fdata.nrel.gov%2Ffiles%2F79%2F2%2520-%2520Microgrid_Load_Profile_Explorer.xlsx&usg=AOvVaw1puui5P8p4B3DOotHUwXjv. 81

Nguyen, N. T., Prodan, I., and Lefèvre, L. (2018). Flat trajectory design and tracking with saturation guarantees: a nano-drone application. *International Journal of Control*, pages 1–14. 45

Nguyen, N. T., Prodan, I., and Lefèvre, L. (2019). On the use of a computed-torque control law for the terminal region of an nmpc scheme. In *2019 American Control Conference (ACC)*, pages 1008–1013. IEEE. 117

Ngwompo, R. F. and Gawthrop, P. J. (1999). Bond graph-based simulation of non-linear inverse systems using physical performance specifications. *Journal of the Franklin Institute*, 336(8):1225–1247. 61

Olaru, S., De Doná, J. A., Seron, M. M., and Stoican, F. (2010). Positive invariant sets for fault tolerant multisensor control schemes. *International Journal of Control*, 83(12):2622–2640. 95

Pahlevaninezhad, M., Das, P., Drobnik, J., Jain, P. K., and Bakhshai, A. (2011). A new control approach based on the differential flatness theory for an ac/dc converter used in electric vehicles. *IEEE Transactions on power electronics*, 27(4):2085–2103. 45

Papadimitriou, C., Zountouridou, E., and Hatziargyriou, N. (2015). Review of hierarchical control in dc microgrids. *Electric Power Systems Research*, 122:159–167. 3

Parisio, A., Rikos, E., and Glielmo, L. (2014). A model predictive control approach to microgrid operation optimization. *IEEE Transactions on Control Systems Technology*, 22(5):1813–1827. 75, 108

Parisio, A., Rikos, E., and Glielmo, L. (2016). Stochastic model predictive control for economic/environmental operation management of microgrids: An experimental case study. *Journal of Process Control*, 43:24–37. 6, 7, 76

Parisio, A., Wiezorek, C., Kyntäjä, T., Elo, J., and Johansson, K. H. (2015). An mpc-based energy management system for multiple residential microgrids. In *Automation Science and Engineering (CASE), 2015 IEEE International Conference on*, pages 7–14. IEEE. 6, 34, 75

Pavlov, D. (2011). *Lead-acid batteries: science and technology*. Elsevier. 4

Paynter, H. M. (1961). *Analysis and design of engineering systems*. MIT press. 19

Pham, T. H., Prodan, I., Genon-Catalot, D., and Lefèvre, L. (2015). *Port-Hamiltonian model and load balancing for DC-microgrid lift systems*. PhD thesis, LCIS, Grenoble-INP. 6, 7, 14, 16, 45

Pham, T. H., Prodan, I., Genon-Catalot, D., and Lefevre, L. (2017). Power balancing in a dc microgrid elevator system through constrained optimization. *IFAC-PapersOnLine*, 50(1):19–24. 4

Planas, E., Andreu, J., Gárate, J. I., de Alegría, I. M., and Ibarra, E. (2015). Ac and dc technology in microgrids: A review. *Renewable and Sustainable Energy Reviews*, 43:726–749. 1

Poultney, A., Kennedy, C., Clayton, G., and Ashrafiuon, H. (2018). Robust tracking control of quadrotors based on differential flatness: Simulations and experiments. *IEEE/ASME Transactions on Mechatronics*, 23(3):1126–1137. 45

Prodan, I., Olaru, S., Bencatel, R., de Sousa, J. B., Stoica, C., and Niculescu, S.-I. (2013). Receding horizon flight control for trajectory tracking of autonomous aerial vehicles. *Control Engineering Practice*, 21(10):1334–1349. 45

Prodan, I., Stoican, F., and Louembet, C. (2019). Necessary and sufficient LMI conditions for constraints satisfaction within a B-Spline framework. In *2019 IEEE 58th Conference on Decision and Control (CDC) December 11-13, Palais des Congrés et des Expositions Nice Acropolis, Nice, France*. xiv, 78

Prodan, I. and Zio, E. (2014). A model predictive control framework for reliable microgrid energy management. *International Journal of Electrical Power & Energy Systems*, 61:399–409. 7, 75

Pyrkin, A., Ortega, R., Bobtsov, A., Aranovskiy, S., and Gerasimov, D. (2015). Ćuk converter full state adaptive observer design. In *Control Applications (CCA), 2015 IEEE Conference on*, pages 1254–1259. IEEE. 15

Rawlings, J. B. and Mayne, D. Q. (2009). *Model predictive control: Theory and design*. Nob Hill Pub. 6, 77, 79

Rawlings, J. B. and Muske, K. R. (1993). The stability of constrained receding horizon control. *IEEE transactions on automatic control*, 38(10):1512–1516. 79

Richard, P.-Y., Buisson, J., and Cormerais, H. (2002). Analysis of flatness using bond graphs and bicausality. *IFAC Proceedings Volumes*, 35(1):25–30. 45, 61

Rigatos, G. G. (2015a). Differential flatness theory and flatness-based control. In *Nonlinear Control and Filtering Using Differential Flatness Approaches*, pages 47–101. Springer. 45

Rigatos, G. G. (2015b). *Nonlinear control and filtering using differential flatness approaches: applications to electromechanical systems*, volume 25. Springer. 46, 47

Riverso, S., Boem, F., Ferrari-Trecate, G., and Parisini, T. (2016). Plug-and-play fault detection and control-reconfiguration for a class of nonlinear large-scale constrained systems. *IEEE Transactions on Automatic Control*, 61(12):3963–3978. 7

Rohm Semiconductors Company, R. s. c. (1997). Information for dc/dc converters. https://www.rohm.com/electronics-basics/dc-dc-converters/linear-vs-switching-regulators. 5

Sáez, D., Ávila, F., Olivares, D., Cañizares, C., and Marín, L. (2014). Fuzzy prediction interval models for forecasting renewable resources and loads in microgrids. *IEEE Transactions on Smart Grid*, 6(2):548–556. 6

Sanseverino, E., Di Silvestre, M., Badalamenti, R., Nguyen, N., Guerrero, J., and Meng, L. (2015). Optimal power flow in islanded microgrids using a simple distributed algorithm. *Energies*, 8(10):11493–11514. 76

Schiffer, J., Fridman, E., Ortega, R., and Raisch, J. (2016). Stability of a class of delayed port-hamiltonian systems with application to microgrids with distributed rotational and electronic generation. *Automatica*, 74:71–79. 6

Schiffer, J., Ortega, R., Astolfi, A., Raisch, J., and Sezi, T. (2014). Conditions for stability of droop-controlled inverter-based microgrids. *Automatica*, 50(10):2457–2469. 14

Sechilariu, M., Wang, B., and Locment, F. (2014). Power management and optimization for isolated dc microgrid. In *2014 International Symposium on Power Electronics, Electrical Drives, Automation and Motion*, pages 1284–1289. IEEE. 6

Shafiee, Q., Guerrero, J. M., and Vasquez, J. C. (2014). Distributed secondary control for islanded microgrids—a novel approach. *IEEE Transactions on power electronics*, 29(2):1018–1031. 75

Shayeghi, H., Shahryari, E., Moradzadeh, M., and Siano, P. (2019). A survey on microgrid energy management considering flexible energy sources. *Energies*, 12(11):2156. 3

Shi, W., Li, N., Chu, C.-C., and Gadh, R. (2015). Real-time energy management in microgrids. *IEEE Transactions on Smart Grid*, 8(1):228–238. 3

Simpson-Porco, J. W., Shafiee, Q., Dörfler, F., Vasquez, J. C., Guerrero, J. M., and Bullo, F. (2015). Secondary frequency and voltage control of islanded microgrids via distributed averaging. *IEEE Transactions on Industrial Electronics*, 62(11):7025–7038. 75

Singhai, M., Pilli, N., and Singh, S. (2014). Modeling and analysis of split-pi converter using state space averaging technique. In *Power Electronics, Drives and Energy Systems (PEDES), 2014 IEEE International Conference on*, pages 1–6. IEEE. 17

Smedley, K. M. and Cuk, S. (1995). Dynamics of one-cycle controlled cuk converters. *IEEE Transactions on Power Electronics*, 10(6):634–639. 5

Soheil-Hamedani, M., Zandi, M., Gavagsaz-Ghoachani, R., Nahid-Mobarakeh, B., and Pierfederici, S. (2016). Flatness-based control method: A review of its applications to power systems. In *2016 7th Power Electronics and Drive Systems Technologies Conference (PEDSTC)*, pages 547–552. IEEE. 7

Spiers, D. (2012). Batteries in pv systems. In *Practical Handbook of Photovoltaics*, pages 721–776. Elsevier. v

Stoican, F., Prodan, I., Popescu, D., and Ichim, L. (2017). Constrained trajectory generation for uav systems using a b-spline parametrization. In *Control and Automation (MED), 2017 25th Mediterranean Conference on*, pages 613–618. IEEE. 45, 79, 130

Stoustrup, J. (2009). Plug & play control: Control technology towards new challenges. *European Journal of Control*, 15(3-4):311–330. 7

Suryawan, F. (2012). *Constrained Trajectory Generation and Fault Tolerant Control Based on Differential Flatness and B-splines*. PhD thesis, School of Electrical Engineering and Computer Science, The University of Newcastle, Australia. 77, 78, 79, 115

Takagi, T. and Sugeno, M. (1985). Fuzzy identification of systems and its applications to modeling and control. *IEEE transactions on systems, man, and cybernetics*, (1):116–132. 6

Thounthong, P. and Pierfederici, S. (2010). A new control law based on the differential flatness principle for multiphase interleaved dc–dc converter. *IEEE Transactions on Circuits and Systems II: Express Briefs*, 57(11):903–907. 45

Tucci, M., Riverso, S., and Ferrari-Trecate, G. (2017). Line-independent plug-and-play controllers for voltage stabilization in dc microgrids. *IEEE Transactions on Control Systems Technology*, 26(3):1115–1123. 7

Unamuno, E. and Barrena, J. A. (2015). Hybrid ac/dc microgrids—part ii: Review and classification of control strategies. *Renewable and Sustainable Energy Reviews*, 52:1123–1134. 7

van der Schaft, A. and Jeltsema, D. (2014). Port-hamiltonian systems theory: An introductory overview. *Foundations and Trends in Systems and Control*, 1:173–378. 17

van der Schaft, A., Jeltsema, D., et al. (2014). Port-hamiltonian systems theory: An introductory overview. *Foundations and Trends® in Systems and Control*, 1(2-3):173–378. 14, 23, 24, 37, 38, 115, 117

Vandoorn, T. L., Vasquez, J. C., De Kooning, J., Guerrero, J. M., and Vandevelde, L. (2013). Microgrids: Hierarchical control and an overview of the control and reserve management strategies. *IEEE industrial electronics magazine*, 7(4):42–55. 75

Vazquez, N., Yu, S. S., Chau, T. K., Fernando, T., and Iu, H. H.-C. (2018). A fully decentralized adaptive droop optimization strategy for power loss minimization in microgrids with pv-bess. *IEEE Transactions on Energy Conversion*, 34(1):385–395. 76

Velarde, P., Valverde, L., Maestre, J., Ocampo-Martinez, C., and Bordons, C. (2017). On the comparison of stochastic model predictive control strategies applied to a hydrogen-based microgrid. *Journal of Power Sources*, 343:161–173. 75

Victron Energy, V. E. (2015). Agm 12165 lead acid battery. https://www.victronenergy.com/batteries/gel-and-agm-batteries. 37, 82

Villalva, M. G., Gazoli, J. R., and Ruppert Filho, E. (2009). Comprehensive approach to modeling and simulation of photovoltaic arrays. *IEEE Transactions on power electronics*, 24(5):1198–1208. 15, 26

Wang, B., Sechilariu, M., and Locment, F. (2012). Intelligent dc microgrid with smart grid communications: Control strategy consideration and design. *IEEE transactions on smart grid*, 3(4):2148–2156. 6, 34

Wang, B., Xian, L., Manandhar, U., Ye, J., Zhang, X., Gooi, H. B., and Ukil, A. (2019). Hybrid energy storage system using bidirectional single-inductor multiple-port converter with model predictive control in dc microgrids. *Electric Power Systems Research*, 173:38–47. 76

Wang, P., Lu, X., Yang, X., Wang, W., and Xu, D. (2015). An improved distributed secondary control method for dc microgrids with enhanced dynamic current sharing performance. *IEEE Transactions on Power Electronics*, 31(9):6658–6673. 75

Wei, C., Fadlullah, Z. M., Kato, N., and Stojmenovic, I. (2014). On optimally reducing power loss in microgrids with power storage devices. *IEEE Journal on Selected Areas in Communications*, 32(7):1361–1370. 76

Weisstein, E. W. (1999-2019). Tangent space. http://mathworld.wolfram.com/TangentSpace.html. A Wolfram Web Resource. v

Weisstein, E. W. (2006). Convex hull. vi

Whaite, S., Grainger, B., and Kwasinski, A. (2015). Power quality in dc power distribution systems and microgrids. *Energies*, 8(5):4378–4399. 2

Yoldaş, Y., Önen, A., Muyeen, S., Vasilakos, A. V., and Alan, İ. (2017). Enhancing smart grid with microgrids: Challenges and opportunities. *Renewable and Sustainable Energy Reviews*, 72:205–214. 5

Yu, S., Maier, C., Chen, H., and Allgöwer, F. (2013). Tube mpc scheme based on robust control invariant set with application to lipschitz nonlinear systems. *Systems & Control Letters*, 62(2):194–200. 94

Zafeiratou, I., Nguyen, D., Prodan, I., Lefèvre, L., and Piétrac, L. (2018a). Flatness-based hierarchical control of a meshed dc microgrid. *IFAC-PapersOnLine*, 51(20):222–227. 4, 7

Zafeiratou, I., Prodan, I., Lefèvre, L., and Piétrac, L. (2018b). Dynamical modelling of a dc microgrid using a port-hamiltonian formalism. *IFAC-PapersOnLine*, 51(2):469–474. 5, 6

Zubieta, L. E. (2016). Are microgrids the future of energy?: Dc microgrids from concept to demonstration to deployment. *IEEE Electrification Magazine*, 4(2):37–44. 2, 5